EVALUATION OF STEEL H-PILES WITH LOCALIZED CORROSION AND REHABILITATION USING FRICTION-TYPE BOLTED STEEL PLATES

A Dissertation

Presented to

the Faculty of the Department of Civil and Environmental Engineering

University of Houston

In Partial Fulfillment

of the Requirements for the Degree

Doctor of Philosophy

in Civil Engineering

by

Cheng Shi

December 2015

EVALUATION OF STEEL H-PILES WITH LOCALIZED CORROSION AND REHABILITATION USING FRICTION-TYPE BOLTED STEEL PLATES

Cheng Shi

Approved:

Chair of the Committee
Dr. Abdeldjelil Belarbi, Hugh Roy and Lillie Cranz Cullen Distinguished Professor,
Civil and Environmental Engineering

Co-Chair of the Committee
Dr. Mina Dawood, Associate Professor,
Civil and Environmental Engineering

Committee Members:

Dr. Reagan Herman, Instructional and Research Associate Professor,
Civil and Environmental Engineering

Dr. Ashraf Ayoub, Professor and Royal Academy of Engineering Pell Frischmann Chair,
Civil Engineering,
City University London

Dr. Sang-Wook Bae, Assistant Professor,
Civil, Environmental, and Construction Engineering,
Texas Tech University

Dr. Suresh K. Khator, Associate Dean,
Cullen College of Engineering

Dr. Roberto Ballarini
Thomas and Laura Hsu Professor and Chair,
Civil and Environmental Engineering

ACKNOWLEDGEMENTS

The research presented in this dissertation was funded by Texas Department of Transportation (TxDOT) on Project 0-6731 Repair Systems for Deteriorated Bridge Piles. The experimental funding was provided by TxDOT; and the license of numerical software was provided by University of Houston. Their generous supports are gratefully acknowledged.

I would like to convey my sincere appreciation to my research advisors, Professor Abdeldjelil Belarbi and Professor Mina Dawood. Their generous guidance, patience, and inspiration are paramount to my research and life. The support from the dissertation committee members is truly appreciated. The criticisms and suggestions from Professor Reagan Herman, Professor Ashraf Ayoub, and Professor Sangwook Bae, are of vital importance to the completion of this dissertation.

My sincere gratitude also goes to the technician staff. The experimental work of this research could not be completed without the assistances of Mr. Gerald McTigret and Mr. Jeff Miller. The assistances from many undergraduate and graduate students are crucial to this research, including but not limited to Dr. Mossab W. El-Tahan, Dr. Qian Li, Dr. Guang Yang, Dr. Yiqun Yan, Mr. Botong Zheng, Mr. Meng Liu, Mr. Prakash Poudel, Mr. Farshid Hosseini, Mr. Hazem Amer, Mr. Mehdi Zomorodian, Ms. Dongmei Pan, and Ms. Florentia Kavoura. Special thanks go to Dr. Hossein Karagah, who worked with me on the same project and provided valuable assistance during these four years.

Finally, I would like to thank my friends and family. With your support, I was able to enjoy such a wonderful adventure in the U.S. Special thanks to my husband, Shuai Fan, for his tireless patience, generosity, and support all the time.

EVALUATION OF STEEL H-PILES WITH LOCALIZED CORROSION AND REHABILITATION USING FRICTION-TYPE BOLTED STEEL PLATES

An Abstract

of a

Dissertation

Presented to

the Faculty of the Department of Civil and Environmental Engineering

University of Houston

In Partial Fulfillment
of the Requirements for the Degree
Doctor of Philosophy
in Civil Engineering

by

Cheng Shi

December 2015

ABSTRACT

The work presented in this dissertation has two major research objectives related to steel bridge piles with severe but localized corrosion: (1) development of a numerical framework to predict the axial capacity of the corroded piles, and (2) development and evaluation of a friction-type bolted steel plate-based rehabilitation system to be used for the repair of corroded piles.

To accomplish the first research objective, an investigation of the remaining compressive capacity of H-piles with simulated corrosion was carried out. This included an experimental program and numerical simulations. Seven 15-ft-long HP12×53 piles were machined to simulate the section loss due to corrosion and tested under uniaxial compression load. The results obtained from the experimental study of corroded piles were used (1) as a validation for the developed numerical framework, and (2) as a control group of experimental investigation of the proposed repair system. A finite element model was developed and validated using the experimental results of this study. A parametric study was carried out using the model to investigate the effects of parameters including slenderness of the corroded flange and web, slenderness of the pile, location and extent of the corroded region, and the magnitude of residual stresses. The results indicated that flange thickness reduction is a critical factor influencing the remaining capacity of partially corroded H-piles. The results also demonstrated that increasing pile slenderness and residual stresses reduce the capacity of piles that fail by flexural buckling but have negligible effect on piles that fail by flange/web local buckling.

To achieve the second objective of this study, a friction-type bolted plate-based repair system was proposed. In this proposed method the applied axial load is transferred from the original pile to the steel repair plates through friction at the interface between the pile flanges and the steel repair plates.

The evaluation of the retrofitted piles consisted of both experimental and numerical programs. Seven piles with the same configurations as the corroded control group were repaired and tested under axial compression. The experimental results demonstrated the effectiveness of

the rehabilitation method by ensuring acceptable axial capacity and stiffness. A finite element analysis was conducted to study the factors that influence the efficiency of the repair system, including the length of the steel plates, the magnitude of bolt pretension and slip resistance. The findings indicated that increases of the length of the repair system, magnitude of bolt pretension and slip resistance can enhance the capacity of pile with local failure within the corroded region. These three factors do not have a significant strengthening effect if a pile fails by flexural buckling.

TABLE OF CONTENTS

LIST OF FIGURES

LIST OF TABLES

NOTATIONS

a	Edge distance of the bolts
A_{rc}	Remaining cross sectional area of corroded region of the pile
A_g	Cross sectional area of original un-damaged pile
b_f	Flange width
b_{pl}	Width of the plates
d	Bolt diameter
d_h	Hole diameter
E	Elastic modulus of steel
E_s	Modulus of elasticity of soil
E_p	Modulus of elasticity of pile
F_y	Yield stress of steel
F_u	Ultimate stress of steel
I_p	Moment of inertia of pile in the plane of buckling
K	Effective length factor
K_h	Hole size factor
K_s	Surface condition factor
l	Clear length of pile
L	Length of the simply supported pile
L_{cr}	Extent of corrosion
L_d	Development length of repair system
L_f	Length of fixity of pile embedded in soil
N_{avg}	Average standard blow count for energy ratio of 0.7
N_s	Number of slip planes per bolt
P_{FEA}	Axial capacity predicted by FEA
$P_{n,u}$	Demanding axial capacity of a pile
$P_{n,c}$	Remaining axial capacity of a corroded pile
$P_{n,r}$	Axial load transferred though friction by repair system
P_t	Minimum required bolt tension
P_{Test}	Axial capacity obtained from test
q_u	Undrained compressive strength of soil
R_n	Friction force provided by one bolt in slip-critical connections
s	Bolt spacing

S_u	Undrained shear strength of clays
t	Thickness of the thinner outside plate or shape
t_f	Flange thickness of un-damaged pile
$t_{f,c}$	Flange thickness of corroded section of the pile
t_{pl}	Thickness of the plates of repair system
t_w	Web thickness of un-damaged pile
$t_{w,c}$	Web thickness of corroded section of the pile
Δ_G	Global initial imperfection
Δ_L	Local initial imperfection
σ_c	Compressive stress
σ_t	Tensile stress

CHAPTER 1 INTRODUCTION

1.1 General

The U.S. Federal Highway Administration (FHWA) reported that among all 607,380 national bridges, 11% were classified as structurally deficient due to deteriorations, cracks, or other flaws, and 24.9% were defined as functionally obsolete (ASCE, 2013).These bridges are potentially need up-to-date evaluation or rehabilitation. Besides, the average age of current U.S. bridges is 43 years (Grevello et al., 2015), while their design life is considered as 50 years. More than 30% of existing bridges have exceeded their design life (ASCE, 2013), which indicates that maintenance, rehabilitation or replacement are in an increasing need. Corrosion is a leading factor in bridge deterioration (NACE, 2013). As a substructure component of bridge, bridge piles suffer the most effects of corrosion since they are partially submerged in the water and soil. Due to the seasoning change of the water level (interface between water and air), localized corrosion occurred and became severe in the piles during their service lives, as shown in Figure 1.1. The left figure shows a bridge with steel H-shaped piles partially submerged in water and partially exposed in air. Severe corrosion can be seen on flanges and web of one pile near the water lever in the right figure. The corrosion reduces the cross sectional area of a pile and as a result reduces the thicknesses of flanges and web which makes these elements more slender.

Figure 1.1 Corroded piles from field view

The research presented in this dissertation is one component of a broader project, as illustrated in Figure 1.2, to first investigate the issue at hand and then develop repair systems for corroded steel bridge piles including design and construction guidelines. The overall objective of the research project was to develop repair systems for corroded steel bridge piles that can be applied without dewatering. Assessment of deteriorated piles and repair systems were achieved by small-scale and full-scale study experimentally and numerically. Environmental durability tests were conducted to provide further information for a life-cycle cost analysis to evaluate different repair systems. Finally, design guidelines that enhance the safety and economy of existing bridge infrastructure were proposed. Field tests with long-term monitoring will be performed.

Figure 1.2 illustrates an overview of the research work plan of the broader project. The subjects of this dissertation are highlighted in the figure, while other components of the research are reported elsewhere.

Task #1 is a rigorous survey of relevant practice nationwide to guide the remaining research. Task #2 includes reviews of various types of systems that are commercially available or currently in use for underwater repair of steel piles. Task #3 is a preliminary study on corroded piles, including experimental and numerical studies on small-scale H-piles. Task #4 includes the full-scale experiments of 7 corroded control piles and 21 retrofitted piles. Task #4 also contains finite element analyses (FEA) on both corroded and retrofitted piles and parametric studies on critical factors affecting the axial behavior of piles. Task #5 includes evaluation of the durability of the repair system by testing specimens in accelerated environmental exposure condition. Task #6 is the life-cycle cost analysis (LCCA) of the repaired systems based on the results from full scale tests in Task #4 and durability tests in Task #5. Task #7 includes the field tests and long-term monitoring. Task #8 is to develop design guidelines for repair systems to facilitate TxDOT bridge maintenance operations.

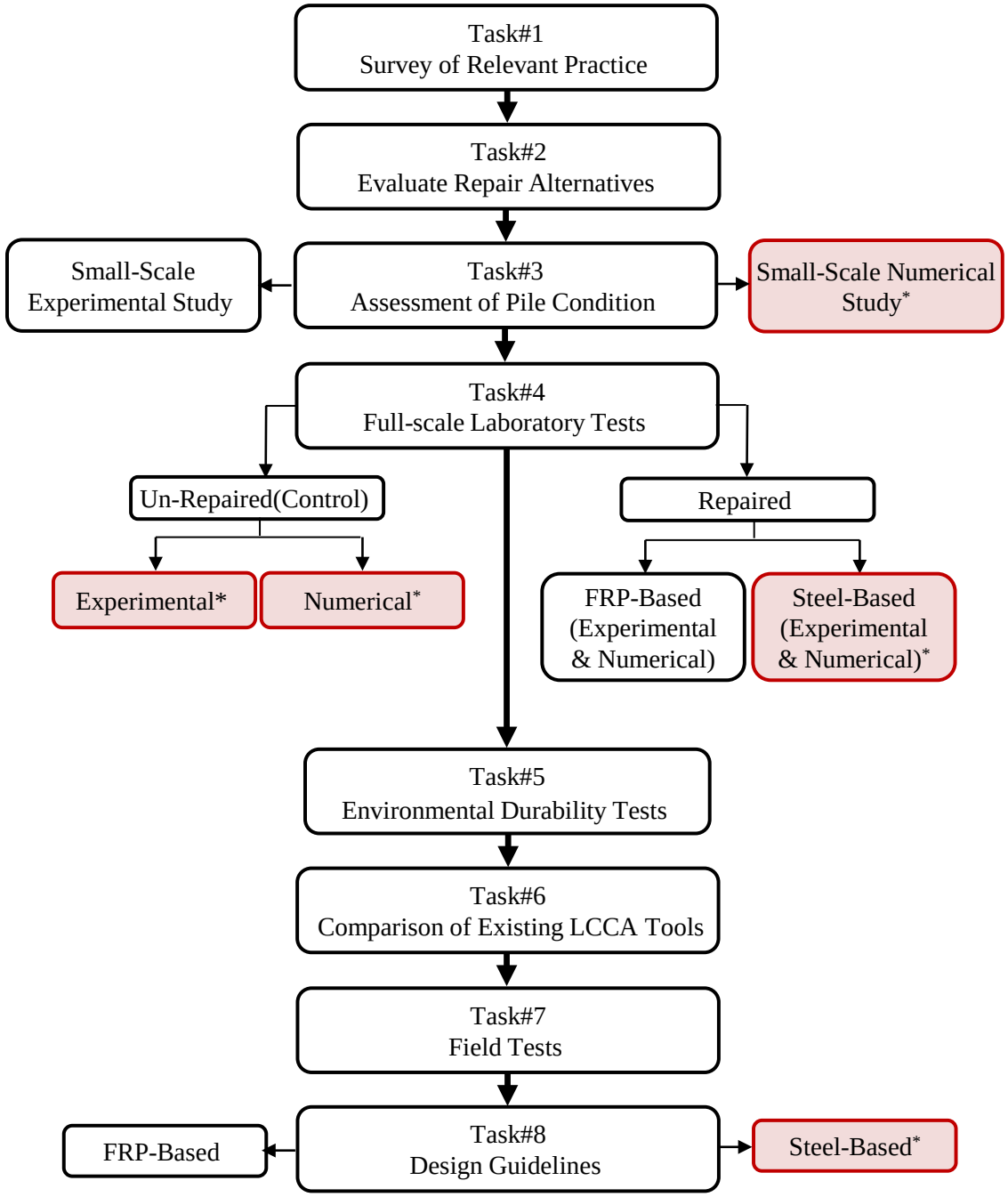

*Research included in this dissertation.

Figure 1.2 Work plan of the overall TxDOT project

1.2 Problem Definition and Research Significance

Since more than 30% of bridges in the U.S. have exceeded their design lives (ASCE, 2013), one of the most critical tasks is evaluation and maintenance/rehabilitation of current bridges. Steel bridge piles under corrosion have more slender elements due to loss of the thicknesses of flanges and web. Current design methods for compression members in bridges were not developed for members with very slender elements (AASHTO, 2012). American Iron and Steel Institute (AISI) provides design specifications for cold-formed steel members that can be used for members with very slender element (AISI, 2007). However, it does not include method for members with localized deterioration. Although enlightening studies on axial members with non-prismatic sections have been conducted (Paik et al., 2003; Nakai et al., 2004; Beaulieu et al., 2005; Liu et al., 2005; Ok et al., 2007; Moen and Schafer, 2008; Oszvald, 2012), steel H-piles with observed cross-section reduction due to corrosion have not been fully investigated. This lack of research led to comprehensive experimental and numerical studies on small-scale W-section piles with various degrees and patterns of corrosion(Karagah et al., 2015), followed by an investigation on full-scale corroded H-piles by an extensive experimental and numerical research program (Shi et al., 2016). The findings provide an in-depth understanding of the axial behavior of corroded H-piles and a reliable numerical framework to predict their remaining capacities.

Current repair systems for compressive members are based on empirical and conservative design instead of thorough understanding of the axial behavior of the corroded piles. Traditional rehabilitation approaches for steel structures include concrete jacking, to bolt or weld steel plates or sections to the deteriorated member. However, concrete jacketing requires curing time of concrete. Welding has its disadvantages when comes to underwater applications: rapid quenching which decreases the ductility and impact strength of the weldment, hydrogen embrittlement, and poor visibility (Verma, K. and Garg, H.K., 2012). Bolting plates to original member requires

drilling holes on existing corroded pile which is a negative effect for original member. Researchers have investigated the use of fiber reinforced polymers for repair of steel compression members, due to their high strength-to-weight ratio and ease application (Shaat and Fam, 2006; Teng and Hu, 2007; Young et al., 2006; Silvestre et al., 2008; Kim and Harries, 2011; Siddique and Damatty, 2012). However, they also found that achieving effective bond between the FRP and the steel is challenging but essential to the effective performance of the system (Teng et al., 2012), which indicates FRP plating repair system may not be a preferable approach for underwater applications like bridge piles.

A steel-based repair system was proposed and studied in this research. It was named as friction-type bolted steel plates repair system, which transfers the axial load from the original pile to new attached steel plates through friction within a development length on both sides of the corroded section. The system is suitable for underwater rehabilitation of steel bridge piles due to its own advantages including easy installation, immediately effective after installation, and keeps original pile integral without drilling through it. However, this repair system has not been commonly used in field applications and no specific design guidelines are available. This dissertation presents the relevant details of a numerical and experimental investigation of the behavior and effectiveness of this type of system. The findings of the research demonstrated that the friction-type bolted plates repair system can effectively enhance the axial capacity and stiffness of the corroded H-piles in underwater conditions.

1.3 Research Objectives

The work presented in this dissertation has two major research objectives related to bridge piles with severe but localized corrosion: (1) development of a numerical framework to predict the axial capacity of the corroded piles, and (2) development and evaluation of a friction-type bolted steel plate-based retrofit system to be used for the repair of deteriorated piles.

***Objective #1*:** Develop a numerical framework that can be used to predict the remaining axial capacity of steel H-piles with different degrees and patterns of corrosion. This is necessary because current design methods were not developed for non-prismatic members and their predictions for non-prismatic members were demonstrated very conservative by assuming the piles have uniform corrosion along the entire lengths. Therefore, a finite element (FE) model was developed and validated by small-scale and full-scale experimental results of corroded H-piles.

***Objective #2*:** Develop a steel-based repair system for corroded H-piles that can be installed in underwater applications. In order to evaluate the effectiveness of the proposed repair system, an experimental and numerical study was conducted. To optimize the repair system, a parametric study on the effects of factors that might have influence the axial capacity of retrofitted piles was performed.

1.4 Research Methodology

Figure 1.3 illustrates the flow of this research. Starting with literature review of previous research, the gaps in the field of study were identified. Second, experimental and numerical studies for both corroded and repaired piles were conducted. The experimental results of corroded piles were used as (1) validation of the FE model and (2) control group for tests of retrofitted specimens. Numerical analysis on corroded piles provided insight knowledge of critical factors that dominate the behavior of piles. Third, the repair system was designed and applied on the corroded piles with the same deterioration patterns as the control piles. The retrofitted piles were tested under concentric, monotonic compression to investigate the effectiveness of the repair system. Verified by tests results, a FE model for repaired piles was developed for parametric study on factors that affect the behavior of the repair system. Conclusions were drawn on the basis of the study on corroded and repaired piles, and future work was proposed at the end.

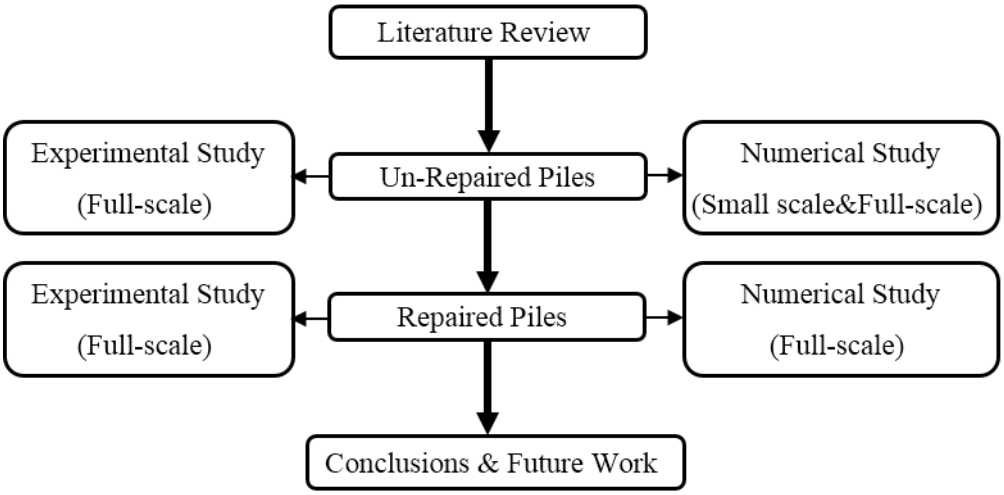

Figure 1.3 Flow chart of the research included in this dissertation

1.5 Dissertation Organization

This dissertation consists of seven chapters:

Chapter 1 provides a general introduction and presents the objective and methodology of the research.

Chapter 2 summarizes the research done related to evaluation and rehabilitation of steel compression members. This chapter includes reviews of numerical assessment methods for compression members with and without local deterioration, and a brief summary of existing repair methods for steel members.

Chapter 3 introduces the experimental program on steel H-piles with simulated localized corrosion. Seven full-scale piles with representative corrosion patterns were tested under uniaxial compression. The results and findings are discussed.

Chapter 4 illustrates the development of a FE model that can be used to predict the compressive behavior of steel H-piles with different degrees and patterns of corrosion. The model was validated by test results from both small-scale (Karagah et al., 2015) and full-scale specimens, and then used for parametric study. The main factors investigated in this chapter include pile

slenderness, severity of flange and web corrosion, location and extent of the corrosion, magnitude of initial imperfection, and the magnitude of residual stresses.

Chapter 5 provides the experimental details of the testing of the repaired piles. Seven piles with the same reduction patterns as the control piles in Chapter 3 were repaired by a friction-based bolted plates system and tested under axial compression. The axial peak load, stiffness, and failure mode were compared between corroded and repaired piles.

The validated numerical framework is implemented to model the repair system in Chapter 6.

The major conclusions of the research are summarized in Chapter 7. Recommendations for future research are also presented.

CHAPTER 2 LITERATURE REVIEW

This research includes two objectives: (1) development of a numerical framework to predict the remaining axial capacity of steel bridge H-piles with localized corrosion, and (2) development of a steel-based repair system for corroded H-piles in underwater applications. Regarding the first aim, review of existing research on corroded steel members is beneficial to a general understanding of the effects on their capacity due to deterioration, although the studied members are of different shape or scale from H-pile. Furthermore, a review of studies on numerical analysis of the axial behavior of metallic axial members was conducted. Despite the existing studies are on prismatic members, the simulation techniques are essential to facilitate the development of the numerical framework for corroded H-piles. Regarding the second aim, the use of attaching plates, steel or FRP, to rehabilitate steel members was also reviewed. The effectiveness of plating method has been demonstrated in axial members, flexural members, and shear and torsional members. However, the technique becomes challenging when it comes to underwater usage without dewatering.

2.1 Members with Local Deterioration

One of common damage affecting steel structures is corrosion. Thus far, it has been investigated on various shapes of members. A number of studies were conducted to evaluate the residual strength of steel axial members with various levels of deterioration. Full-scale and small-scale experimental studies were conducted to gather some understanding of the behavior of deteriorated steel members. Since buckling of deteriorated members is a complex problem, finite element analysis (FEA) was used to evaluate the inelastic flexural and local buckling propagations on members during loading. FEA was also used to conduct parametric studies on large amount of analyses with varying factors to identify critical parameters that affect the behavior of studied members. Besides axial members, corroded members under other types of load were also briefly reviewed in this section to provide a broader view of the effects of corrosion. This section presents the experimental studies of corroded members under uniaxial

compression, numerical studies of corroded members under uniaxial compression, and experimental/numerical studies of corroded members under other types of load.

2.1.1 Experimental studies on corroded members

Experimental studies have been conducted on axial members of various shapes of sections with localized deteriorations, including steel plates with pit corrosion, angles with localized and distributed corrosion, small-scale I-shaped and W-shaped members with localized reductions, and lipped channels with perforated holes.

Paik et al. (2003) conducted a series of collapse tests on steel plates with different degrees of pit corrosion under compression. They defined a parameter denoted as degree of pit (DOP) corrosion intensity, which refers to the ratio of the corroded surface area to the original plate surface area. Three groups of tests were conducted with three values of DOP, 0%, 4.87%, and 10.24%. Each group included 4 identical steel plates. The plates were welded together to form a square box, as shown in Figure 2.1 (Paik et al., 2003). Figure 2.1 shows the box section composed by 4 steel plates welded edge by edge and every group of 4 plates had the same degree and distribution of corrosion. The average values of their loads and displacements were taken as the results of the group. The obtained buckling stress of intact plate was only half of the elastic buckling stress from theoretical calculation, due to the influence of welding residual stresses. The experimental results also showed that the plate buckling stress decreased by 20% when the DOP increased from 0 to 10%. This indicates that the through-thickness pits reduce the ultimate axial capacity of plates in terms of reduction on both cross sectional area and buckling stress. However, the experimental program only contained three values of DOP, and all pit corrosion were assumed as through-thickness holes in a uniformly distribution on plates, which did not represent the realistic situation of corrosion. Also, the influence of residual stresses was acknowledged but not investigated.

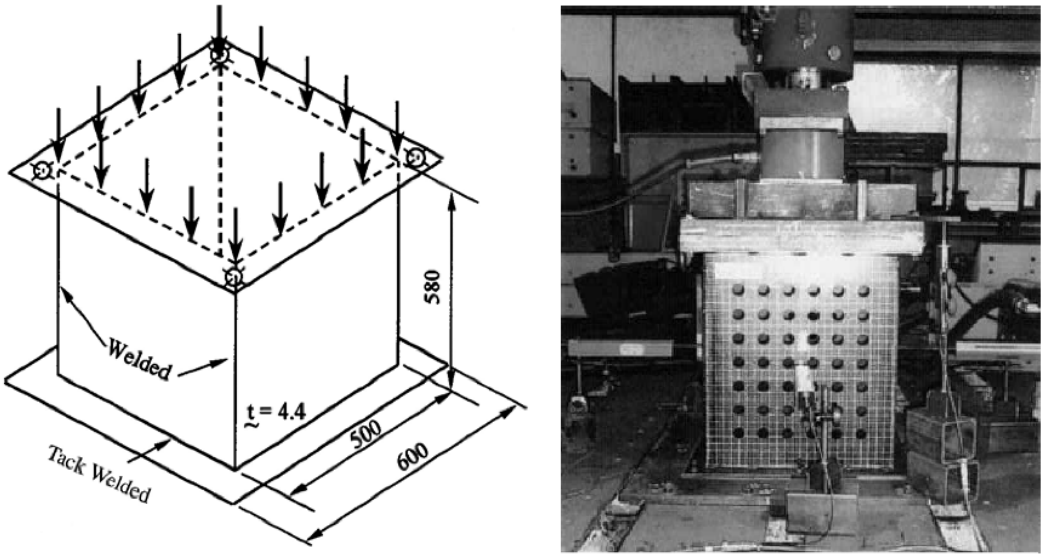

Figure 2.1 Test structure of corroded plates

Beaulieu et al. (2010) tested 24 steel angle members under axial compression, including 8 un-corroded specimens and 16 corroded members. Corrosion was achieved by an accelerated galvanic corrosion process, as shown in Figure 2.2. The corrosion degree was quantified by the mass loss percentage, which ranged from 21% to 47%. The tested sections contained L2 1/2×2 1/2×3/16 and L2 1/2×2 1/2×3/8 with two slenderness ratios of 40 and 110. The test results demonstrated that the loss of mass was not proportional to the loss of the member's capacity. For specimens with low corrosion level, the percentage of capacity loss was less than the loss of mass, however, the loss of capacity was higher than the loss of mass for angles with high corrosion level. The design specifications and codes including CAN/CSA S16-09 (2005), AISC (2005), and ASCE 10-97 (1997) were evaluated on their suitability to predict the behavior of corroded steel angles under axial compression. The comparisons between experimental results and predictions from design codes showed that the remaining capacity was not accurately calculated by the three methods. Beaulieu et al. proposed several general recommendations for better prediction, including taking into account the unevenness of the corrosion and additional experiments on members with degree of corrosion between 0% and 20%. However, the idea of using mass loss to

represent the effect of corrosion in this research ignored key affecting factors such as flange thickness and slenderness ratio, which influenced members with slender element that failed by plate buckling.

Figure 2.2 Corroded steel angles

Other researchers investigated compressive behavior of steel angle section specimens with three types of corrosion effects (Oszvald and Dunai, 2012). They tested 24 steel angles under compression with artificial reduction of thickness in the legs by milling process to simulate corrosion. Three types of corrosion effects, as shown in Figure 2.3 (Oszvald and Dunai, 2012), were considered: (1) uniformly distributed thickness reduction along the specimens, as shown in Figure 2.3(a), (2) pit corrosion was distributed regularly along the specimens, as shown in Figure 2.3(b), and (3) localized thickness reduction was performed at different locations of the specimens, as shown in Figure 2.3(c). Observation from test results indicated that specimens with uniform and pit corrosion were governed by flexural buckling, while cases with localized corrosion tended to fail by local buckling. Inspection of the group with localized corrosion indicated that the initial imperfection had considerable effects on the buckling strength of the specimen. However, the magnitude of initial imperfection was not quantified. Eurocode 3 method was also used to compare its predictions to experimental results. The predictions are conservative, because the method always assumes the most severe corrosion along the entire length. The method predicted capacity less than half of the tested capacity in extreme cases.

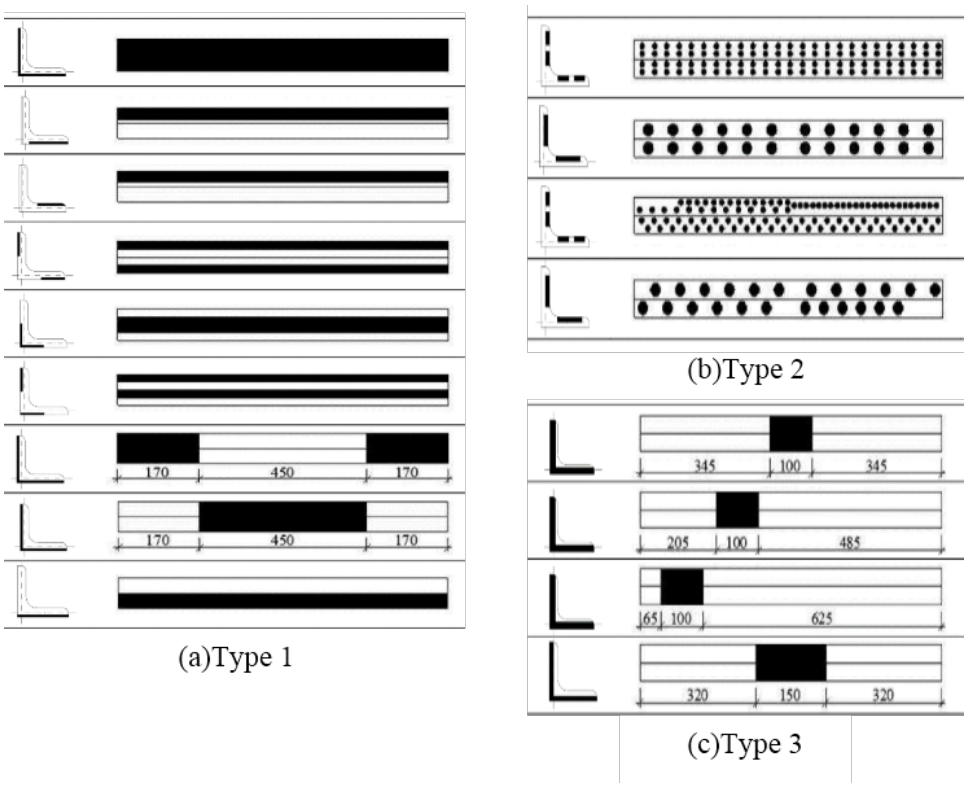

Figure 2.3 Three types of corrosion effects

Liu et al. (2005) tested seven small-scale I-shaped corroded compression braces. The effect of corrosion was simulated by cutting a 12 in by 0.63 in notch on both sides of each flange (four locations in total) at the mid-height of the member, as shown in Figure 2.4. Reducing the width of flanges decreased the cross-sectional area of the member and the slenderness of the flanges. The latter effect is unrepresentative of most patterns of corrosion that have been observed in actual structures, where the flange thickness reduces due to corrosion and its slenderness increases accordingly. The test results illustrated 41% reduction on axial capacity of the column with 22% reduction on its cross sectional area.

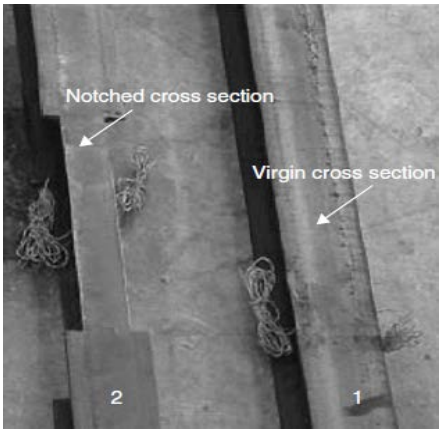

Figure 2.4 Notched small-scale I-shaped member

Karagah et al. (2015) tested 13 small-scale, 32 in long W4×13 short steel columns with different degrees and patterns of sectional deterioration. The deterioration was achieved by machining the flange and web to reduce their thicknesses and flange width, as shown in Figure 2.5. The findings of the research indicated that reduction of the flange thickness resulted in a lower axial capacity than reduction of web thickness. The capacities of the columns were predicted using various design models and the dimensions of the reduced sections of the columns. The axial capacities that were predicted using the American Association of State highway and Transportation Officials (AASHTO) method were overly conservative (up to 56% lower than measured capacities) for severely corroded piles with total section loss greater than 50%. The predicted capacities using the direct strength method were also overly conservative (up to 55% less than measured capacities). The AISI's effective width method provided more accurate predictions compared to the other two methods, but still predicted 40% lower than experimental capacity for extremely corroded specimens. This illustrates the need to develop a method for more reliable prediction of axial members with localized corrosion.

Figure 2.5 Small-scale W-shaped members with flange/web thickness reduction

Researchers have been studying compressive members with perforations, the findings of which may also be applicable for investigation of axial members with such severe corrosion at certain locations that the remaining material barely exists.

Rhodes and Schneider (1994) investigated the behavior of stub columns with a series of different perforation locations and sizes experimentally. The experimental program focused on 48 plain channels, as shown in Figure 2.6, with systematically varied distributions of perforation to study the effects of perforation location, diameter, and number on cross section. The test results indicated that the remaining capacity of a perforated member depends on the location and size of the perforations. It was shown that for slender sections dominated by local buckling. Perforations in the corners exhibited greater weakening effect than other locations away from the corners. Also, for members with compact cross section the capacity can be estimated as the product of the yield stress multiplying the minimum cross sectional area of the member. This study helped identify research needs to be included in this project by investigating the location and size of the deteriorated region.

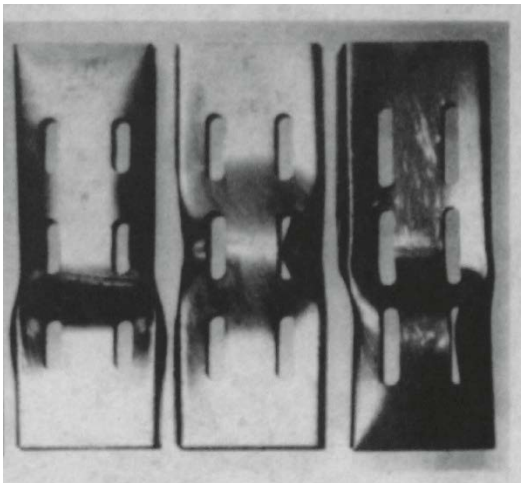

Figure 2.6 Perforated steel channels

Rhodes and Macdonald (1996) studied the compression behavior of stub columns with slotted perforations to investigate the effect of the perforation length. The experimental program contained 5 unperforated plain channel members and 48 members with perforation lengths from 0.315 to 1.417 in in steps of 0.157 in. Two types of perforation distribution were considered, one with slotted holes on web and flanges, and the other one with slotted holes on the junction of web and flanges. The test results demonstrated that while the perforation length had weakening effects on perforated members, the effect was greater on members with holes at the junction of web and flanges. This is expected since the flanges and web away from the junction buckle first under compression due to less constraint and the junction region contributes more to resist applied load.

While Rhodes et al. (1996) focused on stub columns, Pu et al. (1999) investigated slender perforated lipped channels. They tested 63 stub columns to study the effects of perforation size, position, and aspect ratio of rectangular holes on the axial strength. The test results indicated that the size and position of perforations were critical factors for the compression capacity of stub column. The holes located on the edges of the web had more considerable reduction effects than holes distributed at the center or at the quarter-width of the web. This is consistent with the findings of Rhodes (1994) on stub members. The influence of the aspect ratio of rectangular holes was found negligible for slender channel columns.

Moen and Schafer (2008) tested 24 short and intermediate length cold-formed steel lipped C-channel columns with and without pre-punched slotted web holes to failure. The test results indicate that the slotted holes have only minor influence on compressive strength, with the largest reduction as 2.7%. However, for short columns (24 in long column with web width of 3.62/6.00 in and flange width of 1.62 in), the hole reduced the post-peak resistance of web, causing the flanges and lips to carry more of the axial load. This was exhibited in the reduction of the area under load-displacement response of short columns, but this phenomenon was not observed from intermediate length columns (48 in long channel with 3.62/6.00 in of web width and 1.62 in of flange width). The authors also derived design expressions that extended the direct strength method (DSM) in AISI to cold-formed steel columns with holes (Moen and Schafer, 2011). The proposed DSM distortional buckling strength prediction equations provide a transition from the elastic buckling failure regime to the net section strength limit. The proposed model was validated with existing experiments on cold-formed steel columns with holes, and extensive nonlinear FEA results covered a wide range of hole sizes, hole spacings, hole shapes, and column dimensions.

Cinitha et al. (2014) presented an overview of issues related to corrosion and experimental studies on corroded compression members. They proposed approaches to quantify corrosion. One way of quantifying corrosion was taken as the loss of mass of the steel member: mild corrosion was considered when the mass loss was 0%-20%, moderate corrosion for mass loss of 20%-40%, and severe corrosion for mass loss of more than 40%. The other quantification technique was taken as of the thickness loss: mild corrosion was considered when average thickness loss was less than 25%, moderate corrosion for average thickness loss of 25%-50%, and severe corrosion for thickness loss over 50%. However, inspection of the experimental results on corroded tension coupons indicated that the quantification technique based on thickness loss was more representative. Cinitha et al. conducted compression tests on steel angles and hollow tubular specimens. The results indicated that the location and loss of metal due to corrosion has

significant effect on the structural behavior. The irregularity resulted from corrosion led to stress concentration at the most degraded region followed by immediate failure. Mild corrosion did not exhibit substantial reduction on the capacity of member, while severe corroded member required further investigation as it reduced the capacity and was sensitive to factors that would cause stress concentration.

2.1.2 Numerical studies on corroded members

Several researchers have also used numerical analysis to investigate the axial behavior of metallic members with deterioration. Some of the studies presented in the previous section also used finite element analysis to further study the issues at hand. They typically used experimental results to validate the accuracy of numerical model, and then conducted parametric studies. The FEA were used to investigate various factors that affect the behavior of corroded members. This section presents the findings of FEA on corroded axial members.

Paik et al. (2003) performed a numerical study using the ANSYS finite element software package. A convergence study was conducted to determine the mesh size. An elastic- perfectly plastic material model was used ignoring the strain-hardening effect. Measured initial deflections were implemented as initial imperfections. Residual stresses were not measured, but were assumed according to other studies (Paik and Thayamballi, 2003; Smith et al., 1988). The developed numerical framework overestimated the stiffness and ultimate strength by 7-10% compared to test results. However, the FEA correlated well with the experimental results as a function of DOP. A parametric study was conducted by FEA and the results indicated that the plate-buckling capacity was governed by the smallest cross-sectional area of the plate. An equation for predicting the ultimate compressive strength of steel plates with pit corrosion was derived empirically by regression analysis of numerical results. The proposed prediction equation was proven valid for plate with randomly distributed pit corrosion as well as uniformly distributed pit corrosion.

Nakai et al. (2004) investigated the influence of pit corrosion on steel plate. Compression tests were conducted on plates with various distributions of pit corrosion. Figure 2.7(Nakai et al., 2004) shows the test setup. The pit corrosion was simulated by milling the thickness of plate at certain locations. Finite element analysis software MSC.Marc was used for an elasto-plastic analysis to simulate the effect of corrosion pit on compressive buckling behavior. The analysis results indicated that compressive buckling strength of pitted members was smaller than or equal to that with uniform thickness loss in terms of average thickness loss. Therefore, it is conservative to assume average thickness loss when predicting the remaining capacity of plates with pit corrosion.

Figure 2.7 Compression test on steel plate with pit corrosion

Ok et al. (2007) studied the effects of localized pit corrosion concentrated at one or several possible large area on the ultimate strength of unstiffened plates. They ran 256 nonlinear finite element analyses on panels with various locations and sizes of pit corrosion. ANSYS was used for numerical simulation. A shell element, namely SHELL181 in ANASYS, was selected for modeling. It is a four-node element with six degrees of freedom at each node, and is suitable for large rotation, and/or large strain nonlinear applications. Initial imperfection was implemented in the model while the residual stresses were not considered. The parameters considered in the research contained plate slenderness, the location, length, breadth, and depth of pit corrosion.

Five different B/t (width-to-thickness) ratios were investigated: 41.7, 45.5, 50.0, 55.6, and 62.5. The location of pitting corrosion was assumed to start at aft bay (aft end) and the sizes of pitting corrosion had four different length values: 0.25L, 0.5L, 0.75L, and 1.0L, where L was the total length of the plate. The investigated depth of corrosion included 0.25t and 0.5t, where t is the thickness of the plate. The results expressed that the length, breadth, depth, and transverse location of the pit corrosion affected the compressive strength of the plates, while the depth, width, and transverse location of the pit corrosion were three dominant factors. When pitting corrosion on both sides of the plate exceeded 50% of the total length, the axial strength decreased 10%-17%. However, when pitting length increased to 75% and 100% of the total length of the plate, the reduction of axial strength was not significant, only 2% and 5% lower than the case with 0.5L pitting corrosion length, respectively. The most capacity reduction happened when the corrosion spread transversely on both edges, while corrosion simulated at the center resulted in least strength reduction. However, plate slenderness had only negligible effect on the capacity reduction.

Oszvald and Dunai (2013) conducted a numerical study for a comprehensive analysis of angle members with different corrosion patterns, thickness reductions, extension and position of the corrosion. A non-linear model was developed using ANSYS and validated by experimental data. Element types of eight-node (SOLID45) and 20-node (SOLID186) solid elements were used for modeling, in order to consider the corroded geometry more accurately. Elastic-perfectly plastic stress-strain relationship was adopted for material property. Convergence analyses were conducted to determine the mesh size. Geometric imperfections were determined on the basis of the measured ultimate buckling force. The results of the study indicated that corrosion near angle junction caused more reduction on member capacity than corrosion distributed on angle tips. Corrosion near mid-span of the specimen resulted in greater decrease of member capacity than the cases with corrosion near two ends close to supports. The difference was 10% compared to un-corroded specimen.

2.1.3 Corroded members under tension, bending, shear, torsion, and biaxial compression

Many researchers have worked on corroded members under other loads than compression, such as tension, bending moment, shear, torsion, and biaxial compression. These studies provided a general and broad view of the effects caused by corrosion though they are not uniaxial compressive members.

Paik (2007) conducted a study on the ultimate strength of perforated steel plates under edge shear load. Paik ran a series of nonlinear FEA using ANSYS on plates of different aspect ratios and thicknesses with varous diameters of perforations. The results of the study indicated that the plate aspect ratio (length-to-width) had great effects on the ultimate stregnth of perforated plates under shear load. In contrast, the plate thickness was found not a critical factor. Also, the hole size of the perforated plate was a main factor affecting the plate capacity. A hole of width equals to 0.4 plate width, decreased the plate shear capacity by 85%. An empirical formula was proposed by regression analysis of FEA results to estimate the ultimate shear capcity of perforated plates.

Paik (2008) studied plates with perforations under combined biaxial compression and edge shear loads. A series of nonlinear FEA were undertaken on plates with different thicknesses. It was found that the ultimate interaction relationships of perforated plates between combined biaxial compression and edge shear were different from those of un-damaged plates without perforation. An empirical formula for the assessment of the ultimate strength interaction relationships of perforated plates under combined biaxial compression and edge shear loads was proposed based on a series of FEA predictions.

Huang et al. (2010) used the results of numerical studies to develop a function to predict the ultimate capacity reduction of corroded hull plates under biaxial compression. Sensitivity study was conducted for the development of a nonliner FE model investigating the effect of the shape, distribution, and depth of corrosion pits. Also, solid element and shell element were compared on the same configuration of specimens, and the results indicated that both types of

elements exhibited the same deformation and stress distribution at the ultimate state. Therefore, shell element was selected for further FEA for its efficiency. The authors investigated the influences of plate slenderness, loading conditions (compresion, bending, or combined compressoin and bending)at the plates edges and the ratio between the transverse and logitudinal in-plane stresses on the ultimate strength reduction related to the volumn loss due to corrosion. The proposed formula was proven accurate for plates with pit corrosion under biaxial compression.

Appuhamy et al. (2011) obtained the mechanical properties of corroded steel by cutting tension coupons from a corroded steel bridge girder. The test results were used to validate the results of nonlinear finite element analyses. Based on the experimental and numerical studies, equations were proposed to predict the reduction of the yield strength, ultimate strength, and energy dissipation of corroded steel bridge girders under earthquake loading (Appuhamy et al., 2013).

Saad-Eldeen et al. (2011) evaluated the strength of severely corroded full-scale steel box girders by experiments and FEA (Saad-Eldeen et al., 2014). In their experimental work, 3 box girders that could simulate the behavior of mid-ship sections were deteriorated in seawater and tested under four-point loading. Validated by experimental results, the numerical model was used to evaluate the ultimate strength of two box girders subjected to different corrosion degradation levels. Two groups of analyses were conducted for each box girder: consider the corrosion degradation as average thickness reduction and consider the real corrosion thickness from measurements. The main conclusion was that the average thickness reduction model was suitable for predicting the global structural behavior of hull girders while the real corrosion distribution model was good for local stress analysis.

Jiang and Soares (2012) ran a series of nonlinear FEA to investigate the capacity of biaxially compressed rectangular steel plates with pit corrosion. They found that the volumn loss and loading ratio were the dominant factors affecting the remaining capacity of corroded plates.

The authors proposed a formula as well to predict the remaining strength, which was verified applicable.

These previous studies of members with corrosion are generally limited to light-gauged, cold-formed steel sections, and small-scaled hot-rolled sections with limited experimental study. Full-scale experimental investigation and extensive numerical studies are necessary for in-depth understanding of the axial behavior of corroded H-piles.

2.2 Development of Numerical Framework for Modeling Steel Axial Members

In order to develop a numerical framework to predict the axial behavior of corroded H-piles, numerical frameworks of different shapes of axial members were reviewed. The reviewed sections include steel channels, angles, hollow sections, and W-shaped sections.

For steel axial members, shell elements are commonly used over solid element, since the thickness is typically much smaller than other dimensions. In some cases, thin shell theory was adopted due to the negligible contribution of transverse shear deformation (Avery and Mahendran, 2000; Yan and Young, 2002; Gardner and Nethercot, 2004). Most of the cases used general-purpose shell element which uses thick shell theory as the shell thickness is over 1/15 of a characteristic length and becomes discrete Kirchhoff thin shell element as the thickness decreases (Yan and Young, 2004; Ellobody and Young, 2005; Zhu and Young, 2006; Dinis et al., 2007; Ellobody, 2007; Chan et al., 2008; Seif and Schafer, 2009; Dinis and Camotim, 2011; Zhu and Young, 2012; Vani et al., 2013). Reduced integration was popularly used by the researchers to avoid shear locking and save computational time. However, full integration was also used as it does not require hourglass checking like reduced integration. Also, when distortional buckling exists, the element with reduced integration underestimates the column distortional post-critical strength. This is due to the fact that the reduced integration procedure cannot fully capture the column shear stiffness due to the nonlinearity of the wall warping displacements (Dinis and Camontim, 2003; Dinis and Camontim, 2004). Sensitivity study on elastic buckling has been widely used as the way to determine the appropriate element type and mesh size. However, the

author believes sensitivity study based on elastic buckling is not sufficient for inelastic buckling analysis. The determined element type and mesh size from elastic buckling analyses may not capture the inelastic behavior precisely. Geometric imperfections and residual stresses were implemented according to measurements or determined by sensitivity study on nonlinear inelastic buckling analysis in studies when measurements were not taken or the maximum tolerance defined in specifications and codes.

Two steps were typically included for numerical analysis of nonlinear stability problems: first, elastic eigenvalue analysis to obtain the lowest overall and local buckling modes, which were used as initial imperfection shapes in the following analysis; second, nonlinear inelastic analysis incorporated with material and geometric nonlinearities to capture the full load-deformation response (Yan and Young, 2004; Ellobody and Young, 2005; Zhu and Young, 2006; Dinis et al., 2007; Ellobody, 2007; Chan et al., 2008; Dinis and Camotim, 2011; Zhu and Young, 2012; Vani et al., 2013). Another technique to capture the initial global imperfection was to apply a transverse load on the member to create a desired lateral deformation. However, initial local imperfection (i.e. flange/web out-of-square) was difficult to achieve by this method. For elastic analysis, Newton-Raphson method was adopted as the solution scheme. For inelastic analysis, particularly for collapse analysis of members with very slender elements, the modified Riks method (arc length method) was used as it was more robust than Newton-Raphson method (Schafer and Moen, 2010).

2.2.1 FEA of steel channel columns

Young and Yan (2002) developed a nonlinear finite element model to investigate the strength and behavior of cold-formed lipped channel columns. A finite element nonlinear analysis program ABAQUS was used to simulate the fixed-ended cold-formed lipped channel columns. The model implemented the measured material properties and initial geometric imperfections from their experimental program (Young and Rasmussen, 1998). The material properties were determined from tensile coupon tests, and the initial local and overall imperfections were

measured from the test specimens before loading. The geometric imperfections were included by using a linear perturbation analysis to establish the probable buckling modes of the column, and scaling the eigenmodes by a factor (measured maximum magnitudes of local and overall imperfections) for nonlinear analysis. Residual stresses were not considered since the measurements obtained from Young and Rasmussen (1995, 1998) indicated they were negligible. A thin shell element, S4R5, with 4 nodes and 5 degrees of freedom per node, linear shape function, reduced integration, was used for the model. The element type and size were determined according to a sensitivity study which indicated that the chosen type and size provided best prediction. Details of the sensitivity study were not mentioned in the paper. However, the FEA predictions were compared to the experimental results from Young and Rasmussen (1998). The ultimate loads obtained from FEA closely predicted the experimental results. The mean values of the experimental-to-FEA ultimate load ratio were 0.97 and 0.99 with corresponding coefficient of variation (COV) of 0.051 and 0.057 for two series of columns, respectively. The axial load-shortening curves from test and FEA matched perfectly except the post-buckling portion where FEA predicted higher capacity compared to test response. This might be caused by the lack of residual stresses in FEA and unintentional eccentricity of the test set-up. However, this did not have essential effects since the focus of the research was the ultimate load.

Similarly, Yan and Young (2004) investigated the axial behavior of fixed-ended cold-formed steel channel columns with complex stiffeners using a non-linear finite element model built in ABAQUS. The section consisted of simple lips with return lips. The measured dimensions, material properties, and geometric imperfections were implemented in the FE model. The model used a four-node shell element, S4R, with 6 degrees of freedom per node, linear shape function, general-purpose, reduced integration. The mesh size was chosen based on a sensitivity study conducted in Young and Yan's (2002) previous study. The model was validated by four series of experimental results of a total 30 specimens (Yan and Young, 2002). The differences of axial capacity obtained from experimental results and FEA predictions were no more than 12%.

The FEA provided good agreement of failure modes as well. The load-deformation response from FEA and experiments was only compared on one specimen. Although they matched well except for the post-peak portion where the experimental results exhibited slightly higher capacity, one comparison was not adequately convincing.

Dinis et al. (2007) presented a numerical investigation about elastic and elastic-plastic post-buckling behavior of cold-formed steel lipped channel columns affected by local-plate/distortional buckling mode interaction. ABAQUS was used for finite element analysis. A four-node isoparametric fully integrated shell element S4 was chosen for modeling. A preliminary investigation was carried out to determine the level of mesh refinement, according to which 0.394 in mm×0.394 in was adopted. Initial geometric imperfections were implemented by scaling the elastic buckling mode shapes to nonlinear analysis. The solution schemes for elastic and elastic-plastic analyses were Newton-Raphson method and Riks arc-length method, respectively.

In a later research conducted by Dinis and Camotim (2011), the elastic and elastic-plastic post-buckling behavior of cold-formed steel lipped channel columns affected by distortional/global (flexural-torsional) buckling interaction was investigated. ABAQUS was used for FEA and the 4-node shell element S4, full integrated, with linear shape function was still the chosen element type. Imperfections were implemented with both global and distortional shapes obtained from elastic buckling analysis.

Schafer et al. (2010) reviewed computational modeling of elastic buckling and nonlinear collapse analysis on cold-formed steel members. For nonlinear collapse analysis, an example of 47.2 in long cold-formed steel lipped channel column was performed by finite element analysis to evaluate the influences of element type, mesh density, solver, solution step size, plasticity model, number of integration points through thickness, and choice of commercial implementation (ABAQUS and ADINA). The results indicated that collapse analysis of cold-formed members

was very sensitive to the above parameters. However, computational modeling still plays an important role in future research and design of cold-formed steel.

2.2.2 FEA of steel angles

Vani et al. (2013) explored the behavior of cold-formed steel plain angle under compression numerically using ABAQUS. The material properties were taken from tensile coupon test. The 4-node general purpose shell element, S4R, with reduced integration, linear shape function was used for analysis. The mesh size was determined as 0.394 in×0.394 in according to a sensitivity convergence study. The initial imperfections were taken as the measured value. The modified Riks method was used for nonlinear analysis. The model was validated by experimental results of 5 specimens as the differences between experimental and numerical results were less than 5.7%. The numerical predictions of member capacities were compared to the predictions by DSM and EWM from AISI (2007). Both design methods provided conservative predictions. In extreme case, the EWM underestimated the capacity by 96%.

2.2.3 FEA of hollow section columns

Gardner and Nethercot (2004) conducted numerical modeling of structural response of steel hollow sections using ABAQUS, including square, rectangular, and circular hollow sections. The objective of the research was to develop a consistent approach to model stainless steel structures. The model was implemented with general expressions defined for material stress-strain relationship, enhanced strength corner properties, initial geometric imperfection modes and magnitudes, and residual stresses. A thin shell nine-node with five degrees of freedom per node and quadratic shape function, S9R5, was used for analysis. Their research considered the effects of residual stresses, initial imperfections (global and local), extent of corner regions. The initial global and local imperfection shaped were achieved from an eigenmode analysis and taken as the lowest buckling modes of global and local buckling. The complete initial imperfection comprised a superposition of the global and local modes. Initial out-of-straightness was taken as L/2000 according to a parametric study comparing FEA predictions to test results with changing

magnitudes of overall imperfections. Similar parametric study was conducted to determine the residual stresses, although the results indicated that the influence of residual stresses were relatively insignificant to the column response. The modified Riks method was used to solve the material and geometric nonlinearity. The results demonstrated that the ABAQUS-based FE model provided a sound and cost effective alternative to physical testing as a mean of predicting the full load-deformation response of steel structural members with hollow sections.

To investigate the axial compressive behavior of hot-rolled elliptical hollow sections, Chan and Gardner (2008) developed a non-linear FE model using ABAQUS. A four-node shell element with 6 degrees of freedom per node, linear shape function, and reduced integration, designated as S4R, was used for analysis. Sensitivity study based on elastic eigenvalue analysis was conducted to choose the suitable mesh size. Three values of initial imperfection were taken into consideration, t/10, t/100, and t/500. The value of t/100 was adopted as it showed the best agreement with the test results. Residual stresses were not considered. The modified Riks method was used to solve geometric and material nonlinearity. The comparisons of ultimate loads and axial load-shortening responses between experiments and FEA demonstrated the accuracy of the model. Similarly in their later researches, Chan and Gardner (2008) studied the bending behavior of elliptical hollow sections and Gardner et al. (2011) investigated the behavior of elliptical hollow sections under combined compression and uniaxial bending.

Zhu and Young (2006) investigated fix-ended aluminum alloy tubular columns of square and rectangular hollow sections using finite element program ABAQUS. A four-node shell element with reduced integration (S4R) was used based on the evaluation from Yan and Young (2004) and Ellobody and Young (2005). Initial overall and local imperfections were implemented in the model based on measured geometry. The way of implementing initial imperfections was first to obtain the necessary eigenmodes as imperfection shapes from elastic eigenvalue analysis, and then scaled them as the imperfections in non-linear analysis. Residual stresses were not included because the values were very small for extruded aluminum alloy profiles. This

numerical model provided reliable predictions of the axial capacities of studied members. The differences between experimental results and FEA predictions were no greater than 16% among total 36 specimens, and the differences were less than 10% for 28 out of 36 specimens (Zhu and Young, 2006).

In their later study, Zhu and Young (2012) developed a finite element model to simulate the fixed-ended steel column tests of oval hollow sections. The FE model incorporated the initial global and local imperfections and material nonlinearity. The researchers used ABAQUS for FEA and the element type was also determined as S4R recommended by Yan and Young (2004). Comparing with the four series (four types of cross section dimensions) of their test results (Zhu and Young, 2011), the mean values of the experimental-to-FEA ultimate load ratio were 1.04, 1.02, 1.01, and 0.99 with corresponding coefficients of variation of 0.024, 0.053, 0.083, and 0.101 respectively. The FE model predicted the behavior of cold-formed steel oval hollow section columns accurately. A parametric study on a total of 100 columns was performed using the FE model. The FEA predicted capacities were compared to strengths calculated using current North American, Australian/New Zealand, and European specifications for cold-formed steel members. Generally the design methods from specifications overestimated the column strength. The mean values of ratios of FEA predictions to calculations from three specifications were 0.89, 0.89, and 0.90, with the coefficients of variation (COV) of0.076, 0.076, and 0.100, respectively. However, for compact oval hollow sections, the predictions from design specifications were slightly conservative.

Ellobody and Young (2005) developed a finite element model for prediction of stainless steel columns with square and rectangular hollow sections. The software ABAQUS was used. Two steps of analyses were conducted: first a linear elastic eigenvalue analysis was performed to obtain the lowest buckling mode; second a nonlinear analysis was conducted incorporated with geometric and material nonlinearity. The initial imperfection shapes were adopted from the eigenmode shapes from elastic analysis. A general-purpose 4-node shell element, S4R, with 6

degrees of freedom, reduced integration, linear shape function was used for the model. Convergence studies were conducted to determine the mesh size. The results indicated that 0.787 in×0.394 in mesh provided adequate accuracy and minimum computational time. Measured residual stresses were implemented in the model as well. A total of 22 cold-formed high strength stainless steel hollow columns were analyzed and compared to the experimental results. A maximum difference of 8% was observed between experimental results and FEA predictions, which indicated the accuracy of the FE model. Ellobody (2007) further used this FE model to investigate the buckling behavior of cold-formed high strength steel stiffened slender square and rectangular hollow section columns.

2.2.4 FEA of W-shaped columns

Seif and Schafer (2009) conducted a FEA on hot-rolled steel members using AISC W14 and W36 sections. The study focused on collapse response of short columns and beams with slender elements that failed by local buckling. An elastic buckling analysis was performed as sensitivity study on element type and mesh size indicated that the "S4" element provided in ABAQUS with normal mesh size (ten elements along the depth of web and ten elements along the width of flange) delivered adequate accuracy for hot-rolled steel section in their study. The S4 element has six degrees of freedom per node and linear shape function, incorporates finite membrane strains, and its shear stiffness is yielded by full integration. Local imperfections and residual stresses were considered in the model. The local imperfections were determined according to manufacturing tolerances (ASTM A6/A6M-04b, 2003). However, Seif and Schafer used elastic buckling analysis to perform the sensitivity study to determine the element type and mesh size, which might not be representative for nonlinear analysis, especially for non-prismatic member like corroded H-pile. Also, this is a study focused on short length column in which global imperfections were ignored and only local imperfections were taken into consideration.

2.2.5 FEA of steel frame

Avery and Mahendran (2000) presented a detailed description of shell finite element distributed plasticity model for steel frame structures composed with non-compact sections. The model was built in ABAQUS and a thin, shear flexible, isoparametric, quadrilateral shell with 4 nodes and 5 degrees of freedom per node, utilizing reduced integration and bilinear interpolation schemes element was used for analysis. Also a R3D4 rigid surface element was used to create pinned member end restraints, which was a rigid quadrilateral element with 4 nodes and 3 translational degrees of freedom per node. The model was verified by experimental results conducted by the authors (Avery and Mahendran, 2000), which demonstrated that the shell finite element model accurately represented distributed plasticity resulting from the combined effects of applied axial force and bending moment, residual stresses, and local buckling.

The FEA exhibited as a reliable approach for predicting ultimate load, failure mode, and load-displacement response of axial members with different types of sections. However, the results were sensitive to parameters related to simulation techniques, including element type, mesh size, material modeling, initial imperfections and stresses, solver, and step size. The validated models listed above were developed for prismatic members rather than the steel pile with localized corrosion studied in this dissertation. The sensitivity studies to determine the element type and mesh size were conducted for elastic analysis, however, it does not guarantee the accuracy for inelastic analysis, especially for non-prismatic piles studied in this dissertation. Therefore, a numerical framework for predicting the capacity of H-piles with localized reduction was developed in this research.

2.3 Current Repair Systems

To fulfill the second aim of this research, development of a steel-based plating repair system, current plating rehabilitation methods are reviewed in this section. Traditional plating rehabilitation approaches for steel members are bolted and welded steel plates. The design procedures of these methods are straightforward and well specified in current codes and

specifications. However, for underwater rehabilitation of steel piles, welding is not preferred due to cost and quality considerations. Bolting plates to original member is labor intensive and drilling many holes in an already corroded pile is often not preferred by engineers and owners.

FRP sheets have been investigated for steel member retrofit, due to their high strength-to-weight ratio and ease of application. Research on the use of FRP sheets to repair steel columns has been broadly conducted. Shaat and Fam (2006) investigated the behavior of CFRP sheets strengthened short and long square hollow section columns. The study investigated the effects of types of CFRP, fiber orientation, and number of layers by experimental study on 27 short columns and five long columns. The results indicated that while CFRP increased the axial capacity of short and long square hollow columns, transversely wrapped FRP was more efficient than FRP oriented in longitudinal direction for short columns. Further, retrofitted long columns failed by excessive global buckling, which was more correlated to the initial imperfection than the number of layers of CFRP.

Teng and Hu (2007) demonstrated that GFRP jacket was effective for retrofit circular hollow steel tubes under axial compression. Both experimental and numerical results demonstrate that the FRP jackets significantly increase the ultimate load and ductility of circular hollow steel tubes; while FEA results indicate the effectiveness of FRP jacket strengthening thin cylindrical shells under combined axial compression and internal pressure.

Young et al. (2006), Silvestre et al. (2008) carried out both experimental and numerical investigations on lipped channel columns strengthened by CFRP. The study indicates that longitudinally oriented CFRP is more beneficial to increase ultimate loads than transversely oriented. Further, the increment of ultimate capacity is proportional to the number of layers of CFRPs.

Kim and Harries (2011) strengthened steel T-section members with CFRP strips and tested them in axial compression. The results indicated that the CFRP strips effectively reduced

the stresses at the web-flange junction where critical hysteretic stress concentrations could occur. Increment of layers of CFRP had no influence on the tee-section axial members.

Siddique and Damatty (2012) studied the enhancement in buckling capacity of steel plates repaired by GFRP plates numerically. The retrofitted plate capacity was governed by the ultimate shear capacity of the adhesive, ultimate axial capacity of the GFRP, or instability of the system. The failure mode was found depending on the slenderness ratio of the plate and the thickness of the GFRP.

However, as one most critical factor that governs the failure, bond between FRP and steel is difficult to control on site (Teng et al., 2012). Since the adhesion strength of steel/adhesive interface is highly sensitive to the surface preparation, bonded FRP repair system may not be effective or applicable for underwater applications like bridge piles. In contrast, clamped steel plates attached to the steel piles through friction provided by pre-tensioned high strength bolts may not have this disadvantage. The method may be suitable for underwater rehabilitation of steel piles because it is easy to install, immediately effective after installation (does not require a curing time), and maintains the integrity of the original member. The friction-type bolted plates repair system has not been commonly used in practice. Therefore, the axial behavior of the repaired members was investigated and a design model for the repair system was proposed.

2.4 Conclusions

This chapter summarizes studies on corroded steel members, studies on development of numerical framework of steel axial members, and current repair systems for corroded piles. Experimental and numerical studies on corroded steel members were reviewed. Table 2.1 summarizes studies on corroded steel members of different shapes, with different deterioration patterns, and under different loads. The table indicates that corroded steel plates and angles have been comprehensively studied. Typical reduction patterns due to corrosion have been investigated for plates and angles. Further investigations should be expected for other shapes of steel members. As the focus of this dissertation, W-shaped steel member's compressive behavior has been

studied in cases of members with uniform corrosion along entire length, members with localized flange width reduction, and small-scale members with localized flange/web thickness reduction. The first case does not represent the situation of aging bridge piles, which showed severe corrosion concentrated around the water lever. The second case decreased the slenderness of flange despite of the reduction of cross sectional area, which is not representative of the effect of corrosion on flange and web thickness. The third case represented the corroded bridge piles well but at small-scale. Therefore, this dissertation investigates HP-shaped compressive members with localized flange and web thickness reduction by full-scale experiments.

Table 2.1 Studies on corroded steel members

Section	Deterioration	Load	References
Plate	pit corrosion	compression	Paik et al. (2003); Nalai et al. (2004); Ok et al. (2007)
		biaxial compression	Huang et al. (2010); Jiang et al. (2012)
	perforation	shear	Paik et al. (2007); Paik et al. (2008)
		tension	Appuhamy et al. (2011)
Angle	ununiformed corrosion along entire length	compression	Beaulieu et al. (2005)
	uniformly thickness reduction	compression	Oszvald and Dunai, 2012)
	pit corrosion		
	localized thickness reduction		
Channel	perforation	compression	Rhodes and Schneider (1994); Rhodes and Macdonald (1996); Pu et al. (1998); Pu et al. (1999)
Doubly-symmetric I-shape	localized width reduction	compression	Liu et al. (2005)
	localized thickness reduction	compression	Karagah et al. (2015)
	thickness reduction along entire member	bending moment	Sharifi and Rahgozar (2010)
Box	ununiformed corrosion along entire length	bending moment	Saad-Eldeen et al. (2011); Saad-Eldeen et al. (2014)

For the reason that current design methods in specifications and codes show conservative predictions of the remaining capacity of the corroded members, a numerical framework is needed to accurately predict the axial capacity of corroded members. Review of numerical techniques of evaluation of axial metallic members conducted by other researchers indicates critical effects of the selection of element type, mesh size, solution scheme, and how to implement geometric imperfections and residual stresses. It is demonstrated that the numerical framework is quite sensitive to above parameters. The most related numerical model is for W14 and W36 columns with reduction along entire length developed by Seif and Shafer (2009). However, member with localized flange/web thickness reduction may behave totally differently from uniformly degraded members. Therefore, a numerical framework to evaluate hot-rolled H-piles with localized deterioration was developed in this dissertation, which will be presented in chapter 3 and 4.

Existing plating repair methods are reviewed and their advantages and disadvantages are presented. As a more suitable repair method for underwater retrofit of steel piles, friction-type bolted plates repair system was proposed and will be illustrated in detailed of design procedure, experimental and numerical studies in the fifth and sixth chapter.

CHAPTER 3 EXPERIMENTAL STUDY OF CORRODED H-PILES

As part of the overall study that includes: experimental and numerical investigations on corroded and retrofitted H-piles, this chapter presents the experimental program of full-scale corroded H-piles. These piles have different degrees of deterioration with the aim to investigate the behavior of locally corroded piles under axial compression. The test specimens, material properties, test setup, and instrumentations are described and the test results are discussed. The results obtained from the experimental study were used (1) as a validation for the numerical framework presented in Chapter 4, and (2) as a control group for further experimental program of the repair system presented in Chapter 5.

3.1 Experimental Program

The experimental program consisted of seven full-scale H-piles loaded under axial compression to failure. The seven piles included one control pile with no damage and six piles with different degrees and extents of simulated corrosion. The test variables were reduction of flange thickness and web thickness at the corroded region, and the extent of corrosion. The flange width reduction was not considered due to its negligible effect on axial capacity of corroded piles according to the results of small-scale W-shaped piles tested by Karagah et al. (2015). Reduction of the flange width decreases the cross-sectional area of the member at the corroded region and decreases the slenderness of the flange locally. This was found previously to shift the location of local buckling away from the section with reduced width. The test matrix, materials, test set-up, and instrumentations are described in the following sections.

3.1.1 Test matrix

3.1.1.1 Section size and effective length

The research group visited four representative field sites in Texas and summarized the section sizes and clear lengths of observed piles in Table 3.1. The cross-section HP12×53 was selected for experimental study as it is a commonly used section in the TxDOT bridge inventory

(L. Flournoy, personal communication, 2011). The length of tested piles was determined as follows.

Figure 3.1 shows a schematic view of a portion of bridge including a deck, bent caps, and two rows of piles. The clear length (l) of a pile is considered as the distance from ground to the bottom surface of the bent cap. The top side of a pile, which is partially embedded in the bent cap, is considered to be able to rotate about both strong and weak axes but no displacement. Since the base of the pile is embedded in the soil, the soil provides lateral restraint to the base of the pile. As such, the boundary conditions at the base of the pile must be carefully considered. A commonly accepted approach is to define a depth of fixity (L_f) below the soil surface at which the pile can be assumed to be fully fixed (translations and rotations prevented) as illustrated in Figure 3.1. This length of fixity depends on the relative stiffnesses between the pile and the soil in which is embedded. As such, it is a function of the soil type, and the flexural stiffness of the pile E_pI_p. The length of fixity L_f is calculated by the method adopted in AASHTO (2012) for soft clay soil type using Eq. 3.1,

$$L_f = 1.4\left(\frac{E_p I_p}{E_s}\right)^{0.25}, \qquad \text{Eq. 3.1}$$

where E_p and E_s are moduli of elasticity of pile and soil (tons per square foot), respectively, and I_p is moment of inertia of the pile in the plane of buckling in (ft^4).

The effective length of the pile is calculated by adding the length of fixity, L_f , to the clear length of the pile, l, and multiplying by the effective length factor k, as recommended by AASHTO (2012). Table 3.1 presents the calculated effective lengths and slenderness ratios of observed piles about their strong and weak axes. Inspection of Table 3.1 indicates that the failure of all the piles will be dominated by flexural buckling about their weak axes. Considering that the TxDOT bridge inventory is reasonably expected to include longer piles than those observed, the maximum slendereness ratio of the HP12×53 piles was calculated as 38.1 and 59.8 about strong and weak axes, respectively. Hence, the pile was dominated by weak axis buckling with an

effective length of 14.3 ft in that direction. Considering the limitation of the length of test frame, the length of the tested piles were determined as 15ft with pin-pin boundary condition corresponding to a slenderness ratio of 63 about weak axis of the cross section.

Table 3.1 Measured clear lengths of bridge piles

Bridge	Pile Designation	Pile Clear Length [ft]	Pile Effective Length [ft]		Slenderness Ratio	
			Strong Axis	Weak Axis	Strong Axis	Weak Axis
1	HP 10x42	9.7	12.6	11.3	36.7	56.0
1	HP 12x53	6.2	11.2	9.5	26.7	39.8
1	HP 14x73	15.4	18.8	16.9	38.5	58.3
2	HP 12x53	10.5	14.2	12.5	33.8	52.5
2	HP 14x73	16.6	19.6	17.8	40.3	61.2
3	HP 12x53	12.5	15.6	13.9	37.2	58.3
4	HP 12x53	13	15.9	14.3	38.0	59.8

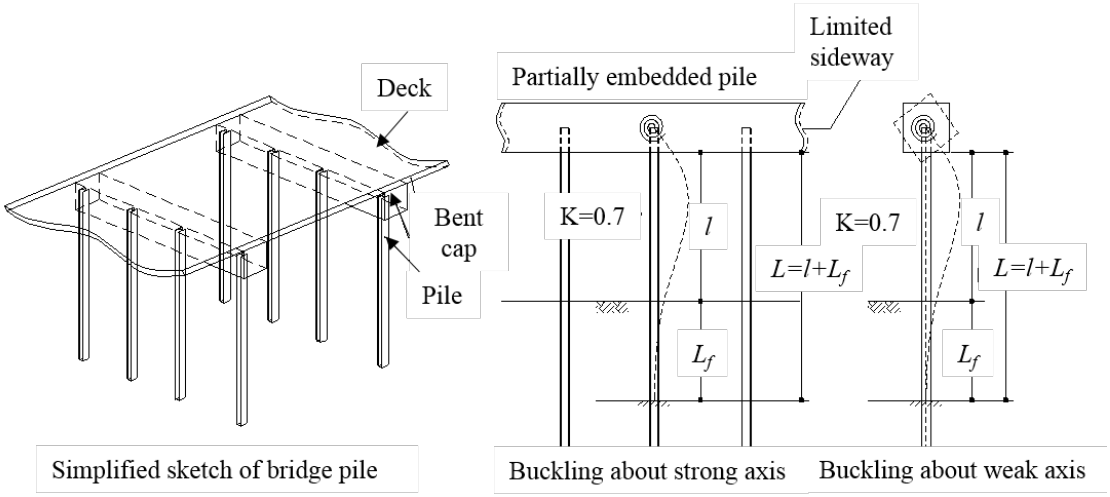

Figure 3.1 Schematic view of bridge piles and buckling modes

3.1.1.2 Deterioration pattern

Except for the control pile with no corrosion, the degrees of section loss of the remaining six piles were determined based on the measurements from filed observation: (1) the flange and web reductions due to corrosion are comparable and (2) degrees of corrosion are within a wide range from relatively minor corrosion to near total section loss. Therefore, three different degrees of flange thickness reduction were selected, 0%, 40%, and 80%; four different degrees of web thickness reduction were investigated, 0%, 20%, 60%, and 100% which indicated a total section

loss (void) on the web. For an HP12×53 section, the flange is at the limit of non-slender section and any reduction on flange thickness results in slender flange(AASHTO, 2012); and web becomes slender element when more than 41% thickness is reduced.

Table 3.2 shows the test matrix of this particular study. Each pile was assigned a two or three part designation. The first number of the pile designation indicates the percentage of reduction of the flange thickness, while the second number indicates the percentage of reduction of the web thickness. The extent of the reduction was determined as 1 ft centered at the third-height of the pile, as shown in Figure 3.2(a). The third part of the designation, if present, "V" indicates a 2in void in the web, as shown in Figure 3.2(b), or "3" indicates the extent of corroded region, L_{cr}, was 3 ft not 1 ft. A computer network control (CNC) mill was used to reduce the thicknesses of flange and web, as shown in Figure 3.3. The measured thicknesses of the reduced flanges and web are presented in Table 3.2.

Table 3.2 Test matrix of HP12×53 corroded piles

Pile designation	Extent of corrosion	Flange reduction	Web reduction	Measured flange thickness		Measured web thickness	
				Un-corroded	Corroded	Un-corroded	Corroded
	L_{cr} [ft]	[%]	[%]	t_f [in]	$t_{f,c}$ [in]	t_w [in]	$t_{w,c}$ [in]
0/0	None	0	0	0.458	--	0.433	--
0/20	1	0	20	0.460	--	0.442	0.375
40/20	1	40	20	0.440	0.289*	0.437	0.308
40/60	1	40	60	0.434	0.242*	0.426	0.161*
80/60	1	80	60	0.432	0.101*	0.430	0.187*
80/60/V	1	80	100	0.432	0.115*	0.430	0.000
80/60/3	3	80	60	0.431	0.142*	0.428	0.176*

*Slender flange or web.

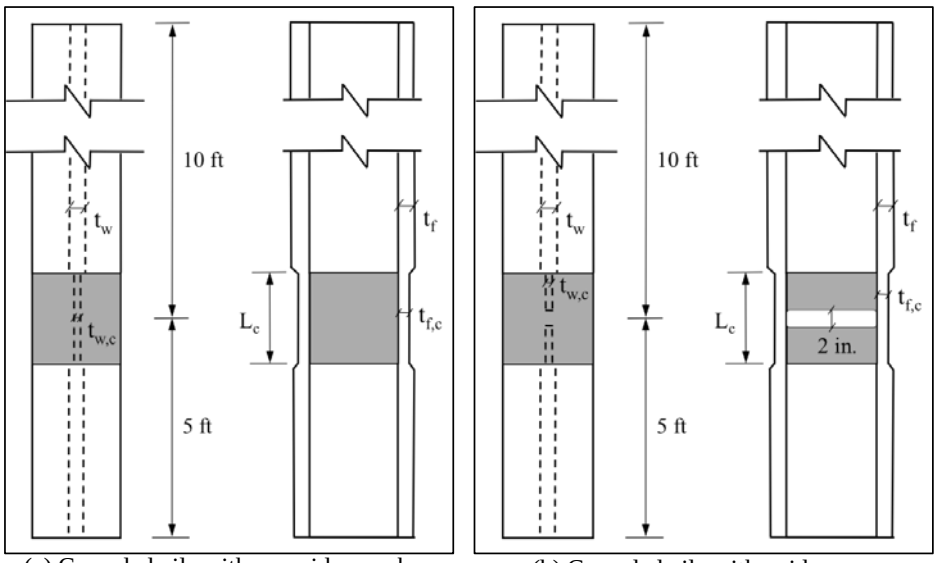

(a) Corroded pile with no void on web (b) Corroded pile with void on

Figure 3.2 Schematic view of the corroded piles (not to scale)

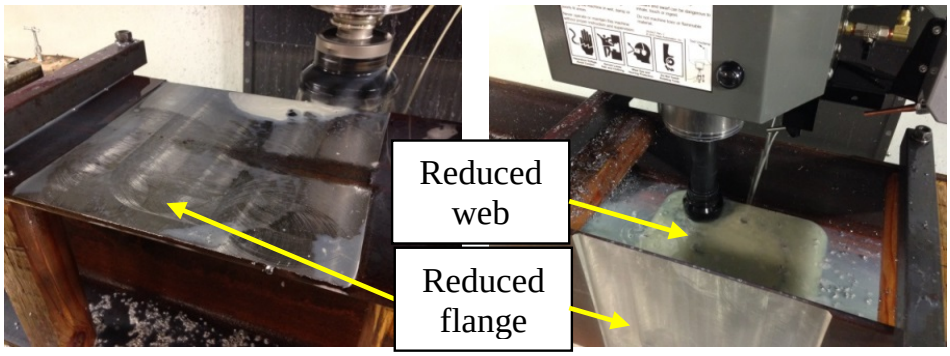

(a)Milling flange thickness (b)Milling web thickness

Figure 3.3 Milling process to simulate corrosion of piles

3.1.2 Material properties

Tension coupons were tested to determine the material properties of the test piles. Four coupons were tested according to ASTM A370 (2014). Three of the coupons were taken from the flanges of the pile and one from the web. The coupons were tested in a 400-kip capacity Tinius-Olsen universal testing machine at displacement rates of 0.025 and 0.2 in/min in the elastic and plastic regions, respectively. The measured load values were divided by the cross-sectional area to obtain the axial stress. An extensometer of 2 in gage length (EPSILON model 3542) was used to measure the axial deformation within the gauge length of the coupon. Data was collected using a Vishay Precision Group System 7000 data acquisition system with a flexible finite impulse

response (FIR) filter enabled and using a data sampling rate of 10 samples/second (Vishay, 2011). No filter was used for post-processing.

Figure 3.4 illustrates the measured stress-strain relationships of the four coupons. The obtained stress-strain curve of the coupon cut from web exhibits higher strength without phenomenon distinct yield plateau, while the coupons cut from flanges exhibit a distinct yield plateau and lower strength. This phenomenon was also observed in material property tests of small-scale piles (Karagah et al., 2015). The possible reason may be the varied magnitudes and distributions of residual stresses in flange and web. The modulus of elasticity was obtained by fitting the slope of the elastic portion of the stress-strain curve. The yield strength was obtained by the 0.2% offset method.

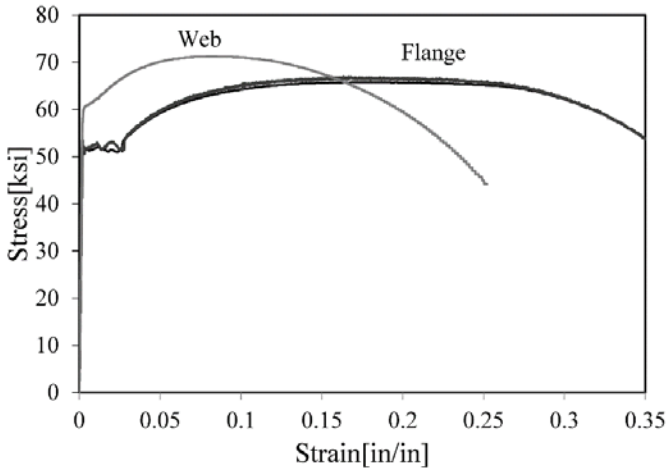

Figure 3.4 Stress-strain curves of four tension coupons

Table 3.3 presents the elastic moduli, yield and ultimate stresses, and ultimate strains of the four coupons. The mean value and coefficient of variation (CoV) of the three coupons cut from flange were calculated.

Table 3.3 Material properties of tested steel piles

Coupon location	Elastic modulus [ksi]	Yielding stress [ksi]	Ultimate stress [ksi]	Ultimate strain [in/in]
Flange	28,700	52.0	66.0	0.18
Flange	29,500	53.0	67.0	0.16
Flange	27,100	52.0	67.0	0.16
Mean	**28,400**	**52.5**	**66.5**	**0.17**
CoV	1%	1%	4%	7%
Web	**32,000**	**60.5**	**71.0**	**0.08**

3.1.3 Test set-up and instrumentations

The piles were tested in a specially designed self-reacting test frame, shown in Figure 3.5, which consisted of a steel reaction frame, 600-kip capacity double-acting hydraulic jack and a 10-ksi electric pump (Enerpac model ZE4204MB) connected to the jack (Enerpac model CLRG3006) to provide/release oil pressure. The setup was designed to test the piles in a simply supported configuration with pins oriented such that the piles were free to rotate about their weak axes. The rotation about the strong axes of the piles was restrained to ensure that the piles failed by buckling about their weak axes if flexural buckling governed. The specimens were loaded manually at a rate of 15 kips per minute (5 kips every 20 seconds) until the peak load was achieved and the descending portion of the load-deformation curve was identified.

Figure 3.6 illustrates the instrumentation of the test. Three 200-kip load cells (Futek model CLC-200k) were mounted behind the jack in a triangular pattern to measure the applied load, as shown in Figure 3.6(a) and Figure 3.6(b). Four string potentiometers (Unimeasure model number PB-20) were installed at the four corners of the supporting plates for the specimen, as shown in Figure 3.6(c). The jack, load cells, and four string potentiometers were all centered at the centroid of the specimen. Therefore, the axial applied load was taken as the sum of the values of three load cells, while the axial shortening of the specimen was taken as the average value of the four string potentiometers. Strain gauges were attached on both sides of the tips of flanges and center point of the deteriorated web to monitor the axial strain and justify occurrence of local buckling during tests. Data was collected using a Vishay Precision Group System 7000 data

acquisition system with a flexible finite impulse response (FIR) filter enabled and using a data sampling rate of 10 samples/second (Vishay, 2011). No filter was used for post-processing.

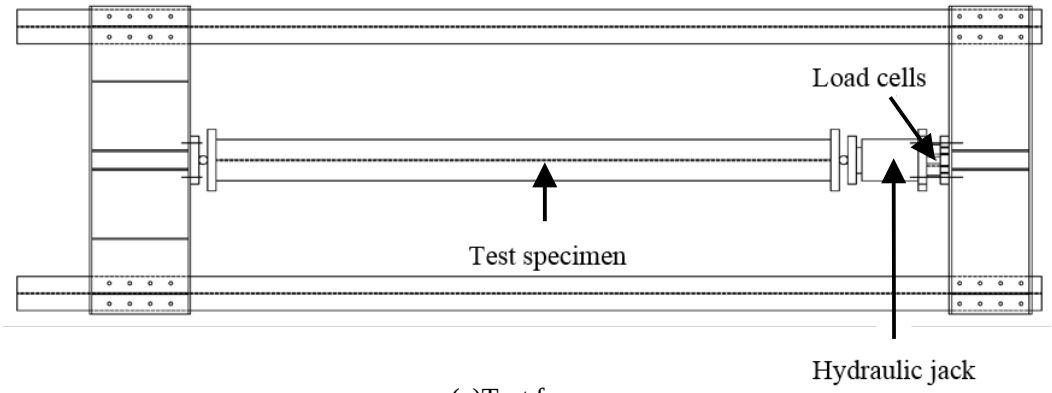

(a)Test frame

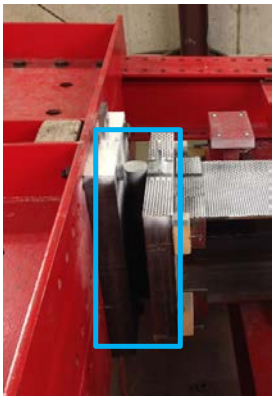

(b) Roller Supports

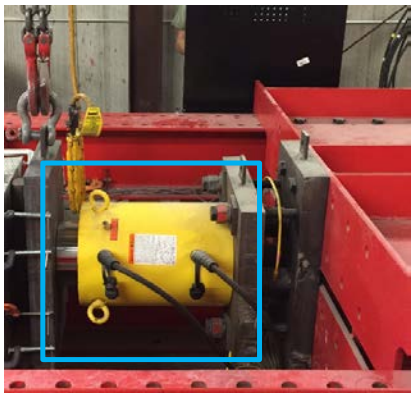

(c)Hydraulic jack

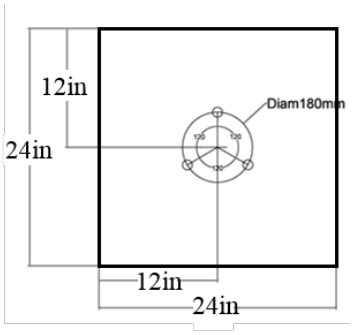

(d)Location of jack on base plate

Figure 3.5 Test frame

(a)Load cells

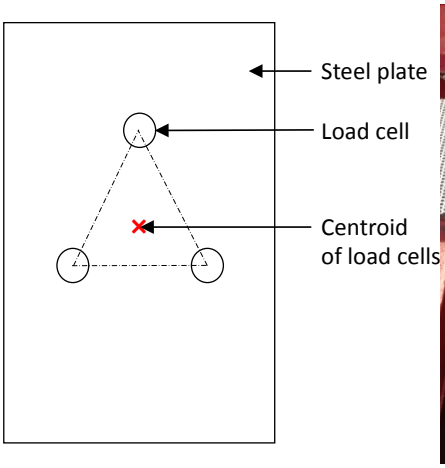

(b)Location of load cells on base plate

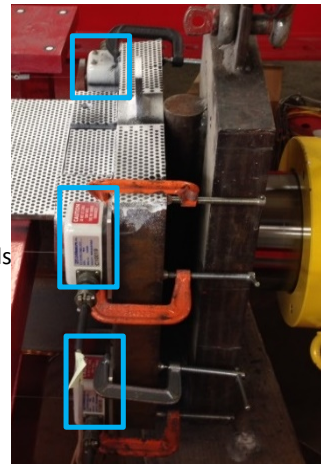

(c)Axial string pots

Figure 3.6 Instrumentations

3.2 Test Results and Discussion

This section presents a summary the axial capacities, axial stiffness, and failure modes of all seven of the corroded control test piles. The axial load-deformation responses of the seven piles are shown in one figure to achieve a general understanding of the axial capacity reduction due to corrosion. Then detailed experimental observations of each pile are presented in this section. The effects of the reduction of flange and web thickness and the extent of the corrosion on the remaining axial capacities of piles and their compressive behaviors are discussed in this section.

3.2.1 Axial capacity and stiffness

Figure 3.7 presents the axial load-shortening relationships of all seven piles. The horizontal axis refers to the measured axial deformation and the vertical axis indicates the applied axial load. Different piles are indicated by arrows pointing to the pile designations. Table 3.4 summarizes the axial capacity (P_{cr}), axial stiffness (K_{cr}), and failure mode of each pile. The subscript *cr* indicates corroded pile, and $P_{0/0}$ and $K_{0/0}$ refer to axial capacity and stiffness of Pile 0/0, respectively. Piles with non-slender flange or web (width-to-thickness ratio satisfies the limitation specified in AISC 2011), 0/0 and 0/20, failed by flexural buckling. Inspection of Figure 3.7 indicates that a 20% reduction of the web thickness did not significantly reduce the axial capacity of the pile. However, as the flange thickness reduction increased, flange became slender and flange local buckling dominated the failure of the pile. The peak loads of pile 40/20 and 40/60 decreased by 30% and 47%, respectively, compared to un-corroded control pile. The significant capacity loss of pile with 40% reduction of flange thickness was caused by two reasons: (1) the loss of cross-sectional area, (2) the loss of weak axis moment of inertia of the section which was mainly due to the loss of flange thickness, and (3) the slender flange contributed less stiffening effects of the web. When flange reduction increased to 80%, i.e. 80/60, 80/60/V, and 80/60/3, reductions of the axial peak load were up to 70%, 80%, and 75%, respectively, as compared to control specimen. Comparing the axial capacities of pile 80/60 and

pile 80/60/3 indicates that increase of the extent of deteriorated region by three times only reduced the axial capacity by 13%. The reduction of axial capacity is due to the lower plate buckling strengths of the corroded flange and web caused by their greater aspect ratios, which also resulted in a higher order mode of plate buckling (Lundquist and Stowell, 1942; Timoshenko and Gere, 2009). Pile 80/60/V exhibited a one-way bending of the two pieces of flanges at the void region. This phenomenon was due to the lack of web at the void region, which caused a lower strength of the flange one-way bending than flexural or plate local buckling. Detailed observations and discussions are illustrated in the following section.

According to ratios of the axial stiffness of piles with reduction to that of un-corroded control pile in Table 3.4, the decreases of axial stiffness of the corroded piles with 1 ft extent of reduction did not exceed 30% compared to the un-corroded control specimen, even with 82% reduction of cross-sectional area (Pile 80/60/V). This is mainly because the extent of degradation is only 1/15 of the total length of the piles. Pile 80/60/3 exhibited more decrease on the stiffness. Its axial stiffness reduced 41% compared to pile 0/0. The dominant reason is that the extent of degradation increases to 1/5 of the total length of the pile. Factors like geometric imperfections of the pile and unintentional eccentricities of the load have effects on the axial stiffness as well.

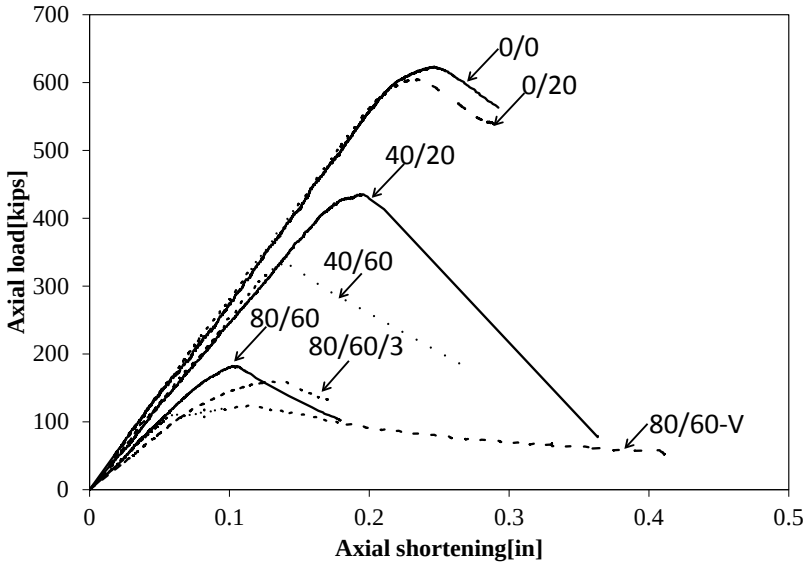

Figure 3.7 Axial load-shortening relationships of corroded piles

Table 3.4 Axial capacity, stiffness, and failure modes of corroded piles

Pile designation	Axial capacity P_{cr}[kips]	$P_{cr}/P_{0/0}$	Axial stiffness K_{cr}[k/in]	$K_{cr}/K_{0/0}$	Failure mode
0/0	623	1.00	2776	1.00	FB[a]
0/20	604	0.97	2816	1.01	FB
40/20	435	0.70	2448	0.88	FLB[b]
40/60	333	0.53	2520	0.91	FLB/WLB[c]
80/60	182	0.29	2001	0.72	FLB/WLB
80/60/V	125	0.20	1930	0.70	FOWB[d]
80/60/3	159	0.26	1645	0.59	FLB/WLB

[a]Flexural Buckling; [b]Flange Local Buckling; [c]Web Local Buckling; [d]Flange One-way Bending.

3.2.2 Experimental observations

3.2.2.1 Pile 0/0

The un-corroded control pile 0/0, was loaded up to 623 kips and failed by flexural buckling. Figure 3.8(a) shows the failed pile and Figure 3.8(b) shows its axial load-deformation response. The axial load-deformation response shown in Figure 3.8(b) is black dots connected by a dashed line. The black dots are data points collected during test, and they are connected by a dashed line (though not obvious in this case) for visual convenience. The maximum lateral deformation was observed at mid-span of the pile. The nominal capacity predicted by the design method in AASHTO (2012) is 603 kips implementing the measured dimensions and material properties, which is 3% lower than tested capacity. The difference may be caused by the magnitude of residual stresses and geometric imperfection between assumption in AASHTO (2012) and the tested pile. The design method in AAHSTO (2012) conservatively assumes 30% of the yield stress as the compressive residual stress at the tips of flanges. The permissible value of out-of-straightness specified in AASHTO is L/1500, where L is the length of the compression member.

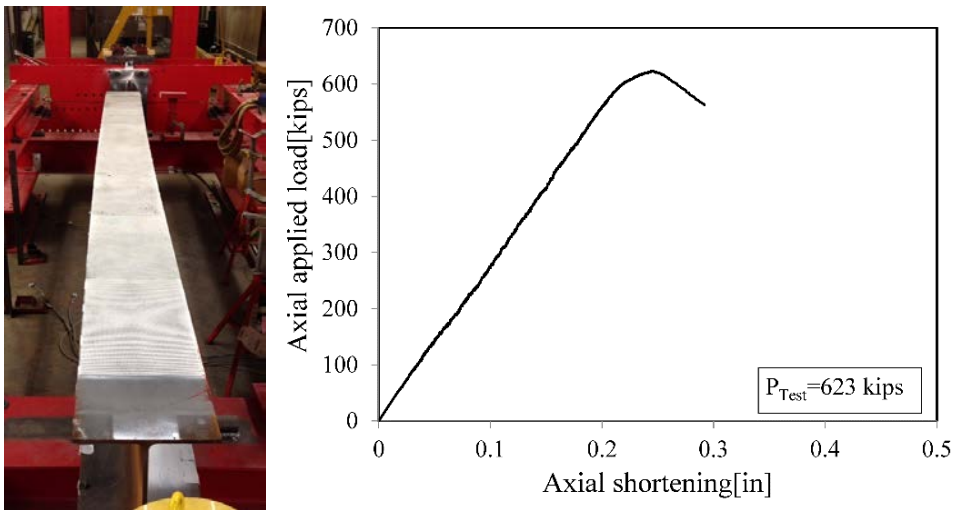

Figure 3.8 Deformed pile and axial load-deformation response of Pile 0/0

3.2.2.2 Pile 0/20

Pile 0/20 was loaded up to 603 kips and failed by flexural buckling. Figure 3.9(a) shows the deformed pile and Figure 3.9(b) shows its axial load-deformation response. The failure mode is the same as the un-corroded control pile, as shown in Figure 3.8(a). Although 20% reduction on web thickness was simulated along 1 ft extent at the third-height of the pile, flanges and web were still non-slender. The axial peak load is 3% lower than un-corroded control pile due to the loss of cross sectional area at the corroded region.

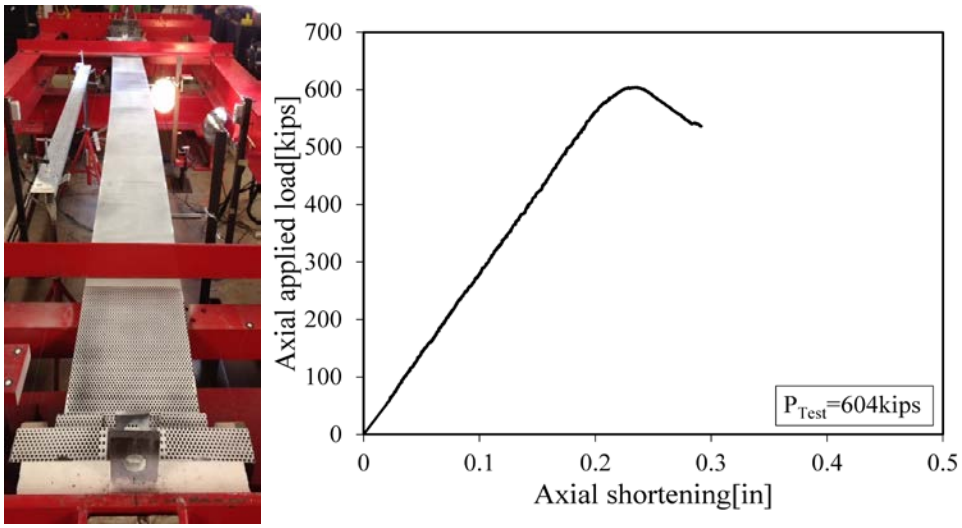

Figure 3.9 Deformed pile and axial load-deformation response of Pile 0/20

3.2.2.3 Pile 40/20

Pile 40/20 was loaded up to 435 kips and failed by flange local buckling. Figure 3.10(a) shows the deformed pile and Figure 3.10(b) shows its axial load-deformation response. The lateral displacement shown in Figure 3.10(a) was observed after peak load, and the maximum lateral displacement happened at the corroded section. Figure 3.11(a) presents the reduced section before and after failure. Two strain gauges were installed on the top and bottom surfaces of one flange tip as shown in Figure 3.11(a), to indicate the occurrence of local buckling. Figure 3.11(b) shows the values of the two strain gauges during the test. The vertical axis shows the applied axial load, and the horizontal axis illustrates the magnitudes of the strain gauges on top and bottom surfaces of the flange tip. The solid line indicates the strain gauge on the bottom surface, marked as 'Bottom SG', and the dash line indicates the strain gauge on the top surface, marked as 'Top SG'. The three red horizontal dash lines refer to three load levels at the time of testing. The tips of the reduced flange started to buckle at the load level of 366 kips, when bifurcation occurred between the top and bottom strain gauges mounted on the tip of upper flange, shown in Figure 3.11(b). At the load level of 421 kips, the yielding of flange tip initiated, which causes the onset of nonlinearity of the load-deformation response of the entire pile shown in Figure 3.10(b). The onset of nonlinearity was taken as the initiation of the slope change of the axial load-deformation curve. After the section deformation caused excessive yield strain, the values obtained from strain gauge were not reliable due to partial detachment between strain gauge and deformed steel surface. After reaching the peak load, the reduced section failed by flange local buckling and the lateral displacement increased substantially which led to the dramatic drop of measured axial load, as shown by the dashed line in Figure 3.10(b).

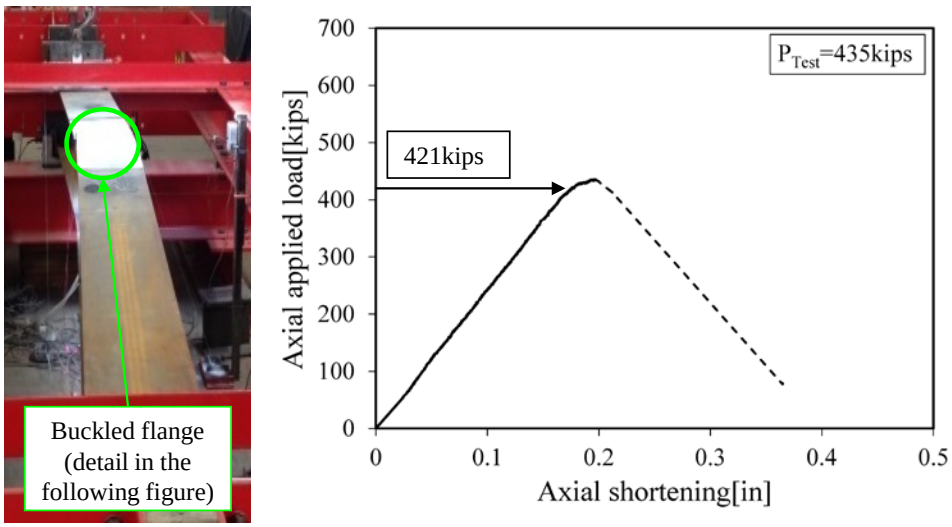

Figure 3.10 Deformed pile and axial load-deformation response of Pile 40/20

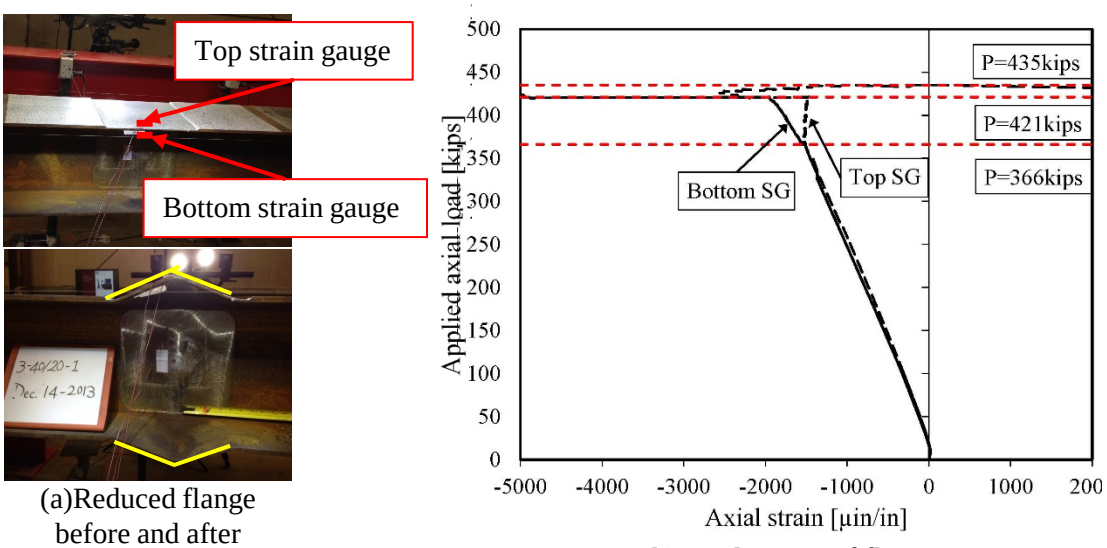

(a)Reduced flange before and after loading

(b)Axial strains of flange tip

Figure 3.11 Buckled flange of Pile 40/20

3.2.2.4 Pile 40/60

Pile 40/60 was loaded up to 333 kips and failed by flange and web local buckling. Figure 3.12(a) shows the failed pile and Figure 3.12(b) shows its axial load-deformation response. The lateral displacement happened after the peak load. Figure 3.13(a) and Figure 3.13(b) presents the flange and web local buckling. Two strain gauges were installed on the top and bottom surfaces of one flange tip, referred as 'Flange top' and 'Flange bottom' in Figure 3.13(c); and two strain

gauges were attached on two sides of the reduced web at the center, marked as 'Web north' and 'Web south', as shown in Figure 3.13(c), to indicate the occurrence of local buckling. Figure 3.13(c) shows the values of the four strain gauges during the test. The vertical axis shows the applied axial load, and the horizontal axis illustrates the magnitudes of the strain gauges on flange and web. The blue solid line and dash line indicate the strain gauges on the top and bottom surfaces of the flange tip, respectively. The black solid and dash line indicate the strain gauges on south and north side of the web, respectively. The two straight red horizontal dash lines refer to two load levels during testing. At the load level of 313 kips, both flange tip and center of web buckled according to the bifurcations occurred between the top and bottom strain gauges mounted on the tip of the flange, and the two strain gauges installed on both sides of the web, shown in Figure 3.13(c). When it reached the peak load, the reduced section failed by flange local buckling and the lateral displacement increased substantially which led to the dramatic drop of measured axial load as shown by the dashed line in Figure 3.12(b).

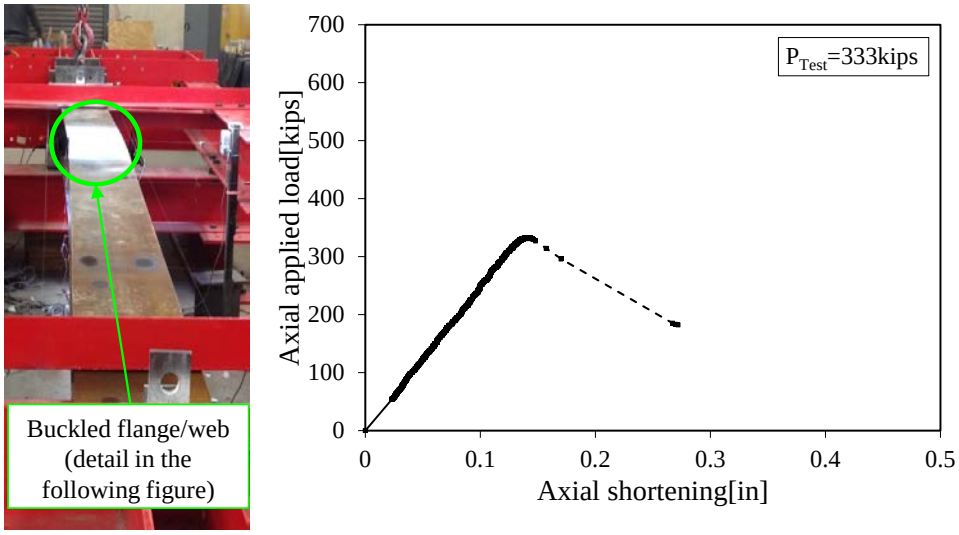

Figure 3.12 Deformed pile and axial load-deformation response of Pile 40/60

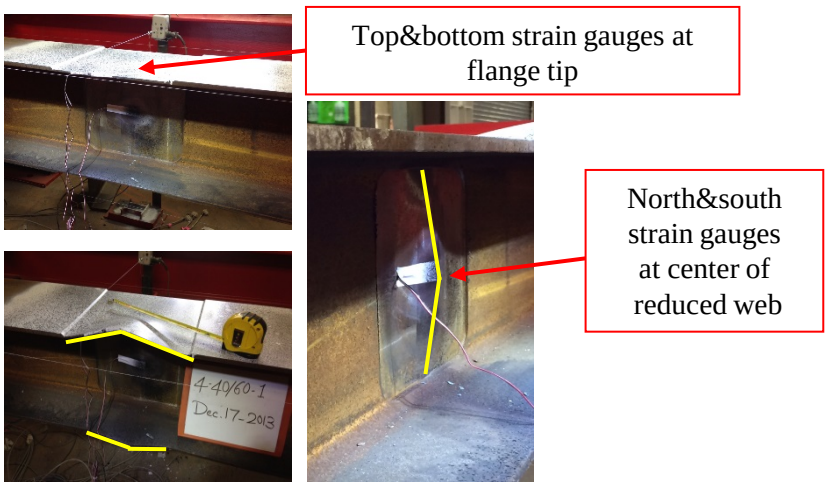

(a)Flange local buckling (b)Web local buckling

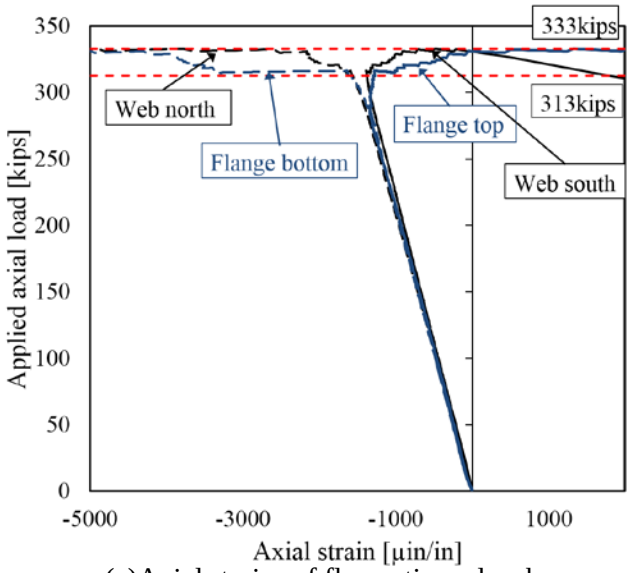

(c)Axial strains of flange tip and web

Figure 3.13 Flange and web local buckling of Pile 40/60

3.2.2.5 Pile 80/60

Pile 80/60 was loaded up to 182 kips monotonically and failed by flange and web local buckling. Figure 3.14(a) shows the failed pile and Figure 3.14(b) shows its axial load-deformation response. The lateral displacement was observed after the peak load. Figure 3.15(a) presents the flange and web local buckling. Two strain gauges were installed on the top and bottom surfaces of one flange tip, referred as ‘Flange top’ and ‘Flange bottom’; and two strain gauges were attached on two sides of the reduced web at the center, marked as ‘Web north’ and ‘Web south’,

as shown in Figure 3.15(b), to indicate the occurrence of local buckling. Figure 3.15(b) shows the values of the four strain gauges during the test. The vertical axis shows the applied axial load, and the horizontal axis illustrates the magnitudes of the strain gauges on flange and web. The blue dashed line and solid line indicate the strain gauges on the top and bottom surfaces of the flange tip, respectively. The black solid and dashed lines indicate the strain gauges on south and north side of the web, respectively. The two red horizontal dashed lines refer to two load levels during testing. At the load level of 67 kips, both flange tip and center of web started to buckle, according to the bifurcations occurred between the top and bottom strain gauges mounted on the tip of the flange, and the two strain gauges installed on both sides of the web, shown in Figure 3.15(b). After the peak load, 182 kips, the reduced section failed by flange local buckling and the lateral displacement increased substantially which led to the dramatic drop of measured axial load as shown by the dashed line in Figure 3.14(b).

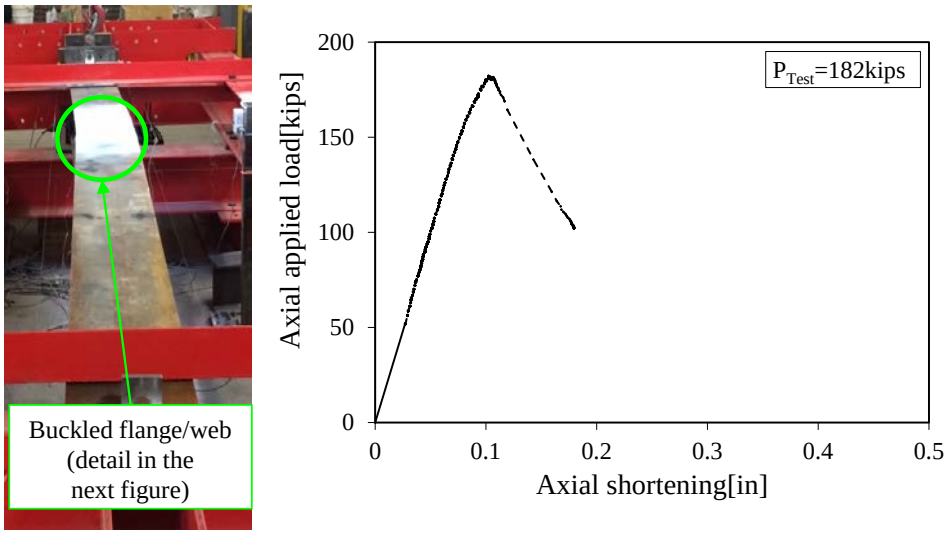

Figure 3.14 Deformed pile and axial load-deformation response of Pile 80/60

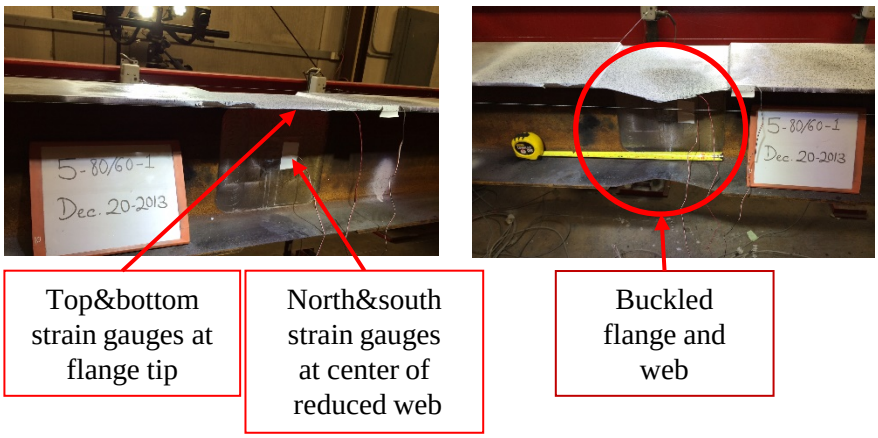

(a) Reduced region before and after loading

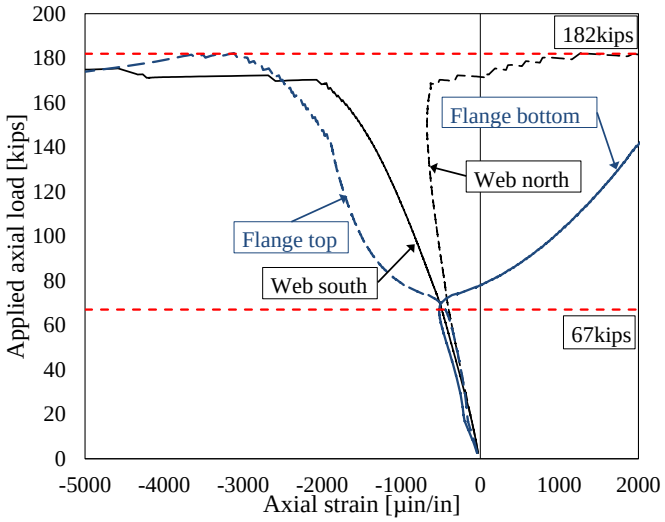

(b) Axial strains of flange tip and web

Figure 3.15 Flange and web local buckling of Pile 80/60

3.2.2.6 Pile 80/60/V

Pile 80/60/V was loaded up to 125 kips monotonically and failed by flange local buckling followed by one-way bending. Figure 3.16(a) shows the failed pile and Figure 3.16(b) shows its axial load-deformation response. The lateral displacement was observed after the peak load. The change of slope in the axial load-deformation response was attributed to the top and bottom flanges at the corroded section did not fail at the same time due to the difference of their thicknesses and probable unintentional eccentricity of the test set-up. The bottom flange failed prior to the top flange (details will be illustrated later), so the axial stiffness decreased at the load

of 109 kips when bottom flange stopped its contribution. Figure 3.17(a)-(d) illustrate the deformations of corroded section at different load levels, and Figure 3.17(e) presents the axial strains obtained from the strain gauges attached on the flanges, where the horizontal axis shows the time of testing and the vertical axis illustrates the magnitudes of the strain gauges. The solid and dash line indicate the strain gauges on top and bottom flanges, respectively. The two straight vertical dash lines refer to two load levels during testing: 109 kips where the slope of axial load-deformation curve changes and the peak load 125 kips. As shown in Figure 3.17(a), two strain gauges were attached at the center of the reduced flanges on the top and bottom surfaces, referred as 'Flange top center' and 'Flange bottom center' in Figure 3.17(e). Figure 3.17(b) shows the flange local buckling at the beginning of loading. At this time, the shape of the void was still rectangular. This is because the center of the flanges was supported by the rest of the fillets although web was totally milled, while the free edges of the flanges buckled locally. Figure 3.17(c) shows the one-way bending happened first to the bottom flange at the load level of 109 kips, which can also be identified from the axial strain value shown in Figure 3.17(e). Yielding of the center region of the bottom flange caused a minor drop of the axial load, followed by a decrease of the axial stiffness, shown in Figure 3.16. Figure 3.17(d) shows the deformed section after failure. Both top and bottom flanges exhibited one-way bending failure along the x-x axis (shown in Figure 3.17(d)) at the junction regions of flanges and web, as the reduced section (only two pieces of flanges left) had greater moment of inertia about x-x axis than y-y axis.

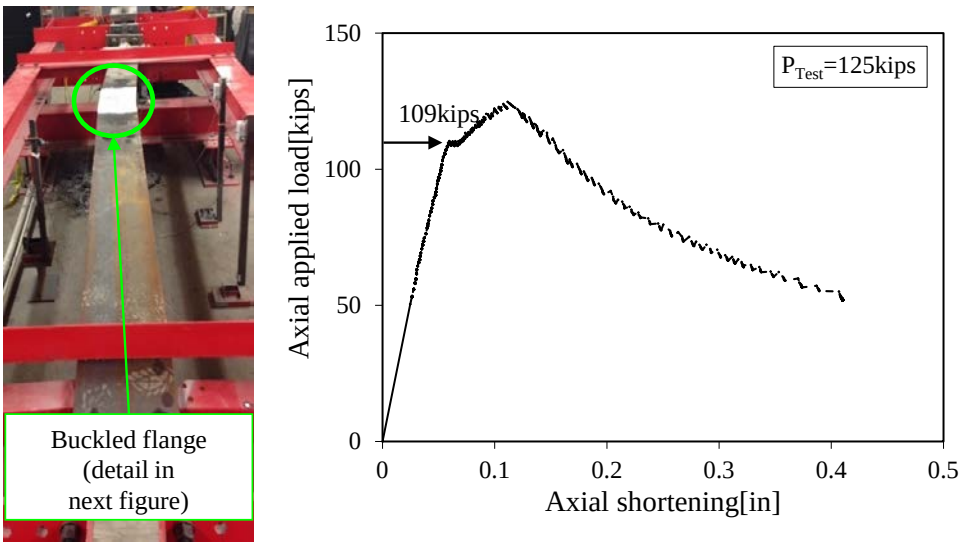

Figure 3.16 Deformed pile and axial load-deformation response of Pile 80/60/V

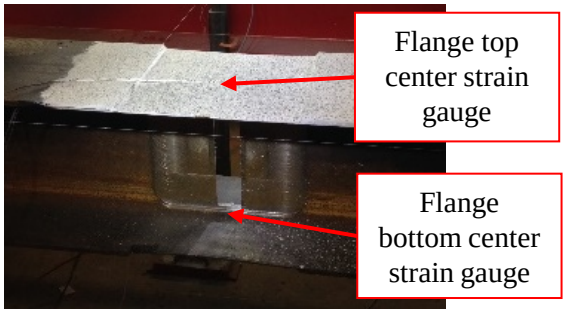

(a) Reduced section before loading

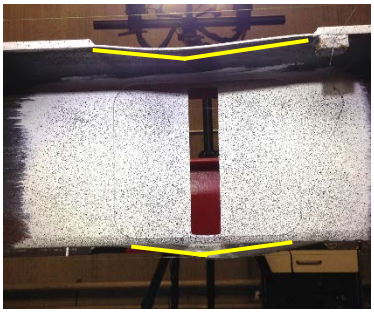

(b) Buckled flange

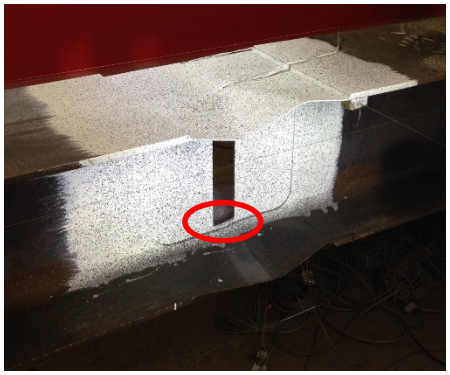

(c) Bottom flange one-way bending

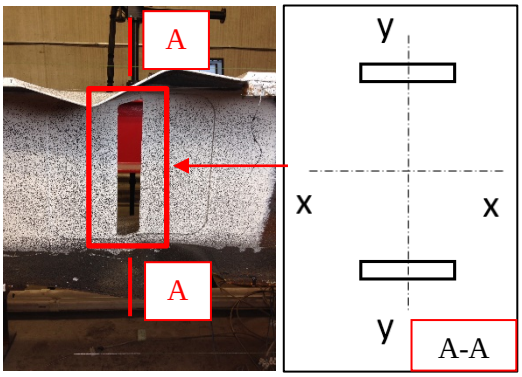

(d) Top&bottom flange one-way bending

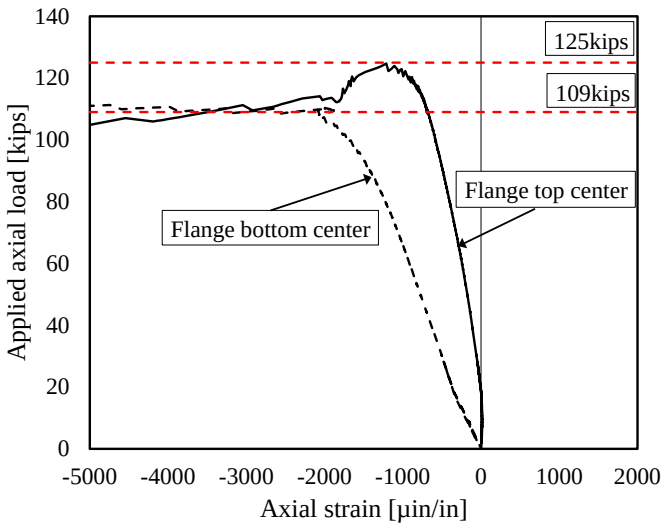

(e) Axial strains of top and bottom flanges

Figure 3.17 Flange local buckling and one-way bending of Pile 80/60/V

3.2.2.7 Pile 80/60/3

Pile 80/60/3 was loaded up to 159 kips monotonically and failed by flange and web local buckling. Figure 3.18(a) shows the failed pile and Figure 3.18(b) shows its axial load-deformation response. The lateral displacement was observed after the peak load. Figure 3.19(a)-(b) illustrate the corroded section before and after failure. The local deformation shape of the 80/60/3 exhibited higher order of buckling, due to the increase of the aspect ratio of the buckled flange.

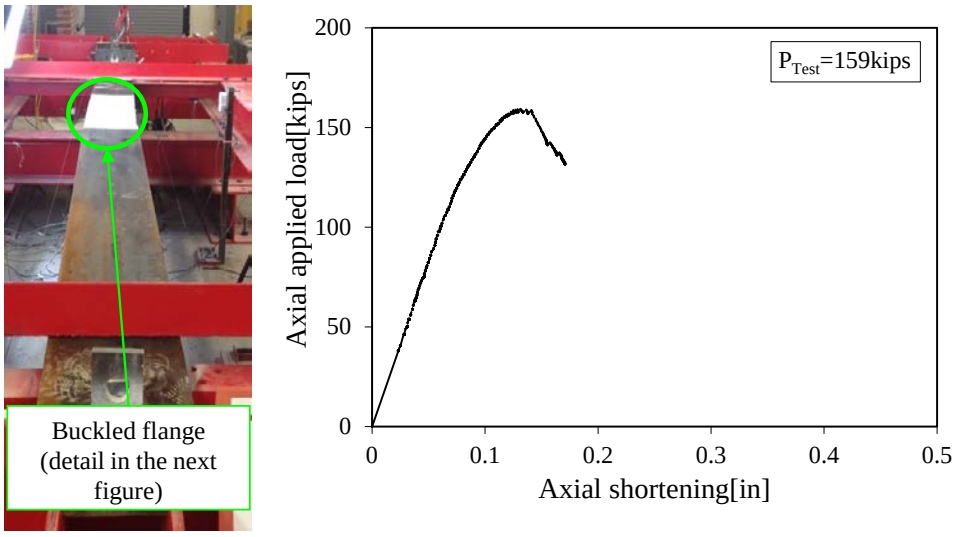

Figure 3.18 Deformed pile and axial load-deformation response of Pile 80/60/3

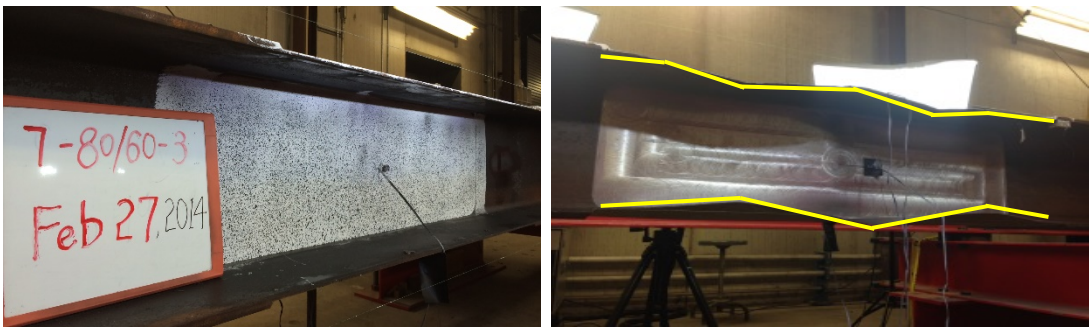

(a)Reduced section before loading (b)Buckled flange

Figure 3.19 Flange local buckling and one-way bending of Pile 80/60/V

3.3 Conclusions

Seven full-scale H-piles with different reduction degrees and patterns at localized region were tested under axial compression. The effects of reduction on flange and web thickness and extent of corroded region were investigated. The obtained conclusions are summarized as follows:

1) A 20% reduction of the web thickness did not significantly reduced the axial capacity of a pile. However, as the reduction of the flange thickness increased and the flange became slender, the axial capacity of the pile decreased significantly due to (1) the loss of cross-sectional area, (2) the loss of weak axis moment of inertia of the section which was mainly due to the loss of flange thickness, and (3) the slender flange contributed less stiffening effects of the web.

2) Extent of corroded region decreased the axial capacity because a greater aspect ratio decreased the plate buckling strength of corroded flange and web, which also resulted in a higher-order of plate buckling mode.

3) Void on web changed the failure mode from flange and web local buckling to flange one-way bending. This phenomenon was due to the lack of web at the void region, which caused a lower strength of the flange one-way bending than flexural or plate local buckling.

The results and findings of the experimental study on corroded piles presented in this chapter were used to validate a 3D non-linear FE model developed to predict the axial behavior of H-pile with local reduction, and were also used as a control group for the tests of repaired piles to investigate the efficiency of a proposed repair system. The validation of the FE model and further

parametric study will be described in Chapter 4. The experimental program of repaired piles will be introduced in Chapter 5.

CHAPTER 4 NUMERICAL STUDY OF CORRODED H-PILES

This chapter presents the development of a numerical framework that can be used to predict the remaining axial capacity of steel H-piles with arbitrary patterns and degrees of localized corrosion. The numerical prediction approach is of critical necessity because existing design methods tend to provide excessively conservative assessment for partially corroded bridge piles. Their application on partially corroded members assumes a uniformly distributed reduction along the entire length. In extreme cases, the design method in AASHTO (2012) can provide predictions that are 90% lower than the measured capacity (Karagah et al., 2015; Shi et al., 2014).

Therefore, a finite element model was developed based on the configuration of test specimens that were reported in Chapter 3. First, the FE model was validated by both small-scale and full-scale experimental results. The small-scale tests of W-shaped piles were conducted by Karagah et al. (2015), and the full-scale experimental program was illustrated in Chapter 3 of this dissertation. The small-scale experiments included 13 W4×13 piles with various distributions simulated corrosion. The dimensions and pile slenderness were not strictly scaled to the full-scale piles. However, the small-scale experimental results provided several findings that revealed the axial behavior of partially corroded H-piles. Furthermore, the model was used for a more in depth parametric study investigating factors that might have effects on the axial behavior of the piles. These factors include slenderness of the reduced flange and web, slenderness of the pile, the location and extent of the corroded region, and the magnitude of residual stresses.

4.1 Finite Element Model

A non-linear, 3D finite element model was developed using the commercial finite element package ABAQUS v6.12 (SIMULIA, 2012). Two consecutive steps were performed in the FEA: 1) eigenvalue analysis to obtain the elastic buckling modes; 2) with elastic buckling modes imposed as the initial imperfections shapes, an inelastic buckling analysis was conducted incorporating the effect of residual stresses and large deformations. Boundary conditions were modeled to represent the test set-up at the supports and only rotation about the weak axis was

permitted while the other degrees of freedom were restrained. The piles were loaded by imposing an axial displacement at one end to simulate the action of the hydraulic jack used in the experimental program. The modified Riks method (Riks, 1979) was employed to solve the geometrically and materially nonlinear model.

4.1.1 Element type and mesh size

To evaluate different types of elements and mesh sizes, a sensitivity study of inelastic buckling analysis was performed on two piles, 0/0 and 80/60 of full-scale experimental program described in Chapter 3. The pile 0/0 refers to the un-corroded control specimen with 0% reduction on flange and web, and 80/60 refers to the pile with 80% and 60% reduction flange and web thickness, respectively. These two representative piles were chosen for sensitivity study because the two cases contain failure modes of flexural buckling, flange and web local buckling. Also, the two cases represent the extreme cases of corrosion that were considered in this research. The FE model adopted the measured dimensions of flange and web thicknesses and material properties from tension coupon tests of the large scale piles. The thickness of the member is relatively small as compared to its length and width. The ratio of thickness to length/width is less than 1/15. Therefore, three commonly used shell element types were compared and evaluated to select an efficient element type for the numerical framework. The first element type was a four-node, six degrees of freedom per node, linear shape function, fully integrated, finite-membrane-strain shell element, S4. It is a general-purpose shell element, which uses thick shell theory (Mindlin-Reissner plate theory) (Mindlin, 1951) as the shell thickness is over 1/15 of a characteristic length and becomes discrete Kirchhoff thin shell element as the thickness decreases, in which transverse shear flexibility is neglected. The second element type is S4R, which is similar to S4 but uses reduced integration to form element stiffness. The third element type is an eight-node, six degree of freedom per node, second-order, thick shell element, S8R, with reduced integration. The elementary mesh size to start investigation was 2 in×2 in. The mesh was subdivided twice, into 1 in ×1 in and 0.5 in×0.5, to evaluate the convergence of the results.

Figure 4.1(a) and Figure 4.1(b) present the axial capacities for pile 0/0 and 80/60, respectively, predicted by FEA using S4, S4R, and S8R element. The horizontal axis refers to the three values of mesh size, and the vertical axis refers to the predicted axial capacity. The dashed line indicates the converged load level as the mesh size refines. The predicted inelastic buckling loads for 0/0 using three element types showed comparable results when the mesh size was 2 in×2 in. However, regarding 80/60 with substantial reduction on flange and web, only S8R showed convergent result when the mesh size was 2 in×2 in. Predictions using element S4 and S4R converged until the mesh size was refined to 1 in×1 in. The reason is that for flexural buckled pile, 0/0, the deformation of the pile was relatively smooth, and both first-order (S4 and S4R) and second-order (S8R) element were able to provide satisfactory prediction with the same mesh size. In contrast, for pile failed by local buckling, 80/60, the buckled region was so curved that element with linear shape function (S4 and S4R) could not capture the deformation properly. Reduction of the mesh size (from 2 in×2 in to 1 in×1 in) or increment of the element polynomial degree (doubly curved shell S8R instead of element with linear shape function) was needed.

The results of sensitivity study indicate that S4 and S4R element with 1 in×1 in mesh size, and S8R element with 2 in×2 in mesh size can be used for current study. When reduced integration is used for linear element as S4R, hourglass effects need to be checked and controlled (Flanagan and Belytschko, 1981). Element S8R was capable to provide reliable predictions of corroded piles. However, it would automatically transfer to element S9R5 in problems with contact (SIMULIA, 2012), to ensure the internally defined center node be positioned on the actual shell surface. To be consistent with the simulations of corroded piles and repaired piles (will be described in Chapter 6), element S4 with mesh size as 1 in×1 in was chosen for the FEA of both corroded piles and repaired piles.

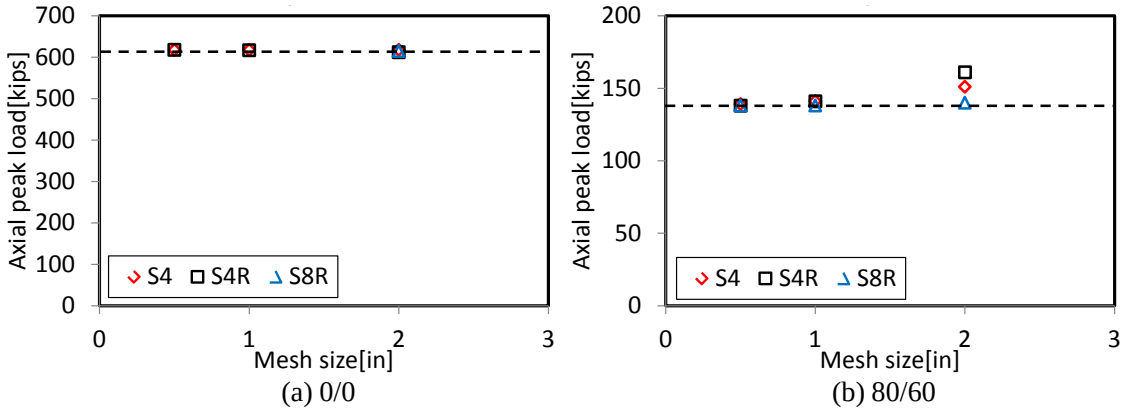

(a) 0/0 (b) 80/60

Figure 4.1 Sensitivity study for element type and mesh size

4.1.2 Material properties

The material model follows classic plasticity: Von-Mises yield criteria, associated flow, and isotropic hardening. The uniaxial stress-strain relationship uses bilinear curve as shown in Figure 4.2, where F_y and F_u refer to yield and ultimate stresses, respectively. As two types of piles, small-scale W4×13 section and full-scale HP12×53 section, were used to validate the numerical framework, the material properties from tension coupon tests and stub column tests of both piles were used. Table 4.1 summarizes the material properties of two sizes of piles. For small-scale W4×13 piles, the moduli of elasticity and yield strengths of the flange and web were adopted values from a stub column test (Karagah et al. 2015). The ultimate strengths were taken from the results of tension coupon tests. For full-scale HP12×53 piles, the elastic moduli, yield and ultimate strengths for flange and web were taken as the mean values obtained from tests of four tension coupons described in Chapter 3(Table 3.3). Detailed procedures of the determination of the material properties were described in Section 3.1.2.

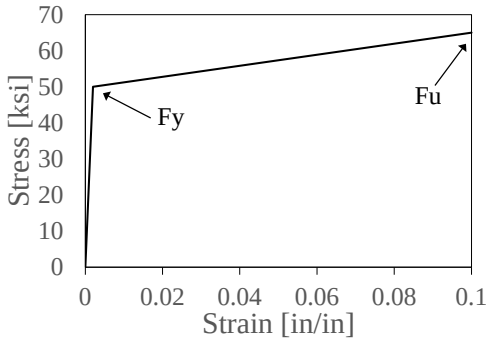

Figure 4.2 Stress-strain relationship of steel used in FEA

Table 4.1 Material properties of W4×13 and HP12×53

Pile	Element	Yield strength [ksi]	Ultimate strength [ksi]	Elastic modulus [ksi]
W4×13	Flange	56.0	69.5	26,900
	Web	63.5	77.0	26,100
	Stub column	53.5	--	30,200
HP12×53	Flange	52.5	66.5	28,400
	Web	60.5	71.0	32,000

4.1.3 Effects of initial imperfections

The first modes of flexural and local buckling shape, as shown in Figure 4.3, were used as the initial global and local imperfection shapes for all simulated piles. This is conservative approach as they represent the most potential failure modes. According to the AISC (2011), the permissible fabrication sweeps for axial member with flange width under and above 6 in are L/480 and L/960, respectively; while the maximum value of out-of-straightness of a compression member is L/1000, where L is the length of the member. In contrast, AASHTO (2012) allows a maximum out-of-straightness of L/1500. Figure 4.4(a) and (b) shows the effects of initial global imperfection, Δ_G, on two representative piles failed by flexural and local buckling, respectively. Figure 4.4(a) shows the axial load-deformation responses of small-scale piles 0/0 (un-corroded control pile) and 75/60 (pile with 75% and 60% reduction on flange and web thicknesses respectively) with three different magnitudes of global imperfections. Figure 4.4(b) shows the axial load-deformation curves of full-scale piles 0/0 and 80/60 with different values of global imperfections. Inspection of Figure 4.4 indicates that the initial global imperfection has very minor influence on the axial capacity of piles. The differences of axial capacities caused by

varying values of global imperfection are less than 5% for piles with no damage and with major cross-section loss, regardless of the section size. It is difficult to achieve the actual magnitude of initial imperfection of the original pile in field. Therefore, the initial global imperfection was taken conservatively as the maximum of the three values in AISC (2011) and AASHTO (2012), which were L/480 and L/960 for W4×13 and HP12×53 sections, respectively. The peak magnitude of the local imperfections, Δ_L, was taken as the fabrication tolerance defined in AISC, which was 0.06 in. The global and local initial imperfections were implemented by scaling the first mode of flexural and local buckling to the values determined above.

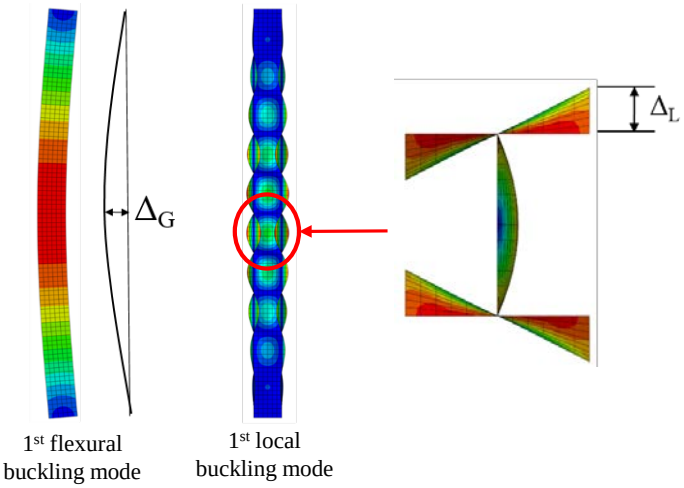

Figure 4.3 Shapes initial global and local imperfections from elastic buckling analysis

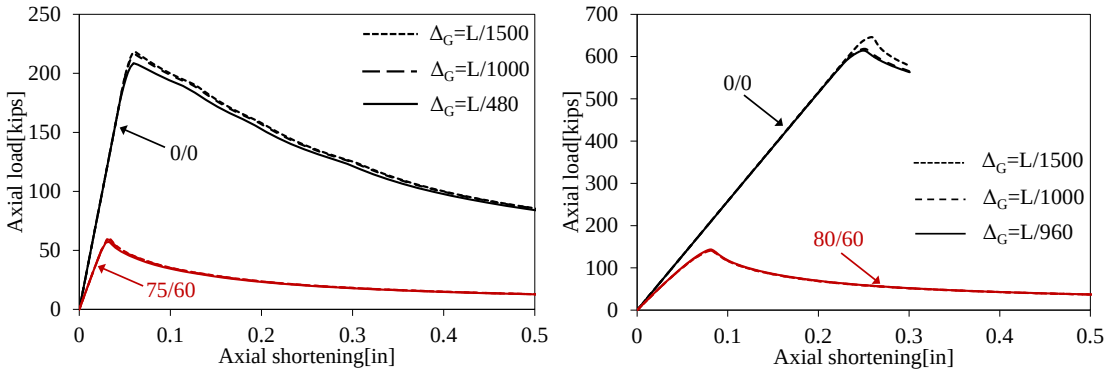

(a) W4×13 (b) HP12×53

Figure 4.4 Effects of initial global imperfection on pile axial capacity

4.1.4 Effects of residual stresses

Figure 4.5 presents the distribution of residual stresses, which was suggested by Ziemian (2010) with maximum compression stresses, σ_c, at the flange tips and uniform tension, σ_t, in the web. The residual stresses were implemented as predefined stresses on selected elements before applying axial load. The maximum magnitude of residual stresses was conservatively assumed as 30% of the yield stress of the material in AISC (2011). However, a sensitivity analysis was conducted on the small-scale and full-scale control specimens, 0/0, to identify a magnitude of residual stress that provides the most accurate axial capacity. Peak residual stresses of 10%, 20%, and 30% of the nominal yield stress (5 ksi, 10 ksi, and 15 ksi, respectively) were considered. Figure 4.6 presents the axial capacities of small-scale and full-scale piles with three values of maximum residual stress. The figure shows the axial load-deformation responses and the horizontal dash line indicates the axial peak load of un-corroded control pile obtained from experiment. The predicted axial capacities of the HP12×53 control specimen were 652 kips, 618 kips and 579 kips in the three cases, while the capacity obtained from test was 623 kips. The predicted capacity with peak residual stresses of 10 ksi ($\sigma_c=\sigma_t=\pm10$ksi in Figure 4.5) matched the axial capacity of the control pile. Therefore, the residual stresses were taken as 10 ksi in compression at the tips of flanges and 10 ksi in tension along the depth of the web for full-scale piles. For W4×13 section, the obtained axial capacities for piles with 5 ksi, 10 ksi, 15 ksi maximum residual stresses were 209 kips, 208 kips, and 208 kips, respectively. Three magnitudes of maximum residual stresses provided almost the same capacity. However, the maximum magnitude of residual stresses for small-scale piles was taken as 5 ksi, because the stress-strain relationship obtained from stub column test indicated minor residual stresses on the section (Shi et al., 2014).

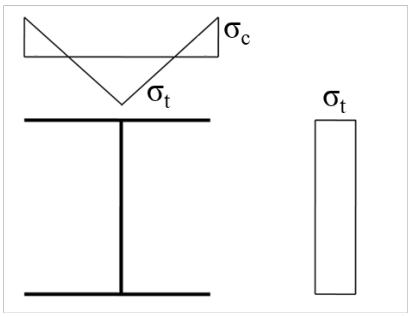

σc=compressive stress
σt=tensile stress

Figure 4.5 Distribution of residual stresses on the flange and web

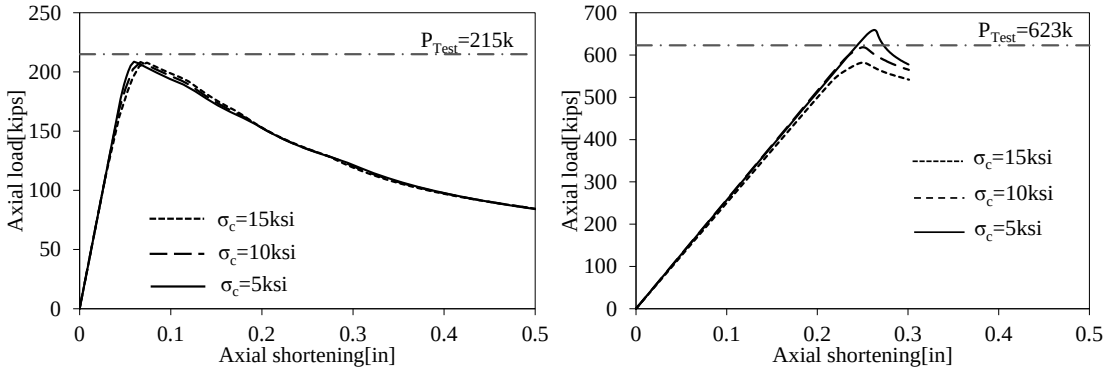

(a) W4×13 (b) HP12×53

Figure 4.6 Effects of residual stresses on axial capacity

4.2 Validation of Numerical Framework

This section presents the comparisons of experimental results and FEA predictions for small-scale and full-scale piles. The comparisons were conducted on the axial capacity, stiffness, axial load-deformation response, and failure mode.

4.2.1 Comparison of axial behavior from FEA and experiments of small-scale corroded piles

Table 4.3 presents the applied axial peak loads and failure modes obtained from FEA and tests. The pile designations were adopted from the experimental program (Karagah et al., 2015). In the example shown in Figure 4.7(a) (Karagah et al., 2015), the first and second numbers indicate the percentages of reduction on flange and web thickness, respectively. “75/60” refers to 75% reduction on flange thickness and 60% reduction on web thickness. The third part, “V” refers to a 2 in void in the web at the center of degraded region, while “NV” means there is no

void in the web. The fourth part of the designation specifies the reduction on two flanges with “S” for symmetric and “US” for un-symmetric cases. The last part “WR”, when applicable, indicates reduction on flange width, as shown in Figure 4.7(b) (Karagah et al., 2015).

Inspection of Table 4.4 indicates that the FEA correctly predicted the failure modes of all of test specimens. The deformed piles failed by typical failure modes are illustrated in Figure 4.8. The deformed shapes predicted by FEA matched the experimental observations. For piles with flange thickness reduction no more than 50%, the differences between FEA and tests results were generally less than 10%. For piles with flange thickness reduction up to 75%, discrepancy between tests results and numerical predictions increased up to 50%. For severely corroded sections the percentage error was relatively large, but the absolute value of the error in kips was a small percentage of the design capacity of the pile. For pile 70/60/V/S/WR, the difference between FEA prediction and test result was 12 kips. For a pile that was designed to carry 200 kips of load, the error was only 6% of the design capacity, which was within an acceptable tolerance when considering the design of the repair system. Moreover, the FEA prediction generally under-predicted the pile capacity.

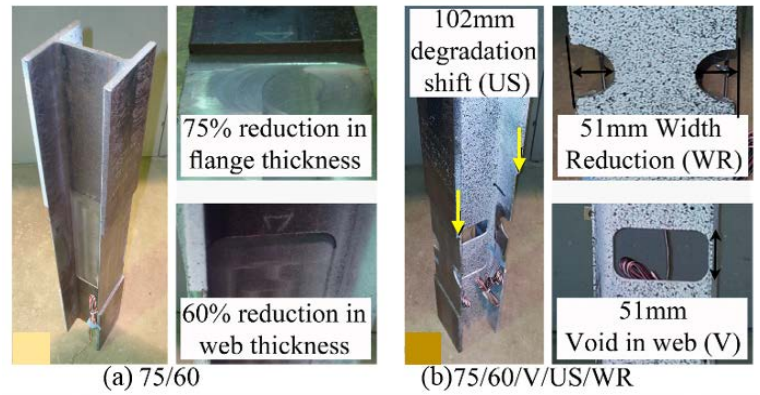

Figure 4.7 W4×13 piles with reduced sections

Table 4.2 Axial peak loads and failure modes of W4×13 from FEA and tests

Pile designation	Axial peak load [kips]		P_{test}/P_{FEA}	Failure mode	
	P_{test}	P_{FEA}		Test	FEA
0/0	215	209	1.03	FB[a]	FB
0/30	201	185	1.09	FB	FB
0/60	178	170	1.05	FB	FB
50/0	117	124	0.94	FLB[b]	FLB
75/0	92	73	1.26	FLB	FLB
50/30	130	116	1.12	FLB/WLB[c]	FLB/WLB
75/60	70	58	1.21	FLB/WLB	FLB/WLB
75/60/V/S	39	34	1.15	FOWB[d]	FOWB
75/60/NV/US	57	43	1.33	FLB/WLB	FLB/WLB
75/60/V/US	40	36	1.11	FOWB	FOWB
75/60/NV/US/WR	70	52	1.35	FLB/WLB	FLB/WLB
75/60/V/S/WR	36	24	1.50	FOWB	FOWB
75/60/V/US/WR	39	34	1.15	FOWB	FOWB

[a]Flexural Buckling; [b]Flange Local Buckling; [c]Web Local Buckling; [d]Flange One-way Bending

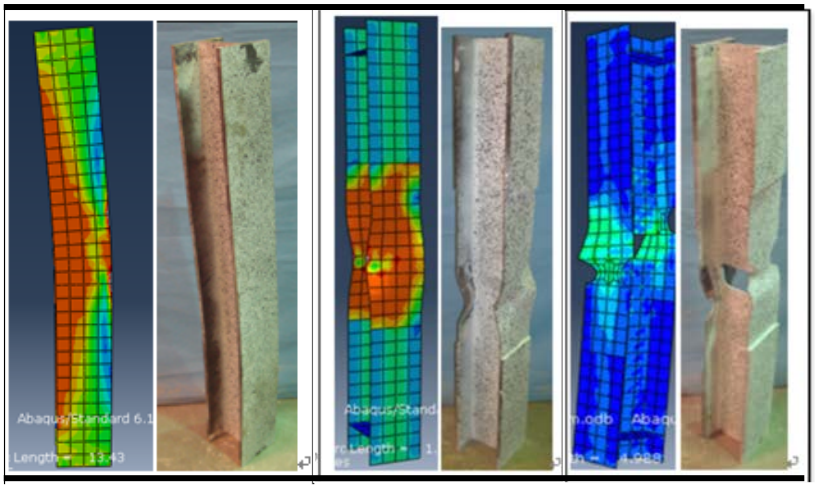

FB FLB&WLB FOWB

Figure 4.8 Deformation of small-scale piles from FEA and test

Figure 4.9 illustrates the comparison of axial load-shortening relationships of the small-scale piles from experiments and FEA. The figure also presents the coefficients of determination, R^2, between experimental and numerical curves. $(R^2)_{total}$ was calculated from the total range of the curves from zero deformation to the maximum deformation of the test or FEA. The end of the range when calculating $(R^2)_{total}$ depended on the maximum deformation point obtained from tests. $(R^2)_{peak}$ was calculated within a range from zero load/deformation to the peak load of the curves,

to quantify the correlation of FEA and experimental results regardless of the post-peak behavior. Inspection of Figure 4.9 indicates excellent correlation between the experimental and FEA results before peak load. The values of $(R^2)_{peak}$ are no less than 0.97 for all piles. The post-peak portions of the load-displacement curves exhibit good correlation when the failure mode of the pile is flexural buckling. In these cases, $(R^2)_{total}$ are no less than 0.97 except for pile 0/60. However, the discrepancy increases as the flange becomes slender. The abnormal post-buckling behavior of 0/60 was attributed to a noisy load signal from electro-magnetic interference during testing (Karagah et al., 2015). The discrepancies between the measured and predicted axial load-displacement relationships were attributed to four reasons: (1) unintentional eccentricity of the applied load during testing; (2) uncertainty of the magnitude and pattern of the residual stresses, especially for piles with degradations, which might contain possible relief of residual stresses during milling of the flange and web; (3) conservativeness of the assumed magnitude and pattern of initial imperfections; (4) effect of the fillet at the junction of flange and web, which was not modeled in the FE simulation but partly existed in tested specimens.

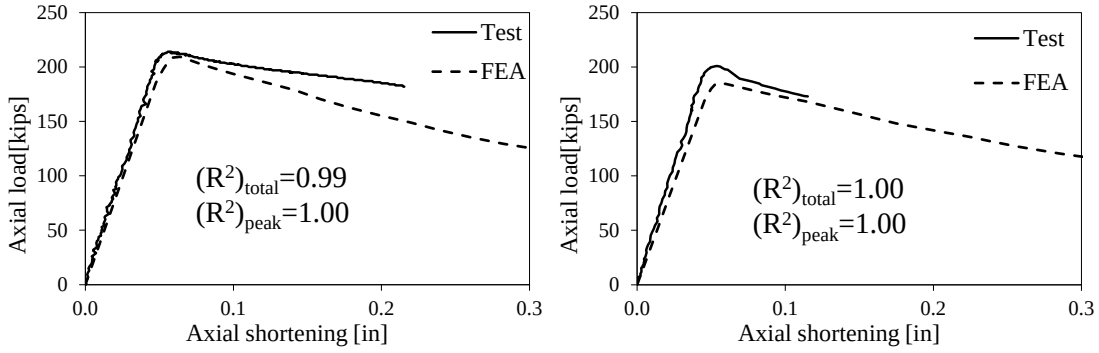

(a) 0/0 (b) 0/30

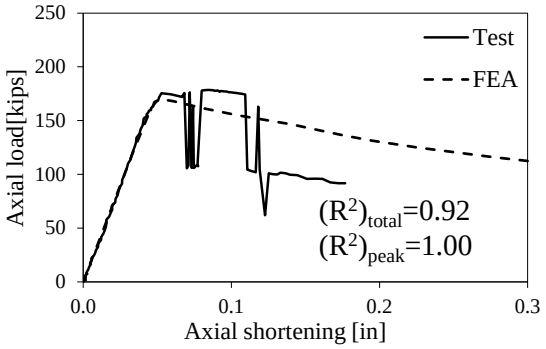

(c) 0/60

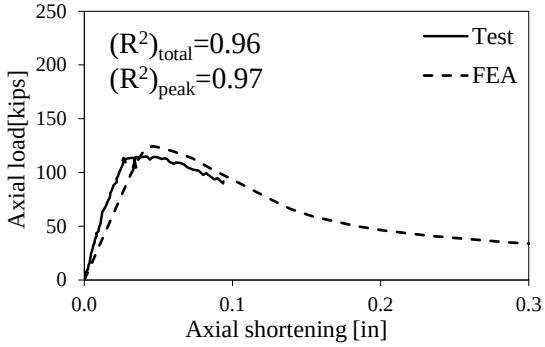

(d) 50/0

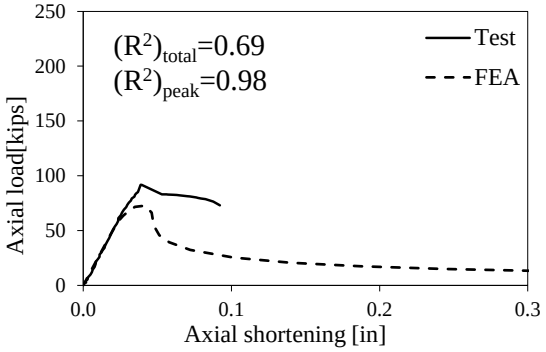

(e)75/0

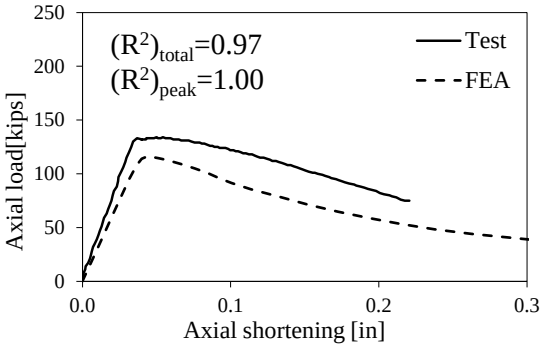

(f) 50/30

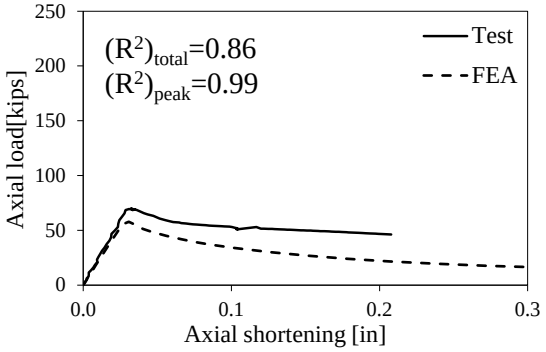

(g) 75/60

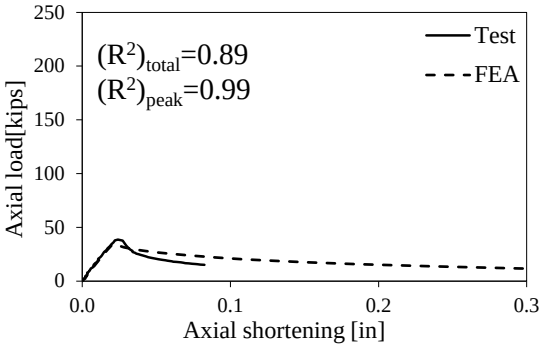

(h)75/60/V/S

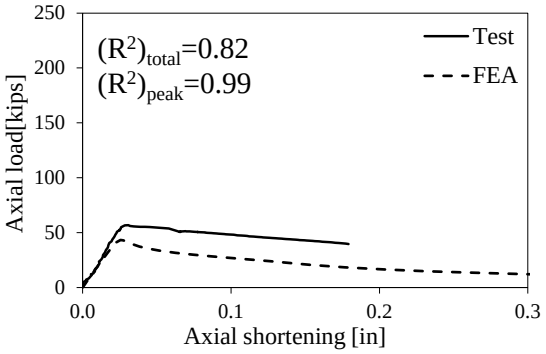

(i) 75/60/NV/US

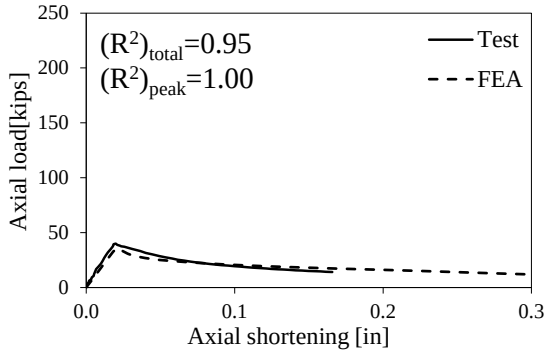

(j) 75/60/V/US

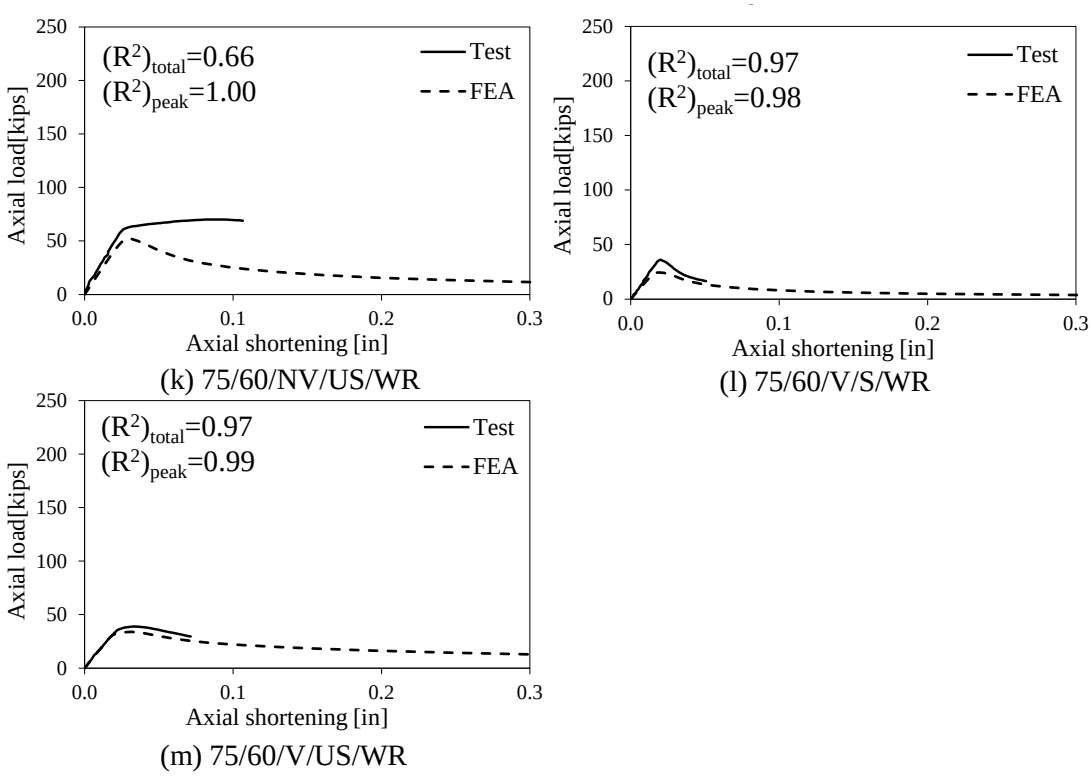

Figure 4.9 Comparison of axial load-shortening responses from tests and FEA of W4×13

4.2.2 Comparison of axial behavior from FEA and experiments of full-scale corroded piles

Similar to small-scale piles, the experimental results from full-scale H-piles presented in Table 4.3 were also used to validate the FE model. Table 4.3 illustrates the axial peak load and failure mode of the full-scale HP12×53 piles from experiments and FEA. The pile designation was defined in previous chapter: the first and second number indicate the percentage of thickness reduction on flange and web, respectively; the third part, when applicable, "V" refers to void on web and "3" refers to 3 ft extent of reduction region. The numerical model accurately predicted the failure mode of all tested piles. The deformed piles failed by typical failure modes are illustrated in Figure 4.10. The deformed shapes predicted by FEA matched the experimental observations. The predicted axial peak loads are slightly conservative except for pile 0/20 and 40/20 for which the capacities are over-predicted by 3% and 8%, respectively. This is attributed to a higher unintentional load eccentricity during testing. This was identified from the test data of four string potentiometers illustrated in Chapter 3 and Appendix A. The ratios of FEA prediction

to experimental result are close to 1.3 for pile 80/60 and 80/60/V due to their absolute values of axial capacity that are relatively low. The absolute differences between FEA and experimental results are 41 kips and 28 kips, respectively. These correspond to only 7% and 5% of the nominal design capacity of the original pile of 580 kips.

Table 4.3 Axial peak loads and failure modes of HP12×53 from FEA and tests

Pile designation	Axial peak load [kips]		P_{test}/P_{FEA}	Failure mode	
	P_{test}	P_{FEA}		Test	FEA
0/0	623	618	1.01	FB[a]	FB
0/20	604	621	0.97	FB	FB
40/20	435	472	0.92	FLB[b]	FLB
40/60	333	303	1.10	FLB/WLB[c]	FLB/WLB
80/60	182	141	1.29	FLB/WLB	FLB/WLB
80/60/V	124	96	1.29	FOWB[d]	FOWB
80/60/3	159	160	1.00	FLB/WLB	FLB/WLB

[a]Flexural Buckling; [b]Flange Local Buckling; [c]Web Local Buckling; [d]Flange One-way Bending.

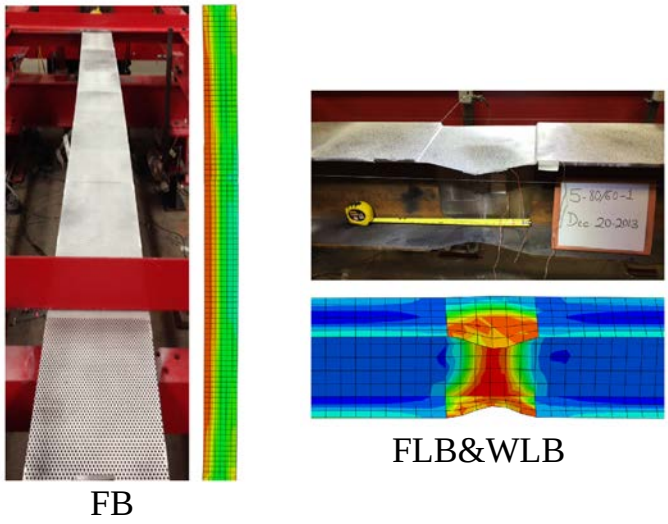

Figure 4.10 Deformation of full-scale piles from FEA and test

Figure 4.11 compares the predicted axial load-deformation relationships from FEA to the measured response. The figure also presents the coefficients of determination, R^2, between experimental and numerical curves. Inspection of Figure 4.11 shows $(R^2)_{peak}$ ranges between 0.98 to 1.00 for all of the examined cases. $(R^2)_{total}$ of 0/0 and 0/20 indicates FEA accurately predicted the full axial load-deformation responses. Regarding pile 40/20 and 40/60, as the axial load dropped dramatically after peak load in experimental program, post-buckling was not captured.

Therefore, the post-peak region of the FEA predictions cannot be verified. The FEA under predicted the post-buckling capacity of pile 80/60, 80/60/V, and 80/60/3 compared to test results. The discrepancies between the measured and predicted axial load-displacement relationships may be caused due to four reasons: (1) unintentional eccentricity of the applied load during testing; (2) uncertainty of the magnitude and pattern of the residual stresses, especially for piles with degradations, which might contain possible relief of residual stresses during milling of the flange and web; (3) conservativeness of the assumed magnitude and pattern of initial imperfections; (4) effect of the fillet at the junction of flange and web, which was not modeled in the FE simulation but partly existed in tested specimens.

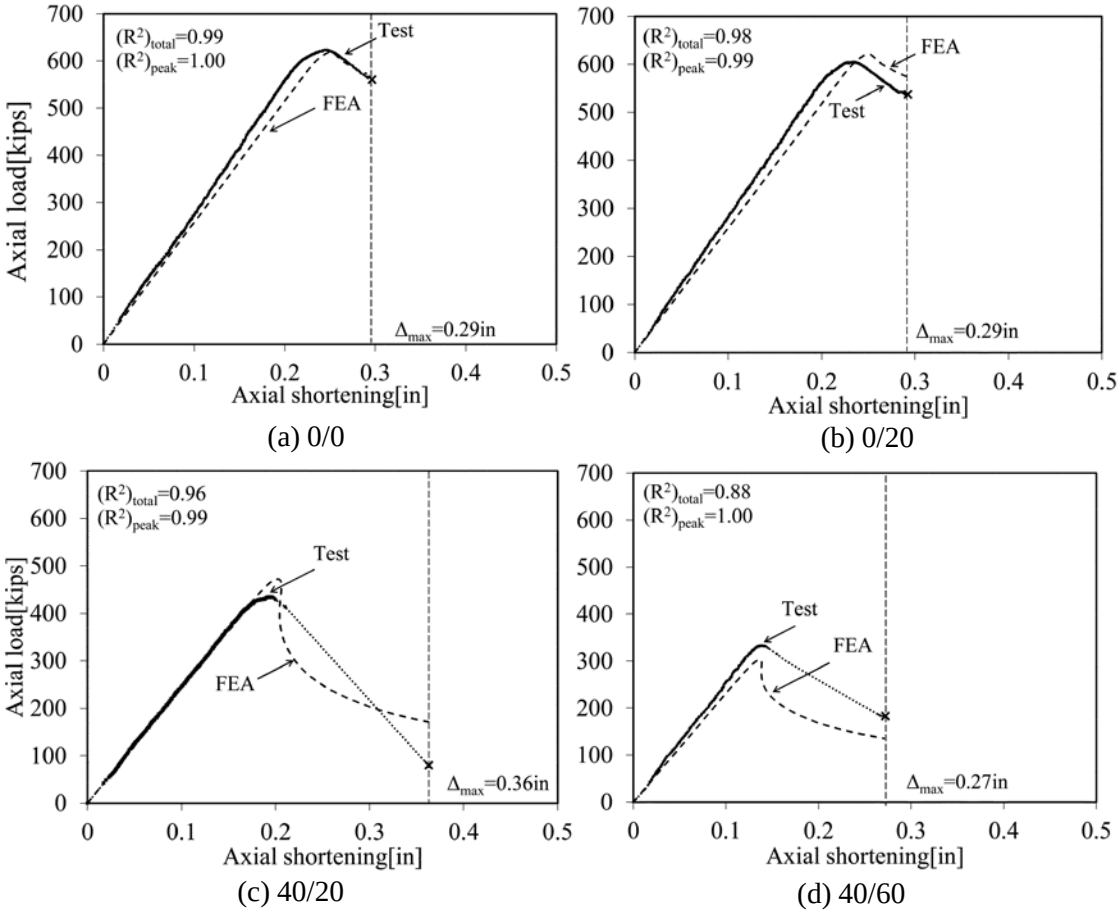

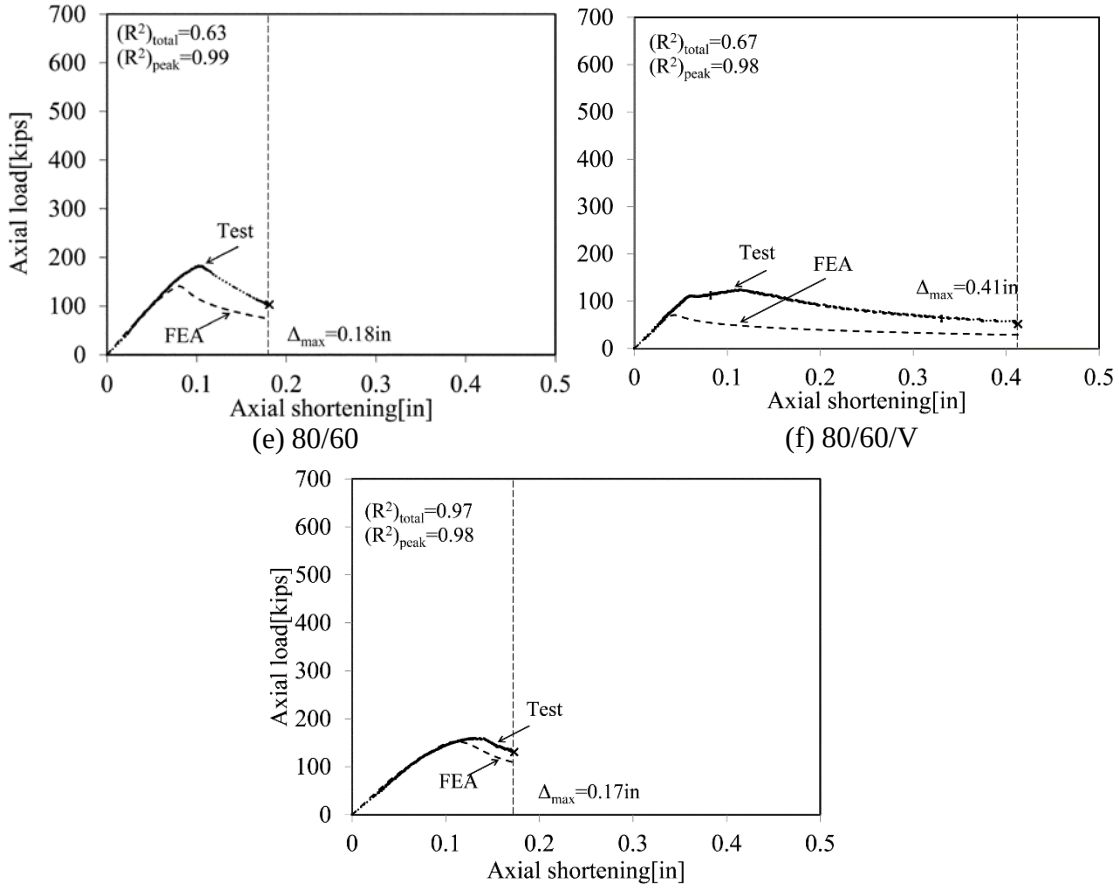

Figure 4.11 Comparison of axial load-deformation responses from test and FEA of HP12×53

4.3 Parametric Study

As the numerical framework was validated above, parametric studies on both small-scale and full-scale piles were performed using the validated FE model, to investigate the factors that might affect the axial behavior of partially corroded H-piles. The parameters include the degree of the reduction of the flange and web thicknesses, slenderness of the piles, location and extent of the degraded regions, and magnitude of the residual stresses.

Each pile that was considered in the parametric study was assigned a unique identifier following a similar naming convention to that used in previous study. The nominal values of the material properties of Grade 50 steel and dimensions of the piles, as specified by AISC (2011) were used in the parametric study. The magnitudes of initial global imperfections were taken as

L/480 and L/960 for W4×13 and HP12×53, respectively. The initial local imperfection was taken as the maximum fabrication tolerance of the out-of-square for the section, 0.06 in. The base configurations of the piles were 32 in long W4×13 pile and 15 ft long HP12×53 pile, with yield and ultimate strengths of 50 ksi and 65 ksi, respectively, an elastic modulus of 29,000 ksi, and a peak magnitude of residual stresses of 15 ksi (conservative assumption of 30% of the yield stress). The corroded region was 1 ft long, centered at the mid-height of the pile.

4.3.1 Effects of flange and web thickness

Figure 4.12 shows the effects of flange and web degradation on the predicted axial capacities of corroded W4×13 and HP12×53 piles with different slenderness ratios, KL/r, where k is the effective length factor, L is the clear length of the member, and r is the radius of gyration of the cross section about the axis of bending. The horizontal and vertical axes illustrate the degree of the reduction of the web thickness and the normalized axial capacity, respectively. For W4×13 shown in Figure 4.12(a), the normalized axial load was taken as the ratio of the axial capacity of all piles to the maximum capacity, which is the capacity of pile 0/0 with slenderness ratio of 32. For HP12×53 shown in Figure 4.12(b), the normalized axial load was taken as the ratio of the capacity of all piles to the capacity of pile 0/0 with slenderness ratio of 42. The points in the figure indicate the predicted peak loads of each pile, and they are connected by lines for visual convenience. The marker styles indicate the degrees of flange thickness reduction. The line styles indicate pile slenderness ratios of 32, 48, and 64 for W4×13 (Figure 4.12 (a)), 42, 63, and 84 for HP12×53 (Figure 4.12 (b)).

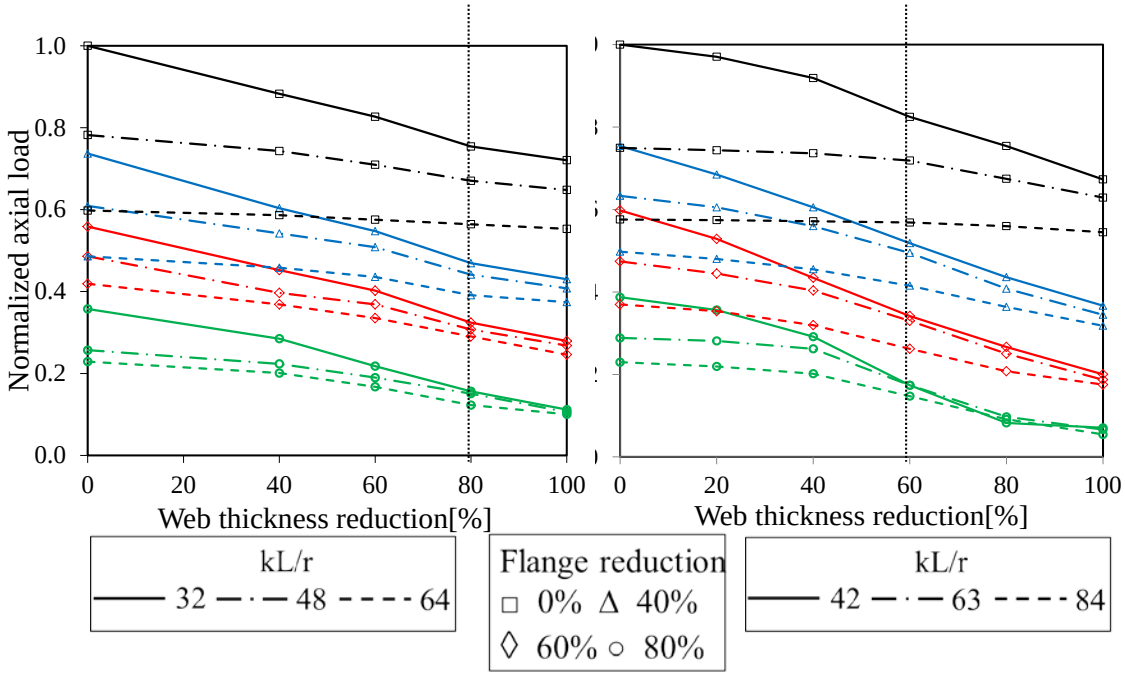

Figure 4.12 Axial peak loads for piles with different reduction on flange and web

Inspection of Figure 4.12 indicates that flange thickness reduction has a greater effect on the remaining axial capacity of corroded piles than web thickness reduction. With the same loss of cross-sectional area, piles with moderate loss of flange thickness and minor loss of web thickness exhibit lower capacity than piles with significant loss of web thickness and minor loss of flange thickness. This can be illustrated by considering two HP12×53 piles with slenderness (kL/r) of 84 and 53% reduction of cross-sectional area. The pile with 80% reduction of flange thickness, 80/0, has remaining capacity of 171 kips; however the pile with 40% reduction of flange thickness and 80% reduction of web thickness, 40/80, exhibits capacity of 282 kips, which is 65% higher than the capacity of 80/0. This could be explained as follows: (1) the flanges contribute more to the weak-axis moment of inertia of the section, (2) reducing the flange thickness causes the flanges to become slender resulting in a local buckling failure mode while reducing the thickness of the web does not since the web is a stiffened element while the flange is an unstiffened element.

4.3.2 Effects of pile slenderness

Figure 4.12 also shows the influence of pile slenderness on the axial capacity of corroded piles. The slenderness of the pile has a significant effect for piles fail by flexural buckling. For un-corroded HP12×53 piles decreasing the slenderness from 84 to 42 increases the axial capacity of the piles by 74%. Similar trend was observed for small-scale piles as well. By decreasing the pile slenderness from 64 to 32 for un-corroded W4×13 piles, the axial capacity increases 67%. However, the effect of pile slenderness becomes negligible when the dominant failure mode of the pile is local buckling of flange or web. Observation of Figure 4.12 indicates that for severely corroded piles with both flange and web slender (the cases at the right bottom corners of the two figures), the slenderness of the piles does not have any influence on their axial capacities as local buckling in the deteriorated region controls the failure. Therefore, bracing a pile to reduce its effective length may only be an effective repair strategy if the pile corrosion is relatively minor with no slender flange or web.

4.3.3 Effects of location of the corrosion

To investigate the effect of location of the degradation, the corroded region was moved to the third-height of the 64 in W4×13 pile and 15 ft HP12×53 pile from mid-height. Five representative cases with different failure modes including flexural buckling, flange or/and web local buckling, were modeled for each section. Inspection of the capacities summarized in Table 4.4 demonstrates that the location of corrosion has negligible effect on the axial capacities of the piles regardless of the failure mode and section scale.

Table 4.4 Comparison of axial capacities for different locations of reduction

Pile designation		Axial peak load [kips]		Difference [%]
		Third-height	Mid-height	
W4×13	20/0	100	99	1
	20/40	97	96	1
	60/40	65	66	1
	60/80	50	52	2
	80/80	23	22	1
HP12×53	0/20	506	505	0
	40/20	406	414	2
	40/60	320	330	3
	80/60	120	127	6
	80/100	44	45	2

4.3.4 Effects of the extent of the corrosion

The effect of the extent of the corroded region was studied by considering three different extents of the corroded region. For small-scale piles, 0.5 ft, 1 ft, and 2 ft were considered within a 64 in long pile. For HP12×53 piles, 1 ft, 3 ft, and 5 ft, centered at the mid-height of a 15 ft pile were considered. These values represent 1.5, 3, 6 times the nominal section depth of W4×13, and 1, 3, and 5 times the nominal section depth of HP12×53.

Figure 4.13 presents the axial peak loads of W4×13 (Figure 4.13(a)) and HP12×53 (Figure 4.13(b)) piles with three different extents of corrosion on each section. Three types of bars in the figures refer to the axial capacities of piles with three different extents of corrosion. Each group of three extents of corrosion indicates piles with flange and web thickness reductions varied from 0% to 80%. Inspection of Figure 4.13 indicates that the small-scale piles and the full-scale piles exhibited similar trend. Inspection of Figure 4.13 indicates that the extent of corrosion has minor effect on the capacity of piles with no slender element and failed by flexural buckling. In these cases, increment of the extent of corrosion by three times only changed the pile capacity at most by 4% and 6% for W4×13 and HP12×53 section, respectively. In contrast, when the flange and web had more thickness reduction and became slender, the effect of the extent of corrosion on pile capacity became substantial. In extreme cases, increment of the extent of corrosion by three times reduced the axial capacity of small-scale and full-scale piles by 41% and

33%, respectively. The reason for this phenomenon is that the aspect ratio of the corroded region of the flange (length of corroded region divided by half of the flange width) significantly affects the plate buckling strength of the corroded flange. The observed result is consistent with the classic plate buckling equations which predict a comparable reduction of strength for higher mode flange buckling (Lundquist and Stowell, 1942; Timoshenko and Gere, 2009).

The current design codes are formulated for prismatic members. To apply these design equations directly to corroded piles one must inherently assume that the loss of thickness is uniform along the entire length of the pile. This results in very high aspect ratios of the buckling plates, and the predictions are thus overly conservative. The results shown in Figure 4.13 (Shi et al., 2014) indicate that in extreme cases of corrosion, when flange reduction differs substantially from web reduction (i.e. 80/0), this assumption could lead to overly conservative predictions of capacity. Seif and Schafer (2013) presented relevant findings that when the slenderness of flange and web differed too much, current design codes provided conservative predictions. The presumption that the local buckling of the markedly slender element initiates the similar buckling of the other element did not happen. However, based on field observations, it is uncommon for the degree of flange and web corrosion to differ dramatically.

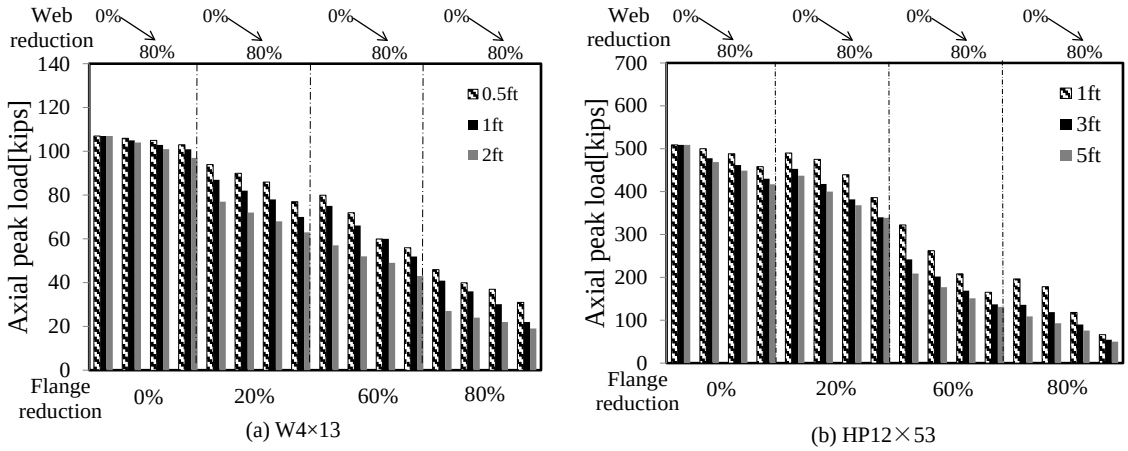

Figure 4.13 Axial peak loads of piles with different corroded extents

4.3.5 Effects of residual stresses

To investigate the effect of the magnitude of residual stresses on the axial remaining capacity of a pile, two different maximum magnitudes of residual stresses were implemented: 10% F_y (5 ksi) and 30% F_y (15 ksi). Figure 4.14 (Shi et al., 2014) presents the axial peak loads of piles with different residual stresses. Different types of bars refer to axial capacity of pile with different values of maximum residual stresses. For each value of flange reduction, five sets of bars indicate five degrees of web thickness reduction, including 0%, 40%, 60%, 80%, and 100% (2 in void). Inspection of Figure 4.14(a) indicates that the magnitude of residual stresses does not show much effect on the axial capacity of small-scale piles. The differences of the axial peak loads from piles with 5 ksi and 15 ksi maximum residual stresses are no more than 4%. In contrast, Figure 4.14(b) indicates a decrease of capacity as the residual stresses increased for piles with minor reduction and with flexural buckling as dominant failure mode. In this case, the differences of axial capacities of piles with 5 ksi and 15 ksi as maximum residual stress are within 10% to 15%. As the degree of corrosion increased, and piles failed by local buckling, the influences of the magnitude of the residual stresses on the pile capacities decreased, which changed the axial capacities by no more than 8%. For small-scale piles with flange thickness reduction greater than 80%, the piles capacities exhibited a slight increase as the residual stresses increased from 5 ksi to 15 ksi, as shown in Figure 4.14(a). This was also observed from full-scale piles with flange thickness reduction over 60%. This was due to the increase of the uniformly distributed tensile residual stresses in the web, σ_t, shown in Figure 4.5, which increased the predicted compression capacity of the piles. However, in practical applications this slight increase of capacity will not likely to be captured since residual stresses are highly variable and some relaxation may occur with the severe loss of section caused by corrosion.

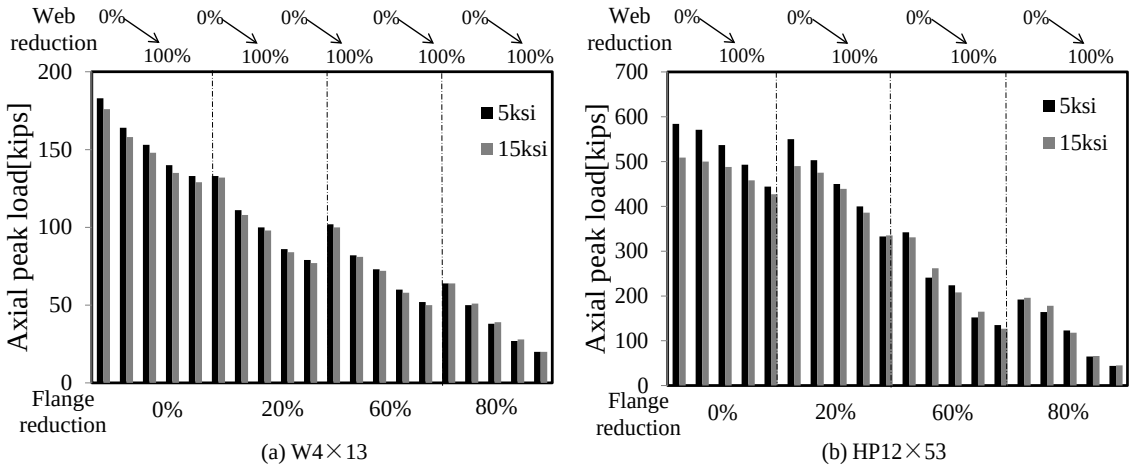

Figure 4.14 Axial peak loads of piles with different residual stresses

4.4 Concluding Remarks

A numerical framework was developed to predict the remaining axial capacity of H-piles with different patterns of corrosion. The nonlinear FE model was validated by experimental results of 13 small-scale W4×13 piles and seven full-scale HP12×53 piles, and used for a parametric study. The studied parameters include reduction of flange and web thickness, slenderness of the pile, the location and extent of the corroded region, and the magnitude of residual stresses. The effects of each factor studied using small-scale and full-scale piles are consistent. The conclusions are summarized as follows:

1) The developed numerical framework is able to provide reliable assessments on the remaining capacities of corroded piles and it can accurately predict the failure modes. The post-buckling behavior of some of the test piles were not well captured by FEA due to four possible reasons: (1) unintentional eccentricity of the applied load during testing; (2) uncertainty of the magnitude and pattern of the residual stresses, especially for piles with degradations, which might contain possible relief of residual stresses during milling of the flange and web; (3) conservativeness of the assumed magnitude and pattern of initial imperfections; (4) effect of the fillet at the junction of flange and web, which was not modeled in the FE simulation but partly

existed in tested specimens. However, this does not have much effect on the design of the repair system.

2) Flange corrosion is the most critical factor that affects the remaining axial capacity of partially corroded H-piles.

3) Pile slenderness only significantly affects the axial capacities of piles without slender flanges or webs that fail by flexural buckling. Therefore, bracing piles to reduce their effective length may not be an effective solution to repair piles with slender flange or web due to severe thickness losses.

4) The magnitude of residual stresses and the extent of corrosion along the length of the pile, are secondary factors affecting the axial capacity. Varying the magnitude of residual stresses changes the pile capacity by 15% at most if the dominant failure mode of the pile is flexural buckling, whereas the changes are less than 8% if the corrosion increases and causes the pile to fail by local buckling. However, only Leigh pattern of residual stresses was investigated in this study. The distribution of residual stresses might change with the varying patterns of corrosion, which needs further study. Increasing the extent of corrosion can decrease the axial capacity by up to 41% and 33% in the extreme cases for W4×13 and HP12×53 section piles, respectively.

5) The location of corrosion does not have much effect on pile capacity regardless of the type of failure mode.

CHAPTER 5 EXPERIMENTAL STUDY OF REPAIR SYSTEM

Based on the axial behavior of corroded H-piles investigated experimentally and numerically in Chapter 3 and Chapter 4, respectively, a friction-type bolted steel plate-based repair system to strengthen the corroded piles is proposed in this chapter. Design concept and procedures of the proposed repair system are presented. An experimental program was conducted on seven full-scale H-piles with simulated corrosion that were retrofitted using the proposed repair system. Seven 15-ft-long HP12×53 piles were degraded intentionally in the same patterns as the corroded control piles described in Chapter 3. The piles were repaired by friction-type bolted plate-based repair system and tested under uniaxial compression. The test results are presented and discussed in this chapter. The objective of the experimental program was to (1) evaluate the effectiveness of the proposed repair system and (2) to validate a numerical model of repaired piles, which is described in Chapter 6.

5.1 Design of the Steel-Based Repair System

According to the findings obtained from the experimental and numerical studies of corroded piles in Chapters 3 and Chapter 4, flange reduction was found to be one most critical factor that decreases the remaining axial capacity of a deteriorated H-pile. This is due to the facts that (1) the flanges contribute more to the weak-axis moment of inertia of the section, and (2) causing the web to become slender requires greater reduction compared to flange, since web is a stiffened element while flange has one free edge unstiffened. Therefore, the repair system was designed to focus on strengthening the flanges, with no additional material attached to the web. Strengthen the flange can increase its plate buckling strength. Also, the strengthened flange contributes to the increment of the rotational fixity of the flange and web junction, which is beneficial to the plate buckling strength of web. This section illustrates the configuration and working concept of the proposed repair system, and the design procedure of the detailed parameters of the system.

Figure 5.1 shows the configuration of the repair system. On each side of the flange, one main steel plate and two clamping plates are bolted to clamp the flange, as shown in Figure 5.1(a). Axial load is transferred to the main plates of the repair system through friction over a development length, L_d, on either end of the corroded region, as shown in Figure 5.1(b). The repair system has two contributions to the strengthening of a corroded pile. First, it stiffens the flange to enhance its plate buckling capacity. Second, the pretension in the bolts creates friction between the main plates of the repair system and the flanges of the deteriorated pile to transfer the axial load from the pile to the steel plates. The main plates are coated by particular coatings that (1) can be used underwater to protect the plates from corrosion and (2) provide adequate slip resistance.

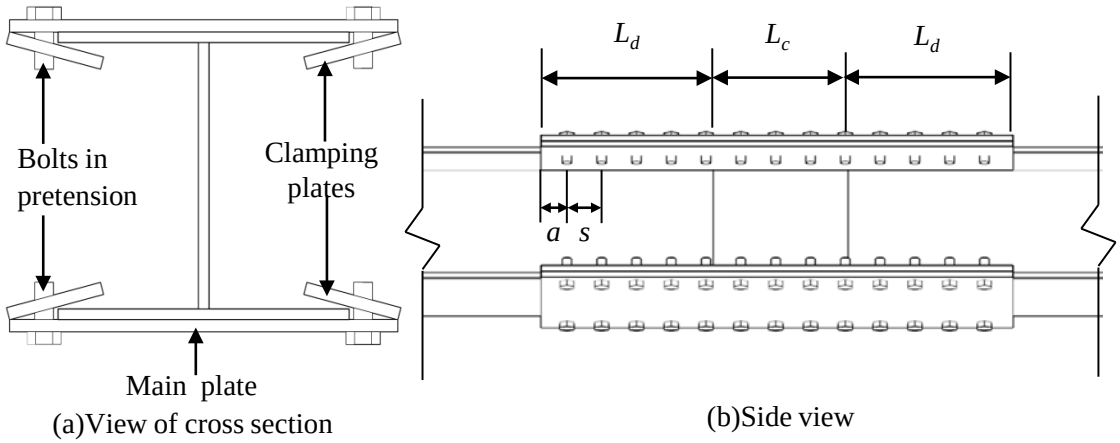

Figure 5.1 Friction-type bolted plate-based repair system

5.1.1 Determination of required friction provided by repair system

The demanding capacity of a bridge pile, $P_{n,u}$, is the target capacity of the corroded pile repaired by the friction-type bolted plate-based repair system. It is commonly determined as the nominal compressive capacity of a given section specified in AASHTO (2012), or lower, depending on the design of the bridge. The remaining capacity of a corroded pile, $P_{n,c}$, is recommended to be predicted using the EWM (AISI, 2007), because the EWM provides relatively accurate although conservative prediction compared to the DSM and design method in

AASHTO (Karagah et al., 2015; Shi et al., 2014). However, the numerical framework developed in this study and illustrated in Chapter 4 exhibited the most accurate prediction of the remaining capacity of the corroded pile. To study the efficiency of the proposed repair system accurately, the remaining capacity of a corroded pile was predicted by FEA in the experimental program. The load that is required to be transferred to the repair system through friction, $P_{n,r}$, can be calculated using Eq 5-1,

$$P_{n,r} = P_{n,u} - P_{n,c}. \quad \textbf{Eq 5-1}$$

Eq 5-1 does not take into account the enhancement of the plate buckling capacity of flanges within the repaired region for conservative design.

5.1.2 Determination of size, number, and spacing of the bolts

Based on the required friction force, $P_{n,r}$, the size and number of bolts can be calculated according to the strength of slip-critical connection specified in AASHTO (2012). The required number of bolts, $N_{b,d}$, over each load introduction regionis determined according to Eq 5-2 and Eq 5-3,

$$N_{b,d} = P_{n,r} / R_n, \quad \textbf{Eq 5-2}$$

and

$$R_n = K_h K_s N_s P_t, \quad \textbf{Eq 5-3}$$

where

R_n= Friction force provided by one bolt in a slip-critical connection;

K_h= Hole size factor;

K_s = Surface condition factor;

N_s = Number of slip planes per bolt, conservatively considering, the contact between the flanges and the clamping plates was ignored, as their contacts were along a line rather than surface;

P_t = Minimum required bolt tension.

The surface condition factor, K_s, between the new coated steel plates and the corroded pile flanges, should be determined by coefficient of friction test. The practical surface conditions should be considered, such as the pressence of corrosion product or moisture on the steel surface.

According to the minimum spacing and clear distance specified in AASHTO (2012) for each diameter of bolt, to ensure sufficient space for installation, Eq 5-4 and Eq 5-5 should be satisfied when

$$s \geq 3d, \text{ for standard holes} \qquad \textbf{Eq 5-4}$$

and $$s \geq 2d+d_h, \text{ for oversize or slotted holes,} \qquad \textbf{Eq 5-5}$$

where

s= Bolt spacing,

d= Bolt diameter,

d_h= Hole diameter.

For built-up members comprised by tightened bolts, the pitch of stitch bolts should not exceed 12t (Eq 5-6) to ensure that the parts act as a unit and to prevent buckling in compression members:

$$s \leq 12t, \qquad \textbf{Eq 5-6}$$

where t = Thickness of the thinner outside plate or shape.

Because the shear distribution in bolts is not uniform and the ends of the connection take higher stress, at the ends of the repair system, the bolts spacing should satisfy Eq 5-7,

$$s \leq 4d \text{ within a length of } 1.5b_{pl}, \qquad \textbf{Eq 5-7}$$

where b_{pl}= Width of the plates.

For practical purposes, the minimum edge distance, a, should satisfy the values specified in AASHTO (2012) for bolts of different diameters. Furthermore, maximum edge distance should satisfy Eq 5-8, to prevent corrosion from accumulating on connecting members and forcing them to separate (AISC 2011),

$$a \leq \min\{8t, 5in\} . \quad \textbf{Eq 5-8}$$

5.1.3 Determination of width and thickness of the plates

The width and thickness of the plates are designed to ensure that the weak axis flexural rigidity of the repaired pile is greater than or equal to that of the un-corroded piles:

$$(EI_y)_c + (EI_y)_{pl} \geq (EI_y)_u \ , \quad \textbf{Eq 5-9}$$

where

E=Elastic modulus of steel, and

$$(I_y)_c = \frac{1}{12}\left[2b_f t_{w,c}^3 + (h_w - 2t_{f,c})t_{w,c}^3 \right], \quad \textbf{Eq 5-10}$$

$$(I_y)_u = \frac{1}{12}\left[2b_f t_w^3 + (h_w - 2t_f)t_w^3 \right], \quad \textbf{Eq 5-11}$$

$$(I_y)_{pl} = \frac{1}{6} t_{pl} b_{pl}^3 \ . \quad \textbf{Eq 5-12}$$

The minimum width of the main plates needs to satisfy Eq 5-13,

$$b_{pl,\min} = b_f + 2a + d \ , \quad \textbf{Eq 5-13}$$

where

b_f = Flange width, as shown in Figure 5.2,

a = Minimum edge distance for bolts as shown in Figure 5.2,

d_h = Diameter of the holes in the repair plates.

The thickness of the plates, t_{pl}, is designed to ensure that the plate satisfied the non-slender element requirements in AASHTO (2012):

$$t_{pl} \geq 0.714(b_{pl} - 2a)\sqrt{\frac{F_y}{E}} \ . \quad \textbf{Eq 5-14}$$

Further, to ensure that the plate does not yield in flexure due to tightening of the bolts, the minimum plate thickness can be calculated according to Eq 5-15,

$$t_{pl,\min} = 1.442 \times \sqrt[3]{\frac{P_t (b_{pl} - b_f - 2a - d_h)}{F_y s}} \quad . \qquad \textbf{Eq 5-15}$$

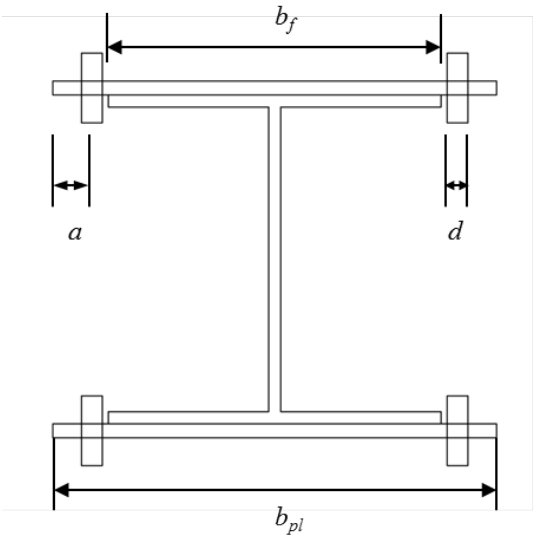

Figure 5.2 Cross section of repaired pile (clamping plates excluded)

5.1.4 Determination of length of the plates

The development length of the plates, L_d, at one end of the corroded region can be calculated based on the required number and spacing of the bolts using Eq 5-16, as shown in Figure 5.1,

$$L_d = (P_{n,r} / R_n - 1) \times s + a \; . \qquad \textbf{Eq 5-16}$$

The total length of the plates is determined by Eq 5-17,

$$L_{pl} = 2 L_d + L_c. \qquad \textbf{Eq 5-17}$$

5.2 Experimental Program

The experimental program included seven full-scale H-piles with simulated corrosion and retrofitted using the proposed repair system. The piles had the same patterns of thickness reduction of flanges and webs as the corroded control piles illustrated in Chapter 3. The configuration of repair system for each pile was designed based on the design method presented in the previous section. The target capacity, $P_{n,u}$, was taken as 580 kips, which is the nominal design capacity of 15-ft-long HP12×53 compression member calculated according to AASHTO

(2012). The following sections present the test matrix, material properties, test set-up, and instrumentation plans of the experimental program.

5.2.1 Test matrix

Table 5.1 illustrates the test matrix of the repaired piles. The pile designation is defined the same way as described in Chapter 3. The first and second numbers indicate the percentages of reduction of flange and web thickness, respectively. The third part, when included, indicate the presence of a 2 in void in the web [V] or corrosion along a 3 ft. extent of the pile [3] rather than along 1 ft which was used for the other piles in the test matrix. The 'S' at the end of each specimen designation indicates that the piles were retrofitted by steel-based repair system. Two piles, 80/60-S(1) and 80/60-S(2), were degraded and retrofitted identically to evaluate the repeatability of the tests. The remaining axial capacities of the seven corroded piles were predicted by the numerical framework proposed in Chapter 4. The designed length of the steel repair plates and the number of bolts for each specimen are listed in Table 5.1. The widths of the main plates and clamping plates were designed as 16 in and 4 in, respectively. The thickness of the plates was 0.5 in. ASTM A325 structural bolts with ¾ in diameter were used.

Table 5.1 Test matrix of repaired H-piles

Pile Designation	Predicted Nominal Strength $P_{n,c}$	Corroded Section		Length of Plates L_{pl}	Number of Bolts per line N_b
		Flange Thickness $t_{f,c}$	Web Thickness $t_{w,c}$		
	[kips]	[in]	[in]	[ft]	
0/20-S	587	0.431	0.362	2	7
40/20-S	475	0.289	0.318	2	7
40/60-S	418	0.289	0.207	3.5	13
80/60-S(1)	181	0.133	0.199	6.5	25
80/60-S(2)	176	0.142	0.181	6.5	25
80/60/V-S	100	0.140	0.213	7.5	29
80/60/3-S	153	0.134	0.196	7.5	29

5.2.2 Material properties

The proposed repair method is a steel-based system. Material properties could be obtained by steel tension coupon tests. However, a critical factor of this repair system was the

friction between the steel repair plates and the pile flanges. The frictional behavior between the contacting surfaces, determined by the property of coatings applied on steel repair plates, was therefore considered as another important material property. This section presents the tension coupon tests of steel and the coefficient of friction test of the contact surfaces.

5.2.2.1 H-piles and steel repair plates

The piles of corroded control group and retrofitted group were made from the same batch, so the material properties of H-piles were determined from tension coupon tests presented in Chapter 3. Three tension coupons were cut from the steel plates of repair system, and tested in a 110-kip MTS machine. The loading rates were 0.01 in/min and 0.2 in/min for elastic and inelastic ranges of the tests, respectively. An extensometer with 2 in gage length (EPSILON model 3542) was used to measure the axial deformation within the gauge length of the coupon. Data was collected using a Vishay Precision Group System 7000 data acquisition system with a flexible finite impulse response (FIR) filter enabled and using a data sampling rate of 10 samples/second (Vishay, 2011). No filter was used for post-processing.

Figure 5.3 shows the stress-strain relationships of the three tension coupons from the steel plates. The yield strength was obtained using the 0.2% offset method. Table 5.2 presents the elastic moduli, yield strengths, ultimate strengths, and ultimate strains of the H-piles and the steel repair plates. The mean values of the material properties of the three coupons cut from steel plate were calculated, along with the coefficient of variation (CoV).

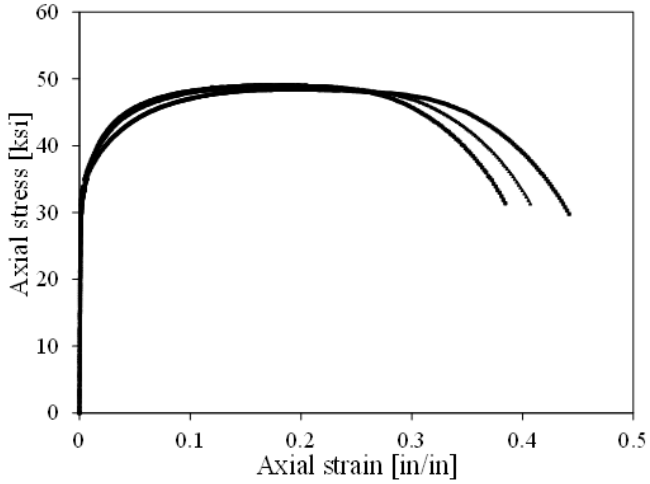

Figure 5.3 Stress-strain responses of the three tension coupons

Table 5.2 Material properties of the steel repair plates and H-piles

Coupon location	Elastic modulus [ksi]	Yielding stress [ksi]	Ultimate stress [ksi]	Ultimate strain [μin/in]
Plate	28,200	33.3	49.0	180,000
Plate	29,200	32.4	48.4	190,000
Plate	28,300	33.7	49.1	200,000
Mean	**28,600**	**33.1**	**48.8**	**190,000**
CoV	2%	2%	1%	5%
Flange	28,400	52.5	66.5	170,000
Web	32,000	60.5	71.0	80,000

5.2.2.2 Contact surface property between steel repair plates and pile flanges

The steel repair plates were sandblasted and coated with two layers of coatings to resist corrosion and to obtain adequate slip resistance. The first layer, directly applied on the steel surface, was a solvent-based, inorganic ethyl silicate, zinc-rich coating. It worked as sacrifice anode to protect the steel plate from corrosion. The second layer, which was applied on the first layer after it cured, was a non-zinc containing, Class B-rated, polyamide epoxy coating. This coating protected the first layer of coating and provided high slip resistance. The slip coefficient that the second coating is able to provide is 0.5 according to its data sheet. However, this value is based on dry clean contact surfaces. To investigate the underwater behavior of the coatings, a coefficient of friction test was conducted.

Table 5.3 summarizes the details of the friction coefficient test program. The double-lap type test specimens, as shown schematically in the last column of the table, consisted of two main steel plates and two splice plates. Figure 5.4 shows the details of the specimens. The main plates were butted against each other with a small gap between their ends. The splice plates were centered on the main plates and clamped in place using ¾ in diameter steel bolts tightened to achieve 28 kips pretension, as shown in Figure 5.4(a). The bolts were installed on either side of the main plates to simulate the clamping effect of the repair system. A 400-kip capacity Tinius-Olsen universal testing machine was used to apply tensile load on the top main plate and the bottom main plate was fixed by clamping force from the machine. The axial tension load and the displacement of the top crosshead of the machine were recorded continuously during testing. A plateau in the load-displacement curve reflected the first slip between the faying surfaces.

Four groups of tests were conducted. Each group had five replicate specimens. Group A was a control group with both contact surfaces abrasive blasted and tested in dry condition. Since the bolting pattern was different from the standard configuration for slip-critical connections, Group A was tested as a reference group to investigate the effects of bolting configuration. In Group B, the main plates were corroded by submerging in hydrochloric acid for several days to form a layer of surface rust on the steel plates, as shown in Figure 5.4(b). This was intended to simulate the condition of a steel pile which has been aggressively cleaned using hand tools and mechanical means to remove extensive pack rust, dirt, and possible marine growth from the surface while leaving surface rust intact. The splice plates were sandblasted to simulate the surface preparation of new steel plates without any coating. All plates were wetted with water before tightening the bolts to simulate the underwater application. The splice plates in Group C were coated with two layers of coatings described above to evaluate the effect of the coatings on the friction coefficient of contacting surfaces. Zinc clad II ethyl silicate (Zinc Clad II Ethyl Silicate Product information, 2012) and Steel-Spec epoxy primer (Steel Spec Epoxy Primer Product information, 2012), distributed by Sherwin Williams, were the product names of the first

and second layer coatings, respectively. The contact surfaces were wetted. Group D has the same configuration as Group C but had an additional coating applied on the main plate. The Armor plate 360 (Armor Plate 360 Date sheet, 2009) is an epoxy based coating that can cure in water.

Table 5.3 Test matrix of coefficient of friction

Group	Main Plate (2 in×0.5 in)	Splice Plate (6 in×0.5 in)	Surface Condition
A	Sand blasted	Sand blasted	Dry
B	Corroded Steel	Sand blasted	Wet
C	Corroded Steel	Steel-Spec epoxy+ Zinc Clad II Ethyl silicate	Wet
D	Corroded Steel+ Armor Plate 360	Steel-Spec epoxy+ Zinc Clad II Ethyl silicate	Wet

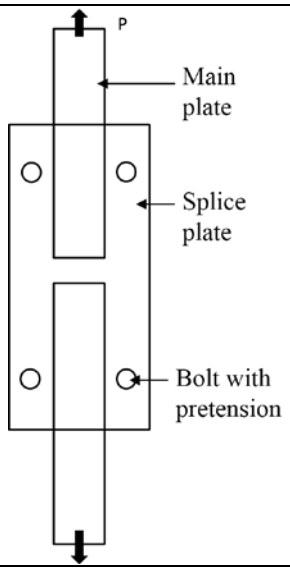

Figure 5.5 shows the measured load-displacement relationships from each group. The figure indicates that Group A, B, and C exhibited similar behavior with a constant load plateau after the initiation of slipping as expected. However, specimens in Group D exhibited softening behavior with decreasing load after reaching a peak load. This this was attributed to the failure of the Armor plate 360 coating, as shown in the bottom right figure of Figure 5.5. The coefficient of friction, K_s, was calculated using Eq 5-3 in which the friction force, R_n, was taken as the plateau load of each specimen.

Table 5.4 summarizes the obtained friction loads and calculated coefficient of friction of each group of specimens. The obtained friction coefficient of Group A was 0.42, which was lower than the standard value 0.5 specified in AASHTO (2012). The reason is the different bolting pattern from the standard configuration for slip-critical connections. Comparison between Group B and Group A shows the effect of surface corrosion and wet surface was negligible. The slip resistant coefficient obtained from Group C was 0.34, which was lower than the specified

value in the coating data sheet. The possible reasons include wet surfaces, surface corrosion, and the pattern of bolting. Although the slip resistance of Group D was higher than Group C, the load-slip relationship showed a descending trend (Figure 5.5 (d)) as discussed before. Inspection of Table 5.4 also indicates that the use of coatings increased the variability of the achieved friction force. Consequently, the mean value of coefficient of friction obtained from Group C, 0.34, was adopted for the design of the repair system of the experimental program.

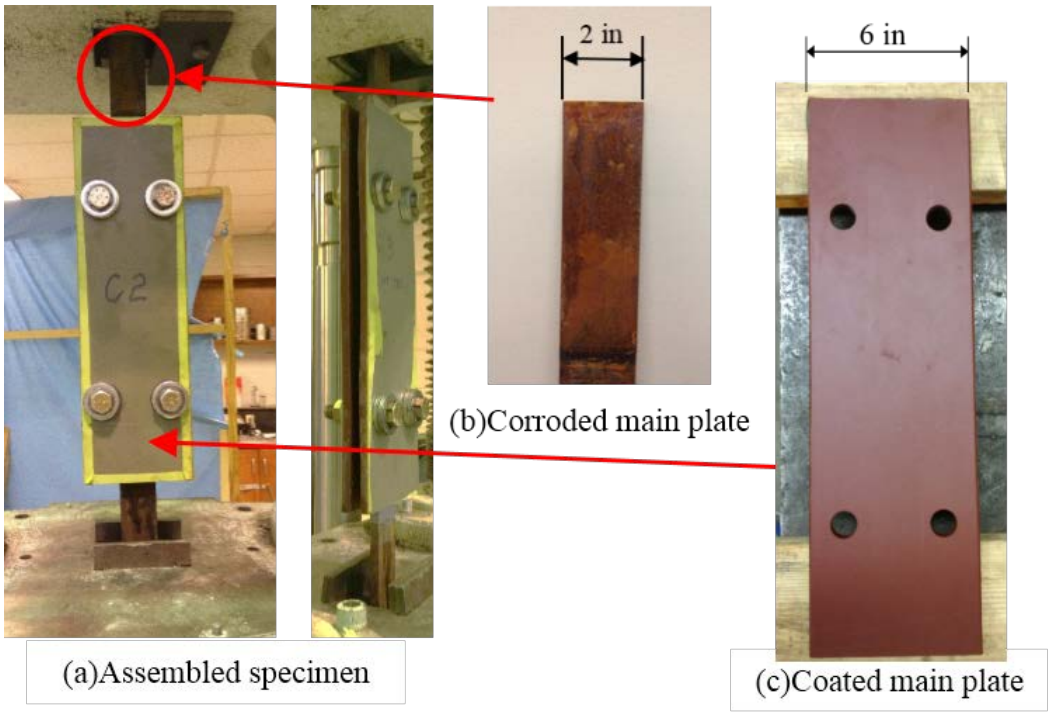

Figure 5.4 Specimen of slip resistance tests

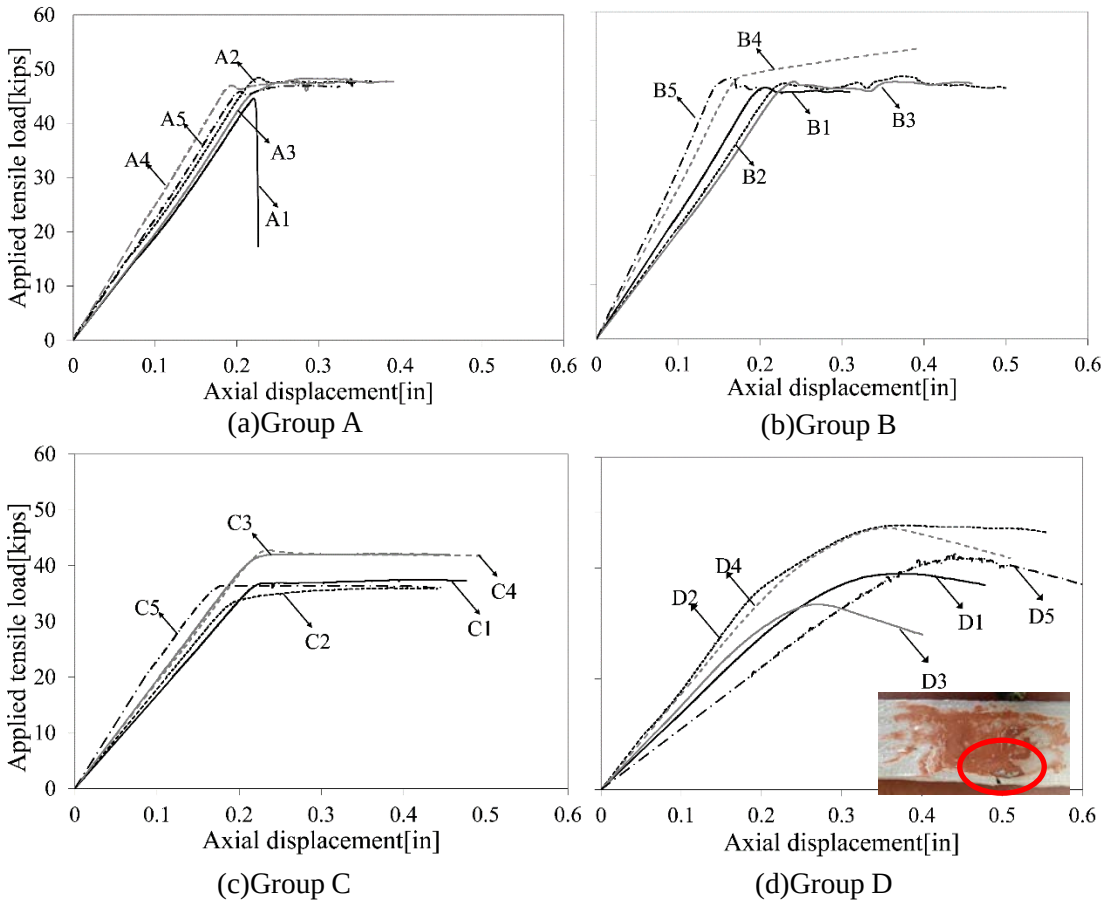

Figure 5.5 Load-slip relationships from slip resistance tests

Table 5.4 Experimental results of coefficient of friction test

Test Group	Friction load R_n [kips]							K_s
	1	2	3	4	5	Mean	CoV	
A	44.6	48.4	48.3	47.9	47.0	47.2	3%	**0.42**
B	47.5	45.5	48.2	47.2	48.0	47.3	2%	**0.42**
C	36.8	33.9	42.1	42.7	36.5	38.4	10%	**0.34**
D	38.9	47.7	33.4	47.1	42.5	41.9	14%	**0.37**

5.2.3 Fabrication of retrofitted piles

Figure 5.6 illustrates the sequence used in the fabrication of the repair system. First, a computer network control (CNC) mill was used to reduce the thickness of flanges and webs, to simulate the corrosion effects as shown in Figure 5.6(a). The reduced thicknesses of flanges and webs are summarized in Table 5.1. Water was spread on the original pile before placing the steel repair plates to simulate fabrication “in-the-wet”, as shown in Figure 5.6(b). All bolts were

tightened using a calibrated torque wrench, as shown in Figure 5.6(d), to reach the minimum pretension for a slip-critical connection specified in AASHTO (2012), which is 28 kips for ¾ in A325 bolts. The bolt pretension was measured by a load cell while calibrating the torque wrench. In field applications, similar tension indicating device (Skidmore or equivalent) must be employed to verify the pretension. In all specimens except 40/60-S, bevel washers were used to balance the angle between the main plate and the clamping plate to keep the bolts straight, as shown in Figure 5.6(c).

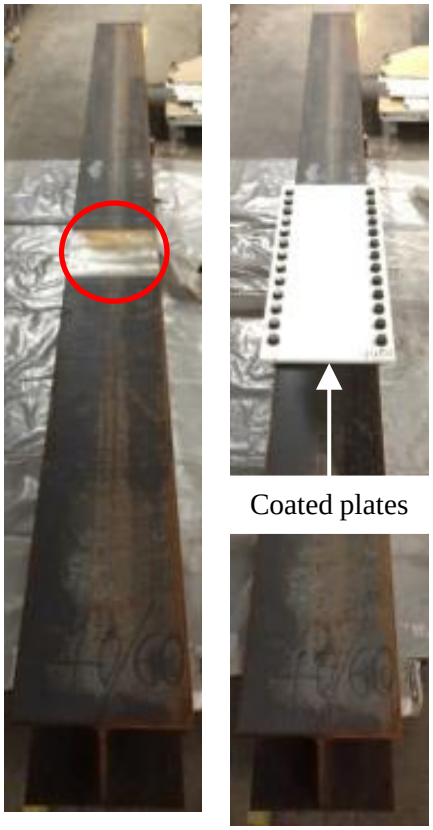

(a) Pile before and after repair

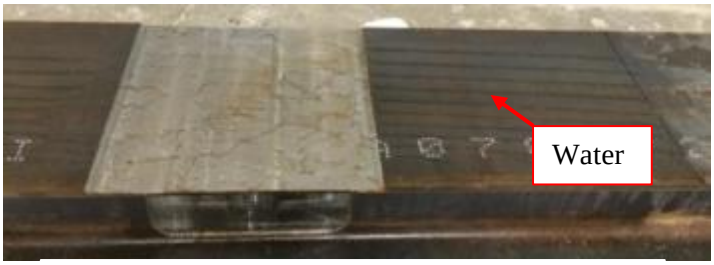

(b) Water spread on pile surface

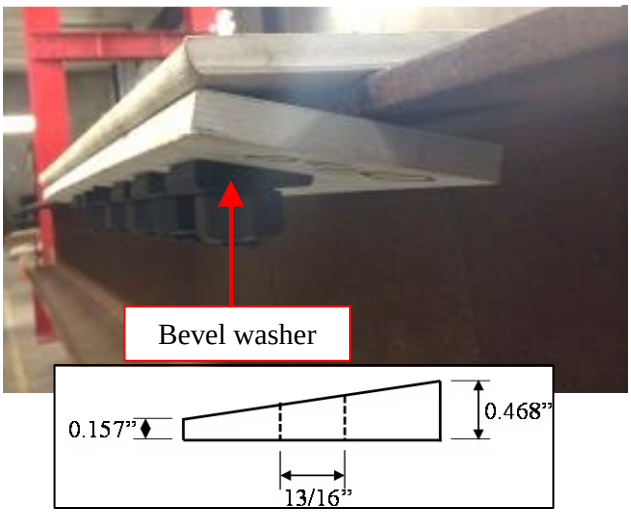

(c) Bevel washers

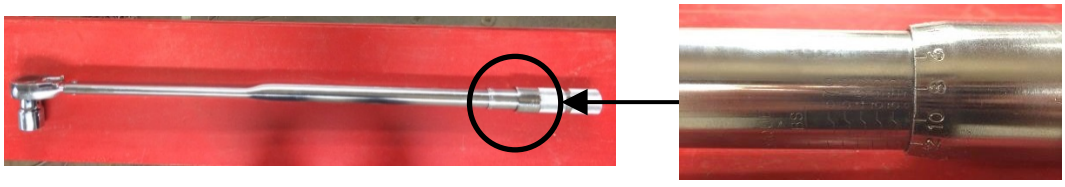

(d) Torque wrench

Figure 5.6 Fabrication of the repair system

5.2.4 Test set-up and instrumentation

The 600-kips self-reacting test frame described in Chapter 3 was used to test the retrofitted piles, as shown in Figure 5.7(a). The same boundary conditions were applied to the repaired piles: the pile was free to rotate along its weak axis, while the strong axis of the pile was restrained from rotation to ensure the pile failed along its weak axis if flexural buckling governs, to simulate the boundary conditions and failure mode of actual bridge piles. The specimens were loaded manually at a rate of 15 kips per minute until the peak load was achieved and the descending portion of the load-deformation curve was identified.

Four string potentiometers (Unimeasure model number PB-20) were installed at the four corners of the base plate to measure axial deformation of the pile, as shown in Figure 5.7(b). Additional string potentiometers (Unimeasure model number PB-4) were mounted at both ends of the steel repair plates to capture the slip between the pile flanges and the steel repair plates, as shown in Figure 5.7(c). Two strain gauges (Micro-Measurements 125BS) were attached at the center of the top main plate and the flange of the original pile at the reduction region, at the same cross section, as shown in Figure 5.7(c). The values obtained from strain gauges indicated the axial load distribution on the original pile and the repair system. Data were collected using a Vishay Precision Group System 7000 data acquisition system with a flexible finite impulse response (FIR) filter enabled and using a data sampling rate of 10 samples/second (Vishay, 2011). No filter was used for post-processing.

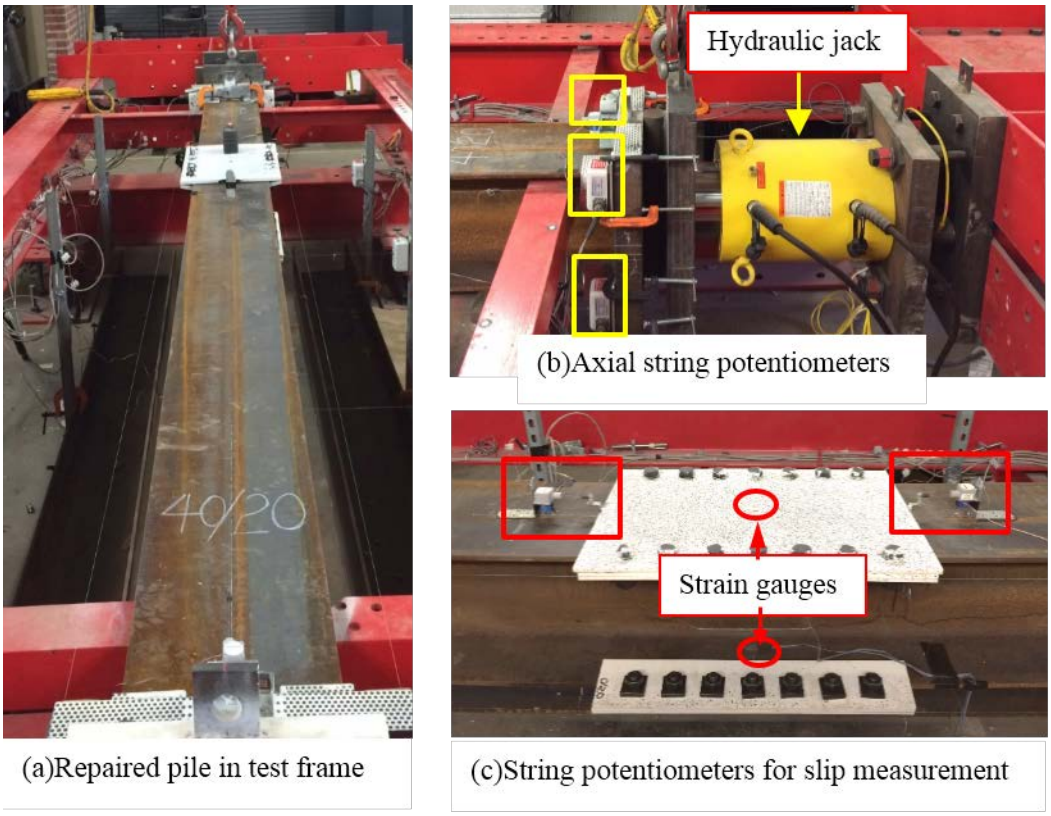

Figure 5.7 Test instrumentation used in the of the test of the repaired piles

5.3 Test Results and Discussion

This section presents the experimental results of the full-scale corroded piles retrofitted by friction-type bolted plate-based repair system. Comparisons of axial capacity and stiffness between corroded control piles and repaired piles are summarized to evaluate the effectiveness of the repair system. This section also presents the detailed experimental observations and the axial load-deformation responses of each pile.

5.3.1 Axial capacity, axial stiffness, and failure modes

Table 5.5 summarizes the axial capacity, axial stiffness, and failure mode of all the corroded control piles and the repaired piles. The target axial capacity of the repaired piles was taken as the nominal axial load of an un-corroded pile, $P_{n,u}$, calculated using the design method adopted in AASHTO (2012), which is 580 kips for 15-ft-long HP12×53 pile. Inspection of Table 5.5 indicates that the repair system did not change the failure modes of the piles except Pile

80/60-S(1), Pile 80/60-S(2), and Pile 80/60/3-S. However, experimental observations (presented in the next section) indicate that with the same failure mode as flange local buckling (i.e., Pile 40/60 and Pile 40/60-S), the repaired piles exhibited higher order of plate buckling while the corroded pile did not. The reason for this phenomenon is that the clamping plates restrained the edges of the flanges, which were originally free edges. Three repaired piles, Pile 80/60-S(1), Pile 80/60-S(2), and Pile 80/60/3-S failed in a crumpling deformation of their flanges and webs. The observed failure (detailed presented in the following section) indicated that the flanges were too slender to stiffen the web at the junction; meanwhile, the destabilization of the web caused the excessive deformation of the flanges. Pile 80/60/V-S exhibited the same failure mode as the corroded control pile 80/60/V (described in Chapter 3), which was flange one-way bending at the void region.

Figure 5.8 shows the comparison of the axial capacity between corroded and retrofitted piles. The horizontal axis represents the loss of the cross-sectional area, and the vertical axis refers to the ratio of axial capacity obtained from tested piles to the nominal design capacity of original un-corroded pile. The horizontal solid line indicates the nominal capacity of the un-corroded piles. The round dots illustrate the corroded control piles, while the square dots represent the repaired piles. Inspection of Table 5.5 and Figure 5.8 shows the effectiveness of the proposed repair system. Six out of seven of the repaired piles were effectively strengthened to the target capacity expect for 80/60/3-S. The exception was due to the limitation of test frame. The Pile 80/60/3-S was intentionally designed to a lower capacity. However, the expected capacity of 80/60/3-S was 496 kips according to the design method proposed at the beginning of this chapter, which was only 7% lower than the test result. Figure 5.8 indicates that even with the most axial capacity loss, 80/60/V, which had only 20% remaining capacity of the nominal capacity of un-corroded pile, the repair system effectively enhanced its capacity back to the nominal value.

Table 5.5 Experimental results of full-scale corroded and repaired piles

Pile Designation	Axial Peak Load [kips]	Stiffness [kip/in]	Failure Mode
$P_{n,u}$	580	2,497	
0/0	623	2,776	FB[a]
0/20	604	2,816	FB
0/20-S	629	2,647	FB
40/20	435	2,448	FLB[b]
40/20-S	665	2,650	FLB
40/60	333	2,520	FLB/WLB[c]
40/60-S	618	2,750	FLB/WLB
80/60	182	2,001	FLB/WLB
80/60-S(1)	632	3,271	Crumpling
80/60-S(2)	615	2,798	Crumpling
80/60/V	124	1,930	FOWB[d]
80/60/V-S	630	2,907	FOWB
80/60/3	159	1,645	FLB/WLB
80/60/3-S	532	3,180	Crumpling

[a]Flexural Buckling (FB); [b] Flange Local Buckling (FLB); [c] Web Local Buckling (WLB); [d]Flange One-way Bending (FOWB).

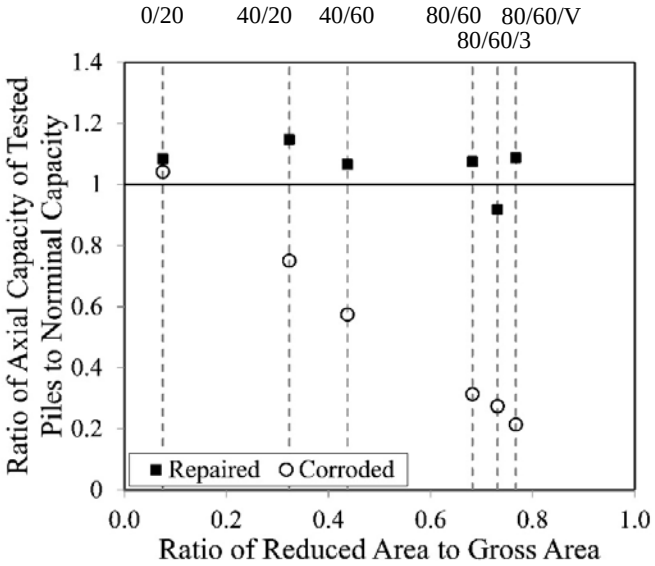

Figure 5.8 Comparison of axial load capacities between corroded and retrofitted piles

Similar to Figure 5.8, Figure 5.9 shows the comparison of axial stiffness of corroded and retrofitted piles. The horizontal axis represents the loss of cross-sectional area, and the vertical axis refers to the ratio of axial stiffness obtained from teste piles to the nominal value of a 15 ft HP12×53 section. The horizontal solid line indicates the axial stiffness of tested pile equals to the

nominal stiffness of un-corroded pile. The round dots refer to the corroded control piles, while the square dots refer to the repaired piles. Observation of Table 5.5 and Figure 5.9 demonstrates that the axial stiffness of the corroded piles did not decrease as severely as their capacities, because the degraded region was only 1/15 of the total length (for 80/60/3 this value was 1/5). The greatest reduction of axial stiffness was found on the pile 80/60/V. It reduced 34% compared to the original stiffness of the un-corroded pile. The repair system increased its stiffness by 51%. The Pile 0/20-S exhibited lower axial stiffness than Pile 0/20 due to its slightly smaller cross-sectional area. Therefore, the repair system efficiently enhanced the axial stiffness of the piles by compensating the cross-sectional area with additional steel repair plates at the deteriorated region. This is beneficial to the serviceability control of the piles, to prevent excessive deformation or differential settlement.

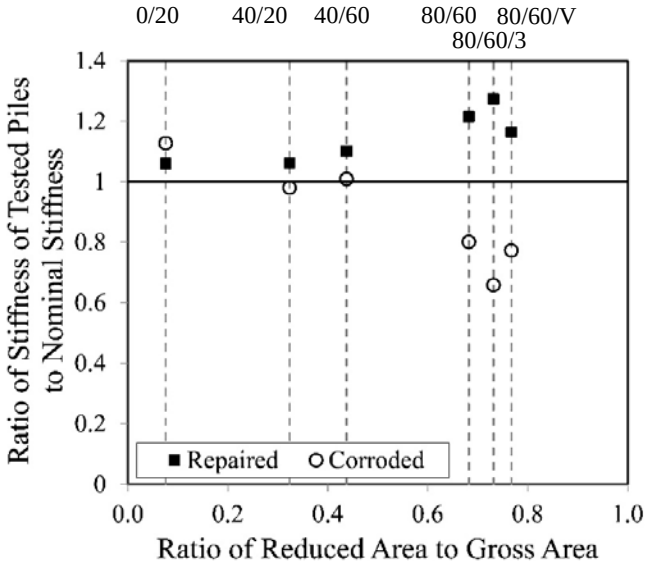

Figure 5.9 Comparison of axial stiffnesses between corroded and retrofitted piles

5.3.2 Experimental observations

5.3.1.1 Pile 0/20-S

The pile was loaded up to 629 kips and failed by flexural buckling. The maximum lateral deformation was observed at mid-height of the column, which was the same as the corroded

control piles, 0/20, as shown in Figure 5.10(a). Figure 5.10(b) shows the axial load-deformation responses of the un-corroded control pile, corroded control pile, and the repaired pile. The red line refers to the repaired pile, while the black solid line and dashed line refer to the corroded control pile and the un-corroded pile, respectively. The horizontal dashed line indicates the target capacity of repaired pile. Similar figures were prepared for each pile in this section. Inspection of Figure 5.10(b) indicates that the repair method strengthened the corroded pile and increased its capacity back to the level of the un-corroded pile. After testing the repair plates were removed and the pile was inspected. No flange or web local buckling was observed after removing the plates, since both flange and web were still non-slender elements. The length of the repair system for 0/20-S was 2 ft, which provided only limited enhancement to resist flexural buckling. Therefore, the pile failed similarly to the un-corroded pile by flexural buckling.

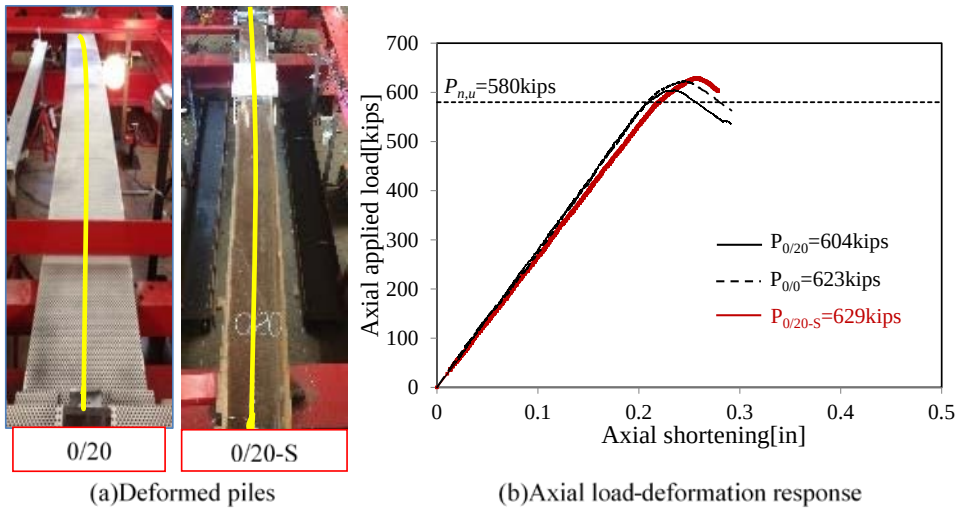

Figure 5.10 Comparison of Pile 0/20 and Pile 0/20-S

5.3.1.2 Pile 40/20-S

The pile was loaded monotonically up to a peak load of 665 kips, failed by flange local buckling. Flexural buckling of the pile, as shown in Figure 5.11(a), was observed after the peak load. After the peak load, the load decreased gradually until 599 kips, when a sudden increase of deformation occurred and the load dropped dramatically, as shown by the dashed line in Figure 5.11(b). Inspection of the pile after failure further indicated the presence of a localized buckle in

the web as shown in Figure 5.12(a). After completing of the test, the strengthening plates were removed to observe the flanges. The inspection indicated a minor local buckle in the flange as shown in Figure 5.12(b).

To understand more details about the observed failure, further inspections were conducted on the axial strains of the plate and the corroded section, and the displacements of the steel repair plates. Figure 5.13 presents the axial strain values obtained from the two strain gauges. One attached on the steel repair plate and the other one attached at the reduced flange close to the junction of flange and web, as shown in Figure 5.7(c). The vertical axis refers to the applied axial load, and the horizontal axis refers to the strains at two locations. Two red horizontal dashed lines refer to two load levels: 615 kips when bottom flange exhibited yield strain, and 665 kips when peak load was achieved. Inspection of Figure 5.13 indicates that the bottom flange buckled before the peak load was achieved, shown as the red dot. Also, the strain of the top plate is almost zero during the test, which indicates that very little axial load was transmitted from the pile to the plate through friction. This indicates that the primary contribution of the repair system was to restrain the slender flanges enabling the deteriorated section to resist higher axial loads than the corroded control pile.

Figure 5.14 shows the displacements between the steel repair plates and the flanges of the pile at the end of test frame with no jack, the locations of which are shown in Figure 5.7(c). The black and grey lines represent the top and bottom plate, respectively. The two horizontal red dashed lines indicate the peak load level of 665 kips and the load level when axial deformation exhibited a sudden increase, which is 599 kips after peak load. Inspection of Figure 5.14 reveals that the bottom plate started to slip at the peak load, and the top plate started to slip when the load decreased to 599 kips. The difference between top and bottom sides of the pile was due to unintentional eccentricity of the test set-up. This was verified by the test results of the four string potentiometers at four corners of the end plate as illustrated in Appendix B. The failure of the pile can be identified as the following sequence: (1) at the load level of 615 kips, the bottom flange

buckled; (2) at the load level of 665 kips, which was the obtained peak load, the top flange buckled, and the bottom plate slipped as the axial deformation of the reduced section of the pile increased; (3) at the load level of 599 kips, the slip of top plate occurred, the reduced section deformed dramatically, which also led to a lateral deformation of the pile. The visual inspection also revealed localized damage and flaking of the protective coating on the main steel repair plate as shown in Figure 5.12(c). This did not appear to have an effect on the strength of the piles. However, it is a disadvantage for long-term durability of the system.

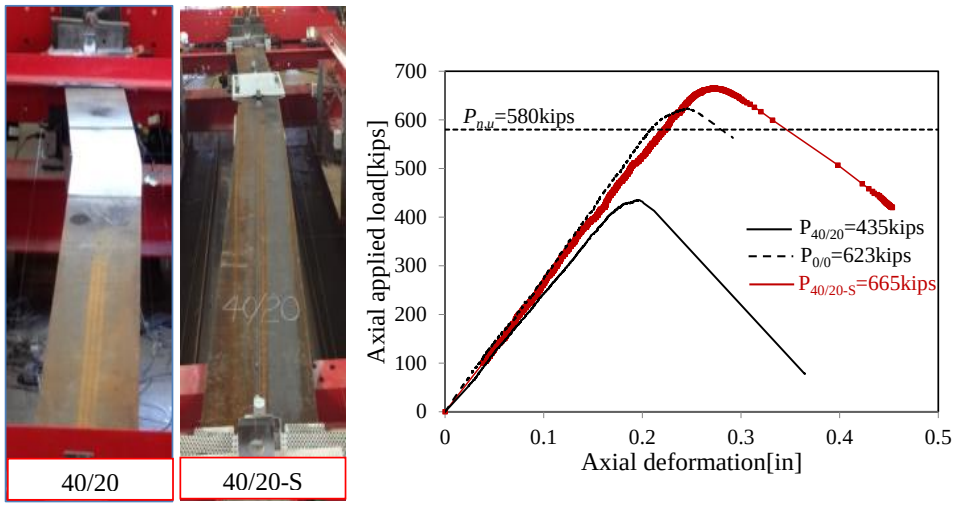

Figure 5.11 Comparison of Pile 40/20 and Pile 40/20-S

(a)Web local buckling (b)Flange local buckling (c)Coating damage

Figure 5.12 Observed local failure on Pile 40/20-S

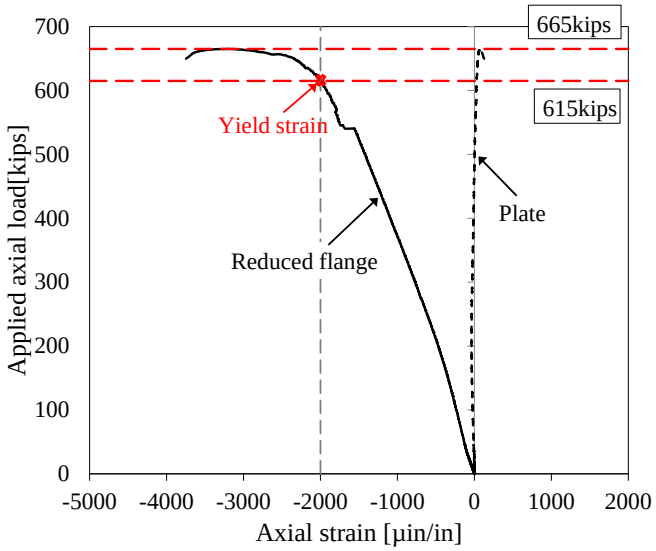

Figure 5.13 Axial strains of the plate and the reduced flange of Pile 40/20-S

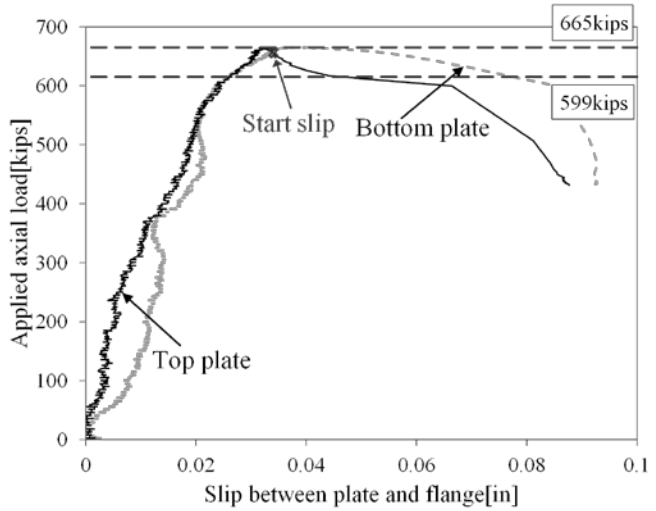

Figure 5.14 Slip of the steel repair plates of Pile 40/20-S

5.3.1.3 Pile 40/60-S

The pile was loaded monotonically up to a peak load of 618 kips, failed by flange and web local buckling. Lateral displacement of the pile, as shown in Figure 5.15(a), was observed after the peak load. After the peak load, the load dropped to 575 kips and increased again, and then exhibited a slight peak of 593 kips followed by a gradual decrease, as shown in Figure 5.15(b). Web buckling was observed during testing before the peak load as shown in Figure 5.16(a). After completing of the test, the strengthening plates were removed to observe the flanges. A higher order plate buckling on flanges was observed as shown in Figure 5.16(b).

Additionally, all bolts were bent and one of them ruptured as shown in Figure 5.16(c). This happened during test and was due to the bevel washers (shown in Figure 5.6(c)) were not used for this pile. Bolts were observed straight after test for other piles with bevel washers.

To understand more details about the observed failure, further inspections were conducted on the axial strains of the plate and the corroded section, and the displacements of the steel repair plates plotted in Figure 5.17. Figure 5.17(a) presents the axial strain values obtained from the two strain gauges, one attached on the steel repair plate and the other attached at the reduced flange close to the junction of flange and web, as shown in Figure 5.7(c). The vertical axis refers to the applied axial load, and the horizontal axis refers to the strains at two locations. Two red horizontal dashed lines refer to two load levels, the first peak load 618 kips, and the second peak at 593 kips. Inspection of Figure 5.17 indicates that the bottom flange buckled at the peak load. .

Figure 5.18 shows the deformation between the steel repair plates and the pile flanges. The black and blue lines represent the top and bottom plate, respectively. The two red horizontal dashed lines indicate the two peak loads of 618 kips and 593 kips, respectively. Inspection of Figure 5.18 reveals that the top plate slipped at the peak load, and the bottom plate slipped at the second peak load of 593 kips. This explains the load drop after the first peak load, which was caused by the sudden increment of axial shortening of the pile due to buckled top flange. Then the bottom flange buckled at the second peak load and slip happened between the bottom flange and the bottom plate, followed by lateral displacement. The difference between top and bottom sides of the pile was due to unintentional eccentricity of the test set-up. The inspection also revealed localized damage and flaking of the protective coating on the main steel repair plate similar to pile 40/20-S, which did not influence the pile capacity but might have negative effect on the durability of the repair system.

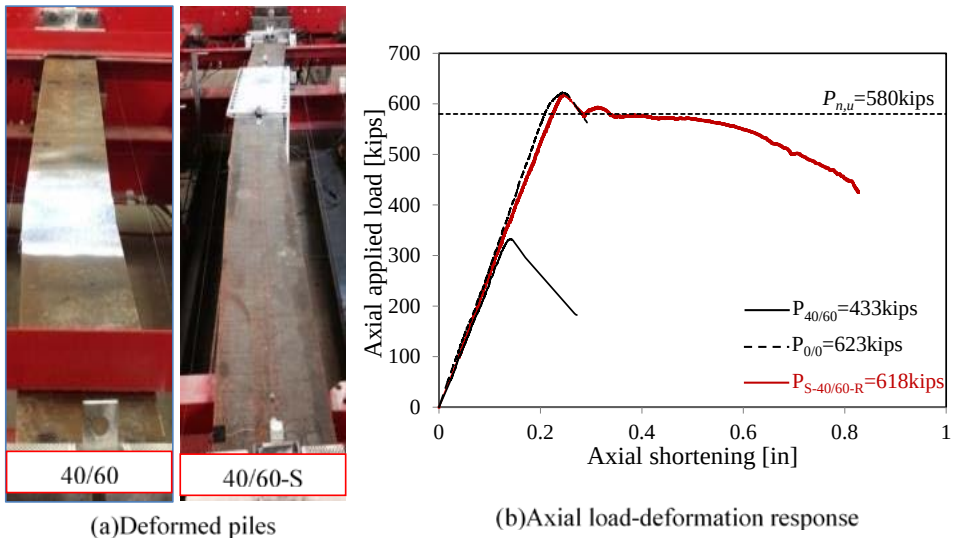

(a)Deformed piles

(b)Axial load-deformation response

Figure 5.15 Comparison of Pile 40/60 and Pile 40/60-S

(a)Web local buckling

(b)Flange local buckling

(c)Ruptured and bended bolts

Figure 5.16 Buckled flange and web and damaged bolts of Pile 40/60-S

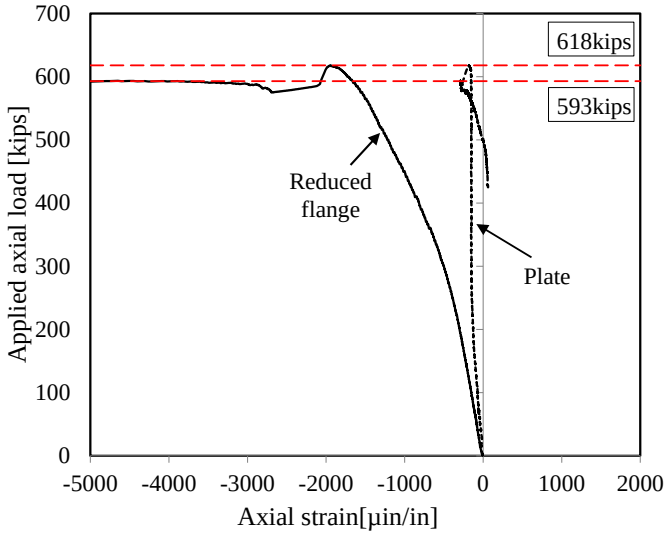

Figure 5.17 Axial strains of the plate and the reduced flange of Pile 40/60-S

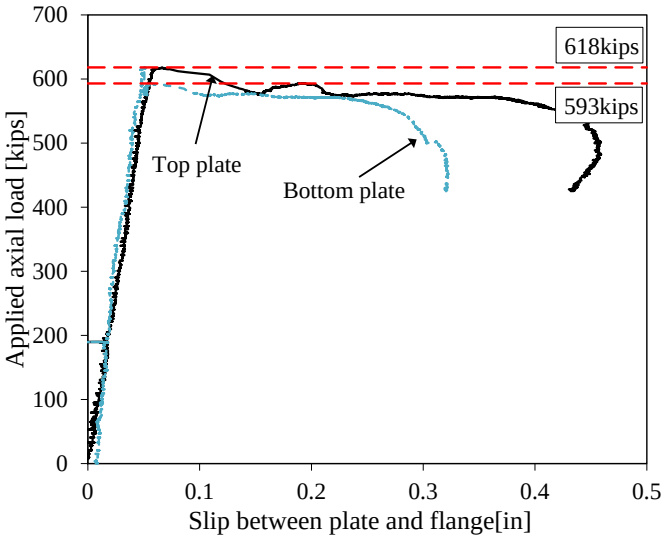

Figure 5.18 Slip of the steel repair plates of Pile 40/60-S

5.3.1.4 Pile 80/60-S(1) and 80/60-S(2)

Two piles were milled and repaired identically to evaluate the repeatability of the results. The piles were loaded monotonically to failure. Both pile exhibited the same failure, a crumpling deformation of flanges and web at the corroded region, and their peak loads were comparable. The comparable behaviors of these two piles indicate the replicability of the proposed repair system. The piles failed at the load levels of 632 kips and 615 kips for Pile 80/60-S(1) and Pile 80/60-S(2), respectively. No lateral displacement was observed for two piles, as shown in Figure 5.19(a). The onset of non-linearity was observed at a load level of 600 kips and 580 kips for 80/60-S and 80/60-S^{d}, respectively, as show in Figure 5.19(b). At this stage, web local buckling was observed, along with sounds of the coating cracking. After the test, the steel plates were removed to inspect the failure of the corroded region, as shown in Figure 5.20(a). Flanges and web within the corroded region showed a crumpling deformation. The deformation indicated that the flanges were too slender to stiffen the web at the junction; meanwhile, the destabilization of the web caused the excessive axial deformation of the flanges.

Figure 5.21 shows the slip between steel repair plates and pile flanges during testing. The vertical axis refers to applied axial load, and the horizontal axis refers to the relative displacement

between plates and flanges. The top plate exhibited an increase of slip before the peak load was achieved and a sudden slip at the peak load, as shown by the black line in Figure 5.21. This indicated that the applied load exceeded the friction force between the pile flanges and repair plates, and the pile shortening started to increase dramatically. This led to the crumpling deformation of the corroded section. Also, the outer layer of the coatings cracked and peeled near the edge of the flange tips while both layers of coatings exhibited damage at the region of the most deformed flanges, as shown in Figure 5.20(b).

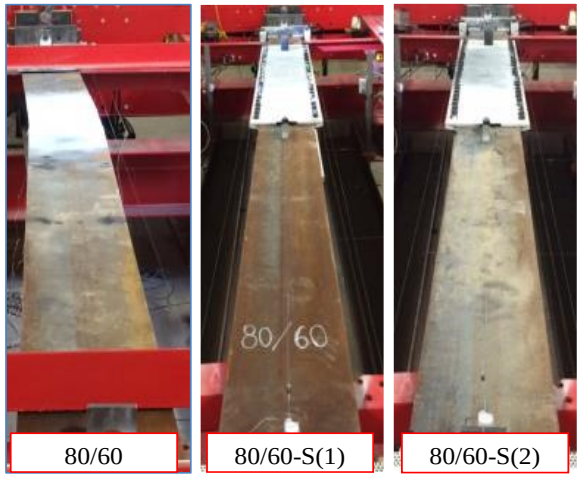

(a)Deformed piles

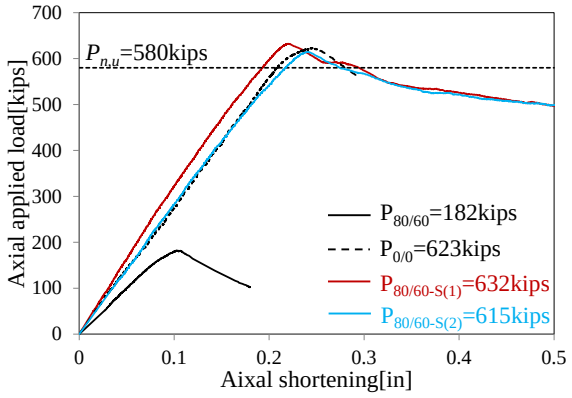

(b)Axial load-deformation response

Figure 5.19 Comparison of Pile 80/60 and Piles 80/60-S(1) and 80/60-S(2)

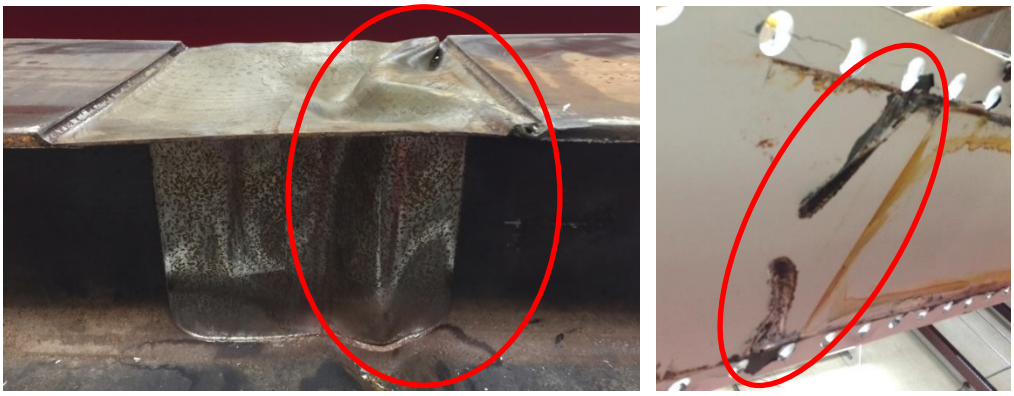

(a)Flange and web crumpling (b)Coating damage

Figure 5.20 Buckled flange and web and coating damage of Pile 80/60-S(1) and 80/60-S(2)

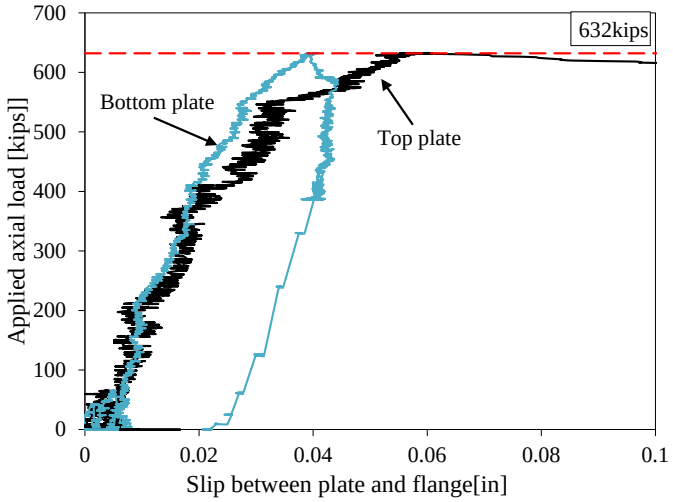

Figure 5.21 Slip of the steel repair plates of Pile 80/60-S

5.3.1.5 Pile 80/60/V-S

The pile 80/60/V-S was loaded up to 630 kips and no lateral deformation was captured (Figure 5.22). The failure shape of the flange was similar to the corroded control specimen as shown in Figure 5.23(a), flange one-way bending failure was observed during testing. Figure 5.24 shows the slip between the steel repair plates and the flanges of the piles. Inspection of Figure 5.24 indicates a slippage between top flange of the pile and the repair plate (indicated by the black line) at the load level of 620 kips, and it increased dramatically after peak load. After test, the steel repair plates were removed. The deformations of the corroded flanges of the repaired and corroded control piles were slightly different as shown in Figure 5.23(b), due to difference of the

plate boundary conditions of the flanges of two piles. The repair system provided a restraining effect by clamping the flange edge.

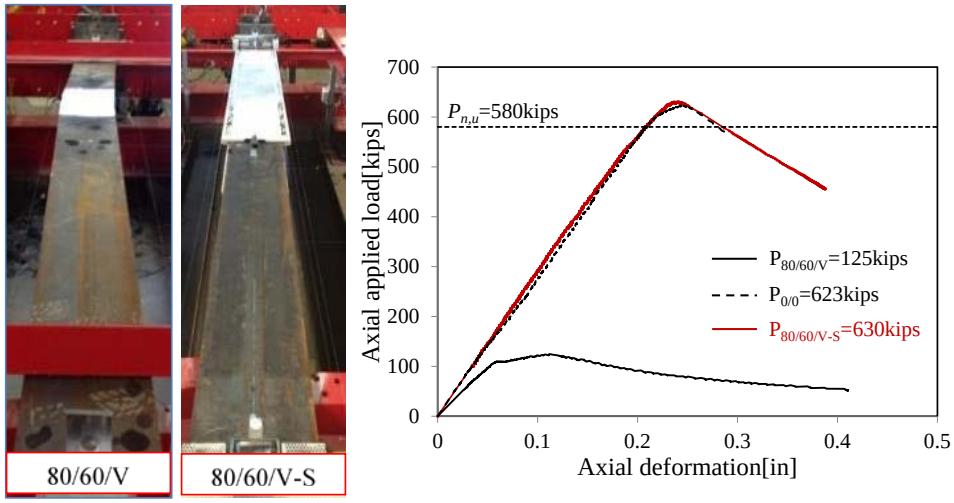

(a)Deformed piles

(b)Axial load-deformation response

Figure 5.22 Comparison of Pile 80/60/V and Pile 80/60/V-S

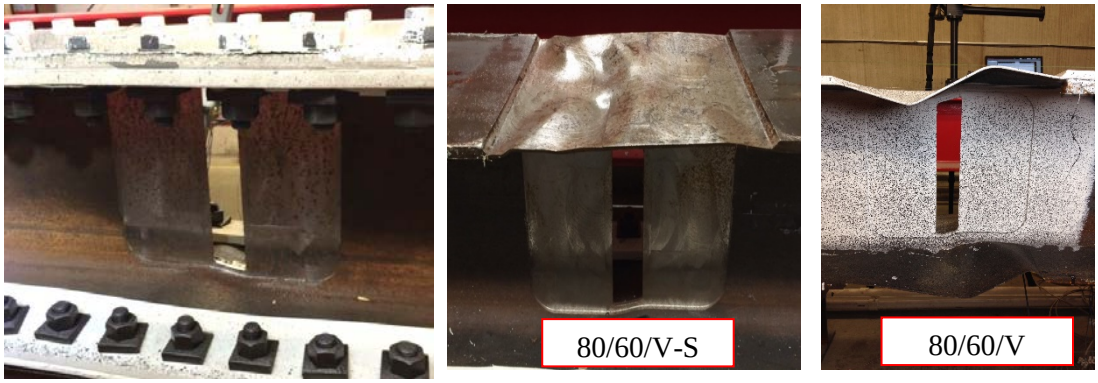

(a)Flange one-way bending

(b)Comparison of deformations of corroded and repaired piles

Figure 5.23 Observed failure on Pile 80/60/V-S and Pile 80/60/V

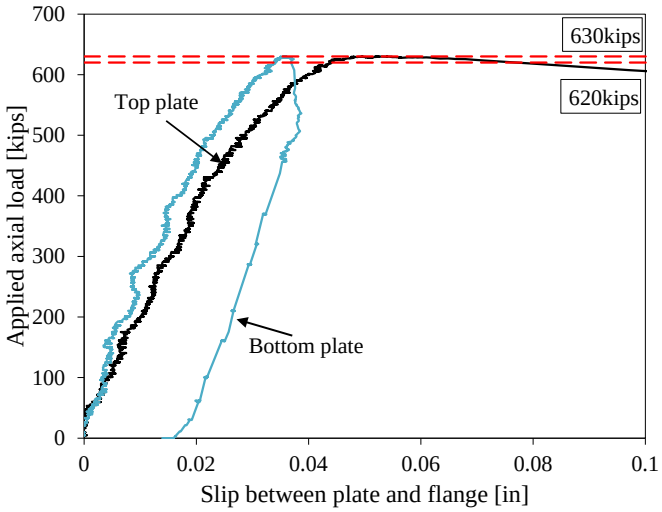

Figure 5.24 Slip of the steel repair plates of Pile 80/60/V-S

5.3.1.6 Pile 80/60/3-S

The pile was loaded up to 532 kips and failed by buckling crumpling deformation of flanges and web within the corroded region, with no visible lateral displacement (Figure 5.25(a)). The load dropped substantially after it reached the peak, as shown in Figure 5.25(b). Figure 5.26 shows the slip between the top plate and top flange during test. The top plate slipped dramatically at the peak load as shown by the black line in Figure 5.26. This was due to the substantial axial deformation resulted from the buckled flanges and web at the corroded region. The obtained capacity was lower than the nominal capacity, because the location of the rollers of the test frame limited the length of the repair system, as shown in Figure 5.27(a). The designed length of repair system should be 8.5 ft to obtain the nominal capacity of the pile. However, the location of the roller on the test frame limited the length of repair system to 7.5 ft. With the limited length of repair system, the pile capacity predicted by the design procedure described at the beginning of this chapter is 496 kips, 7% lower than the experimental result. The coatings started to crack when the applied load reached 450 kips. Removing the steel repair plates after test, the flanges and web deformed in the same configuration as 80/60-S and 80/60-S^{d}, as shown in Figure 5.27(b).

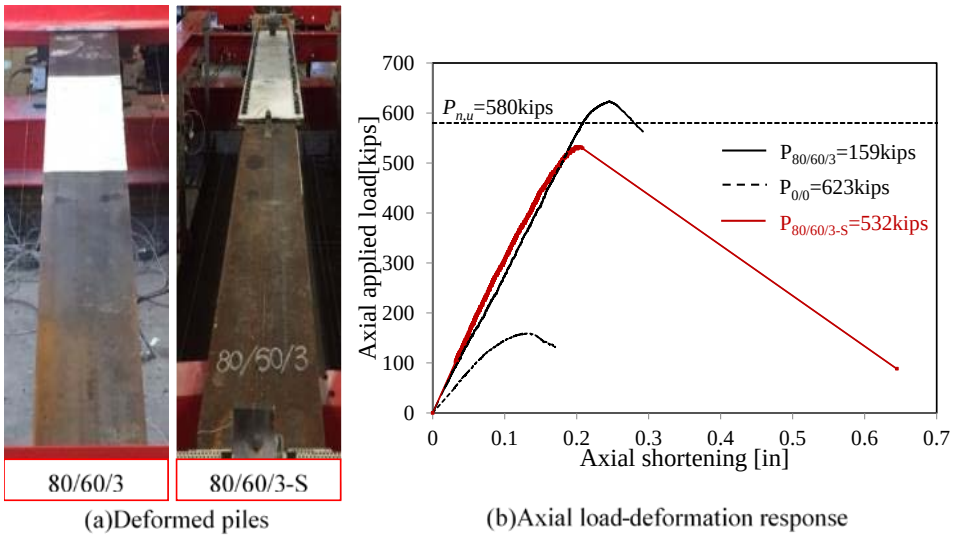

Figure 5.25 Comparison of Pile 80/60/3 and Pile 80/60/3-S

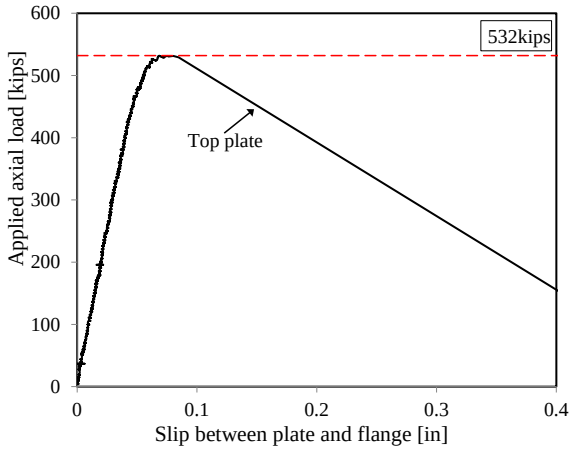

Figure 5.26 Slip of the steel repair plates of Pile 80/60/3-S

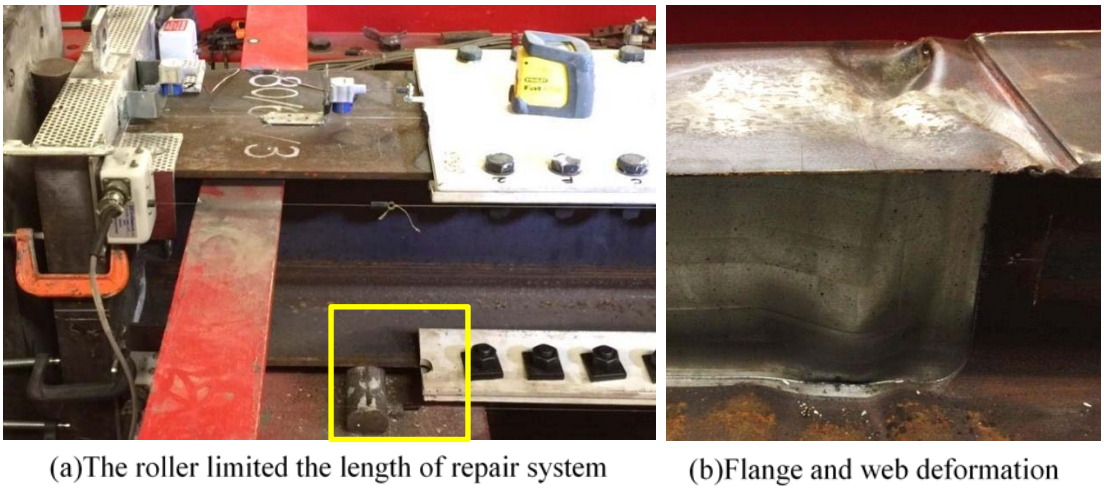

Figure 5.27 Observed failure on Pile 80/60/3-S

5.4 Conclusions

A friction-type bolted plate-based system was developed for repair of steel piles with localized corrosion. The design method for the repair system was presented and applied to seven full-scale corroded H-piles. An experimental program was conducted and the results were compared to the corroded control piles introduced in Chapter 3. The main findings are summarized as follows:

1) The friction-type bolted steel plate-based repair system can effectively restore the capacity of H-piles with localized corrosion. All the retrofitted piles except one (80/60/3-S) exceeded the nominal axial capacity of an un-corroded 15ft HP12×53 pile.

2) The Pile 80/60/3-S was designed intentionally weak due to the limitation of the test frame. The expected capacity of Pile 80/60/3-S was only 7% lower than the test result.

3) The repair system successfully restored the axial stiffness of the corroded piles. This may be beneficial to the serviceability of bridges that are supported on repaired piles, to minimize excessive deformation or differential settlement.

4) The piles with extremely thin flanges and webs as Pile 80/60-S(1), Pile 80/60-S(2), and Pile 80/60/3-S, showed a crumpling deformation at the corroded region. The deformation indicated that the flanges were too slender to stiffen the web at the junction; meanwhile, the destabilization of the web caused the excessive axial deformation of the flanges.

5) Bevel washers are necessary for this repair system, in order to prevent bolts from bending or rupturing during tightening or in service.

6) The first layer of the coatings, a solvent-based, inorganic ethyl silicate, zinc-rich coating, was applied directly on the surface of the steel repair plates. It exhibited strong bond to the plates until the increment of the scratching force generated by extremely deformed flanges in cases with 80% reduction of flange thickness. However, the second layer coating, a non-zinc containing, Class B-rated, polyamide epoxy coating, which was applied on top of the first layer. It showed a brittle performance. Although the damage of the coatings did not appear to have any

negative effect on the axial capacity of the repaired piles, it may represent a shortcoming of the durability of the repair system.

The test results were used to validate a 3D non-linear FE model developed in Chapter 6 to study the repair system. The numerical analysis provided more information about the behavior of the retrofitted piles that could not be captured in experimental program. The verified FE model was used for parametric study on factors that might affect the axial capacity of the retrofitted piles.

CHAPTER 6 NUMERICAL STUDY OF REPAIR SYSTEM

Chapter 5 presented the experimental study on the axial behavior of the proposed repair system. This chapter presents a numerical analysis on partially corroded H-piles repaired by friction-type bolted plate-based system. The objective of the numerical analysis was to evaluate factors that might affect the axial behavior of retrofitted piles and optimize the design of proposed repair system. A FE model was developed to simulate the repaired piles. The model was first validated using the full-scale experimental results of seven retrofitted piles presented in Chapter 5. Then the model was used for a parametric study to further investigate different factors that might affect the strengthened axial capacity of the pile. The studied factors included coefficient of friction between the faying surfaces, magnitude of bolt pretension, and length of steel plates (which is also taken as the length of the repair system).

6.1 Finite Element Model

The numerical framework developed for prediction of corroded H-piles (details presented in Chapter 4) was used for the simulation of repaired piles. The bolts, steel plates, and interface behavior between flanges of original pile and the steel plates were also included in the FE simulation in addition to the corroded piles. The details of the FE model are presented in the following sections.

6.1.1 Simulation of corroded piles

The FE model developed for corroded H-piles in Chapter 4 was used for piles of the repaired group. The thicknesses of flanges and webs measured from the repaired group were presented in Table 5.1 of Chapter 5. The element type, mesh size, material properties, initial global and local imperfections, and distribution of residual stresses were implemented the same way as they were in the FE models of the corroded control piles in Chapter 4. The four-node fully integrated finite-membrane-strain shell element with linear shape function, S4, was used and the pile was discretized into 1 in×1 in elements. The material model follows classic plasticity: Von-Mises yield criteria, associated flow, and isotropic hardening. The yield strengths of the flanges

and webs were 52.5 ksi and 60.5 ksi, respectively, with elastic moduli of 28,400 ksi and 32,000 ksi, respectively. The ultimate strengths of flange and web were taken as 66.5 ksi and 71.0 ksi, respectively. The magnitudes of the initial global and local geometric imperfections were taken as 0.18 in and 0.06 in, respectively. The distribution of residual stresses was assumed to have maximum compression stresses at the flange tips and uniform tension stress in the web. The maximum value of residual compressive and tensile stresses was assumed as 10 ksi. Boundary conditions were modeled to represent the test set-up at the supports with only rotation about the weak axis was permitted while the other degrees of freedom were restrained. The piles were loaded by imposing an axial displacement at one end to simulate the action of the hydraulic jack in the experimental program. The modified Riks method, was employed to solve the geometrically and materially nonlinear model.

6.1.2 Simulation of steel plates

The steel plates of the repair system were modeled using the same element type as the H-piles. The FEA results of corroded H-piles (Chapter 4) demonstrated that this element type provided accurate predictions for members loaded in compression and failing by plate buckling. The mesh size was determined as 0.5 in×0.5 in according to a preliminary sensitivity study, in which coarser mesh sizes did not converge. The difficulty of convergence was caused by the large stress concentration in the steel plates around the bolts due to bolt pretension. The yield and ultimate strengths of the plates were taken as 33.1 ksi and 48.8 ksi, respectively, based on the tension coupon tests presented in Chapter 5. The elastic modulus was taken as 28,600 ksi.

Figure 6.1(a) shows the assembly of the plates and the pile in FEA: the two main steel plates were assembled on the outside surfaces of each flange, and the four clamping plates were positioned inside the surfaces of the flanges. After tightening the bolts, the clamping plates rotated (θ) along the edges of flanges until the outer edges of the clamping plates were contacting the edges of the main plates, as shown in Figure 6.1(b). For stabilization purpose, the main plates and the clamping plates were restrained along their transverse edges from translational

movements while applying bolts pretension, and the constraint was released before applying axial load.

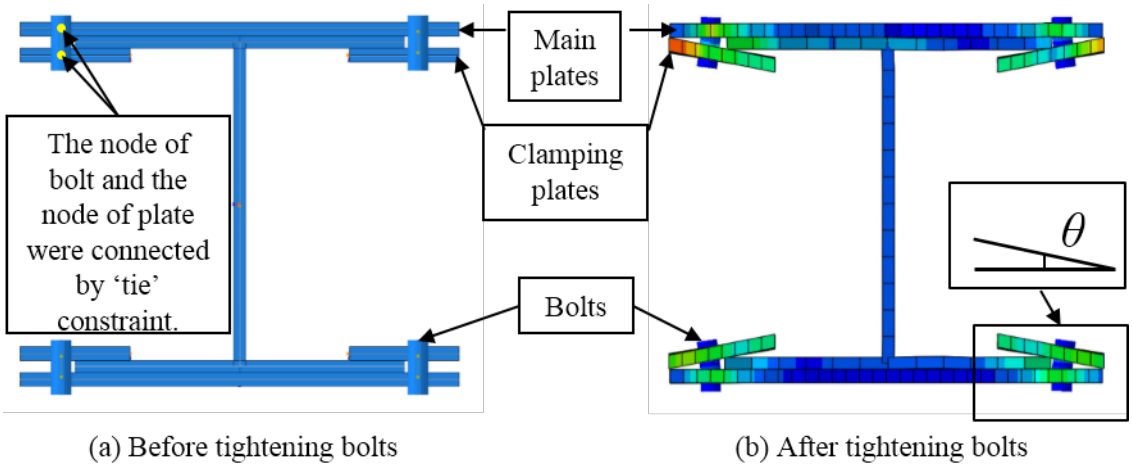

Figure 6.1 Cross sectional views of the repaired piles simulated in FEA

6.1.3 Simulation of high-strength bolts

The bolts were simulated using a two-node linear beam element, B31, which is a Timoshenko beam that allows for transverse shear deformation. According to ASTM A325 (2014), the minimum yield strength and tensile strength for A325 bolts are 92 ksi and 120 ksi, respectively, which were determined as the strengths of material properties for the bolts in FEA. The head of the bolts, flat washers, bevel washers, and nuts were not modeled for two reasons: (1) the detailed behavior of the bolts (i.e. the magnitudes and distributions of stress and strain within each bolt across its section) was not the focus of this study, and (2) for the efficiency of calculation. Instead, the bolts were simulated to be connected to the main plates and clamping plates using 'tie' constraint, as shown in Figure 6.1(a). This indicated that the node of the bolt and the node of the plate displaced as one node in all degrees of freedom at their intersections. The pretension was applied on each bolt as 'bolt load' between the main plates and clamping plates. The bolts bent after full pretensions were applied, as shown in Figure 6.1(b), since the bevel washers were not included in the model. This caused a force from the clamping plates acting on the bolts in the direction perpendicular to the bolt axis. However, the bolts had adequate shear

strength to resist the transverse load. As long as the bolts provided required pretensions, the effect of bent bolts on the axial capacity of the repaired pile was negligible to the investigation of the behavior of strengthen piles. This was supported by the test results of Pile 40/60-S, which did not have bevel washers but was repaired effectively.

6.1.4 Simulation of the interface property of pile flanges and steel plates

An interface containing normal direction and tangential direction behaviors was defined between the steel main plates and the outer surfaces of the flanges. The normal direction behavior was defined as 'hard contact' allowing separation between contacting surfaces. This type of contact prevents the penetration between contacting surfaces and does not allow tensile stress across the interface but allows only compression. The tangential direction behavior was defined using isotropic penalty friction formulation with friction coefficient K_s, as shown in Figure 6.2. Figure 6.2 shows the relationship between the friction force versus the normal force between the contact surfaces. In Figure 6.2, the coefficient of friction is shown as 0.34. However, two values of K_s were considered in FEA: the mean value (0.34) and the minimum value (0.30) of the slip resistance factor obtained from the coefficient of friction test that was presented in Chapter 5. The purpose of running two series of analyses using the two values of friction coefficients was to consider the statistical uncertainty since the coefficient of friction test was conducted on small-scale specimens, and the value of friction resistance might decrease on the full-scale specimens.

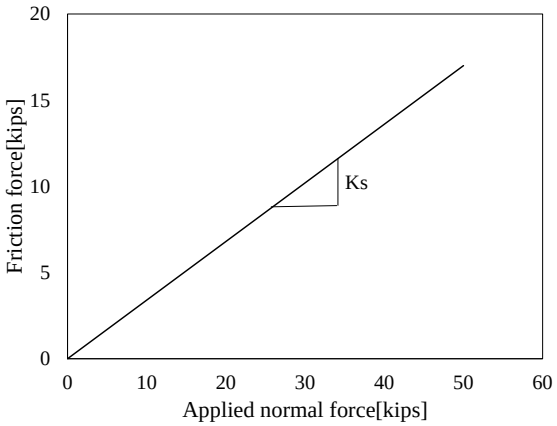

Figure 6.2 Relationship of friction force and normal force defined in FEA

6.2 Validation of the FE model

Table 4.3 illustrates the axial capacities of the repaired piles obtained from FEA and experiments. The pile designations were adopted from the experimental program (presented in Chapter 3): the first and second numbers indicate the percentage of thickness reduction of flange and web, respectively; the third part indicates a void on web with a 'V' and 3 ft extent of reduction with a '3'; the 'S' at the end indicates the piles were repaired by the steel-based repair system. Pile 80/60-S refers to Pile 80/60-S(1) as Pile 80/60-S(2) was a duplicate specimen of 80/60-S(1) as mentioned in Chapter 5, with only slight differences of flange and web thicknesses.

The ratios of the axial capacities obtained from tests and FEA indicate that the FEA with slip resistance of 0.34 and 0.3 showed comparable predictions on piles with less than 80% reduction of flange thickness. However, for piles with 80% reduction of flange thickness, FEA overestimated their capacities if slip resistance of 0.34 was adopted; while the FEA showed more accurate though slightly conservative predictions using 0.30 as the friction coefficient. Moreover, the failure modes of piles with 80% reduction of flange thickness obtained from numerical simulation indicated that 0.3 provided better match between FEA and experiments. Figure 6.3 shows the predicted failure of Pile 80/60-S by FEA with two values of slip resistance. The pile showed three failure modes almost at the same time in Figure 6.3(a): flexural buckling, flange local buckling at the corroded region, and flange local buckling at the un-corroded region outside the repair system. In contrast, FEA using slip resistance of 0.3 predicted failure only at the corroded region. According to the experimental observation of Pile 80/60-S, the failure occurred only at the corroded section with no lateral displacement or damage outside the repair system. Similar phenomenon was observed for Pile 80/60/3-S. This fact illustrates the concern that the obtained friction force in full-scale experiments was lower than the expected value.. The friction force that can be achieved may decrease in full-scale applications for several reasons: (1) the larger contact area increases the likelihood of defects in the coating that would potentially reduce the coefficient of friction, (2) the increased number of bolts increases the likelihood that some of

the bolts may not be fully tightened due to the statistical variability of the bolt tightness, (3) the edge of the strengthening plate being in contact with the edge of the clamping plate would cause some of the bolt pretension force to be transferred through that interface rather than at the interface between the strengthening plate and the pile, and (4) localized out-of-straightness of the flanges may influence the frictional force that can be achieved at the interface. To accurately capture the capacities of the retrofitted piles, the results of FEA using 0.30 as the coefficient of friction were used for comparison and validation in the following sections.

The differences of the FEA predicted capacities and tested capacities are no more than 5% except for Pile 40/20-S. The unexpected high capacity of Pile 40/20-S obtained from experimental program is attributed to its lower unintentional eccentricity during testing compared to other cases, which was demonstrated by the difference of the values of the four axial string potentiometers.

Table 6.1 Axial peak loads and failure modes of repaired piles from FEA and tests

Pile designation	Axial peak load [kips]			P_{test}/P_{FEA}	
	P_{test}	P_{FEA}			
		K_s=0.34	K_s=0.30	K_s=0.34	K_s=0.30
0/20-S	629	603	603	1.04	1.04
40/20-S	665	569	567	1.17	1.17
40/60-S	618	600	587	1.03	1.05
80/60-S	632	639	600	0.99	1.05
80/60/V-S	630	677	632	0.93	1.00
80/60/3-S	532	584	525	0.91	1.01

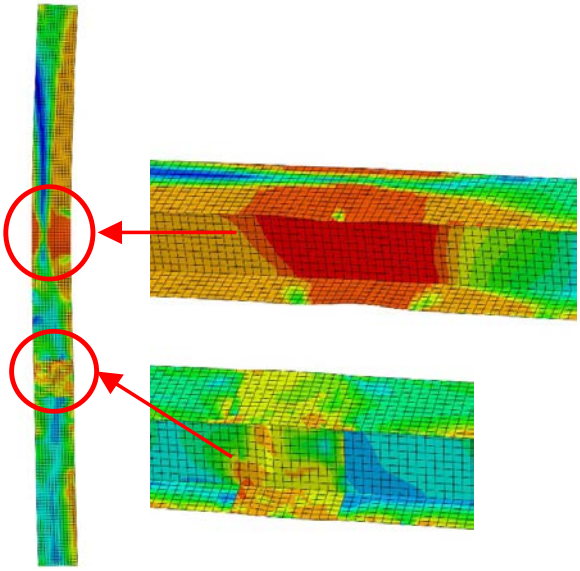

(a) Predicted failure of Pile 80/60-S by FEA with slip resistance of 0.34

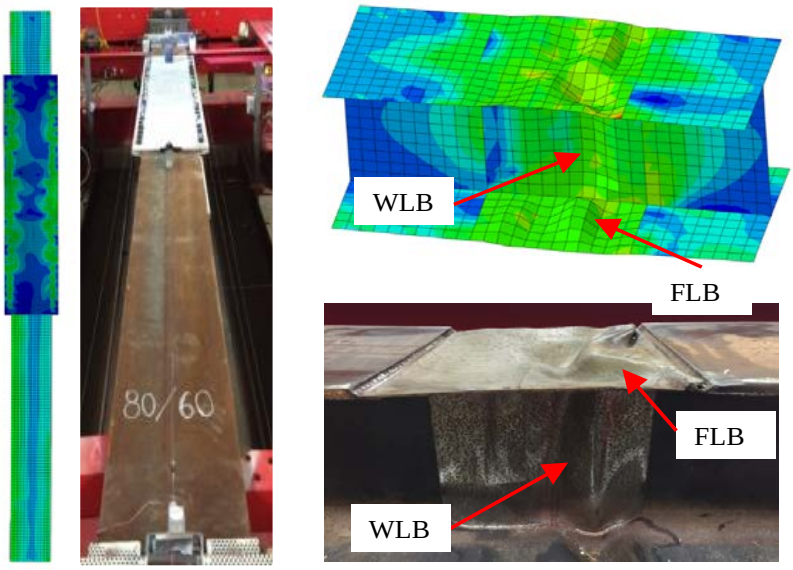

(b) Predicted failure of Pile 80/60-S by FEA with slip resistance of 0.3

Figure 6.3 Predicted failure of Pile 80/60-S

Figure 6.4 presents the comparison of deformed piles from FEA and experiments. The figure shows a close agreement between the piles deformations between FEA predictions and experimental observations. Detailed global and local deformations include (1) the flexural buckling failure of Pile 0/20-S, as shown in Figure 6.4(a), (2) the minor buckled flanges of Pile 40/20-S, as shown in Figure 6.4(b), (3) the higher order mode of plate buckling on flanges of Pile 40/60-S (Figure 6.4(c)), the crumpling deformation observed from Pile 80/60-S (Pile 80/60/3-S

showed the same failure) as shown in Figure 6.4(d), and (4) the one-way bending mode exhibited on flanges of Pile 80/60/V-S, as shown in Figure 6.4(e). The flexural buckling shape of 40/60-S shown in Figure 6.4(c) was observed after peak load for both FEA and test.

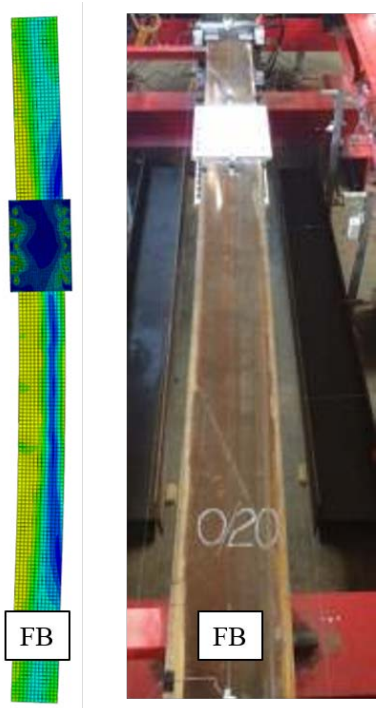

(a) 0/20-S
(FB=Flexural buckling)

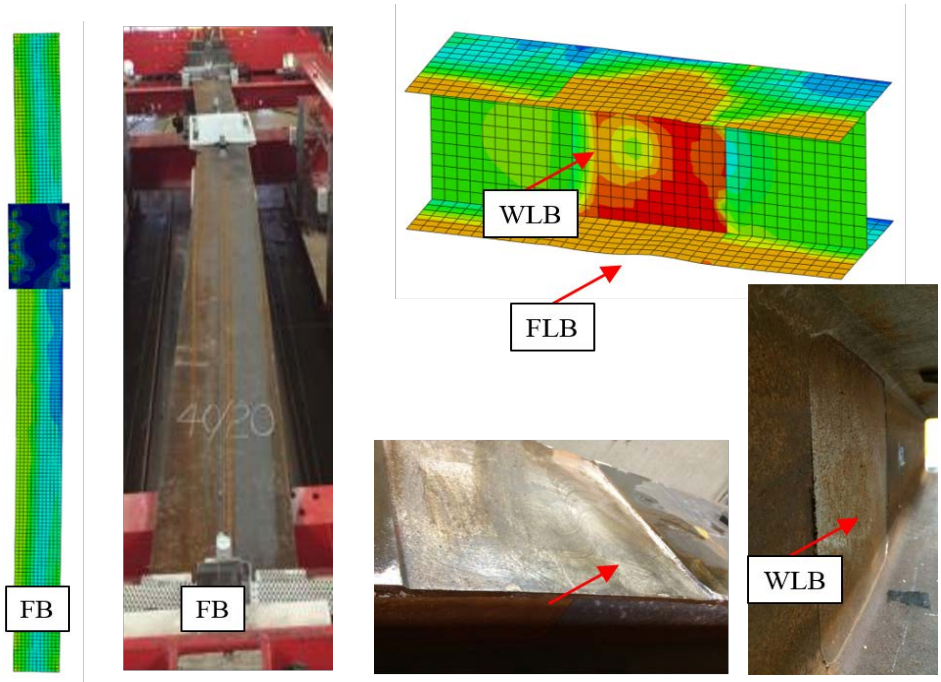

(b) 40/20-S (FLB=Flange local buckling; WLB=Web local buckling)

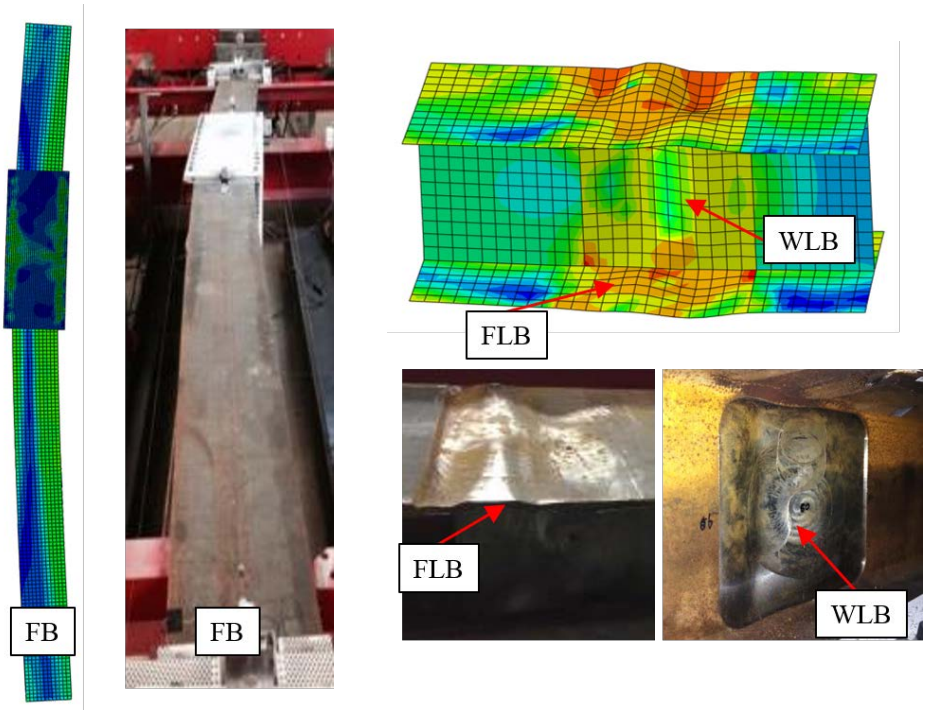

(c) 40/60-S

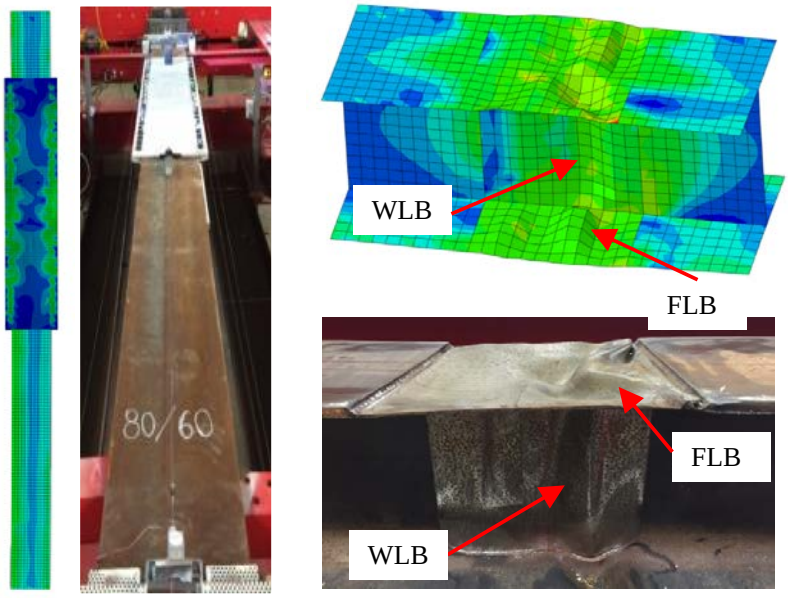

(d) 80/60-S

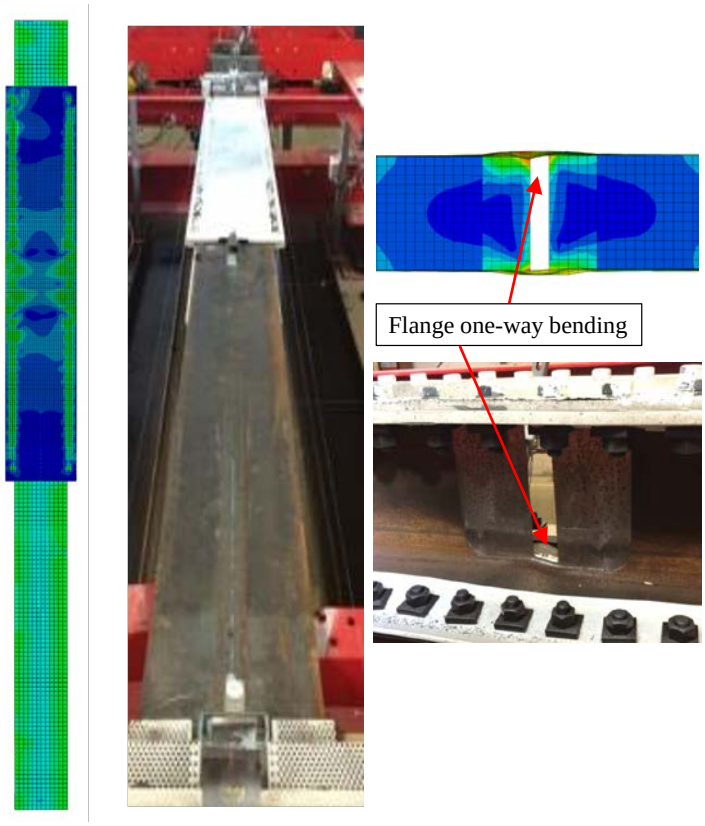

(e) 80/60/V-S

Figure 6.4 Comparison of deformations of FEA and experiments for repaired piles

Figure 6.5 compares the predicted axial load-deformation relationships from FEA to the measured response. The solid curves refer to the compression responses obtained from experimental study, and the dashed curves indicate the responses predicted by FEA (K_s=0.3). The figure also presents the coefficients of determination, R^2, between experimental and numerical curves. $(R^2)_{total}$ was calculated from the total range of the curves from zero deformation to the maximum deformation of the test or FEA, whichever ended first. The maximum deformation obtained from tests was determined as the last data point before the sudden drop of axial load. The maximum deformation of FEA predictions was defined as the end of analysis. $(R^2)_{peak}$ was calculated within a range from zero load (deformation) to the peak load of the curves, to quantify the correlation of FEA and experimental results regardless of the post-peak behavior. Inspection of Figure 6.5 indicates that $(R^2)_{total}$ for all the piles presents satisfactory correlation ranging from

0.93 to 1.00, except for pile 40/60. The post-peak response from experiment exhibits higher capacity than FEA prediction. The discrepancies were attributed to five possible reasons: (1) unintentional eccentricity of the applied load during testing; (2) uncertainty of the magnitude and pattern of the residual stresses; (3) conservativeness of the assumed magnitude and pattern of initial imperfections; (4) effect of the fillet at the junction of flange and web, which was not modeled in the FE simulation but partly existed in tested specimens; (5) the difference of the actual slip resistance obtained from the tests and the value used in FEA. For pile with failure occurred within the corroded region, its capacity is highly sensitive to the friction force between steel plates and pile flanges (this was demonstrated in parametric study in the following section). For piles with 80% reduction on flange thickness, the FEA did not capture the post-peak response, because the excessive deformation of flanges led to convergence issue of the FE model. However, the values of $(R^2)_{peak}$ range between 0.99 to 1.00 for all of the examined cases indicate the accuracy of the FE model on predicting the strengthened capacity.

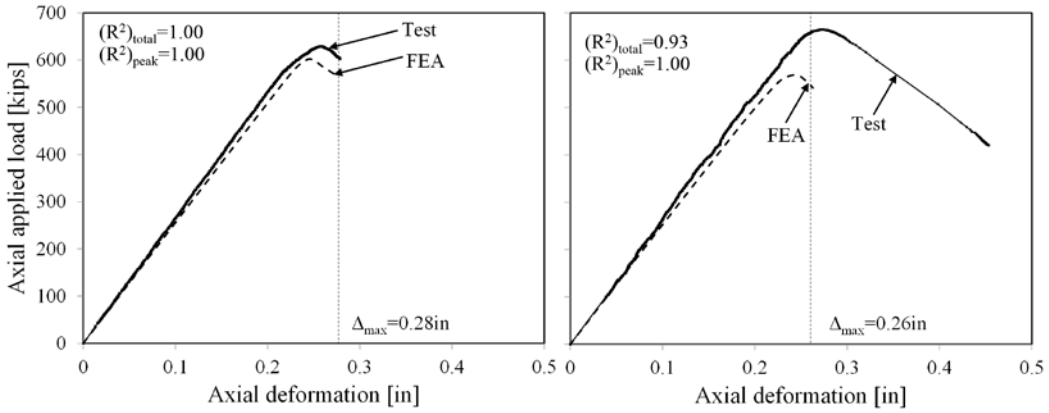

(a)0/20-S (b)40/20-S

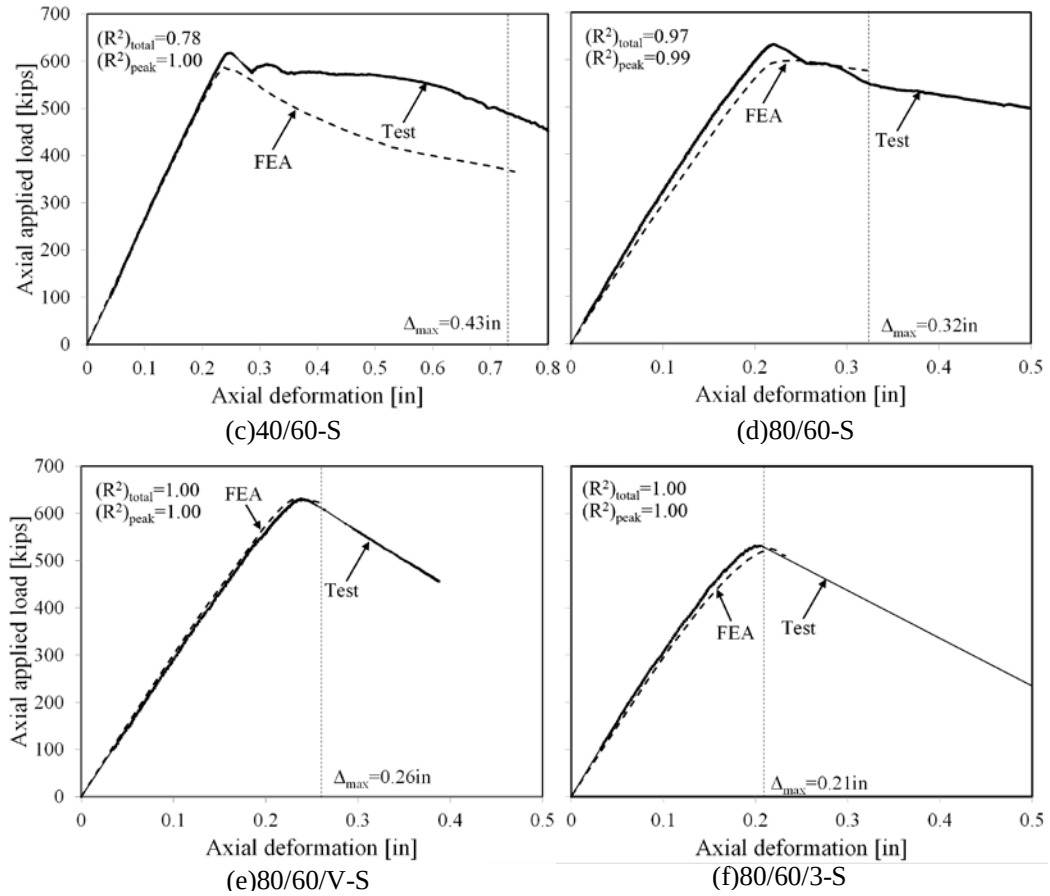

Figure 6.5 Axial load-deformation responses of repaired piles from tests and FEA

6.3 Parametric Study

After validating the numerical model using the experimental results of repaired piles, a parametric study on retrofitted piles was performed to investigate the factors that affect the strengthened capacity of partially corroded H-piles. The parameters include (1) the slip resistance between steel main plates and pile flanges, (2) the pretention in bolts, and (3) the length of steel plates. The parametric study was carried out by taking the FE model of 40/60-S and changed one parameter each time while keeping the other two constant.

Pile 40/60-S was selected as a base configuration for two reasons. First, its deterioration degree was so severe that the pile failed by flange and web local buckling, which was a representative case for piles that require rehabilitation. Second, to investigate the effect of different lengths of the steel repair plates, Pile 40/60-S had adequate range of the increment of the

plate length. For a 15-ft-long pile with corroded region centered at its third-height, the maximum length of its repair system could be 10 ft. Pile 40/60-S needed 3.5 ft repair system to gain its original un-corroded capacity according to the design which was verified by the experimental result. Therefore, additional increment of 6.5 ft could be implemented in FEA to study the capacity enhancement caused by greater extent of repair plates.

6.3.1 Effect of slip resistance of contact surfaces of steel plates and pile flanges

Figure 6.6 shows the effect of the slip resistance on the axial capacity of repaired piles. The bolt pretension was kept constant at 28 kips for each case. The horizontal and vertical axes illustrate the values of friction coefficients and the axial capacities, respectively. The dots in the figure indicate the predicted peak load of each pile. The three marker styles indicate three different lengths of the steel plates: the circular dots refer to 3.5 ft steel plates, the square dots refer to 5 ft, and the triangular dots refer to 6.5 ft steel plates. The four cases marked by red circles are piles failed by local buckling at the corroded region, see Figure 6.7; otherwise the piles failed by flange local buckling followed by flexural buckling outside the repair system, as shown in Figure 6.8. Five values of slip resistance were investigated, 0.1, 0.2, 0.34, 0.5, and 0.75. The value 0.34 is the mean value of slip resistance factors obtained from coefficient of friction test, which is very close to the Class A slip coefficient of 0.33 defined in AASHTO (2012). The value of 0.5 is the Class B slip coefficient specified in AASHTO (2012). The other three values were selected to form a trend with uniform increment of slip resistance magnitude.

Figure 6.6 indicates that increasing the slip resistance enhanced the strengthened axial capacity of the pile which failed at the corroded region. However, as soon as the failure moved from the corroded region to the un-corroded portion of the pile outside the repair system, increment of slip resistance did not increase the pile in achieving more capacity. At this stage, the capacity was dominated by the axial capacity of the un-corroded pile. For HP12×53 pile, the dominant failure mode is flexural buckling and flange local buckling since its flange slenderness ratio is right above the limit of slender element defined in AISC (2011).

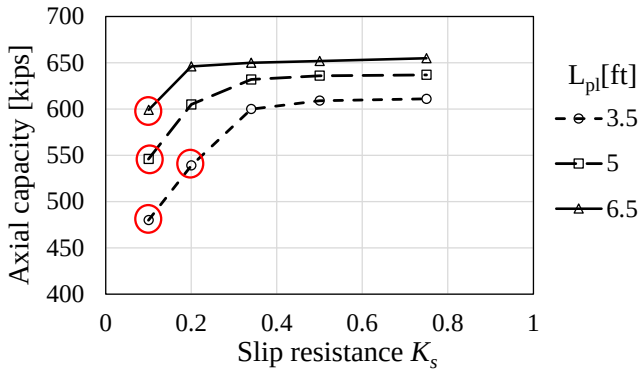

Figure 6.6 Axial peak loads of repaired piles as function of different slip resistances

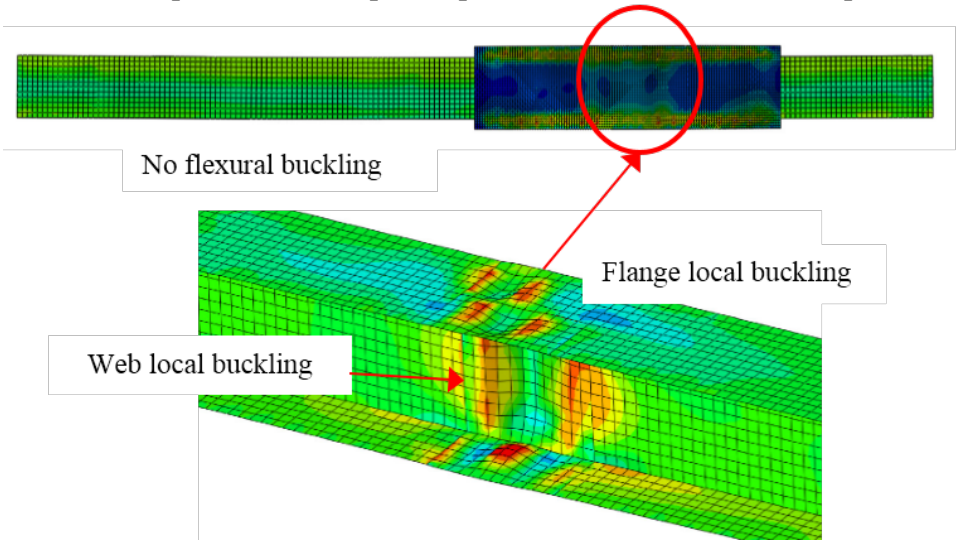

Figure 6.7 Failure within the corroded region

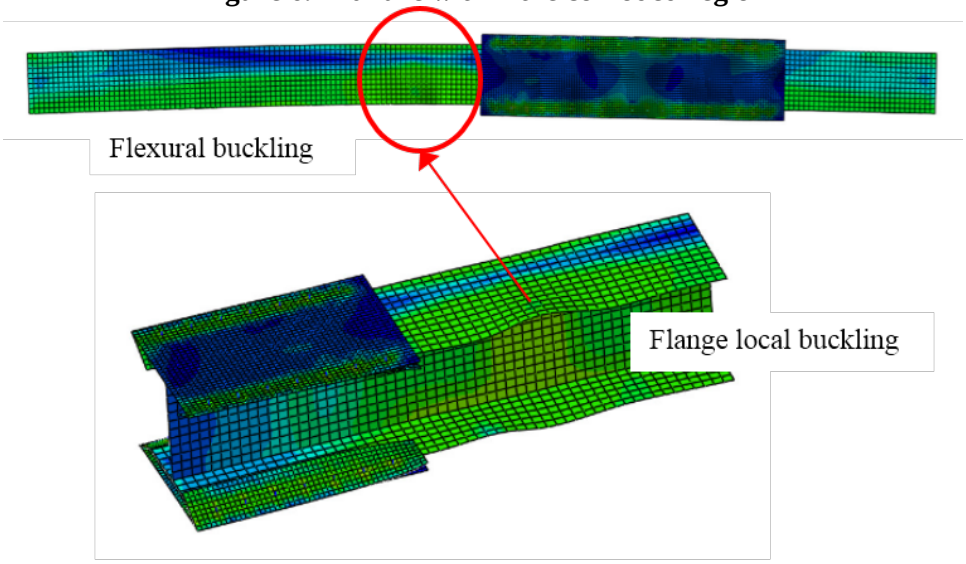

Figure 6.8 Failure outside the repair system

6.3.2 Effect of bolt pretension

Figure 6.9 presents the influence of bolt pretension on the axial capacity of retrofitted piles. A constant value of slip resistance was simulated as 0.34. Similar to Figure 6.8, the horizontal and vertical axes illustrate the values of bolt pretensions and the axial capacities, respectively. The marker styles indicate various lengths of repair system. Three magnitudes of bolt pretension were evaluated, 12 kips, 19 kips, and 28 kips, which corresponded to the minimum pretension for slip-critical connection using A325 bolts with diameters of 1/2 in, 5/8 in, and 3/4 in, respectively (AASHTO, 2012). The red circle points indicate the piles that failed by local buckling within the corroded region (see Figure 6.7), while in other case, the failure occurred outside the repair system (see Figure 6.8). The results demonstrate that the axial capacity increases as the bolt pretension increases if the pile fails by flange/web local buckling at the corroded region. However, once the friction obtained from repair system was adequate to support the corroded region and the failure transferred to the un-corroded part of the pile, increment of bolt pretension did not enhance the strengthened axial capacity. This is reflected in Figure 6.9 by comparing axial capacities of piles with 5 ft and 6.5ft long repair systems. The three values of axial capacities were almost the same despite of three different bolt pretensions that were applied to the repaired piles.

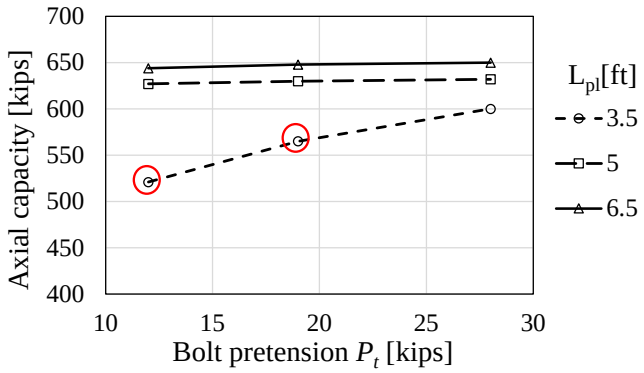

Figure 6.9 Axial peak loads of repaired piles as function of varying bolt pretension

6.3.3 Effect of length of steel plates

Three different lengths of the steel repair plates were investigated, namely: 3.5 ft, 5 ft, and 6.5 ft. The results are shown in Figure 6.6 and Figure 6.9. In order to illustrate the effect of the plate length, the results are reorganized and shown in Figure 6.10. The vertical axis refers to the FEA predicted axial capacity of each pile, and the horizontal axis refers to the length of steel plates. Different styles of markers indicate five values of slip resistance. The bolt pretension was 28 kips for all cases. The red circle cases failed by local buckling within the corroded region, while the other piles failed by flange local buckling and flexural buckling outside the repair system. Inspection of the red circle cases indicates that increment of the length of steel plates increased the axial capacity of the pile. This is attribute to the increment of the plate length led to more bolts and thus more friction. Inspection of the un-circled cases, slight increment of axial capacity was observed although these piles failed at the un-corroded region. The reason for this phenomenon is that the piles were simulated with initial imperfections, and greater extent of repair plates provided more strength to resist flexural buckling of the repaired piles.

As stated above, the increment of axial capacity is not substantial once the failure transfers to the un-corroded region outside the extent of repair system, as shown in Figure 6.8. In this situation, elongate the steel plates from 3.5 ft to 5 ft only increased the axial peak load by 4%. Similarly, 6.5 ft long repair system only improved the pile capacity by 3% comparing to piles with 5 ft long repair system. Therefore, as long as the friction between the pile flanges and steel plates transfers adequate axial load to repair system so that the failure is not dominated by corroded region, additional length of steel plates does not contribute substantially to the improvement of pile capacity.

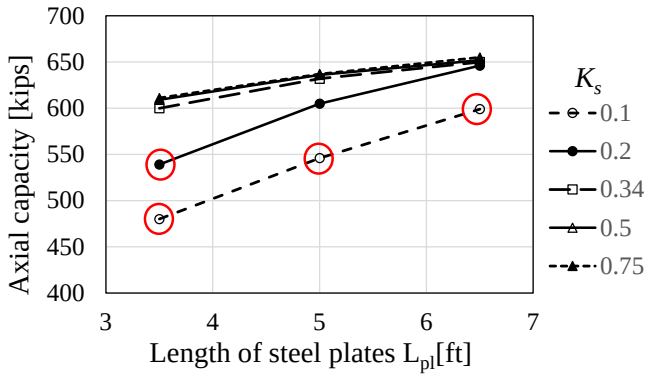

Figure 6.10 Axial peak loads of repaired piles with different lengths of plates

Results of the parametric study demonstrated that the optimized design of the friction-type bolted plates repair system is when the sum of the remaining capacity of a corroded pile, and the obtained friction between the pile flanges and the plates of repair system, equals to the nominal design capacity of the un-corroded pile. In this case, the failure is transferred from the corroded region to the un-corroded region beyond the repair system. Extra slip resistance, bolt pretension, or length of steel plates would not result in significant increment of pile capacity.

6.5 Conclusions

A numerical analysis was conducted to evaluate the effects of three factors on the axial capacity of repaired H-piles: the magnitude of coefficient of friction between steel repair plates and pile flanges, applied bolt pretension, and the length of steel repair plates. A 3D nonlinear finite element model developed for corroded H-piles repaired by friction-type bolted steel plates, was validated by full-scale experimental results presented in Chapter 5, and used for the parametric study in this chapter. The main findings and observations are summarized as follows:

1) Increment of slip resistance and bolt pretension can enhance the axial capacity of a retrofitted pile if the failure occurs at the corroded region. In contrast, if the repair system provides adequate friction to protect the corroded region and transfers the failure to the un-corroded portion of the pile, increment of the slip resistance or bolt pretension would not enhance the axial capacity of the retrofitted pile.

2) For pile fails by local buckling within the corroded region, increasing the length of steel plates can improve its capacity due to greater friction resulted from more bolts. However, if the pile fails by flexural buckling or local buckling outside the repaired region, increment of length of plates has minor effect on enhancement of the pile capacity.

3) The optimized design of the friction-type bolted plate-based repair system is when the sum of the remaining capacity of the corroded pile and the load transferred to the repair system through friction equals to the nominal capacity of the un-corroded pile.

4) The obtained friction force in full-scale tests was lower than the expected value calculated by the slip-critical connection formula specified in AASHTO (2012). The possible reasons include (1) the larger contact area increases the likelihood of defects in the coating that would potentially reduce the coefficient of friction, (2) the increased number of bolts increases the likelihood that some of the bolts may not be fully tightened due to the statistical variability of the bolt tightness, (3) the edge of the strengthening plate being in contact with the edge of the clamping plate would cause some of the bolt pretension force to be transferred through that interface rather than at the interface between the strengthening plate and the pile, and (4) localized out-of-straightness of the flanges may influence the frictional force that can be achieved at the interface.

CHAPTER 7 SUMMARY, CONCLUSIONS, LIMITATIONS AND RECOMMENDATIONS FOR FUTURE WORK

This dissertation presents experimental and numerical research studies on H-shaped bridge piles with localized corrosion that are rehabilitated using a friction-type bolted steel plate repair system. Chapter 1 illustrates the general condition of existing steel piles and states the necessity and importance of evaluation and rehabilitation of corroded piles. Chapter 2 summarizes the state-of-the-art and the state-of-practice in this field. Chapter 3 and Chapter 4 present the details of experimental and numerical studies on corroded H-piles. Chapter 5 and Chapter 6 present the experimental and numerical studies on corroded H-piles retrofitted using a steel-based repair system. The findings and overall observations of this research and recommendations for future work are presented in the following two sections.

7.1 Summary and Conclusions

The work presented in this dissertation has two major research objectives related to bridge piles with severe but localized corrosion: (1) development of a numerical framework to predict the axial capacity of the corroded piles, and (2) development and evaluation of a friction-type bolted steel plate-based retrofit system to be used for the repair of deteriorated piles.

To accomplish the first research objective, experimental and numerical studies of the remaining compressive capacity of corroded H-piles were carried out. Seven 15-ft-long HP12×53 corroded piles were tested under uniaxial load. A finite element model was developed and validated using the experimental results of small-scale H-piles (Karagah et al., 2015) and full-scale piles from this study. A parametric study was carried out using the model to investigate the influence of slenderness of the corroded flange and web, slenderness of the pile, location and extent of the corroded region, and the magnitude of residual stresses.

To achieve the second objective of this study, a friction-type bolted plate-based repair system was proposed based on the findings of investigation of corroded piles. The evaluation of

the retrofitted piles consisted of both experimental and numerical programs. Seven piles with the same configurations as the corroded control group were repaired and tested under compression. A finite element analysis was conducted to study the factors that influence the efficiency of the repair system, including the length of the steel plates, the magnitude of bolt pretension, and slip resistance. The research led to the following conclusions:

1) The developed numerical framework provided accurate predictions of the remaining capacities and failure modes of corroded piles. The differences between FEA predictions and test results are no more than 19 kips and 41 kips for small-scale and full-scale specimens, respectively, which are 8.8% and 6.6% of the capacity of the un-corroded piles.
2) Flange thickness reduction is the most critical parameter affecting the remaining axial capacity of an H-pile with localized corrosion. This is because the flanges contribute more to the weak-axis moment of inertia of the section. Additionally, the web can sustain a more severe degree of corrosion than the flange before becoming slender and being susceptible to local buckling. This is because the web is a stiffened element while the flange is an unstiffened element. . Therefore, stabilizing the flanges of a corroded pile is the primary function of the repair system.
3) Pile slenderness has only substantial effects on the axial capacity of piles without slender elements that fail by flexural buckling. Reducing the effective length of a pile by bracing it will not be beneficial to increasing its capacity if the pile has corrosion so severe that the deteriorated flanges and web become slender.
4) The magnitude of residual stresses and the extent of corrosion along the length of the pile are secondary factors affecting the axial capacity of the pile. The magnitude of residual stresses affects the axial capacity of corroded piles that fail by flexural buckling. But, a threefold increase in the magnitude of the residual stresses resulted in only a 15% reduction of the capacity. In contrast, varying the magnitude of residual stresses does not have noticeable influence on piles with slender element that fail by local buckling. Therefore, even without

the measurements of residual stresses, which are difficult to obtain from bridge piles in use, prediction by FEA of their capacities is reliable. The extent of the corroded region has noticeable effects only on piles that fail by local plate buckling in the corroded region. Increasing the extent of corrosion can decrease the axial capacity by up to 41% and 33% in the extreme cases that were considered for W4×13 and HP12×53 section piles, respectively, due to the reduction of plate buckling capacity of a larger aspect ratio element.

5) The location of the corroded region does not have much effect on pile capacity regardless of the type of failure mode.

6) The proposed friction-type bolted plate-based repair system can effectively restore the capacity of a corroded pile to its nominal design capacity. For retrofitted piles that fail by local buckling within the corroded region, the increase of the capacity is directly proportional to the increase of the slip resistance (or coefficient of friction) and the bolt pretension level. Increasing the length of the steel plates also enhances the capacity since more friction force can be developed across the interface by increasing the number of bolts used to clamp the repair plates to the deteriorated pile. For retrofitted piles that fail by flexural buckling or local buckling at the un-corroded region beyond the repair system, the capacity is governed by the original strength of the un-corroded pile rather than the configuration of the repair system. Therefore, increasing the slip resistance or bolt pretension beyond the level that is required to force the failure into the un-corroded portion of the pile does not provide any additional capacity to the system. In this case, though the capacity can be enhanced by increasing the length of the steel plates due to the increased contribution of the plates to the lateral stiffness of the pile. However, the effect is nominal since doubling the plate length only increases the capacity by 7%.

7) The repair system can increase the axial stiffness of the corroded piles. This may be beneficial to the serviceability control of the piles, to prevent excessive deformation or differential settlement.

8) The piles with extremely thin flanges and webs as Pile 80/60-S(1), Pile 80/60-S(2), and Pile 80/60/3-S, showed a crumpling deformation at the corroded region. The deformation indicated that the flanges were too slender to stiffen the web at the junction; meanwhile, the destabilization of the web caused the excessive axial deformation of the flanges.

9) The coatings applied on the steel plates of the repair system can provide the required friction resistance. However, numerical analysis suggests that the slip resistance achieved at the interface between the repair plates and the deteriorated pile is nearly 12% lower than the values obtained from small-scale double-lap tension coupon tests. This is attributed to the increased contact area of the piles which increases the probability of the existence of a flaw in the coating and also the increased number of bolts which increases the probability that some of the bolts may not be fully tightened to the target prestress level.

10) The non-zinc containing, class B-rated, polyamide epoxy coating that was used in this system was brittle and locally cracked and peeled off of the repair plates during testing. Although the damage of the coatings did not appear to have any negative effects on the axial capacity, it may affect the durability of the repair system.

11) Bevel washers are essential to be used in the proposed repair system, to prevent bolts from bending and rupture during tightening or during service of the piles.

7.2 Research Limitations

Despite of the findings summarized in the previous section, there were several limitations in this study. They were illustrated in the discussions of the experimental and numerical studies in Chapter 3 to Chapter 6, and are summarized as follows.

1) In the numerical framework for prediction of corroded piles developed in this study, the initial imperfections were not measured values of the tested piles. The effect of the magnitude of initial imperfections was only considered in a relatively small range, which were within the fabrication tolerances.

2) When modeling the corroded piles, the distribution of residual stresses was assumed and considered as the Leigh pattern only. However, the distribution may follow other patterns. Also, the corroded region may have different pattern of residual stresses from the un-corroded region due to the stress relaxation. These effects were not studied in this research.

3) The proposed repair system was designed and tested on piles with no initial axial loads. However, in practical usage, the piles under a bridge have already taken some level of axial load. In this situation, the compression behavior of the repaired piles may be different from the studied piles.

7.3 Recommendations of Future Work

The research presented in this dissertation was one component of a broader project to develop repair systems for corroded steel bridge piles. The investigation of the other repair method, FRP-based repair system, was presented in another dissertation (Karagah, 2015). The environmental durability tests are underway by a research group at Texas Tech University (TTU). While the findings of the project benefit the assessment and rehabilitation of steel bridge H-piles with localized corrosion, additional work is recommended for future research. This includes but is not limited to the following items:

1) Development of design equations to calculate the remaining capacity of corroded H-piles. The developed numerical framework provided sufficiently accurate predictions of the axial capacity of corroded H-piles. However, it is impractical for engineers to build sophisticated numerical models and run time-consuming analyses for every case. Simplified design equations or curves that can be used to calculate the capacity are preferred for practical use. They may be derived from extensive predictions from FEA.
2) Evaluation of alternative coatings to be applied on the steel plates. As stated in the findings, the second layer of coating exhibited brittle behavior during testing, which may result in durability defects of the pile. Therefore, other types of coatings should be evaluated to obtain

alternatives that are durable, and can provide corrosion resistance and the required slip resistance.

3) Evaluation of the performance of the retrofitted piles under different loading conditions including eccentric axial loads (or combined axial and lateral loads) and dynamic loads (such as in seismic events).

4) The repaired piles in the experimental program were retrofitted in the situation with no axial load. However, piles in field are under certain load before rehabilitation. The design of the repair system for loaded piles needs further investigation.

5) The effect of other patterns of the residual stresses. This research assumed one pattern of residual stresses, however, other patterns of residual stresses have not been studied. Moreover, the distribution and magnitude of residual stresses might change during corrosion, and the influence needs further evaluation.

REFERENCES

AASHTO (2012). Bridge Design Specifications (LRFD), Washington, DC, MD, Section 6, 77-93.

AISC (2011). American Institute of Steel Construction, Manual of Steel Construction, Chicago, IL, 16.1-22-298.

AISI (2007). North American Specification for Design of Cold-formed Steel Structure Members, Washington, D.C., MD, Appendix 1, 3-8, 57-62.

ASTM (2014). Standard Test Methods and Definitions for Mechanical Testing of Steel Products, Washington, D.C., MD, 10-19.

ASCE 10-97 (1997). Design of Latticed Steel Transmission Structures. *American Society of Civil Engineers*, New York, NY, 3-9.

ASCE. (2013). Report Card for America's Infrastructure. *American Society of Civil Engineers*, New York, NY, 35-37.

Appuhamy, J., Ohga, M., Chun, P., and Dissanayake, P. (2013). Numerical Investigation of Residual Strength and Energy Dissipation Capacities of Corroded Bridge Members under Earthquake Loading. *Journal of Earthquake Engineering*, 17(2), 171-186.

Appuhamy, J., Ohga, M., Kaita, T., Fujii, K., and Dissanayake, P. (2011). Development of Analytical Method for Predicting Residual Mechanical Properties of Corroded Steel Plates. *International Journal of Corrosion*, 1-10.

Avery, P. and Mahendran, M. (2000). Distributed Plasticity Analysis of Steel Frame Structures Comprising Non-Compact Section. *Engineering Structures*, 22, 901-919.

Beaulieu, L.V., Legeron, F., and Langlois, S. (2010). Compression Strength of Corroded Steel Angle Members. *Journal of Constructional Steel Research*, 66, 1366-1373.

Bisagni, C. (2000). Numerical Analysis and Experimental Correlation of Composite Shell Buckling and Post-Buckling. *Composites Part B: Engineering*, 31(8), 655-667.

Chan, T.M. and Gardner, L. (2008). Compressive Resistance of Hot-Rolled Elliptical Hollow Sections. *Engineering Structures*, 30, 522-532.

Chen, Y., Cheng, X., and Nethercot, D. (2013). An Overview Study on Cross Section Classification of Steel H-Sections. *Journal of Constructional Steel Research*, 80, 386-393.

Cinitha, A., Umesha, P.K., Iyer, R. (2014). An Overview of Corrosion and Experimental Studies on Corroded Mild Steel Compression Members. *KSCE Journal of Civil Engineering*, 18(6), 1735-1744.

Davisson, M. T., and Robinson, K. E. (1965). Bending and Buckling of Partially Embedded Piles. *Proceedings of the 6th International Conference on Soil Mechanics and Foundation Engineering*, Montreal, CANADA, 243-246.

Dinis, P.B., Camotim, D., Silvestre, N. (2007). FEM-Based Analysis of the Local-Plate/Distortional Mode Interaction in Cold-Formed Steel Lipped Channel Columns. *Computers and Structures*, 85, 1461-1474.

Dinis, P.B. and Camotim, D. (2011). Post-Buckling Behavior and Strength of Cold-Formed Steel Lipped Channel Columns Experiencing Distortional/Global Interaction. *Computers and Structures*, 89, 422-434.

Ellobody, E. (2007). Buckling Analysis of High Strength Stainless Steel Stiffened and Unstiffened Slender Hollow Section Columns. *Journal of Constructional Steel Research*, 63, 145-155.

Flanagan, D. P., and Belytschko, T. (1981). A Uniform Strain Hexahedron and Quadrilateral with Orthogonal Hourglass Control. *International Journal for Numerical Methods in Engineering*, 17(5), 679-706.

Gardner, L. and Nethercot, D.A. (2004). Numerical Modeling of Stainless Steel Structural Components- A Consistent Approach. *Journal of Structural Engineering*, 130, 1586-1601.

Huang, Y., Zhang, Y., Liu, G., and Zhang, Q. (2010). Ultimate Strength Assessment of Hull Structural Plate with Pitting Corrosion Damnification under Biaxial Compression. *Ocean Engineering*, 37(17-18), 1503-1512.

Jiang, X., & Soares, C. (2012a). Ultimate Capacity of Rectangular Plates with Partial Depth Pits under Uniaxial Loads. *Marine Structures*, 26(1), 27-41.

Jiang, X., & Soares, C. (2012b). A Closed Form Formula to Predict the Ultimate Capacity of Pitted Mild Steel Plate under Biaxial Compression. *Thin-Walled Structures*, 59, 27-34.

Karagah, H., Shi, C., Dawood, M., and Belarbi, A. (2015). Experimental Investigation of Short Steel Columns with Localized Corrosion. *Thin-Walled Structures*, 87, 191-199.

Khedmati, M.R., Roshanali, M.M., Nouri, Z.H.M.E. (2011). Strength of Steel Plates with Both-Sides Randomly Distributed with Corrosion Wastage under Uniaxial Compression. *Thin-Walled Structures*, 49, 325-342.

Liu, X.D., Nanni, A., and Silva. P. F. (2005). Rehabilitation of Compression Steel Members osing FRP Pipes Filled with Non-Expansive and Expansive Light-Weight Concrete. *Advances in Structure Engineering*, 8(2), 129-142.

Lundquist, E. E. & Stowell, E. Z. (1942). Critical Compressive Stress for Outstanding Flanges. *Report No. 734*, NACA.

Mateus, A.F.., & Witz, J.A. (1998). On the Post-Buckling of Corroded Steel Plates Used in Marine Structures. *RINA Transactions*, 140, 165-183.

Mindlin, R.D. (1951). Influence of Rotatory Inertia and Shear on Flexural Motions of Isotropic Elastic Plates. *ASME Journal of Applied Mechanics*, 18, 31–38.

Moen, C., & Schafer, B. (2008). Experiments on Cold-Formed Steel Columns with Holes. *Thin-Walled Structures*, 46(10), 1164-1182.

Moen, C., & Schafer, B. (2011). Direct Strength Method for Design of Cold-Formed Steel Columns with Holes. *Journal of Structural Engineering*, 137(5), 559-570.

NACE. (2013). Highways and Bridges. *Corrosion Central*. Retrieved from https://www.nace.org/Corrosion-Central/Industries/Highways-and-Bridges/

Nakai, T., Matsushita, H., Yamamoto, N., Arai, H. (2004). Effect of Pitting Corrosion on Local Strength of Hold Frames of Bulk Carriers. *Marine Structures*, 17, 403-432.

Ok, D., Pu, Y., Incecik, A. (2007). Computation of Ultimate Strength of Locally Corroded Unstiffened Plates under Uniaxial Compression. *Marine Structures*, 20, 100-114.

Oszvald, K., Dunai, L. (2012). Effect of Corrosion on the Buckling of Steel Angle Members-Experimental Study. *Civil Engineering*, 56, 175-183.

Oszvald, K., Dunai, L. (2013). Behavior of Corroded Steel Angle Compression Members-Numerical Study. *Civil Engineering*, 57, 63-75.

Paik, J.K., Lee, J.M., and Ko, M.J. (2003). Ultimate Compressive Strength of Plate Elements with Pit Corrosion Wastage. *Proceeding of the Institution of Mechanical Engineers, Part M: Journal of Engineering for the Maritime Environment*, 217, 185-200.

Paik, J.K., Lee, J.M., and Lee, D.H. (2003). Ultimate Strength of Dented Steel Plates under Compressive Loads. *International Journal of Mechanical Sciences*, 45, 433-448.

Paik, J.K., Lee, J.M., and Ko, M.J. (2004). Ultimate Shear Strength of Plate Elements with Pit Corrosion Wastage. *Thin-Walled Structures*, 42, 1161-1176.

Paik, J.K. (2007). Ultimate Strength of Perforated Steel Plates under Edge Shear Loading. *Thin-Walled Structures*, 46, 207-213.

Paik, J.K. (2008). Ultimate Strength of Perforated Steel Plates under Combined Biaxial Compression and Edge Shear Loads. *Thin-Walled Structures*, 45, 301-306.

Pu, Y., Godley, M.H.R., Beale R.G., and Lau, H.H. (1999). Prediction of Ultimate Capacity of Perforated Lipped Channels. *Journal of Structural Engineering*, 125(5), 510-514.

Rahgozar, R. (2009). Remaining Capacity Assessment of Corrosion Damaged Beams Using Minimum Curves. *Journal of Constructional Steel Research*, 65, 299-307.

Ranji, A.R. (2012). Ultimate Strength of Corroded Steel Plates with Irregular Surfaces under In-Plane Compression. *Ocean Engineering*, 54, 261-269.

Rhodes, J. and Schneider, F.D. (1994). The Compression Behavior of Perforated Elements. *Twelfth International Specialty Conference on Cold-Formed Steel Structures*, St. Louis, MO, 11-28.

Rhodes, J. and Macdonald, M. (1996). The Effects of Perforation Length on the Behavior of Perforated Elements in Compression. Thirteenth *International Specialty Conference on Cold-Formed Steel Structures,* St. Louis, MO, 91-101.

Riks, E. (1979). An Incremental Approach to the Solution of Snapping and Buckling Problems. *International Journal of Solids and Structures*, 15(7), 529-551.

Saad-Eldeen, S., Garbatov, Y., and Soares, C. G. (2011). Experimental Assessment of the Ultimate Strength of a Box Girder Subjected to Severe Corrosion. *Marine Structures*, 24(4), 338-57.

Saad-Eldeen, S., Garbatov, Y., and Soares, C. G. (2013). Ultimate Strength Assessment of Corroded Box Girders. *Ocean Engineering*, 58, 35-47.

Saad-Eldeen, S., Garbatov, Y., and Soares, C. (2014). Strength Assessment of a Severely Corroded Box Girder Subjected to Bending Moment. *Constructional Steel Research*, 92(1), 90-102.

Sadovsky, Z. and Drdacky, M. (2001). Buckling of Plate Strip Subjected to Localized Corrosion-a Stochastic Model. *Thin-Walled Structures*, 39, 247-259.

Sarawit, A.T., Kim, Y., Bakker, M.C.M., and Pekoz, T. (2003). The Finite Element Method for Thin-Walled Members- Applications. *Thin-Walled Structures*, 41, 191-206.

Schafer, B. W. (2002). Local Distortional and Euler Buckling of Thin-Walled Columns. *Journal of Structural Engineering.* 128(3), 289-99.

Schafer, B.W. (2008). Review: the Direct Strength Method of Cold-Formed Steel Member Design. *Journal of Constructional Steel Research*, 64, 766-778.

Seif, M.,and Schafer, B. (2009). Finite Element Comparison of Design Methods for Locally Slender Steel Beams and Columns. *Proceedings of the Structural Stability Research Council's Annual Stability Conference*, Phoenix, AZ, 69-90.

Seif, M., and Schafer, B. W. (2010). Local Buckling of Structural Steel Shapes. *Journal of Constructional Steel Research*, 66(10), 1232-1247.

Seif, M., and Schafer, B. W. (2010). Design Methods for Local-Global Interaction of Locally Slender Steel Members. *Annual Stability Conference Proceedings*, Orlando, FL, 553-572.

Seif, M., and Schafer, B. (2011). Towards a Strain Energy Based Strength Prediction for Locally Slender Steel Columns. *Annual Stability Conference Proceedings*, Pittsburgh, PA, 344-57.

Seif, M., and Schafer, B. (2013). Design of Locally Slender Structural Steel Columns. *Journal of Structural Engineering*, 140(4), 04013086.

Shi, C., Karagah, H., Dawood, M., and Belarbi, A. (2014). Numerical Investigation of H-shaped Short Steel Piles with Localized Severe Corrosion. *Engineering Structures*, 73, 114-124.

Shi, C., Karagah, H., Belarbi, A., and Dawood, M. (2016). Inelastic Buckling Behavior of Steel H-Piles with Localized Severe Corrosion. *ASCE Journal of Bridge Engineering*. (Accepted).

SIMULIA Abaqus Analysis User Manual, Version 6.12, RI, 2012.

Smith, C.S., Davidson, P.C., Chapman, J.C., and Dowling, P.J. (1988). Strength and Stiffness of Ships' Plating under In-Plane Compression and Tension. *RINA Trans*, 130, 277-296.

Timoshenko, S.P., Gere, J.M. (2009). Theory of Elastic Stability (2nd edition). New York, Dover, 353. (Original work published 1961 by Mcgraw-Hill).

Vani, G., Jayabalan, P., Joseph, J. (2013). Numerical Analysis of Cold Formed Steel Plain Angle Compression Members. *International Journal of Emerging Technology and Advanced Engineering*, 3, 22-29.

Verma, K. and Garg, H.K. (2012). Underwater Welding- Recent Trends and Future Scope. *International Journal on Emerging Technologies*, 3(2), 115-120.

Vishay. (2011). System 7000 Instruction Manual Version 1.10. Raleigh, NC.

Yan, J., Young, B. (2002). Column Tests of Cold-Formed Steel Channels with Complex Stiffeners. *Journal of Structural Engineering*, 128(6), 737-745.

Yan, J., Young, B. (2004). Numerical Investigation of Channel Columns with Complex Stiffeners-Part I: Test Verification. *Thin-Walled Structure*, 42(6), 883-893.

Zhu, J. and Young, B. (2006). Aluminum Alloy Tubular Columns-Part I: Finite Element Modeling and Test Verification. *Thin-Walled Structures*, 44(9), 961-968.

Zhu, J. and Young, B. (2010). Cold-Formed-Steel Oval Hollow Sections under Axial Compression. *Journal of Structural Engineering*, 137, 719-727.

Zhu, J. and Young, B. (2012). Design of Cold-Formed Steel Oval Hollow Section Columns. *Journal of Constructional Steel Research*, 71, 26-37.

Ziemian, R.D. (2010). Guide to Stability Design Criteria for Metal Structures, 6th Ed., Wiley, New York, 993-1001.

APPENDIX A Test Data of Corroded Control Piles

The detailed experimental results of the steel H-piles with localized corrosion are presented in this appendix. The test data include axial load measured by load cells, axial deformations measured by four string potentiometers, and axial load calculated using measured pressure from pressure transducer. The sequence of the presented data follows the order of the results presented in Chapter 3. The configuration of each pile as presented in Chapter 3 is repeated in Table A.1. Figure A.1 through Figure A.3 show the components of test frame and the locations of instrumentations. The symbols used in the following plots are summarized as follows:

LC: load cell;
PT: pressure transducer;
NT: string potentiometer mounted on North Top side of the specimen;
NB: string potentiometer mounted on North Bottom side of the specimen;
ST: string potentiometer mounted on South Top side of the specimen;
SB: string potentiometer mounted on South Bottom side of the specimen.

In Figure A.4 through Figure A.10, there are three graphs: (a) represents to the axial loads measured by three load cells versus time of testing; (b) represents the applied axial load versus the axial deformations measured by four string potentiometers; and (c) represents to the applied load measured by load cells and load calculated using measured pressure from pressure transducer versus time of testing.

Table A.1 Test matrix of corroded control piles

Pile designation	Extent of corrosion L_{cr} [ft]	Flange reduction [%]	Web reduction [%]
0/0	None	0	0
0/20	1	0	20
40/20	1	40	20
40/60	1	40	60
80/60	1	80	60
80/60/V	1	80	100
80/60/3	3	80	60

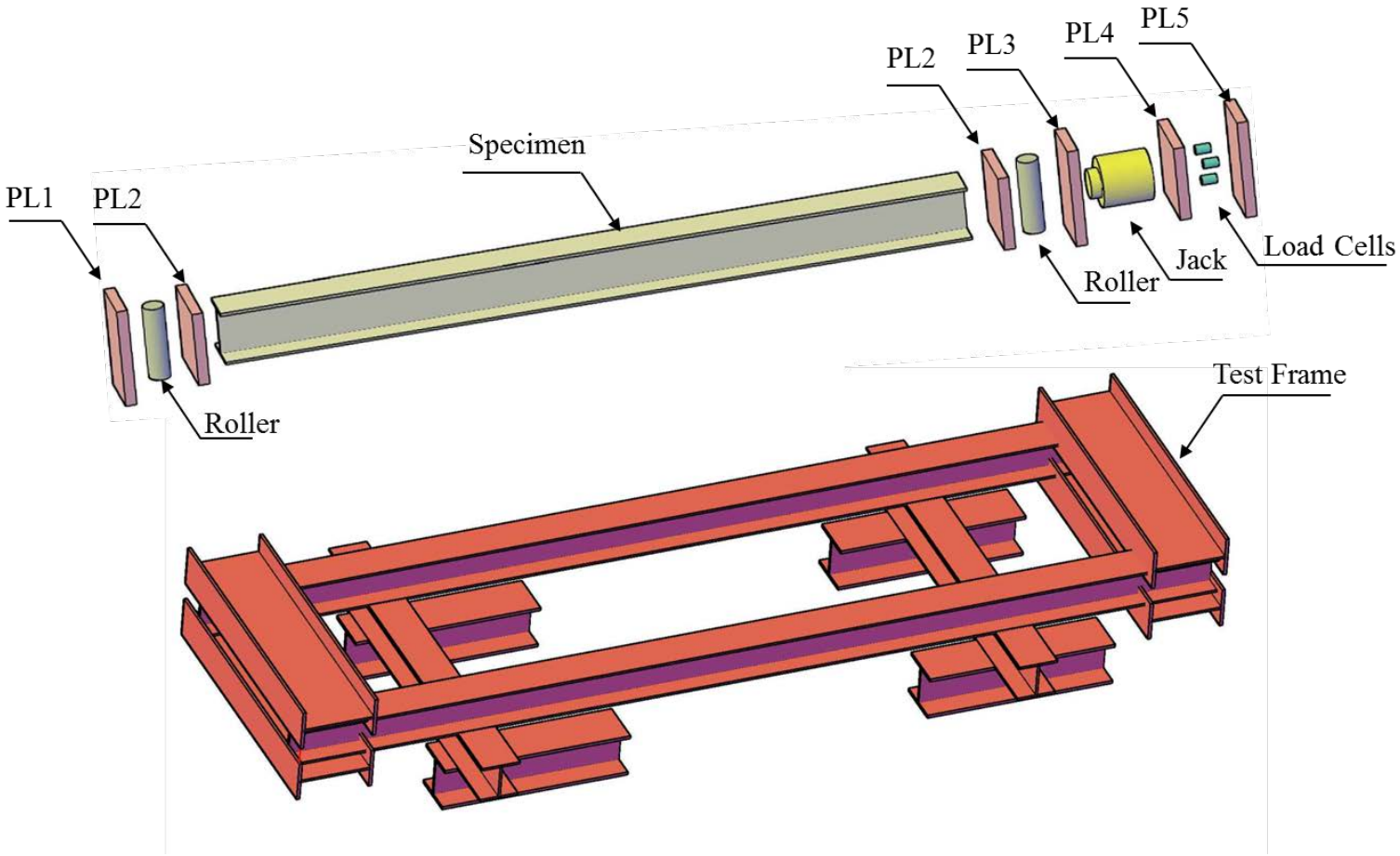

Figure A.1 3D various components of test frame and instrumentations

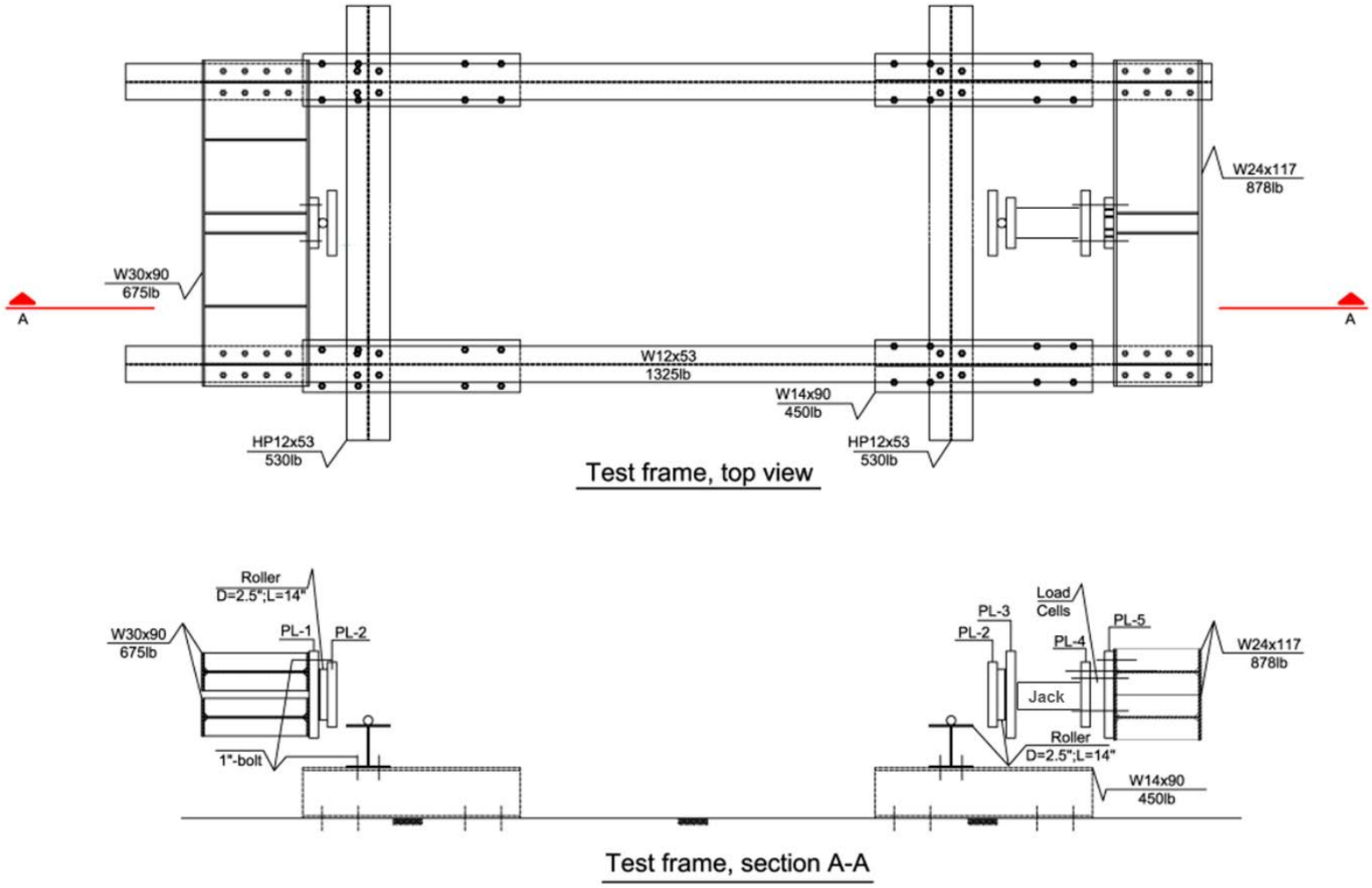

Figure A.2 2D drawings of test frame and locations of instrumentations

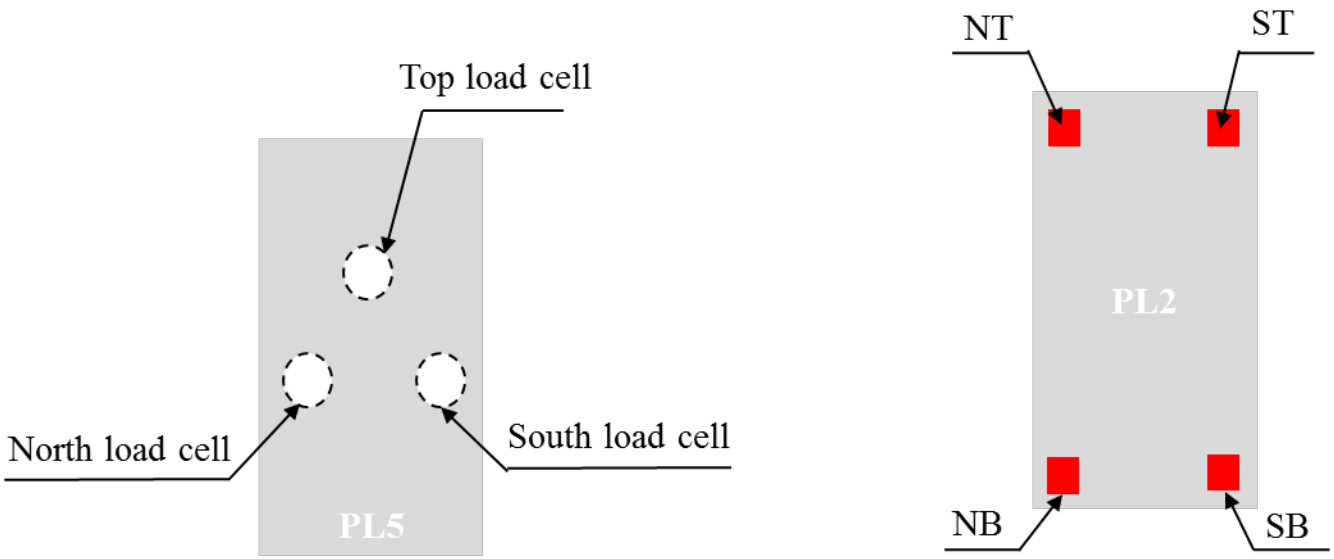

Figure A.3 Locations of three load cells and four string potentiometers

A.1 Pile 0/0

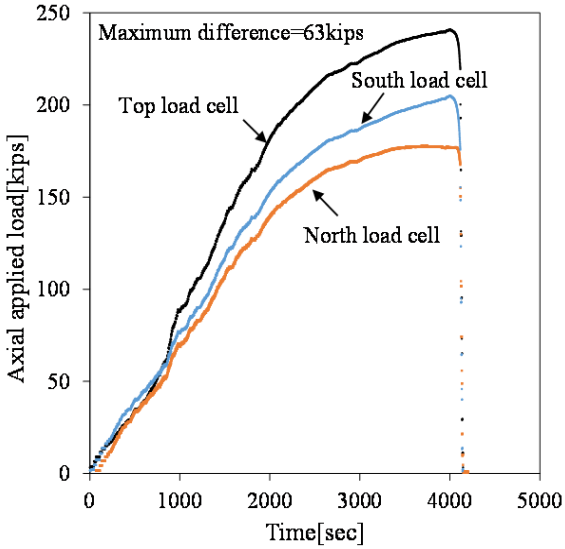

(a) Axial loads measured by three load cells versus time of testing

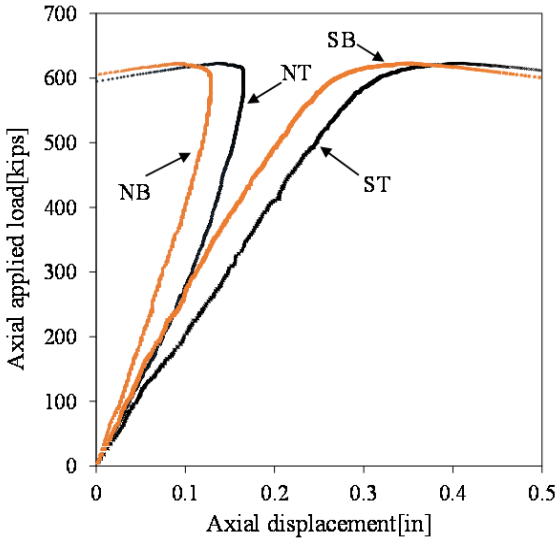

(b) Applied load versus axial deformations measured by four string potentiometers

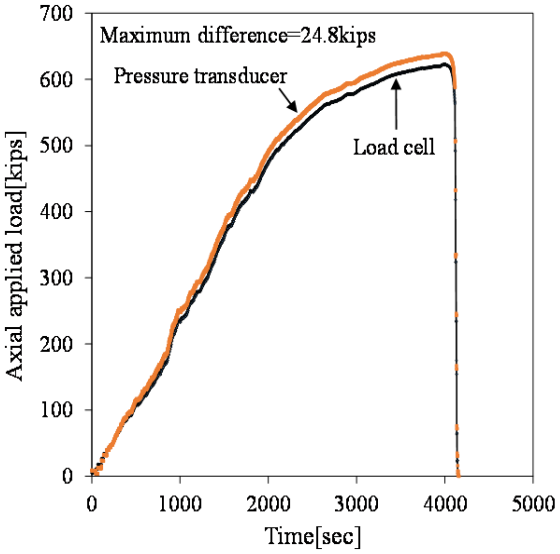

(c) Axial load measured by load cells and pressure transducer versus time of testing

Figure A.4 Test data of Pile 0/0

A.2 Pile 0/20

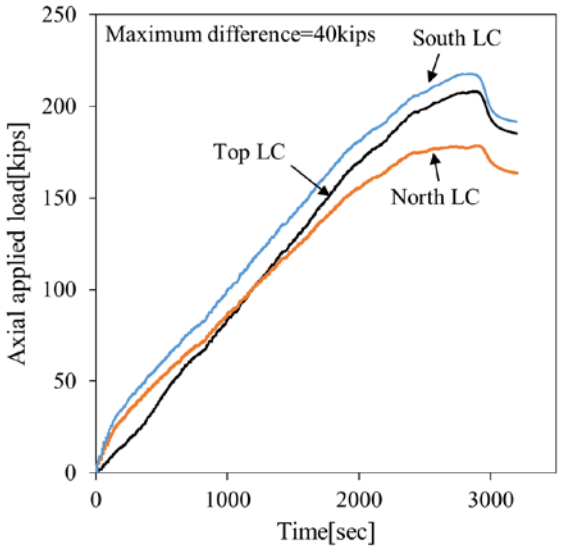

(a) Axial loads measured by three load cells versus time of testing

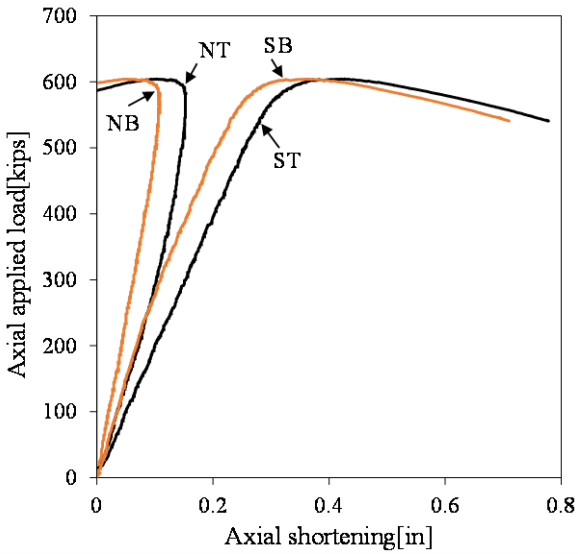

(b) Applied load versus axial deformations measured by four string potentiometers

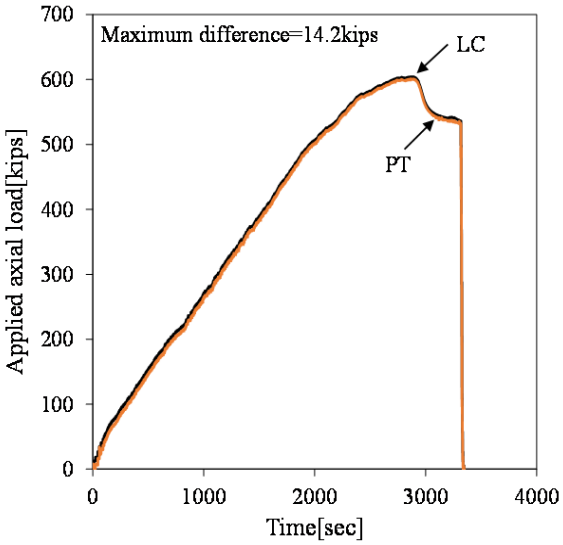

(c) Axial load measured by load cells and pressure transducer versus time of testing

Figure A.5 Test data of Pile 0/20

A.3 Pile 40/20

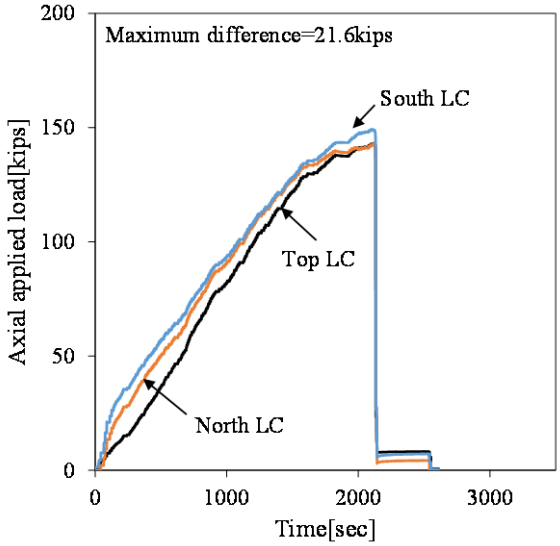

(a) Axial loads measured by three load cells versus time of testing

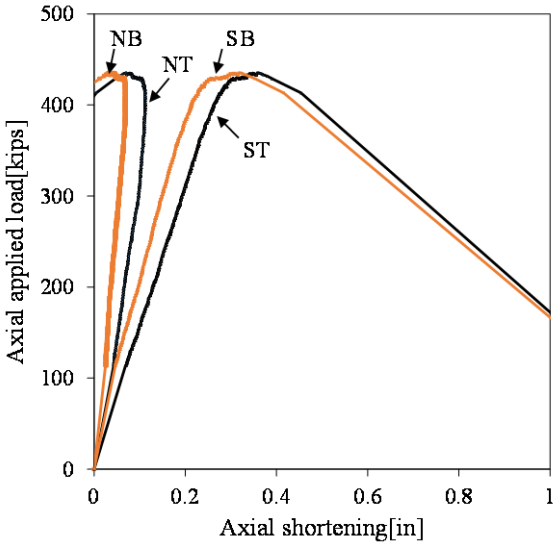

(b) Applied load versus axial deformations measured by four string potentiometers

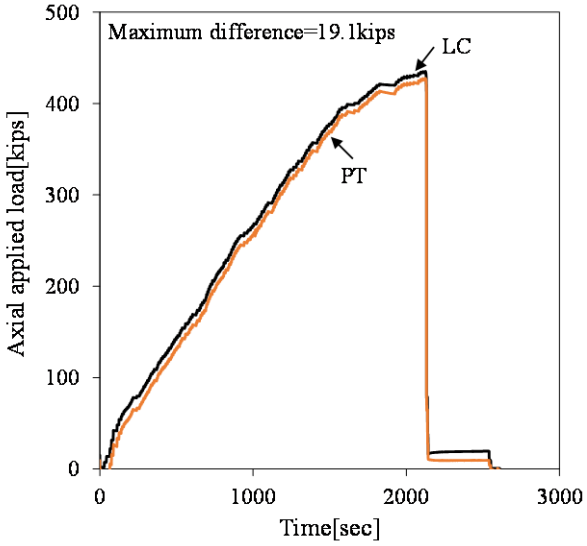

(c) Axial load measured by load cells and pressure transducer versus time of testing

Figure A.6 Test data of Pile 40/20

A.4 Pile 40/60

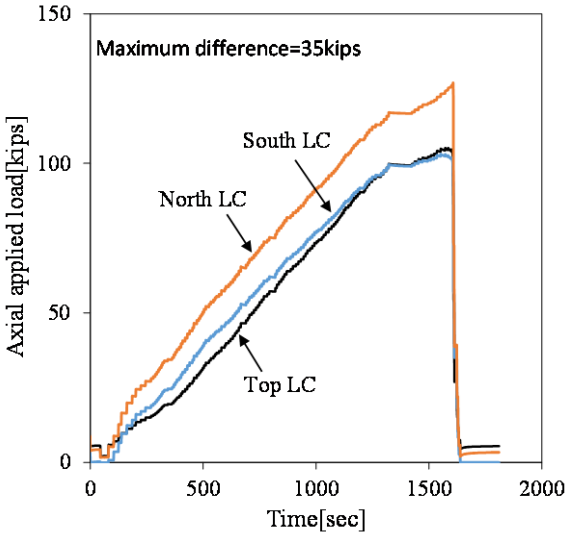

(a) Axial loads measured by three load cells versus time of testing

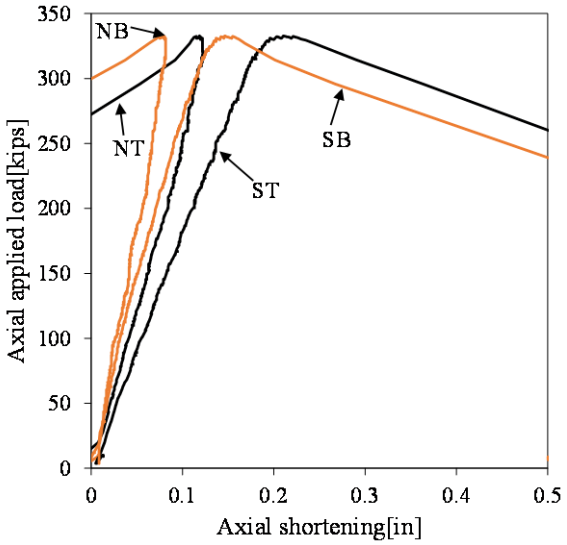

(b) Applied load versus axial deformations measured by four string potentiometers

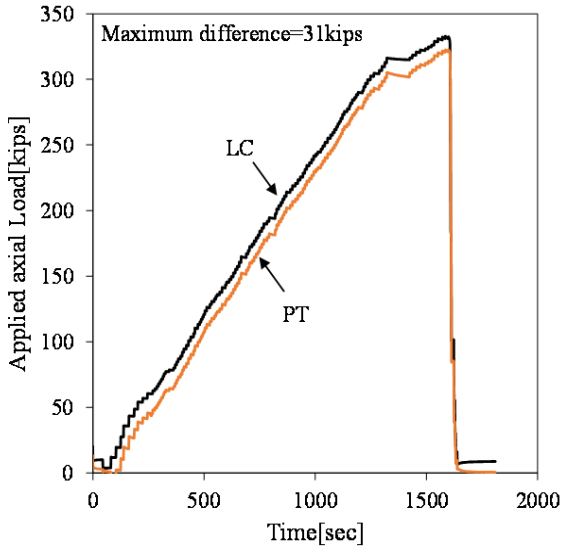

(c) Axial load measured by load cells and pressure transducer versus time of testing

Figure A.7 Test data of Pile 40/60

A.5 Pile 80/60

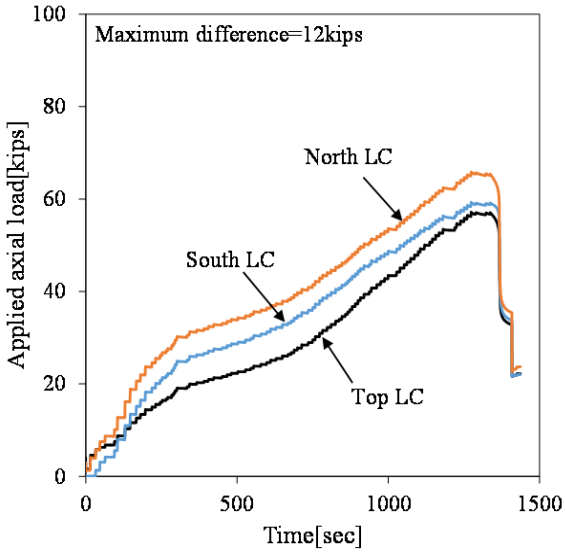

(a) Axial loads measured by three load cells versus time of testing

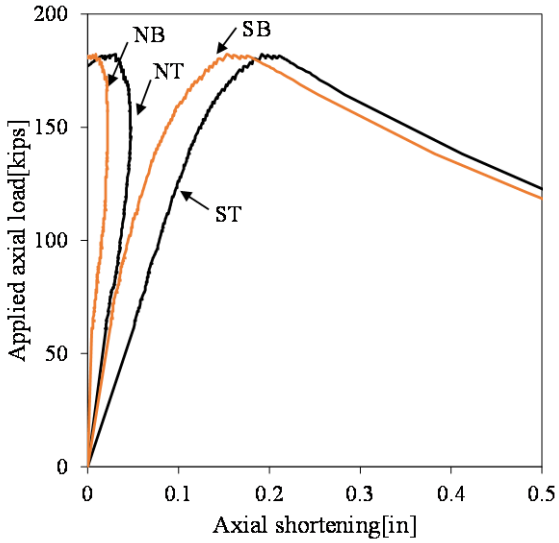

(b) Applied load versus axial deformations measured by four string potentiometers

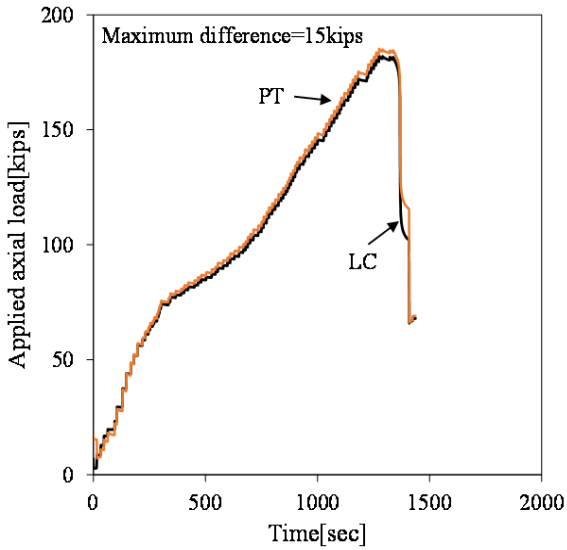

(c) Axial load measured by load cells and pressure transducer versus time of testing

Figure A.8 Test data of Pile 80/60

A.6 Pile 80/60/V

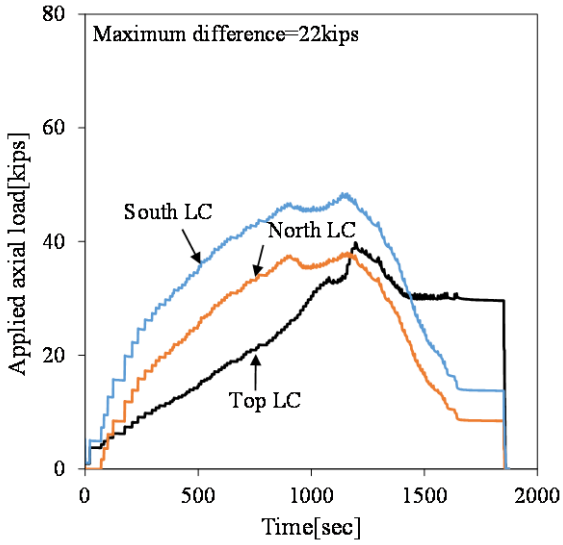

(a) Axial loads measured by three load cells versus time of testing

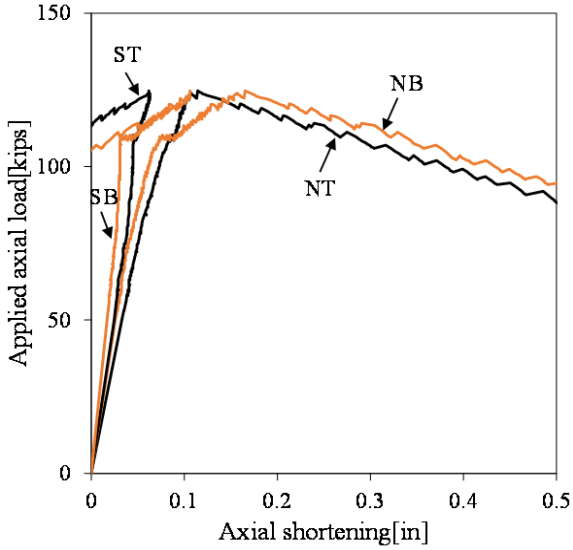

(b) Applied load versus axial deformations measured by four string potentiometers

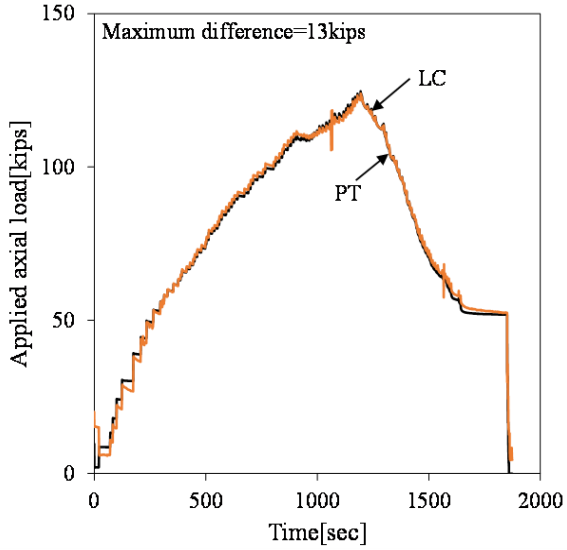

(c) Axial load measured by load cells and pressure transducer versus time of testing

Figure A.9 Test data of Pile 80/60/V

A.7 Pile 80/60/3

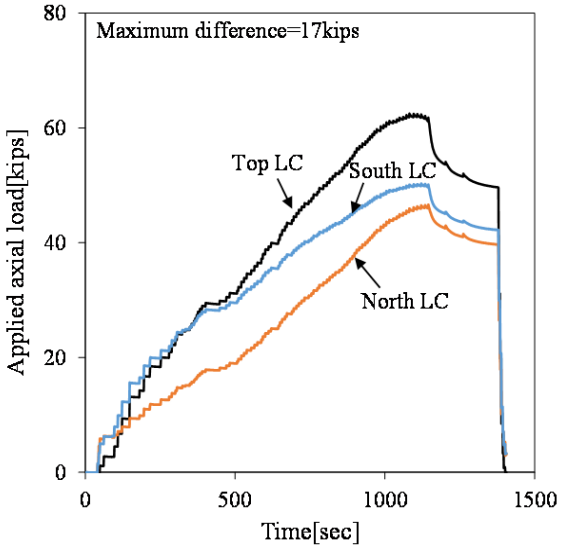

(a) Axial loads measured by three load cells versus time of testing

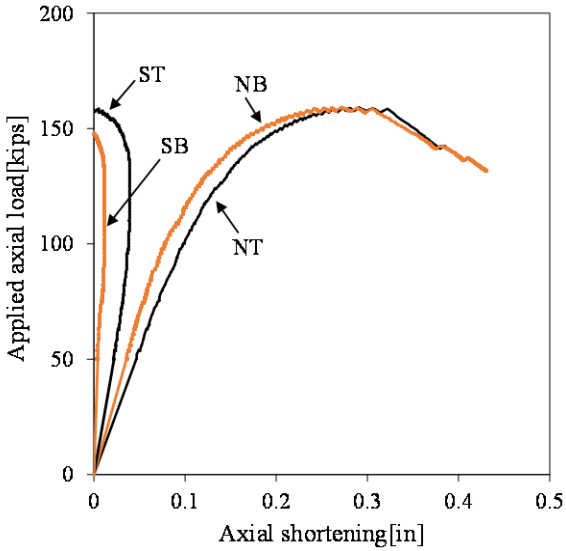

(b) Applied load versus axial deformations measured by four string potentiometers

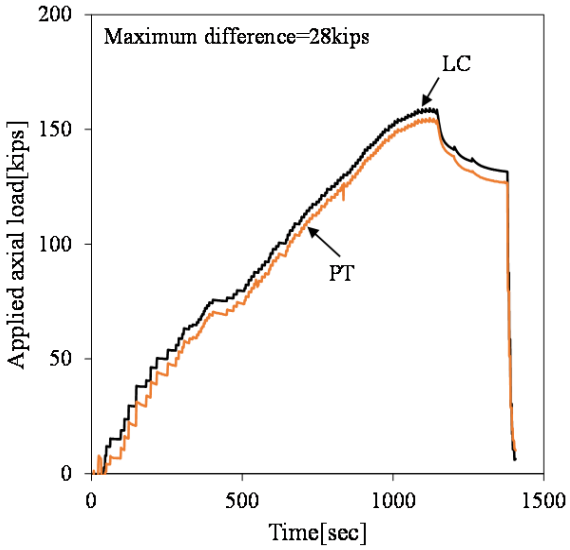

(c) Axial load measured by load cells and pressure transducer versus time of testing

Figure A.10 Test data of Pile 80/60/3

APPENDIX B Test Data of Retrofitted Piles

The detailed experimental results of the corroded H-piles repaired using friction-type bolted steel plate-based repair system are presented in this appendix. The test data include axial load measured by load cells, and axial deformations measured by four string potentiometers. The sequence of the presented data follows the order of the results presented in Chapter 5. The configuration of each pile as presented in Chapter 5 is repeated in Table B.1. The symbols used in the following plots are summarized as follows:

The symbols used in the following plots are summarized as follows:

LC: load cell;

NT: string potentiometer mounted on North Top side of the specimen;

NB: string potentiometer mounted on North Bottom side of the specimen;

ST: string potentiometer mounted on South Top side of the specimen;

SB: string potentiometer mounted on South Bottom side of the specimen.

In Figure B.1 through Figure B.16, there are two graphs: (a) represents to the axial loads measured by three load cells versus time of testing; and (b) represents the applied axial load versus the axial deformations measured by four string potentiometers.

Table B.1 Test matrix of corroded control piles

Pile designation	Extent of corrosion L_{cr} [ft]	Flange reduction [%]	Web reduction [%]	Length of repair system [ft]	Number of bolts
0/20-S	None	0	0	2	28
40/20-S	1	0	20	2	28
40/60-S	1	40	20	3.5	52
80/60-S(1)	1	40	60	6.5	100
80/60-S(2)	1	80	60	6.5	100
80/60/V-S	1	80	100	7.5	116
80/60/3-S	3	80	60	7.5	116

B.1 Pile 0/20-S

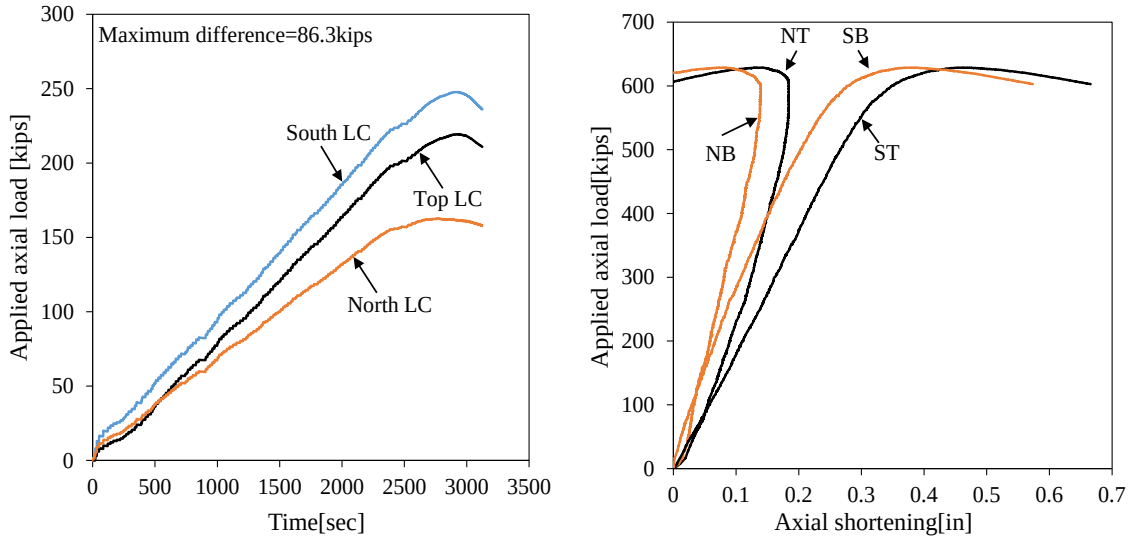

(a) Axial loads measured by three load cells versus time of testing

(b) Applied load versus axial deformations measured by four string potentiometers

Figure B.1 Test data of Pile 0/20-S

B.2 Pile 40/20-S

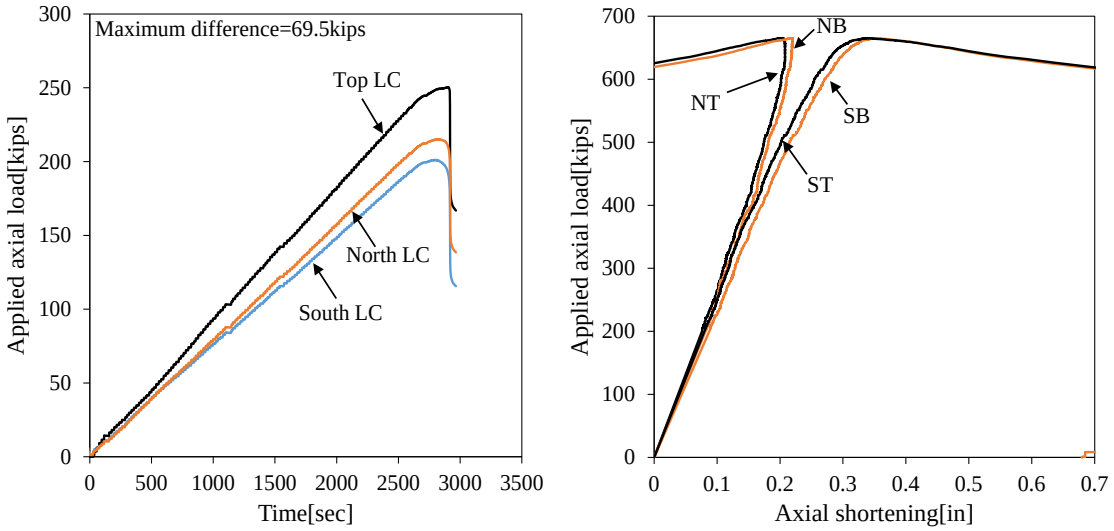

(a) Axial loads measured by three load cells versus time of testing

(b) Applied load versus axial deformations measured by four string potentiometers

Figure B.11 Test data of Pile 40/20-S

B.3 Pile 40/60-S

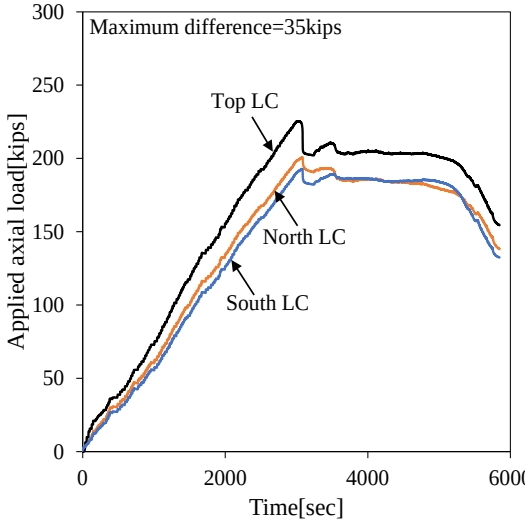

(a) Axial loads measured by three load cells versus time of testing

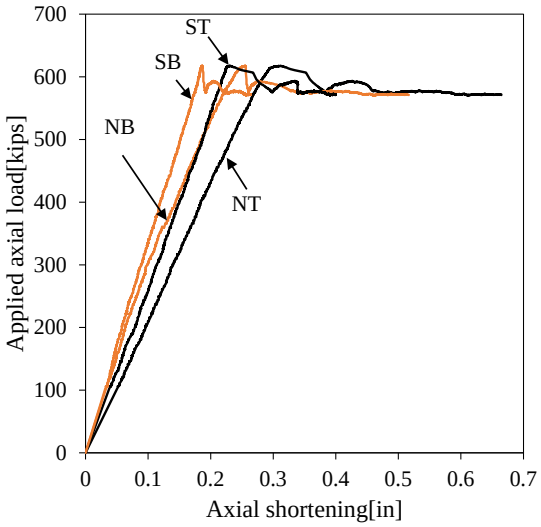

(b) Applied load versus axial deformations measured by four string potentiometers

Figure B.12 Test data of Pile 40/60-S

B.4 Pile 80/60-S(1)

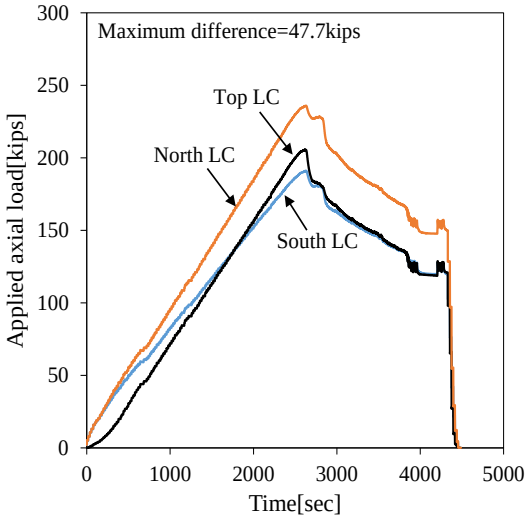

(a) Axial loads measured by three load cells versus time of testing

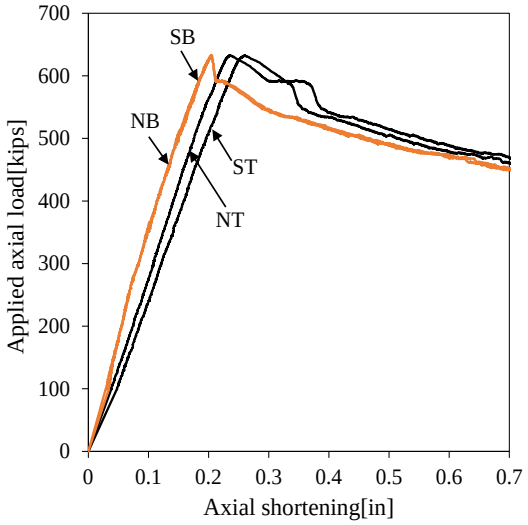

(b) Applied load versus axial deformations measured by four string potentiometers

Figure B.13 Test data of Pile 80/60-S(1)

B.5 Pile 80/60-S(2)

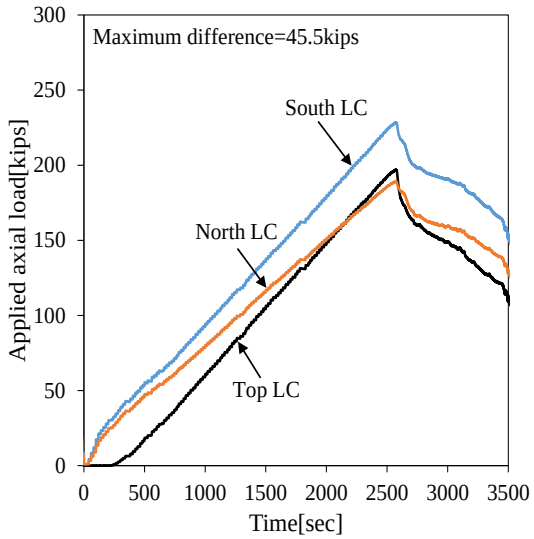

(a) Axial loads measured by three load cells versus time of testing

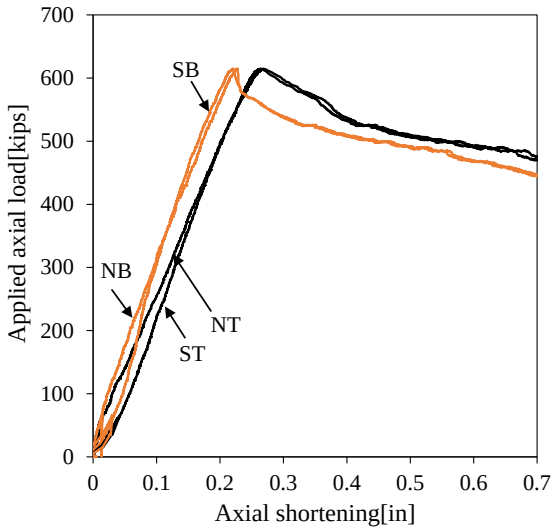

(b) Applied load versus axial deformations measured by four string potentiometers

Figure B.14 Test data of Pile 80/60-S(2)

B.6 Pile 80/60/V-S

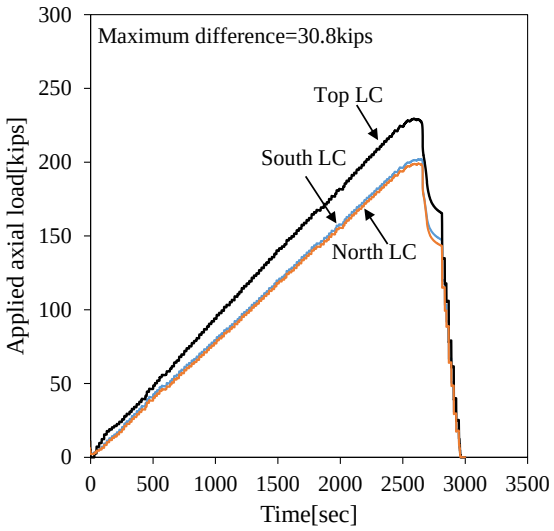

(a) Axial loads measured by three load cells versus time of testing

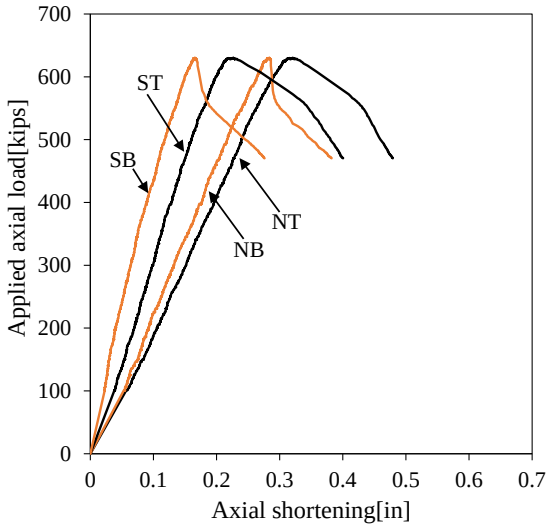

(b) Applied load versus axial deformations measured by four string potentiometers

Figure B.15 Test data of Pile 80/60/V-S

B.7 Pile 80/60/3-S

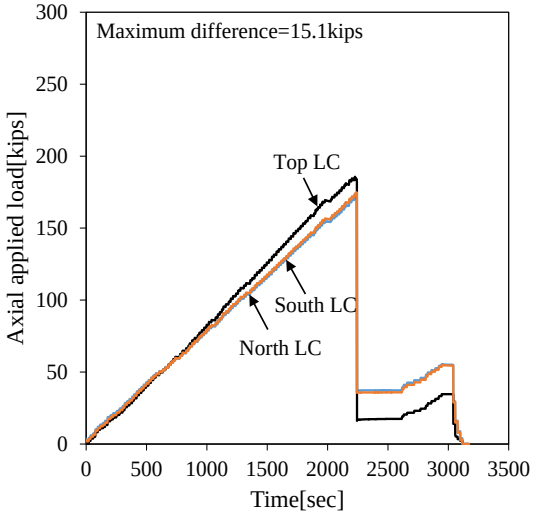

(a) Axial loads measured by three load cells versus time of testing

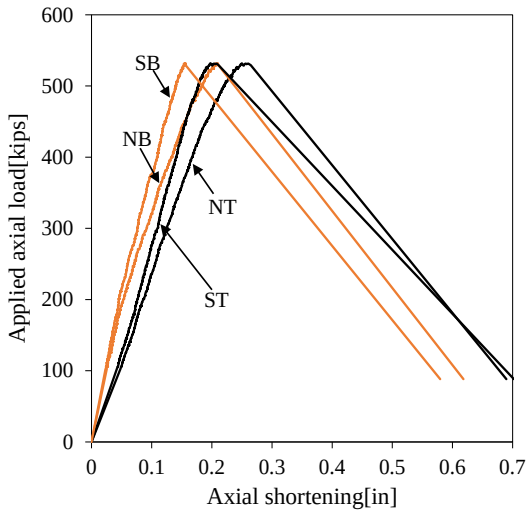

(b) Applied load versus axial deformations measured by four string potentiometers

Figure B.16 Test data of Pile 80/60/3-S

APPENDIX C Specifications of Coatings

In the experimental study of retrofitted piles presented in Chapter 5, two types of coatings that were applied on the steel plates of the proposed repair system were introduced. Their specifications are attached as shown in Figure C.1 through Figure C.8.

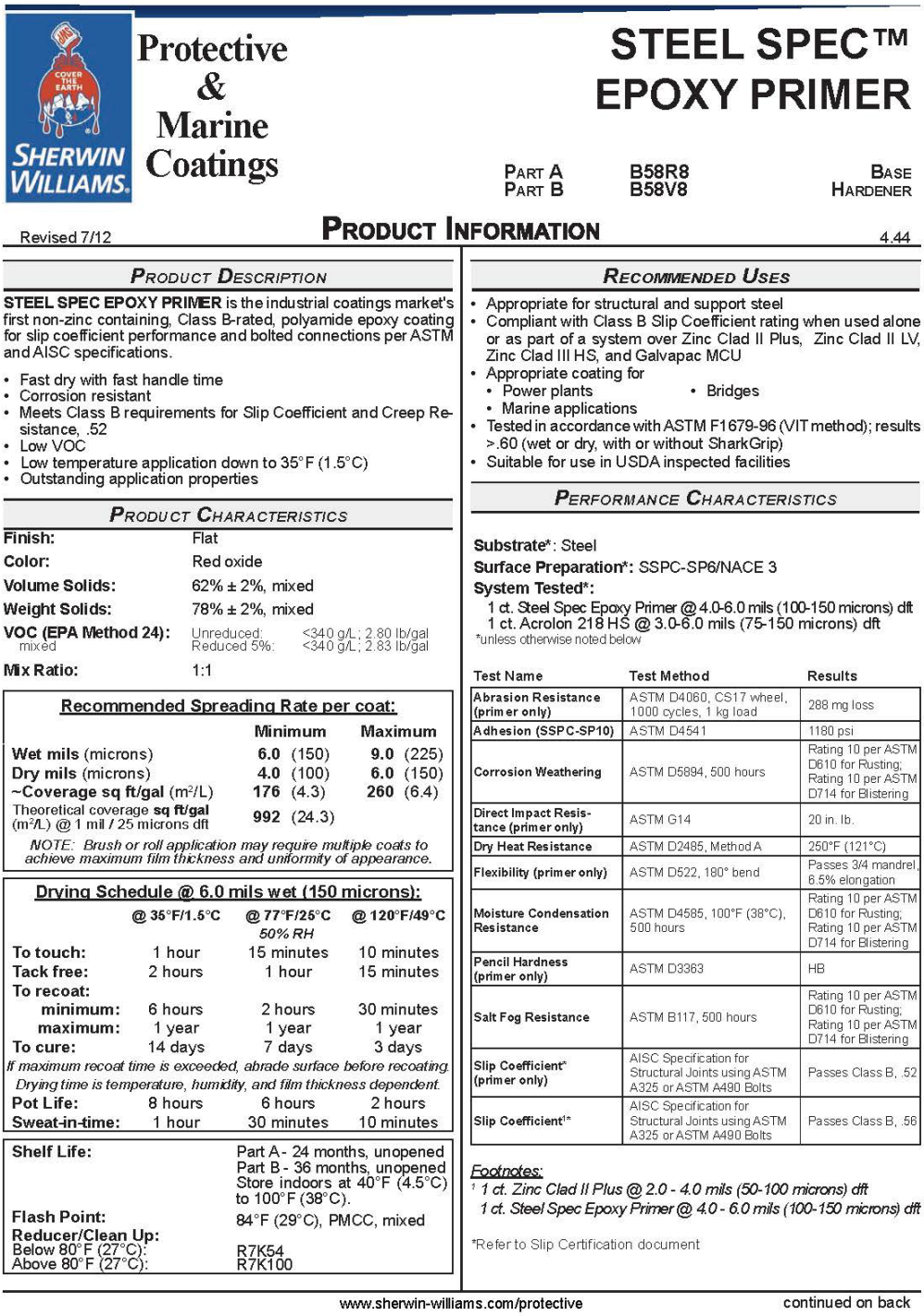

SHERWIN WILLIAMS. COVER THE EARTH

Protective & Marine Coatings

STEEL SPEC™ EPOXY PRIMER

PART A B58R8 BASE
PART B B58V8 HARDENER

Revised 7/12

PRODUCT INFORMATION

4.44

PRODUCT DESCRIPTION

STEEL SPEC EPOXY PRIMER is the industrial coatings market's first non-zinc containing, Class B-rated, polyamide epoxy coating for slip coefficient performance and bolted connections per ASTM and AISC specifications.

- Fast dry with fast handle time
- Corrosion resistant
- Meets Class B requirements for Slip Coefficient and Creep Resistance, .52
- Low VOC
- Low temperature application down to 35°F (1.5°C)
- Outstanding application properties

PRODUCT CHARACTERISTICS

Finish:	Flat
Color:	Red oxide
Volume Solids:	62% ± 2%, mixed
Weight Solids:	78% ± 2%, mixed
VOC (EPA Method 24): mixed	Unreduced: <340 g/L; 2.80 lb/gal Reduced 5%: <340 g/L; 2.83 lb/gal
Mix Ratio:	1:1

Recommended Spreading Rate per coat:

	Minimum	Maximum
Wet mils (microns)	**6.0** (150)	**9.0** (225)
Dry mils (microns)	**4.0** (100)	**6.0** (150)
~Coverage sq ft/gal (m^2/L)	**176** (4.3)	**260** (6.4)
Theoretical coverage **sq ft/gal** (m^2/L) @ 1 mil / 25 microns dft	**992** (24.3)	

NOTE: Brush or roll application may require multiple coats to achieve maximum film thickness and uniformity of appearance.

Drying Schedule @ 6.0 mils wet (150 microns):

	@ 35°F/1.5°C	@ 77°F/25°C 50% RH	@ 120°F/49°C
To touch:	1 hour	15 minutes	10 minutes
Tack free:	2 hours	1 hour	15 minutes
To recoat:			
minimum:	6 hours	2 hours	30 minutes
maximum:	1 year	1 year	1 year
To cure:	14 days	7 days	3 days
Pot Life:	8 hours	6 hours	2 hours
Sweat-in-time:	1 hour	30 minutes	10 minutes

If maximum recoat time is exceeded, abrade surface before recoating. Drying time is temperature, humidity, and film thickness dependent.

Shelf Life:	Part A - 24 months, unopened Part B - 36 months, unopened Store indoors at 40°F (4.5°C) to 100°F (38°C).
Flash Point:	84°F (29°C), PMCC, mixed
Reducer/Clean Up: Below 80°F (27°C): Above 80°F (27°C):	 R7K54 R7K100

RECOMMENDED USES

- Appropriate for structural and support steel
- Compliant with Class B Slip Coefficient rating when used alone or as part of a system over Zinc Clad II Plus, Zinc Clad II LV, Zinc Clad III HS, and Galvapac MCU
- Appropriate coating for
  - Power plants
  - Bridges
  - Marine applications
- Tested in accordance with ASTM F1679-96 (VIT method); results >.60 (wet or dry, with or without SharkGrip)
- Suitable for use in USDA inspected facilities

PERFORMANCE CHARACTERISTICS

Substrate*: Steel
Surface Preparation*: SSPC-SP6/NACE 3
System Tested*:
1 ct. Steel Spec Epoxy Primer @ 4.0-6.0 mils (100-150 microns) dft
1 ct. Acrolon 218 HS @ 3.0-6.0 mils (75-150 microns) dft
*unless otherwise noted below

Test Name	Test Method	Results
Abrasion Resistance (primer only)	ASTM D4060, CS17 wheel, 1000 cycles, 1 kg load	288 mg loss
Adhesion (SSPC-SP10)	ASTM D4541	1180 psi
Corrosion Weathering	ASTM D5894, 500 hours	Rating 10 per ASTM D610 for Rusting; Rating 10 per ASTM D714 for Blistering
Direct Impact Resistance (primer only)	ASTM G14	20 in. lb.
Dry Heat Resistance	ASTM D2485, Method A	250°F (121°C)
Flexibility (primer only)	ASTM D522, 180° bend	Passes 3/4 mandrel, 6.5% elongation
Moisture Condensation Resistance	ASTM D4585, 100°F (38°C), 500 hours	Rating 10 per ASTM D610 for Rusting; Rating 10 per ASTM D714 for Blistering
Pencil Hardness (primer only)	ASTM D3363	HB
Salt Fog Resistance	ASTM B117, 500 hours	Rating 10 per ASTM D610 for Rusting; Rating 10 per ASTM D714 for Blistering
Slip Coefficient* (primer only)	AISC Specification for Structural Joints using ASTM A325 or ASTM A490 Bolts	Passes Class B, .52
Slip Coefficient[1]*	AISC Specification for Structural Joints using ASTM A325 or ASTM A490 Bolts	Passes Class B, .56

Footnotes:
[1] *1 ct. Zinc Clad II Plus @ 2.0 - 4.0 mils (50-100 microns) dft*
1 ct. Steel Spec Epoxy Primer @ 4.0 - 6.0 mils (100-150 microns) dft

*Refer to Slip Certification document

www.sherwin-williams.com/protective

continued on back

Figure C.1 Steel spec epoxy primer-1

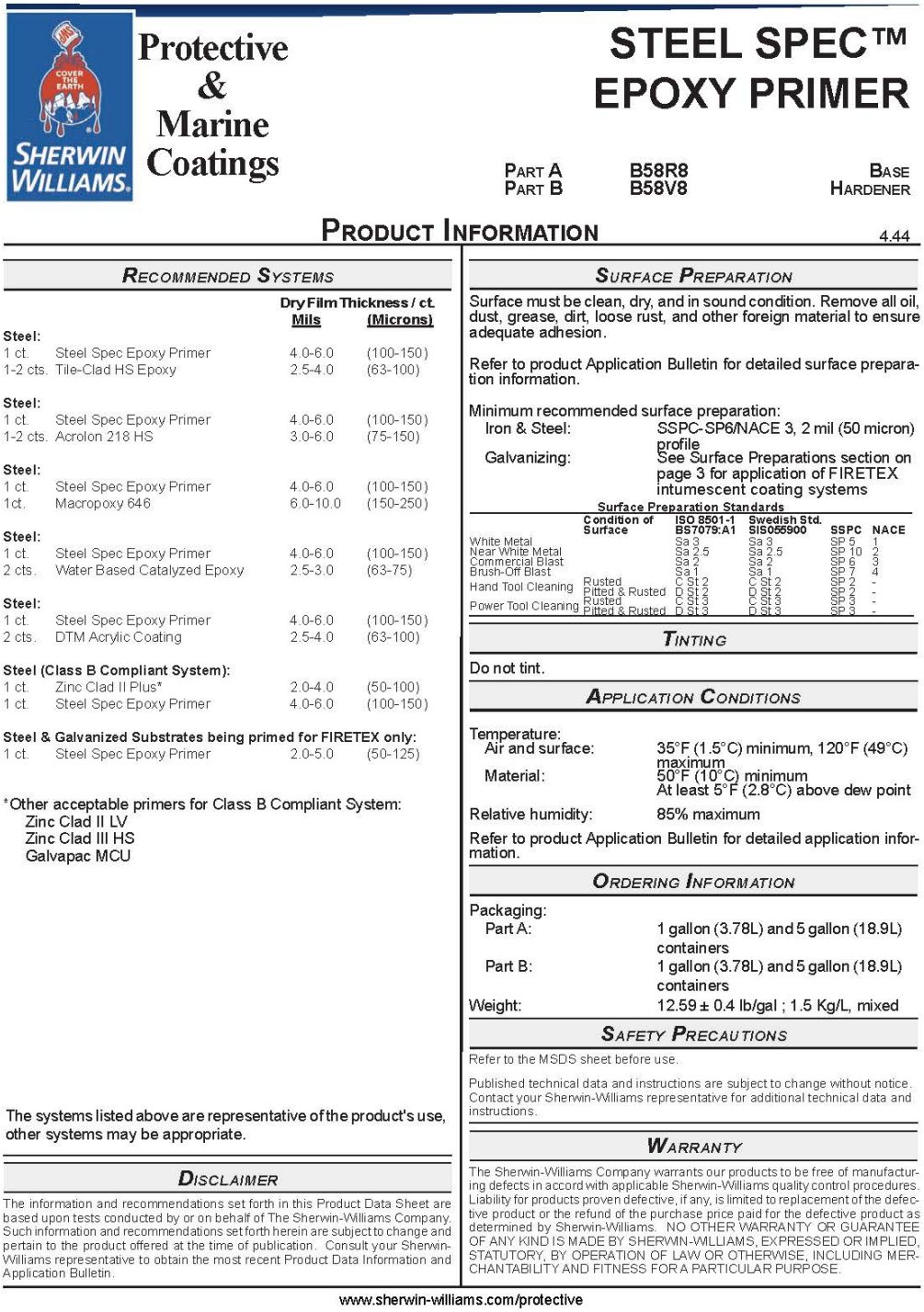

Protective & Marine Coatings

STEEL SPEC™ EPOXY PRIMER

PART A B58R8 BASE
PART B B58V8 HARDENER

PRODUCT INFORMATION

4.44

RECOMMENDED SYSTEMS

		Dry Film Thickness / ct. Mils	(Microns)
Steel:			
1 ct.	Steel Spec Epoxy Primer	4.0-6.0	(100-150)
1-2 cts.	Tile-Clad HS Epoxy	2.5-4.0	(63-100)
Steel:			
1 ct.	Steel Spec Epoxy Primer	4.0-6.0	(100-150)
1-2 cts.	Acrolon 218 HS	3.0-6.0	(75-150)
Steel:			
1 ct.	Steel Spec Epoxy Primer	4.0-6.0	(100-150)
1ct.	Macropoxy 646	6.0-10.0	(150-250)
Steel:			
1 ct.	Steel Spec Epoxy Primer	4.0-6.0	(100-150)
2 cts.	Water Based Catalyzed Epoxy	2.5-3.0	(63-75)
Steel:			
1 ct.	Steel Spec Epoxy Primer	4.0-6.0	(100-150)
2 cts.	DTM Acrylic Coating	2.5-4.0	(63-100)
Steel (Class B Compliant System):			
1 ct.	Zinc Clad II Plus*	2.0-4.0	(50-100)
1 ct.	Steel Spec Epoxy Primer	4.0-6.0	(100-150)
Steel & Galvanized Substrates being primed for FIRETEX only:			
1 ct.	Steel Spec Epoxy Primer	2.0-5.0	(50-125)

*Other acceptable primers for Class B Compliant System:
Zinc Clad II LV
Zinc Clad III HS
Galvapac MCU

The systems listed above are representative of the product's use, other systems may be appropriate.

DISCLAIMER

The information and recommendations set forth in this Product Data Sheet are based upon tests conducted by or on behalf of The Sherwin-Williams Company. Such information and recommendations set forth herein are subject to change and pertain to the product offered at the time of publication. Consult your Sherwin-Williams representative to obtain the most recent Product Data Information and Application Bulletin.

SURFACE PREPARATION

Surface must be clean, dry, and in sound condition. Remove all oil, dust, grease, dirt, loose rust, and other foreign material to ensure adequate adhesion.

Refer to product Application Bulletin for detailed surface preparation information.

Minimum recommended surface preparation:
Iron & Steel: SSPC-SP6/NACE 3, 2 mil (50 micron) profile
Galvanizing: See Surface Preparations section on page 3 for application of FIRETEX intumescent coating systems

Surface Preparation Standards

Condition of Surface		ISO 8501-1 BS7079:A1	Swedish Std. SIS055900	SSPC	NACE
White Metal		Sa 3	Sa 3	SP 5	1
Near White Metal		Sa 2.5	Sa 2.5	SP 10	2
Commercial Blast		Sa 2	Sa 2	SP 6	3
Brush-Off Blast		Sa 1	Sa 1	SP 7	4
Hand Tool Cleaning	Rusted	C St 2	C St 2	SP 2	-
	Pitted & Rusted	D St 2	D St 2	SP 2	-
Power Tool Cleaning	Rusted	C St 3	C St 3	SP 3	-
	Pitted & Rusted	D St 3	D St 3	SP 3	-

TINTING

Do not tint.

APPLICATION CONDITIONS

Temperature:
Air and surface: 35°F (1.5°C) minimum, 120°F (49°C) maximum
Material: 50°F (10°C) minimum
At least 5°F (2.8°C) above dew point
Relative humidity: 85% maximum

Refer to product Application Bulletin for detailed application information.

ORDERING INFORMATION

Packaging:
Part A: 1 gallon (3.78L) and 5 gallon (18.9L) containers
Part B: 1 gallon (3.78L) and 5 gallon (18.9L) containers
Weight: 12.59 ± 0.4 lb/gal ; 1.5 Kg/L, mixed

SAFETY PRECAUTIONS

Refer to the MSDS sheet before use.

Published technical data and instructions are subject to change without notice. Contact your Sherwin-Williams representative for additional technical data and instructions.

WARRANTY

The Sherwin-Williams Company warrants our products to be free of manufacturing defects in accord with applicable Sherwin-Williams quality control procedures. Liability for products proven defective, if any, is limited to replacement of the defective product or the refund of the purchase price paid for the defective product as determined by Sherwin-Williams. NO OTHER WARRANTY OR GUARANTEE OF ANY KIND IS MADE BY SHERWIN-WILLIAMS, EXPRESSED OR IMPLIED, STATUTORY, BY OPERATION OF LAW OR OTHERWISE, INCLUDING MERCHANTABILITY AND FITNESS FOR A PARTICULAR PURPOSE.

www.sherwin-williams.com/protective

Figure C.2 Steel spec epoxy primer-2

Protective & Marine Coatings

STEEL SPEC™ EPOXY PRIMER

PART A B58R8 BASE
PART B B58V8 HARDENER

Revised 7/12

APPLICATION BULLETIN

4.44

SURFACE PREPARATIONS

Surface must be clean, dry, and in sound condition. Remove all oil, dust, grease, dirt, loose rust, and other foreign material to ensure adequate adhesion.

Iron & Steel:
Remove all oil and grease from surface by Solvent Cleaning per SSPC-SP1. Minimum surface preparation is Commercial Blast Cleaning per SSPC-SP6/NACE 3. For better performance, use Near White Metal Blast Cleaning per SSPC-SP10/ NACE 2. Blast clean all surfaces using a sharp, angular abrasive for optimum surface profile (2 mils / 50 microns). Remove all weld spatter and round all sharp edges. Prime any bare steel within 8 hours or before flash rusting occurs.

Galvanized Steel
In preparing galvanized steel substrates for the application of FIRETEX intumescent coating systems, Surface Preparation Specification SSPC-SP 16 must be followed obtaining a surface profile of minimum 1.5 mils (38 microns). Optimum surface profile will not exceed 2.0 mils (50 microns).

Surface Preparation Standards

	Condition of Surface	ISO 8501-1 BS7079:A1	Swedish Std. SIS055900	SSPC	NACE
White Metal		Sa 3	Sa 3	SP 5	1
Near White Metal		Sa 2.5	Sa 2.5	SP 10	2
Commercial Blast		Sa 2	Sa 2	SP 6	3
Brush-Off Blast		Sa 1	Sa 1	SP 7	4
Hand Tool Cleaning	Rusted	C St 2	C St 2	SP 2	-
	Pitted & Rusted	D St 2	D St 2	SP 2	-
Power Tool Cleaning	Rusted	C St 3	C St 3	SP 3	-
	Pitted & Rusted	D St 3	D St 3	SP 3	-

APPLICATION CONDITIONS

Temperature:
Air and surface: 35°F (1.5°C) minimum, 120°F (49°C) maximum
Material: 50°F (10°C) minimum
At least 5°F (2.8°C) above dew point

Relative humidity: 85% maximum

APPLICATION EQUIPMENT

The following is a guide. Changes in pressures and tip sizes may be needed for proper spray characteristics. Always purge spray equipment before use with listed reducer. Any reduction must be compliant with existing VOC regulations and compatible with the existing environmental and application conditions.

Reducer/Clean Up
Below 80°F (27°C) R7K54
Above 80°F (27°C).....R7K100

Airless Spray
Pressure.....2400 psi
Hose.....1/4" ID
Tip.....017" - .021"
Filter.....60 mesh
Reduction.....As needed up to 5% by volume

Brush
Brush.....Natural Bristle
Reduction.....Not recommended

Roller
Cover.....3/8" - 1/2" woven with solvent resistant core
Reduction.....Not recommended

If specific application equipment is not listed above, equivalent equipment may be substituted.

continued on back

Figure C.3 Steel spec epoxy primer-3

Protective & Marine Coatings

STEEL SPEC™ EPOXY PRIMER

PART A B58R8 BASE
PART B B58V8 HARDENER

APPLICATION BULLETIN

4.44

APPLICATION PROCEDURES

Surface preparation must be completed as indicated.

Mixing Instructions: Mix contents of each component thoroughly with low speed power agitation. Make certain no pigment remains on the bottom of the cans. Then combine one part by volume of Part A with one part by volume of Part B. Thoroughly agitate the mixture with power agitation. Allow the material to sweat-in as indicated prior to application. Re-stir before using.

If reducer solvent is used, add only after both components have been thoroughly mixed, after sweat-in.

Apply paint at the recommended film thickness and spreading rate as indicated below:

Recommended Spreading Rate per coat:

	Minimum	Maximum
Wet mils (microns)	**6.0** (150)	**9.0** (225)
Dry mils (microns)	**4.0** (100)	**6.0** (150)
~Coverage sq ft/gal (m^2/L)	**176** (4.3)	**260** (6.4)
Theoretical coverage **sq ft/gal** (m^2/L) @ 1 mil / 25 microns dft	**992** (24.3)	

NOTE: Brush or roll application may require multiple coats to achieve maximum film thickness and uniformity of appearance.

Drying Schedule @ 6.0 mils wet (150 microns):

	@ 35°F/1.5°C	@ 77°F/25°C 50% RH	@ 120°F/49°C
To touch:	1 hour	15 minutes	10 minutes
Tack free:	2 hours	1 hour	15 minutes
To recoat:			
minimum:	6 hours	2 hours	30 minutes
maximum:	1 year	1 year	1 year
To cure:	14 days	7 days	3 days
Pot Life:	8 hours	6 hours	2 hours
Sweat-in-time:	1 hour	30 minutes	10 minutes

If maximum recoat time is exceeded, abrade surface before recoating.
Drying time is temperature, humidity, and film thickness dependent.

Application of coating above maximum or below minimum recommended spreading rate may adversely affect coating performance.

CLEAN UP INSTRUCTIONS

Clean spills and spatters immediately with Reducer R7K54 (below 80°F / 27°C) or R7K100 (above 80°F / 27°C). Clean tools immediately after use with Reducer R7K54 (below 80°F / 27°C) or R7K100 (above 80°F / 27°C). Follow manufacturer's safety recommendations when using any solvent.

DISCLAIMER

The information and recommendations set forth in this Product Data Sheet are based upon tests conducted by or on behalf of The Sherwin-Williams Company. Such information and recommendations set forth herein are subject to change and pertain to the product offered at the time of publication. Consult your Sherwin-Williams representative to obtain the most recent Product Data Information and Application Bulletin.

PERFORMANCE TIPS

Stripe coat all crevices, welds, and sharp angles to prevent early failure in these areas.

When using spray application, use a 50% overlap with each pass of the gun to avoid holidays, bare areas, and pinholes. If necessary, cross spray at a right angle

Spreading rates are calculated on volume solids and do not include an application loss factor due to surface profile, roughness or porosity of the surface, skill and technique of the applicator, method of application, various surface irregularities, material lost during mixing, spillage, overthinning, climatic conditions, and excessive film build.

Excessive reduction of material can affect film build, appearance, and adhesion.

Excessive film build, poor ventilation, and cool temperatures may cause solvent entrapment and premature coating failure.

Do not mix previously catalyzed material with new.

Do not apply the material beyond recommended pot life.

Material must be at least 50° F (10°C) prior to catalyzing.

Refer to Product Information sheet for additional performance characteristics and properties.

SAFETY PRECAUTIONS

Refer to the MSDS sheet before use.

Published technical data and instructions are subject to change without notice. Contact your Sherwin-Williams representative for additional technical data and instructions.

WARRANTY

The Sherwin-Williams Company warrants our products to be free of manufacturing defects in accord with applicable Sherwin-Williams quality control procedures. Liability for products proven defective, if any, is limited to replacement of the defective product or the refund of the purchase price paid for the defective product as determined by Sherwin-Williams. NO OTHER WARRANTY OR GUARANTEE OF ANY KIND IS MADE BY SHERWIN-WILLIAMS, EXPRESSED OR IMPLIED, STATUTORY, BY OPERATION OF LAW OR OTHERWISE, INCLUDING MERCHANTABILITY AND FITNESS FOR A PARTICULAR PURPOSE.

www.sherwin-williams.com/protective

Figure C.4 Steel spec epoxy primer-4

SHERWIN WILLIAMS.

Protective & Marine Coatings

ZINC CLAD® II ETHYL SILICATE
INORGANIC ZINC-RICH COATING

PART E	B69V3	BINDER
PART F	B69D11	ZINC DUST

Revised 8/12

PRODUCT INFORMATION

6.02

PRODUCT DESCRIPTION

ZINC CLAD II ETHYL SILICATE is a solvent-based two-package, inorganic ethyl silicate, zinc-rich coating.

- Meets Class B requirements for Slip Coefficient and Creep Resistance, .56
- Meets AASHTO M-300 specification
- 85% zinc content in dry film
- Coating self-heals to resume protection if damaged
- Provides cathodic/sacrificial protection by the same mechanism as galvanizing. Also protects steel by forming an inorganic moisture and solvent barrier

PRODUCT CHARACTERISTICS

Finish:	Flat
Color:	Gray-green
Volume Solids:	62% ± 2%, ASTM D2697, mixed
Weight Solids:	82% ± 2 %, mixed
VOC (calculated): mixed	Unreduced: <500 g/L; 4.17 lb/gal Reduced 10%: <500 g/L; 4.17 lb/gal
Zinc Content in Dry Film:	85% by weight
Mix Ratio:	2 components; premeasured 5 gallons (18.9L) mix

Recommended Spreading Rate per coat:

	Minimum	Maximum
Wet mils (microns)	**3.5** (88)	**6.5** (163)
Dry mils (microns)	**2.0** (50)	**4.0** (100)
~Coverage sq ft/gal (m^2/L)	**248** (6.1)	**496** (12.2)
Theoretical coverage **sq ft/gal** (m^2/L) @ 1 mil / 25 microns dft	**995** (24.3)	

Dry film thickness in excess of 6.0 mils (150 microns) per coat is not recommended.

NOTE: Brush or roll application may require multiple coats to achieve maximum film thickness and uniformity of appearance.

Drying Schedule @ 5.0 mils wet (125 microns):

	@ 55°F/13°C	@ 77°F/25°C 50% RH	@ 100°F/38°C
Rain resistant:	1 hour	20-30 minutes	15 minutes
To touch:	30 minutes	15 minutes	5 minutes
To handle:	3 hours	1-2 hours	20 minutes
To recoat:	48 hours	18 hours	18 hours
To cure:	7 days	7 days	7 days
Immersion service:	14 days	14 days	14 days

Drying time is temperature, humidity, and film thickness dependent.

Pot Life:	18 hours	8 hours	6 hours

Note: High humidity will shorten the pot life.

Sweat-in-Time: None required

Shelf Life:	Part E: 9 months, unopened Part F: 24 months, unopened Store indoors at 40°F (4.5°C) to 100°F (38°C).
Flash Point:	55°F (13°C), PMCC, mixed
Reducer/Clean Up:	
Below 80°F (27°C):	Xylene, R2K4
Above 80°F (27°C):	Reducer #58, R7K58 or Reducer 100, R2K5

RECOMMENDED USES

For use over properly prepared blasted steel.

- As a one-coat maintenance coating or as a permanent primer for severely corrosive environments (pH range 5-9)
- Economical replacement for galvanizing with similar performance
- Ideal for application at low temperatures or service at high temperatures and/or humidity conditions
- Water intake and discharge lines (non-potable)
- Where abrasion resistance and hardness is required
- Bridges, refineries, drilling rigs
- Shop or field application
- Not recommended for severe acid or alkali exposure
- This product meets specific design requirements for non-safety related nuclear plant applications in Level II, III and Balance of Plant, and DOE nuclear facilities*.
- Nuclear Power Plants
- Nuclear fabrication shops
- DOE Nuclear Fuel Facilities
- DOE Nuclear Weapons Facilities

* Nuclear qualifications are NRC license specific to the facility.

PERFORMANCE CHARACTERISTICS

Substrate*: Steel

Surface Preparation*: SSPC-SP10/NACE 2

System Tested*:

1 ct. Zinc Clad II @ 3.0 mils dft (75 microns)

*unless otherwise noted below

Test Name	Test Method	Results
Abrasion Resistance	ASTM D4060, CS17 wheel, 1000 cycles, 1 kg load	326 mg loss
Adhesion	ASTM D4541	6.77 MPa = 982 lb psi
Direct Impact Resistance	ASTM D2794	60 in. lbs.
Dry Heat Resistance	ASTM D2485	750°F (399°C)
Immersion Resistance (untopcoated)	1 year	Acceptable for: crude oil, fresh and demineralized water, gasoline
Moisure Condensation Resistance	ASTM D4585, 100°F (38°C), 2000 hours	No Failure
Pencil Hardness	ASTM D3363	3H
Radiation Tolerance	ASTM D4082 / ANSI 5.12	Pass at 5 mils (125 microns)
Salt Fog Resistance	ASTM B117, 2000 hours	No Failure
Slip Coefficient* (zinc only)	AISC Specification for Structural Joints Using ASTM A325 or ASTM A490 Bolts	Class B, 0.56
Wet Heat Resistance	Non-immersion	115°F (46°C)

Provides performance comparable to products formulated to Federal Specifications: Mil-P-38336, Mil-P-46105, and SSPC Paint 20.

*Refer to Slip Certification document

continued on back

Figure C.5 Zinc clad II ethyl silicate-1

Protective & Marine Coatings

ZINC CLAD® II ETHYL SILICATE
INORGANIC ZINC-RICH COATING

PART E	B69V3	BINDER
PART F	B69D11	ZINC DUST

PRODUCT INFORMATION

6.02

RECOMMENDED SYSTEMS

		Dry Film Thickness / ct. Mils	(Microns)
Steel, Zinc Primer/Finish, immersion or atmospheric:			
1 ct.	Zinc Clad II Ethyl Silicate	2.0-4.0	(50-100)
Steel, Acrylic Topcoat, atmospheric:			
1 ct.	Zinc Clad II Ethyl Silicate	2.0-4.0	(50-100)
2 cts.	DTM Acrylic Coating	2.5-4.0	(63-100)
Steel, Coal Tar Epoxy Topcoat, atmospheric:			
1 ct.	Zinc Clad II Ethyl Silicate	2.0-4.0	(50-100)
1 ct.	Hi-Mil Sher-Tar Epoxy	16.0-20.0	(400-500)
Steel, Epoxy Topcoat, atmospheric:			
1 ct.	Zinc Clad II Ethyl Silicate	2.0-4.0	(50-100)
1-2 cts.	Macropoxy HS	3.0-6.0	(75-150)
Steel, Epoxy Topcoat, atmospheric:			
1 ct.	Zinc Clad II Ethyl Silicate	2.0-4.0	(50-100)
2 cts.	Tile-Clad HS Epoxy	3.0-4.0	(75-100)
Steel, Urethane Topcoat, atmospheric:			
1 ct.	Zinc Clad II Ethyl Silicate	2.0-4.0	(50-100)
1 ct.	Macropoxy HS	3.0-6.0	(75-150)
1 ct.	Sherthane 2K Urethane	2.0-4.0	(50-100)

NOTE: 1 ct. of DTM Wash Primer or Pro-Cryl Universal Primer can be used as an intermediate coat under recommended topcoats to prevent pinholing.

Steel, Class B Compliant System			
1 ct.	Zinc Clad II Ethyl Silicate	2.0-4.0	(50-100)
1 ct.	Steel Spec Epoxy Primer (red)	4.0-6.0	(100-150)
or			
1 ct.	Zinc Clad II Ethyl Silicate	2.0-4.0	(50-100)
FIRETEX ONLY:			
Steel Substrates being primed for FIRETEX only:			
1 ct.	Zinc Clad II Ethyl Silicate	2.0-5.0	(50-125)
1 ct.	Macropoxy 920 Pre-Prime	1.0-2.0	(25-50)

The systems listed above are representative of the product's use, other systems may be appropriate.

DISCLAIMER

The information and recommendations set forth in this Product Data Sheet are based upon tests conducted by or on behalf of The Sherwin-Williams Company. Such information and recommendations set forth herein are subject to change and pertain to the product offered at the time of publication. Consult your Sherwin-Williams representative to obtain the most recent Product Data Information and Application Bulletin.

SURFACE PREPARATION

Surface must be clean, dry, and in sound condition. Remove all oil, dust, grease, dirt, loose rust, and other foreign material to ensure adequate adhesion.

Refer to product Application Bulletin for detailed surface preparation information.

Minimum recommended surface preparation:
Iron & Steel
Atmospheric: SSPC-SP6/ NACE 3, 2 mil (50 micron) profile
Immersion: SSPC-SP10/NACE 2, 2 mil (50 micron) profile

Surface Preparation Standards

	Condition of Surface	ISO 8501-1 BS7079:A1	Swedish Std. SIS055900	SSPC	NACE
White Metal		Sa 3	Sa 3	SP 5	1
Near White Metal		Sa 2.5	Sa 2.5	SP 10	2
Commercial Blast		Sa 2	Sa 2	SP 6	3
Brush-Off Blast		Sa 1	Sa 1	SP 7	4
Hand Tool Cleaning	Rusted	C St 2	C St 2	SP 2	-
	Pitted & Rusted	D St 2	D St 2	SP 2	-
Power Tool Cleaning	Rusted	C St 3	C St 3	SP 3	-
	Pitted & Rusted	D St 3	D St 3	SP 3	-

TINTING

Do not tint.

APPLICATION CONDITIONS

Temperature:	
air and surface:	0°F (-7°C) minimum, 120°F (49°C) maximum
material:	40°F (4.5°C) minimum At least 5°F (2.8°C) above dew point
Relative humidity:	40% - 90% maximum Water misting may be required at humidities below 50%

Refer to product Application Bulletin for detailed application information.

ORDERING INFORMATION

Packaging:	5 gallons (18.9L) mixed
Part E:	3.75 gallons (14.2L) in a 5 gallon (18.9L) can
Part F:	73 lb (33.1 Kg) zinc dust
Weight:	20.9 ± 0.2 lb/gal ; 2.5 Kg/L, mixed

SAFETY PRECAUTIONS

Refer to the MSDS sheet before use.

Published technical data and instructions are subject to change without notice. Contact your Sherwin-Williams representative for additional technical data and instructions.

WARRANTY

The Sherwin-Williams Company warrants our products to be free of manufacturing defects in accord with applicable Sherwin-Williams quality control procedures. Liability for products proven defective, if any, is limited to replacement of the defective product or the refund of the purchase price paid for the defective product as determined by Sherwin-Williams. NO OTHER WARRANTY OR GUARANTEE OF ANY KIND IS MADE BY SHERWIN-WILLIAMS, EXPRESSED OR IMPLIED, STATUTORY, BY OPERATION OF LAW OR OTHERWISE, INCLUDING MERCHANTABILITY AND FITNESS FOR A PARTICULAR PURPOSE.

www.sherwin-williams.com/protective

Figure C.6 Zinc clad II ethyl silicate-2

Protective & Marine Coatings

ZINC CLAD® II ETHYL SILICATE
INORGANIC ZINC-RICH COATING

PART E B69V3 BINDER
PART F B69D11 ZINC DUST

Revised 8/12 **APPLICATION BULLETIN** 6.02

SURFACE PREPARATIONS

Surface must be clean, dry, and in sound condition. Remove all oil, dust, grease, dirt, loose rust, and other foreign material to ensure adequate adhesion.

Zinc rich coatings require direct contact between the zinc pigment in the coating and the metal substrate for optimum performance.

Iron & Steel (atmospheric service)
Remove all oil and grease from surface by Solvent Cleaning per SSPC-SP1. Minimum surface preparation is Commercial Blast Cleaning per SSPC-SP6/NACE 3. For better performance, use Near White Metal Blast Cleaning per SSPC-SP10/NACE 2. Blast clean all surfaces using a sharp, angular abrasive for optimum surface profile (2 mils / 50 microns). Prime any bare steel the same day as it is cleaned or before flash rusting occurs.

Iron & Steel (immersion service)
Remove all oil and grease from surface by Solvent Cleaning per SSPC-SP1. Minimum surface preparation is Near White Metal Blast Cleaning per SSPC-SP10/NACE 2. Blast clean all surfaces using a sharp, angular abrasive for optimum surface profile (2 mils / 50 microns). Remove all weld spatter and round all sharp edges by grinding. Prime any bare steel the same day as it is cleaned or before flash rusting occurs.

Note: If blast cleaning with steel media is used, an appropriate amount of steel grit blast media may be incorporated into the work mix to render a dense, angular 1.5-2.0 mil (38-50 micron) surface profile. This method may result in improved adhesion and performance.

Surface Preparation Standards

	Condition of Surface	ISO 8501-1 BS7079:A1	Swedish Std. SIS055900	SSPC	NACE
White Metal		Sa 3	Sa 3	SP 5	1
Near White Metal		Sa 2.5	Sa 2.5	SP 10	2
Commercial Blast		Sa 2	Sa 2	SP 6	3
Brush-Off Blast		Sa 1	Sa 1	SP 7	4
Hand Tool Cleaning	Rusted	C St 2	C St 2	SP 2	-
	Pitted & Rusted	D St 2	D St 2	SP 2	-
Power Tool Cleaning	Rusted	C St 3	C St 3	SP 3	-
	Pitted & Rusted	D St 3	D St 3	SP 3	-

APPLICATION CONDITIONS

Temperature:
- air and surface: 0°F (-7°C) minimum, 120°F (49°C) maximum
- material: 40°F (4.5°C) minimum
  At least 5°F (2.8°C) above dew point

Relative humidity: 40% - 90% maximum
Water misting may be required at humidities below 50%

APPLICATION EQUIPMENT

The following is a guide. Changes in pressures and tip sizes may be needed for proper spray characteristics. Always purge spray equipment before use with listed reducer. Any reduction must be compliant with existing VOC regulations and compatible with the existing environmental and application conditions.

Reducer/Clean Up
- Below 80°F (27°C) .....Xylene, R2K4
- Above 80°F (27°C).....Reducer #58, R7K58 or Reducer 100, R2K5

Airless Spray
(use Teflon packings and continuous agitation)
- Pressure.....1800 - 2000 psi
- Hose.....3/8" ID
- Tip .....017" - .021"
- Reduction.....As needed up to 10% by volume

Conventional Spray
(continuous agitation required)
- Gun .....Binks 95
- Fluid Nozzle 66
- Air Nozzle.....63PB
- Atomization Pressure.....30 - 40 psi
- Fluid Pressure.....10 - 20 psi
- Reduction.....As needed up to 10% by volume

Keep pressure pot at level of applicator to avoid blocking of fluid line due to weight of material. Blow back coating in fluid line at intermittent shutdowns, but continue agitation at pressure pot.

Brush .....For touch-up only

If specific application equipment is not listed above, equivalent equipment may be substituted.

continued on back

Figure C.7 Zinc clad II ethyl silicate-3

Protective & Marine Coatings

Protective ZINC CLAD® II ETHYL SILICATE
INORGANIC ZINC-RICH COATING

PART E B69V3 BINDER
PART F B69D11 ZINC DUST

APPLICATION BULLETIN 6.02

APPLICATION PROCEDURES

Surface preparation must be completed as indicated.

Zinc Clad II comes in 2 premeasured containers which when mixed provides 5 gallons (18.9L) of read-to-apply material.

Mixing Instructions: Thoroughly agitate Binder Part E using low speed continuous air driven agitation. Slowly mix all of Zinc Dust Part F into all of Binder Part E until mixture is completely uniform. After mixing, pour mixture through 30-60 mesh screen. Mixed material must be used within 8 hours. Do not mix previously mixed material with new.
If reducer solvent is used, add only after both components have been thoroughly mixed.
Continuous agitation of mixture during application is required, otherwise zinc dust will quickly settle out.

Apply paint at the recommended film thickness and spreading rate as indicated below:

Recommended Spreading Rate per coat:

	Minimum	Maximum
Wet mils (microns)	**3.5** (88)	**6.5** (163)
Dry mils (microns)	**2.0** (50)	**4.0** (100)
~Coverage sq ft/gal (m^2/L)	**248** (6.1)	**496** (12.2)
Theoretical coverage **sq ft/gal** (m^2/L) @ 1 mil / 25 microns dft	**995** (24.3)	

Dry film thickness in excess of 6.0 mils (150 microns) per coat is not recommended.

NOTE: Brush or roll application may require multiple coats to achieve maximum film thickness and uniformity of appearance.

Drying Schedule @ 5.0 mils wet (125 microns):

	@ 55°F/13°C	@ 77°F/25°C 50% RH	@ 100°F/38°C
Rain resistant:	1 hour	20-30 minutes	15 minutes
To touch:	30 minutes	15 minutes	5 minutes
To handle:	3 hours	1-2 hours	20 minutes
To recoat:	48 hours	18 hours	18 hours
To cure:	7 days	7 days	7 days
Immersion service:	14 days	14 days	14 days

Drying time is temperature, humidity, and film thickness dependent.

Pot Life:	18 hours	8 hours	6 hours

Note: High humidity will shorten the pot life.
Sweat-in-Time: None required

Application of coating above maximum or below minimum recommended spreading rate may adversely affect coating performance.

CLEAN UP INSTRUCTIONS

Clean spills and spatters immediately with Xylene, R2K4. Clean tools immediately after use with Xylene, R2K4. Follow manufacturer's safety recommendations when using any solvent.

DISCLAIMER

The information and recommendations set forth in this Product Data Sheet are based upon tests conducted by or on behalf of The Sherwin-Williams Company. Such information and recommendations set forth herein are subject to change and pertain to the product offered at the time of publication. Consult your Sherwin-Williams representative to obtain the most recent Product Data Information and Application Bulletin.

PERFORMANCE TIPS

Topcoating: Note minimum cure times at normal conditions before topcoating. Longer drying periods are required if primer cannot be water mist sprayed when humidity is low. Water misting may be required at humidities below 50%.
Occasionally topcoats will pinhole or delaminate from zinc-rich coatings. This is usually due to poor ambient conditions or faulty application of topcoats. This can be minimized by:

- Providing adequate ventilation and suitable application and substrate temperature.
- Avoid dry spray of topcoat.
- If pinholing develops, apply a mist coat of the topcoat, reduced up to 50%. Allow 10 minutes flash off and follow with a full coat.
- Applying a wet full coat, but at minimum film build, prior to applying a complete full coat.

Excessive film build, poor ventilation, and cool temperatures may cause solvent entrapment and premature coating failure.

Any salting on the zinc surface due to weathering exposure must be removed prior to topcoating.

An intermediate coat is recommended to provide uniform appearance of the topcoat.

Stripe coat all crevices, welds, and sharp angles to prevent early failure in these areas.

When using spray application, use a 50% overlap with each pass of the gun to avoid holidays, bare areas, and pinholes. If necessary, cross spray at a right angle.

Spreading rates are calculated on volume solids and do not include an application loss factor due to surface profile, roughness or porosity of the surface, skill and technique of the applicator, method of application, various surface irregularities, material lost during mixing, spillage, overthinning, climatic conditions, and excessive film build.

Excessive reduction of material can affect film build, appearance, and performance.

Do not mix previously catalyzed material with new.

Do not apply the material beyond recommended pot life.

In order to avoid blockage of spray equipment, clean equipment before use or before periods of extended downtime with Xylene, R2K4.

Keep pressure pot at level of applicator to avoid blocking of fluid line due to weight of material. Blow back coating in fluid line at intermittent shutdowns, but continue agitation at pressure pot.

Application above recommended film thickness may result in mud cracking.

Not recommended for severe acid or alkali exposures.

Oil base, alkyd, epoxy ester, and silicone alkyd topcoats are not recommended.

Polyurethane topcoats require a tie coat of catalyzed epoxy or Pro-Cryl Universal Primer.

Topcoats may be applied once 50 MEK double rubs are achieved. No zinc or only slight traces should be visible. Coin hardness test can also be used.

Cured films of inorganic zinc coatings contain no appreciable amounts of combustible materials. Both Fire and Smoke Indices would be expected to approach 0.

Refer to Product Information sheet for additional performance characteristics and properties.

SAFETY PRECAUTIONS

Refer to the MSDS sheet before use.
Published technical data and instructions are subject to change without notice. Contact your Sherwin-Williams representative for additional technical data and instructions.

WARRANTY

The Sherwin-Williams Company warrants our products to be free of manufacturing defects in accord with applicable Sherwin-Williams quality control procedures. Liability for products proven defective, if any, is limited to replacement of the defective product or the refund of the purchase price paid for the defective product as determined by Sherwin-Williams. NO OTHER WARRANTY OR GUARANTEE OF ANY KIND IS MADE BY SHERWIN-WILLIAMS, EXPRESSED OR IMPLIED, STATUTORY, BY OPERATION OF LAW OR OTHERWISE, INCLUDING MERCHANTABILITY AND FITNESS FOR A PARTICULAR PURPOSE.

www.sherwin-williams.com/protective

Figure C.8 Zinc clad II ethyl silicate-4